THE UNIVERSITY OF WARWICK

# Identification of a Binary gas mixture from a single resistive microsensor

Sherzad Al-Khalifa

*Submitted in fulfilment of the requirements*
*for the degree of Doctor of Philosophy*

School of Engineering
University of Warwick

September 2000

# Contents

# List of Figures

# List of Tables

# Acknowledgements

I would like to thank my academic supervisor Professor Julian Gardner for giving me the opportunity of studying in this field and for his constant guidance and support during my PhD research. I am also grateful to all my friends and colleagues for their support and encouragement during the course of this study.

# Declaration

This thesis is presented in accordance with the regulations for the degree of doctor of philosophy. The work described by the author is entirely original and my own unless otherwise indicated.

Part of this work has been presented at the Institute of Physics Sensors and their Applications VIII conference, September 1997, Glasgow, *Characterisation of a Thermal Wave Microsensor for the Intelligent Analysis of Atmospheric Gases*, S Al-Khalifa, J W Gardner, J F Craine.

The following paper has been submitted to *IEE – Sci. Meas. Technol.*

*Identifying atmospheric CO and $NO_2$ using a single thermally modulated resistive microsensor*, Sherzad Al-Khalifa, Julian W. Gardner, Nicolae Bârsan.

# Summary

Increasing concern about the rapid escalation of environmental pollution has led to strong legislation to ensure, for example, that the emission of pollutants from vehicles and industries is controlled to an acceptable level. As a consequence, there has been a rapid expansion of research into developing more efficient and low-cost gas monitoring systems.

Currently, commercial solid-state atmospheric gas detection systems are based on one sensor for each gas, while research systems are an array of sensors for the detection of multiple gases. In this research, techniques are developed whereby more than one gas is detected using a single resistive gas sensor.

A novel modulated temperature technique was used to enhance the selectivity of the resistive $SnO_2$ gas sensor. Fast Fourier transforms was used to extract the Fourier coefficients. These in turn were used as input to neural networks for training and subsequently for prediction purposes. The result has shown that a single doped $SnO_2$ resistive microsensor can be used to classify binary gas mixture in air.

The research objectives have been fulfilled in that a novel way in detecting the components and the concentration level of a binary gas mixture was developed. Additionally, a low-cost low-power intelligent gas monitoring system was designed. This included the design of a novel temperature/thermometer circuit.

# Abbreviations

| | |
|---|---|
| ADC | Analogue to digital converter |
| ANN | Artificial neural network |
| BAW | Bulk acoustic wave |
| BP | Back-propagation |
| BPN | Back-propagation neural network |
| DAC | Digital to analogue converter |
| DAQ | Data acquisition |
| EC | Electrochemical |
| FFT | Fast Fourier Transform |
| LPCVD | Low pressure chemical vapour deposition |
| MLP | Multi-layer perceptron |
| MOS | Metal oxide semiconductor |
| OSN | Olfactory sensory neurone |
| PARC | Pattern recognition |
| PCA | Principle components analysis |
| RH | Relative humidity |
| SAW | Surface acoustic wave |
| SRL | Sensors Research Laboratory |
| TTL | Transistor-transistor logic |
| VI | Virtual instrument |

VOC Volatile organic compound

# Glossary of Symbols

| Symbol | Description | Units |
|---|---|---|
| $A$ | Adsorption gas species | - |
| $C$ | Electrical capacitance | F |
| $C$ | Gas concentration | $m^{-3}$ |
| $C_{ext}$ | External gas concentration | $m^{-3}$ |
| $C_x$ | Local gas concentration at $_x$ | $m^{-2}$ |
| $D_A$ | Diffusion coefficient of gas species A | $m^2s^{-1}$ |
| $E$ | Electric field | $V\ m^{-1}$ |
| $F$ | Volumetric flow-rate | $m^3\ s^{-1}$ |
| $F_m$ | Measured volumetric flow-rate | $m^3\ s^{-1}$ |
| $G_c$ | Thermal conductance (convection) | $WK^{-1}$ |
| $G_r$ | Thermal conductance (radiation) | $WK^{-1}$ |
| $h$ | Heat transfer coefficient | $WK^{-1}m^{-2}$ |
| $i$ | Current | A |
| $l$ | Electrode length | m |
| $L_D$ | Debyé length | m |
| $n$ | Electron concentration | $m^{-3}$ |
| $n_b$ | Bulk concentration of electrons | $m^{-3}$ |
| $N$ | Number of active sites | - |

| | | |
|---|---|---|
| $N_x$ | Local number of active sites | - |
| $P_E$ | Electrical power | W |
| $P_H$ | Electrical microheater power | W |
| $R$ | Resistance | Ω |
| $R_B$ | Baseline resistance | Ω |
| $R_H$ | Microheater resistance | Ω |
| $t$ | Time | s |
| $T$ | Temperature | K |
| $T_a$ | Ambient temperature | K |
| $T_H$ | Heater temperature | K |
| $\Delta T$ | Change in temperature | K |
| $V$ | Voltage | V |
| $w$ | Inter-electrode gap | m |
| $x$ | Distance through gas-sensitive film | m |
| $x_d$ | Gas-sensitive material thickness | m |
| $\alpha$ | Temperature coefficient of resistivity | $K^{-1}$ |
| $\delta n$ | Change in number of immobilised electrons | - |
| $\kappa$ | Thermal conductivity | $W\ m^{-1}\ K^{-1}$ |
| $\mu_e$ | Electron mobility | $m^2\ V^{-1}\ s^{-1}$ |
| $\mu_h$ | Hole mobility | $m^2\ V^{-1}\ s^{-1}$ |
| $\theta$ | Site occupancy | - |
| $\rho$ | Electrical resistivity | Ω m |

# Chapter 1. Introduction

## 1. Introduction

The primary aim of this chapter is to outline briefly the background in gas and odour detection and the techniques used in the detection process. The case is summarised for developing a portable gas and odour instrument.

The research objectives and an outline of this thesis are also considered.

### 1.1 Atmospheric gas monitoring

The requirement for sensing hazardous gases and odours has been a preoccupation for many scientists and industrialists for a long time. One of earliest applications in gas sensing was in the mining industry. Here some of the hazardous combustible gases are difficult to detect by smell or sight such as carbon monoxide (CO). The methods used previously to detect combustible gases ranged from [1.1], employing canaries to detect the CO to igniting areas in the mine susceptible to methane (CH4) build-up.

The unreliability of these methods continues to be of concern to science and industry. The increase in atmospheric pollution and an increasing number of requirements for gas detection in many different environments and applications, such as detection of pollutant gases in cars and in aircraft cabins, as well as in industrial establishments. Potential application in medicine, in detecting illness and disease at any early stages, has stimulated an increasing interest in the research and development of gas and odour systems. The legislation of safety levels in occupational environment [1.2] has made it important for the employer to ensure a safe working environment. Therefore the requirement for a reliable, low-cost gas detection system has become increasingly important.

The great majority of gas detection systems produced so far are targeted to detect only one particular gas and are used as gas alarm system (i.e. triggered at a particular ppm level). In addition these systems consumes a large amount of energy which make it difficult to use as a portable system.

In this research an attempt is made to investigate and develop a novel method to produce a gas detection system based on only one gas sensor ($SnO_2$) to identify an individual gas in a binary gas mixture by developing thermal wave technique applied to a microsensor. Since the response of sensor is not linear upon the application of sinusoidal thermal wave, neural networks would be used to extract the relevant data for the purpose of gas identification in a gas mixture.

**1.2 Techniques used in analysing gas sensor signal**

A basic gas sensor system converts the physical gas concentration to an electrical signal. The electrical signal will be filtered, processed and then displayed to the user indicating the gas concentration. Figure 1.1 shows a block diagram for a basic gas monitoring system.

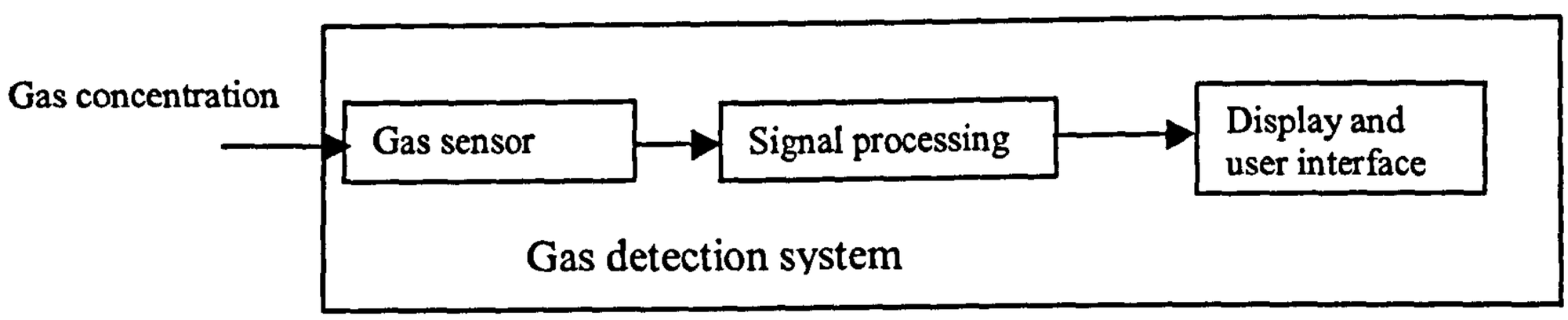


Figure 1.1 Block diagram of a basic gas monitoring system

In a basic gas monitoring system the gas molecule reacts with the surface of the gas sensor which in turn alters the physical characteristics of the sensor material. A block of a typical sensor system is shown in Figure 1.2.

Depending on the sensor type, the change could be resistance, frequency or voltage. These changes on exposure to the sensing material to the gas are filtered and amplified by the electronic circuit. These signals are processed by the software to extract a meaningful result to be presented to the user.

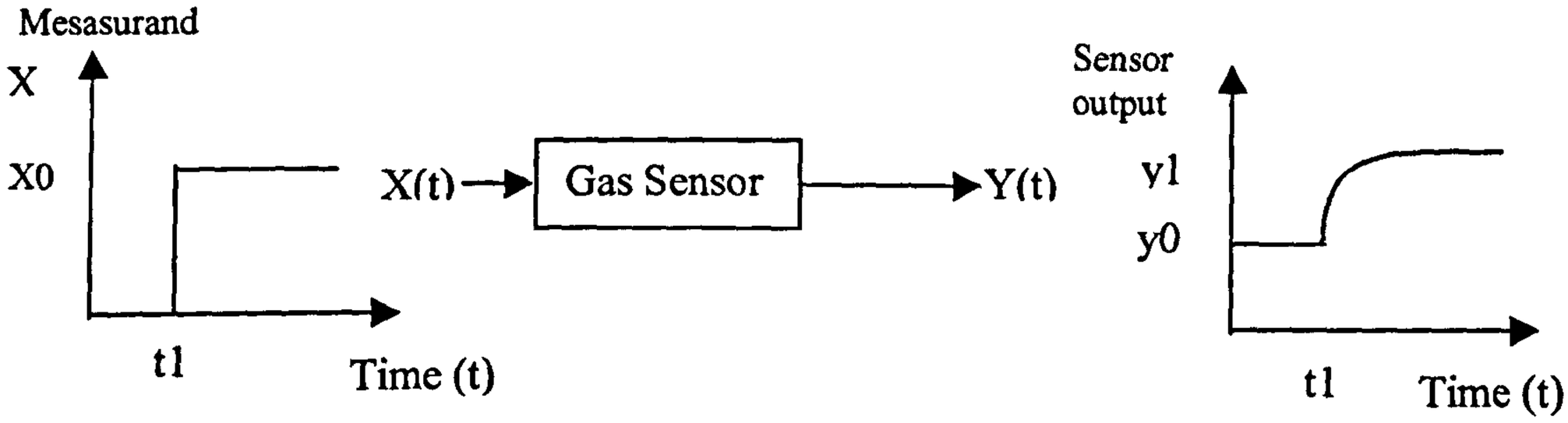


Figure 1.2 A block diagram of a typical response of gas sensor to a step input in measurand

The sensor output y0 in an ideal sensor is constant, as long as the input parameters are constant, such as temperature, humidity and pressure. This output is known as the base-line signal of the sensor. However, if the sensor is exposed to a relevant gas or odour at time t1 then the sensor output will change to a new value exponentially until it reaches the steady state condition at y1. The steady-state response is usually defined as a dimensionless parameter e.g. $\frac{\Delta y}{y_0}$. Response times are defined as a certain percentage of the steady state of the sensor response signal e.g. $\tau_{90}$ indicates that the signal has reached 90% of the final response. It is important to remember that the base-line could change even though when ambient conditions such as temperature, humidity and pressure are held constant. This change is known as the drift in the sensor, which could be due to many factors such as poisoning, ageing and other effects such as interfering gases.

The signal from the sensor should be fully reversible, that is the sensor output should go back to the base line output after removing the exposure to the gas. Ideally the sensor should be sensitive to one type of gas species, but in a real situation the sensor could respond to more that one species. However, if the response of the sensor is much greater to exposure to a particular species, then the sensor is regarded as specific. Owing to the need for gas detection systems in a large number of applications, such as industrial environment, aircraft cabins [1.3] medical applications, food industry, customs control, quality control in wine and perfume and other applications has promoted the development of chemical sensors that employs a wide variety of technologies and materials [1.4]. In most cases the gas sensors have to be used in specially designed electronic circuits and software packages such as neural networks or characteristic look-up tables to compensate for the shortcomings of the sensor technology.

## 1.3 Research objectives

The main objectives of this research are:

- Investigate the use of one resistive sensor for binary gas identifications as opposed to an array of gas sensors..
- To characterise the $SnO_2$ resistive gas sensor to the CO and $NO_2$ gases, by using thermal wave signals.
- To signal process sensor outputs response.
- To use neural networks to analyse the data produced when sensor subjected to sinusoidal heat wave.

- To incorporate the developed techniques into an intelligent microcontroller based portable instrument.

## 1.4 Outline of the thesis

The thesis describes the design and development of circuitry associated with sensor resistive measurement, signal-processing techniques and data processing to be used for a low power hand held gas monitor instrument.

Chapter 1 summarises requirement and application for gas monitoring systems and also methods used in analysing gas sensor signals were introduced.

Chapter 2 introduces conventional and chemical sensors including thin and thick film devices as well as doping effect on $SnO_2$ characterisation. Chapter 3 the fabrication of microsensors was outlined. Chapter 4 the theory of thermally modulated gas sensor was described. Chapter 5 describes the characterisation of the sensors being used in this research, also the detailed design, development and testing of virtual instrumentation. Chapter 6 describes the signal processing techniques and the use of the neural networks to extract the relevant signal of interest. Chapter 7 details the design and development of the intelligent microcontroller based hand-held gas monitoring system. Chapter 8 gives a general conclusion and future work.

## 1.5 References

1.1 Anon., Monitoring the Atmosphere in Underground Mines, Mining Magazine, December, 1988, 483-487.

1.2 Healyh and Safety Executive, *EH40/96 Occupational Exposure Limits 1996*, HMSO, London, 1996.

1.3 Ray Munn, *The aircraft cabin environment*, Thirteenth Colloquium of Gas Analysis and sensors Group, 1998.

1.4 A. C. Pike, *Design of chemoresistive silicon sensors for application in gas monitoring,* Ph.D. Thesis, University of Warwick, UK, 1996.

# Chapter 2. Review of gas sensors

## 2.1 Introduction

The main aim of this chapter is to review the field of conventional sensors and then discus chemical microsensors and their mechanisms. There are many types of gas sensors, which are used, in a wide range of applications in fields as diverse as domestic gas alarm, pollution detection, medical applications and many other applications. There are also, many research teams in different countries developing sensor materials with better sensitivities and selectivities to a particular gas. The main objectives of manufacturing gas sensors are:

- High sensor specificity towards a particular gas or odour
- High reliability and repeatability of the sensor
- Production of intelligent or smart sensors
- Low cost
- Longetivity and Robustness

## 2.2 Conventional sensors

The need to measure physical phenomena has been of great concern [2.1] for a very long time. These needs have been an extension of human perception and intellect. The produced measurement tools consequently have become an essential part of the scientific analysis of the physical world.

Because of the vast number of sensor types and their applications, it is now common to categorise sensors in terms of the main forms of energy that transfer the signal. Table 2.1 shows the categories of sensors according to the energy forms that carry the signal [2.2] as well as some representative measurands.

**Table 2.1** Categorisation of sensors by signal form.

| **Signal form** | **Measurands** |
|---|---|
| Thermal | Temperature, heat, heat flow, entropy, heat capacity etc |
| Radiation | Gamma rays, X-rays, ultra-violet, visible, infra-red, micro-waves, radio waves, etc. |
| Mechanical | Displacement, velocity, acceleration, force, torque, pressure, mass, flow, acoustic wavelength and amplitude etc. |
| Magnetic | Magnetic field, flux, magnetic moment, magnetisation, magnetic permeability etc. |
| Chemical | Humidity, pH level and ions, concentration of gases, vapours and odours, toxic and flammable materials, pollutants etc. |
| Biological | Sugars, proteins, hormones, antigens etc |
| Electrical | Charge, current, voltage, resistance, conductance, capacitance, inductance, dielectric permittivity, polarisation, frequency etc |

### 2.2.1 Chemical microsensor

The devices, which are capable of converting a chemical quantity into an electrical signal, are referred to as chemical sensors. These chemical microsensors may detect the presence of $NO_2$ in air as in a gas sensor, or water molecules in air as in a humidity sensor. The presence of a more complex molecule, such as sugar or protein in liquid, is also possible by using a chemical sensor [2.2].

The need for monitoring all aspects of our environment is increasing rapidly. This has been brought about by our increasing concern with environmental pollution and legislation on health and safety [2.3]. There is also a drive to produce sensors with the

ability of detecting much lower limits than possible now. As a consequence of this need and desire to monitor everything in our world, a huge input of time and resources is been allocated into research and development of sensors in a wide range of applications.

A sensor, which is capable of responding to a particular analyte, in a controlled way through a chemical reaction, is called a chemical sensor.

There are ranges of chemical sensors, which are categorised into different groups or classes. Table 2.2 shows chemical sensors classified by transducer types [2.3].

Table 2.2 Chemical sensors classified by transducer types

| **Transducer** | **Features** |
|---|---|
| Conductometric | These include potentiometric sensors and voltammetric/amperometric |
| Optical | In optical sensors there is a spectroscopic measurement associated with the chemical reaction. Many biosensors make use of optical measurements. Absorbance, reflectance, and luminescence measurements are used in different types of optical sensors. |
| Mass sensitive | These make use of the piezoelectric effect and include devices such as surface acoustic wave (SAW) sensor and are particularly useful as potential gas sensors. They relay on a change in mass on the surface of an oscillation crystal, which shift frequency of oscillation. The extend of the frequency shift is a measure of the amount of material adsorbed on the surface. |
| Heat sensitive | These are often called calorimetric sensors in which the heat of a chemical reaction involving the analyte is monitored with a transducer such as thermister or platinum thermometer. |

The range of chemical sensor applications is enormous. The following are some typical and potential application [2.4] of chemical gas sensors:

- **Motor industry**: It is a well-known fact that motor cars contribute enormously to the increase in air pollution, by emitting by-products of the engine combustion process. These include noxious gases particulate which all have detrimental effects on the environment by increasing the green house effect and it is also harmful for

human and other living things. Sensors have been developed or prototyped for engine control and air quality in car emissions as well as monitoring the air quality inside the car.

- **Aerospace:** The fuel used by [2.5] civil aircraft is kerosene, a fairly pure hydrocarbon with low levels of sulphur retained to maintain the fuel's self-lubricating properties. Incomplete combustion will produce poisonous carbon monoxide, potentially carcinogenic unburned hydrocarbons. Also at hot, high-pressure conditions, the oxygen and nitrogen combine to form oxides of nitrogen, toxic gases, which affect the ozone content of the atmosphere and contribute to acid rain. The pollution in aircraft cabins is large and diverse. The sources of this could be ground fumes from aircraft/ground vehicles emission [2.6] which includes CO, $NO_2$ and hydrocarbons or from the structure of the aircraft such as volatile organic compounds which have their sources from adhesives, sealing compounds, furnishings and engine generated contaminants. All this makes it vital to have sensors monitoring the aircraft cabin and engine emissions.
- **Agriculture:** The extensive use of insecticides, pesticides and a large number of other agriculture and animal husbandry related dangerous chemicals has made it important to monitors these material in this field.
- **Chemical analysis:** Laboratory testing of material and other substances.
- **Safety (flammable and toxic gases):** The extensive use of natural gases for domestic and industrial application, the possibility of incorrect burning of heating and cooking appliances as well as the increased number of flammable materials used in home and work environments makes it vital to use sensors which detect and give early warning to danger of fire and poisonous gases. This area of application is expanding rapidly mainly to detect $CH_4$, CO, $H_2$, $NO_2$, $CO_2$.

- **Process control:** The production of chemical material and goods such as pharmaceuticals and paints may generate dangerous gas by-products, which need to be monitored. The use of chemical sensors in food industry will become increasingly important in controlling the quality of food processing. The perfume industry is another potential field of application.
- **Environmental monitoring:** The detection of pollutants in the air, water and soil becoming increasingly important for health reasons with a need to comply with rules of health and safety legislation.
- **Medicine:** The use of smells as a diagnostic for some illnesses and diseases was apparently widely used by doctors before the use of modern days soaps, shampoos and the extremely wide range of personal hygiene products. The use of specific gas and odour sensors is used in certain applications in this field. The potential for using sensors in diagnostics of certain illnesses and diseases such as throat cancer or the identification of certain bacterium in infected areas.
- **Customs:** The tremendous increase in drug trafficking across the borders and its abuse by a large number of people, makes the development of a gas sensor specifically targeted to detect extremely low levels of a range of drugs, of great interest for customs and police across the world [2.7]. Additionally developing gas sensors to detect minute signs from concealed bomb and other plastic explosives would be of interest to customs and police.

The use and application of gas and odour sensors are bound to increase in almost all aspects of life. The actual market and the application will no doubt be increasing over the next few years.

## 2.3 Metal oxide semiconductor (MOS) materials

There are a number of MOS materials, which have shown responses to a particular gas. Semiconductor materials, which adsorb gases onto its surface, can produce a significant change to its resistivity. This effect has been noticed in a number of MOS materials such as ZnO, $TiO_2$ and $In_2O_3$ [2.2]. The most widely used and understood of MOS material is tin dioxide ($SnO_2$). The gas sensing mechanism of $SnO_2$ is based on surface reaction with the gas of interest. This reaction produces a few oxygen species at different temperatures and oxygen pressure such as $O^-$, $O^-_2$, $O^{2-}$. More details of this will be discussed below. When a sensor of this type is exposed to a particular gas it will change the electrical conductivity of the sensing film as mentioned above. This type of sensor is generally called a chemoresistor. Figure 2.1 shows the general structure of a chemoresistive gas sensor with a constant current supply.

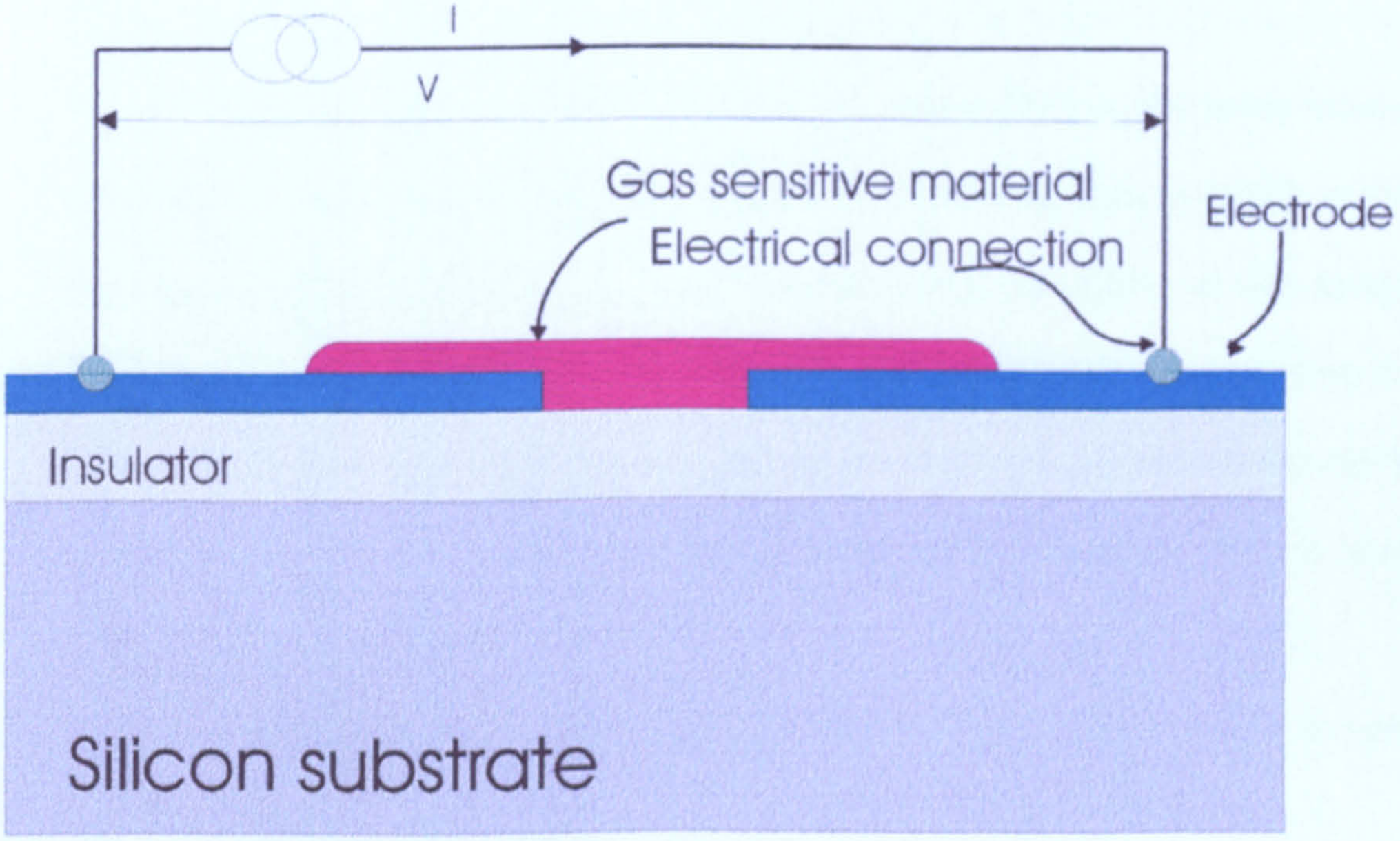


Figure 2.1 General structure of a chemoresistive sensor with a constant current supply.

### 2.3.1 Thin film

In general the structure of $SnO_2$ deposited by thin film techniques are shown [2.7] to be polycrystalline with randomly oriented crystallites. These crystallites size are shown to be dependent on the deposition process and post–thermal processing.

In thin film the changes of the electric conductivity is achieved in the surface region of the thin film layer in contact with the gases. In thin film structure the width of the depletion layer $L_D$ covers the whole of the thickness of the film, and because of this the concentration of electron changes dramatically within the nanocrystals when exposed to adsorbing species. The mechanism of effecting [2.7] conduction at the intercrystallite region has been generally modelled as a potential barrier across which a charge has to pass.

### 2.3.2 Thick film

The gas sensitive part of any chemoresistive gas sensor [2.8] is the semiconducting oxide layer deposited on an insulating substrate. The insulating layer is usually made of high purity material otherwise at high temperature the impurities in the substrate material will diffuse into the sensing material, which will affect the sensor operation. This oxide layer usually is connected with two electrodes of good ohmic contact with the oxide layer. A heater is usually positioned underneath to ensure the uniform heating of the oxide-sensing layer.

The sensing material (e.g. $SnO_2$) deposited by thick film deposition technique has shown a large sensitivity to the gases of interest such as CO [2.9] and $NO_2$. These sensors also exhibit poor selectivity as they are sensitive to a large number of gases, therefore a careful examination of the operating conditions of the actual use of these sensors should be taken into consideration. The sensitivity of these sensors cannot

be explained by a single-crystal thin film model [2.11]. Hence, other mechanisms have been put forward, which are associated [2.7] with material morphology. The porous thick film structure of $SnO_2$ usually consists of grains with an average size of ~ 3 μm. The structure of these grains consists of nanocrystals of 5 – 30 nm diameter [2.12] and it is these that determine the gas sensitivity. Because of the porous nature of the thick film the gas of interest can therefore diffuse through the film. Consequently it may be adsorb with the internal site [2.7].

## 2.4 Mechanism of gas sensing in SnO2

The total change in conductance of a $SnO_2$ with gas concentration in the atmosphere is a function of a number of mechanisms. In clean air, oxygen is chemically adsorbed onto the surface of a metal oxide grains [2.11]. As a result of this electrons will be removed from the conducting band of the semiconductor, which then results in an increase in the resistivity. Subsequently when a combustible gas reaches the grain surface it will react with the chemisorbed oxygen already there. This process will inject electrons into the semiconductor by removing, the adsorbed oxygen which in turn causes a decrease in the resistivity of the sensor. The oxygen chemisorbed onto the surface of a MOS sensor removes electron from the bulk so forming of negatively charged species, $O_2^-$, $O^-$ and $O^{2-}$ according to [2.10],

$$O_2 + e^- \Leftrightarrow (O^-_2)_{ads} \qquad (2.1)$$

$$(O^-_2)_{ads} + e^- \Leftrightarrow (2O^-)_{ads} \qquad (2.2)$$

$$(O^-)_{ads} + e^- \Leftrightarrow (O^{2-})_{lat} \qquad (2.3)$$

At about 150°C, $O^-$ species is predominant the other two usually appear at about 400°C. At higher temperatures the adsorbed $O^-$ species [2.7] can form an $O^{2-}$ which become stable at a lattice site. This interaction at the surface of the oxide will dominates the mechanism of the change in surface charge concentration. The effect on the depletion layer [2.7] by the interaction with a reducing gas such as CO and an oxidising gas such as $NO_2$ is shown in Figure 2.2 for $SnO_2$.

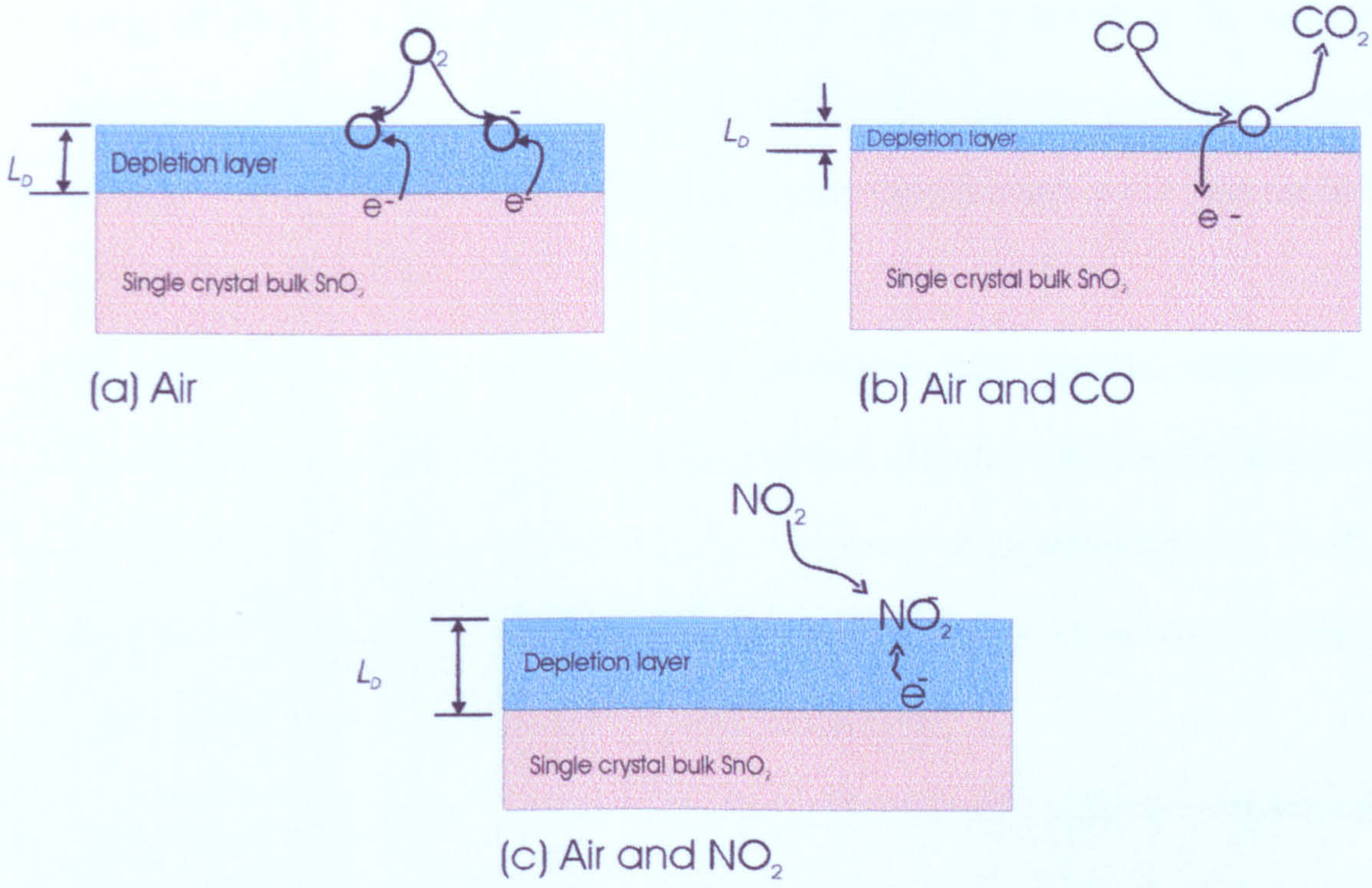


Figure 2.2 Block diagram displaying the depletion layer in a single crystal $SnO_2$ in (a) air, (b) reducing gas (e.g. CO) and (c) oxidising gas (e.g. $NO_2$).

The effect of humidity has been extensively researched and because water vapour exists in most applications of gas sensors [2.14]. An example of an adsorption mechanism with water [2.7] may proceed according to the following formula,

$$H_2O + (O^-)_{ads} \Leftrightarrow 2(OH^-)_{ads} + e^- \qquad (2.4)$$

The mechanisms of gas sensing in a MOS sensor such as $SnO_2$ presented so far are simplified models of a more complex interactive Microsystems. The sensing mechanism is also affected by several other factors such as catalytic additives, temperature, humidity and the presence of varieties of other species in the air and in the oxide layer. It has been shown that the Debyé depth (concentration of adsorbed oxygen ions) has a significant effect on the sensitivity of chemoresistors. To achieve a high sensitivity the Debyé depth should be a significant portion of the overall thickness of the bulk of the oxide layer. This is one reason for using a thin film technique for depositing the oxide-sensing layer. However, some researchers have hypothesised other alternative gas sensing mechanisms.

One of these alternative mechanisms is associated with material structures. The composition of porous $SnO_2$ thick film is composed of grains with average size [2.7] of around ~ 3 μm. These grains in turn are composed of nanocrystals of 5 – 30 nm diameter. The gas of interest can diffuse through the porous oxide layer which may interact with the inside surface of the porous sensing film.

It has been reported that the conductivity of the sensing oxide layer is essentially determined by the boundaries of the oxide nanocrystals. If the grains [2.7] touch but are not sintered, the depletion layer forms a Schottky barrier, over which the charge must thermally [2.2] "hop" over to transfer from one grain to the next as shown in Figure 2.3. More detailed treatment of this is discussed in chapter 4.

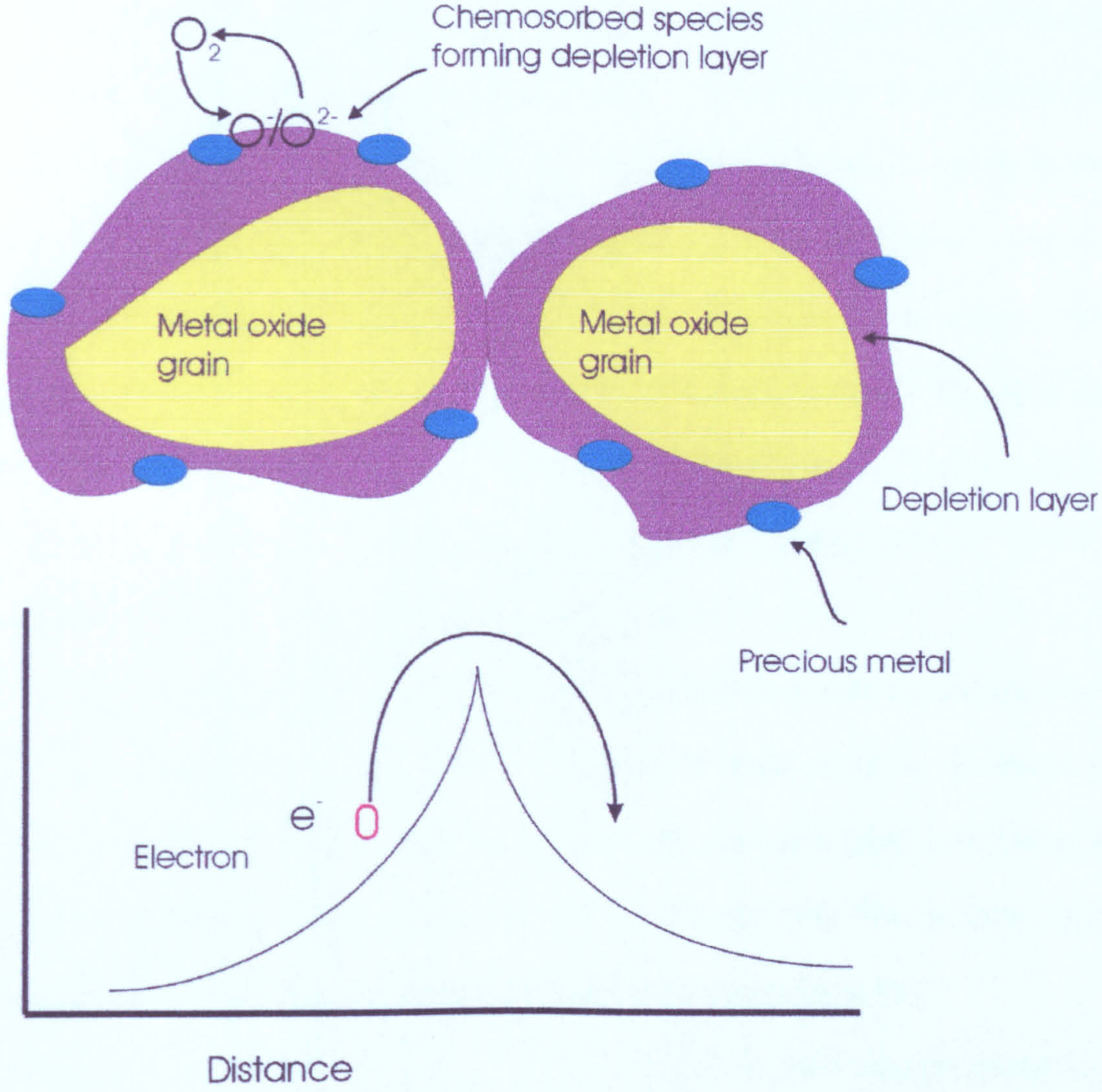


Figure 2.3 Charge transfer mechanism in semiconducting oxide chemoresistor. The top figure shows the presence of catalytic metal on the surface of two oxide grains. The shaded area shows the depletion layer that penetrates the oxide grains formed as a result of chemosorbed atmospheric $O_2$. The bottom figure shows the electronic potential barrier, which forms between the oxide, grains which the electron must "hop" over.

## 2.5 Doping effect on $SnO_2$ characterisation

The high sensitivity of chemoresistive sensors is excellent for many practical applications [2.8]. Poor selectivity unfortunately often accompanies these high sensitivity sensors.

The increase of selectivity of chemoresistive sensors is primarily obtained by careful selection of the catalyst, and the best choice of the operating temperature. There are two interaction mechanisms between the catalyst and the oxide [2.12]. The first one is a

chemical interaction in which the additive assists the redox processes of the sensor oxide contributing to the interaction of the gas which results in an increase in the surface conductivity of the semiconductor. The second interaction is an electronic one $SnO_2$. A Schottky barrier is produced at the contact of some metals whereby the catalysts interact electronically as a source of donor or acceptor with the semiconductors. When these metals come in contact with some reducing gases such as CO, their electronic state, and indirectly also, the conductivity of the surface of the oxide will be changed. This mechanism is explained by the 'spillover' of the ions, which are formed, on the catalyst onto the oxide layer.

There are ranges of additive which are used to modify the sensitivity and the selectivity of the oxide-sensing layer. Some of commonly used catalysts in Metal Oxide Semiconductors, are palladium (Pd), platinum (Pt), and gold (Au). It has been shown that Pd is a potent oxidation additive for both CO and $CH_4$. This additive [2.8] will greatly increase the sensitivity to $CH_4$, but lower the sensitivity to CO.

The operating stability of a sensor may be [2.8] lost by poisoning phenomena, which destroy the performance of the additives. The existence of some components such as lead and phosphorus in the air can adversely affect the sensor responses.

**2.6 Summary**

This chapter has given an outline of the chemical microsensors, including metal oxide thin and thick film. The effect of adding a catalyst to the sensing characterisation of the sensors and the mechanism of gas sensing is discussed. The use of sensors and its applications have been outlined.

The sensing properties of the $SnO_2$ with regard to CO and $NO_2$ have been outlined. As these two gases are of interest to this research, the research will investigate and

characterise the $SnO_2$ response to these. Table 2.3 show the $SnO_2$ resistance response [2.7] to the to gases of interest.

Table 2.3 $SnO_2$ resistance changes in relation with gases of interest.

| Target gas | Behaviour |
|---|---|
| CO | Large decrease in resistance |
| $NO_2$ | Large increase in resistance |
| $H_2O$ | Decrease in resistance |

## 2.7 References

2.1 R. Ohba , *Intelligent Sensor Technology*, Wiley, New York, 1992

2.2 J. W. Gardner, *Microsensors*: *Principles and applications*, John Wiley and Sons, Chichester, 1994

2.3 R. W. Cattrall, Chemical Sensors, Oxford Science Publications, 1997.

2.4 W.Göpel, T. A. Jones, I. Lundstrom Iand T. Seiyama (eds) (1991) *Sensors: A Comprehensive Survey, Vol. 2/3: Chemical and Biochemical Sensors,* VCH publishers, Weinheim, Germany.

2.5 R. Burrows, *Aircraft engine exhaust emissions*, Thirteenth Colloquium of gas analysis and sensing group, 1998.

2.6 R. Munn, *The aircraft cabin environment*, Thirteenth Colloquium of gas analysis and sensing group, 1998.

2.7 A. C. Pike, Design of chemoresistive silicon sensors for application in gas monitoring, *Ph.D. Thesis, University of Warwick, UK, 1996.*

2.8 P. Ciureanu and S. Middelhoek. *Thin Film Resistive Sensors* Institute of Physics Publishing, 1992.

2.8 M. C. Horrillo, J. Gutiérrez, L. Arés, J. I. Robla, I. Sayago, J. Getino and J.A. Agapito, *The influence of the tin-oxide deposition technique on the Sensitivity to CO, Sensors and Actuators* B, 24-25 (1995) 507-511.

2.9 S. R. Morrison, Mechanisim of Semiconductor Gas Sensor Operation, *Sensors and Actuators,* 11 (1987) 283-287

2.10 K. Ihokura and J. Watson, *The Stannic Oxide Gas Sensor*, CRC Press, London, 1994.

2.11 N. Yamazoe, Y. Kurokawa and T. Seiyama, Effects of additives on *Semiconductors Gas Sensors, Sensors and Actuators,* 4 (1983) 283-289.

2.12 Y. Mizokawa, et al., *ESR study of adsorbed oxygen on tin dioxide*, Ouyou Buturi (Jpn. J. Appl. Phys.), 46, 580, 1977.

2.13 P.T. Moseley and B.C. Tofield, *Solid State Gas Sensors*, Adam Hilger, Bristol, 1987.

# Chapter 3 Design and fabrication of microsensor – an overview

## 3.1 Introduction

This chapter outlines the design requirement, processing and technique for chemoresistive sensor fabrication.

A range of chemoresistive sensors with different configurations has been produced in the Sensor Research Laboratory (SRL) at the School of Engineering of the University of Warwick. A list of these sensors together with their properties is [3.1] shown in table 3.1. The choice of MOS gas-sensitive material and its associated deposition process places particular demands on the chemoresistive design [3.1]. These considerations include the structure, geometry, and composition of electrodes, the width and purity of the insulating layer, substrate and the heating element design. The silicon technology is very widely used and understood and also it lends its self to miniturализation, low cost fabrication process and better yields, all this made the use of silicon technology to be used in sensor fabrication. There are also a large number of highly miniaturised electronic circuits such as analogue signal processing, filtering and amplifying and also digital circuits that could be employed in intelligent sensor design like multiplexers and controllers.

Recent development in manufacturing technology of sensors has concentrated on the reduction of sensor sensitivity to humidity and shortening of the break-in time [3.2]. Improvements in the properties of the new sensors have been significantly enhanced compared to older sensors. However, these new sensors (e.g. $Ga_2O_3$) [3.2] suffer a disadvantage, as the working temperature is typically higher than that of $SnO_2$, which means a more demanding heating supply and structural and connection processing.

Table 3.1 Details of chemoresistive sensors produced at SRL.

| SRL Device number | Electrode Gap (μm) | Design details |
|---|---|---|
| 108/CP | 10 | Hex SAD for characterising CP films |
| 108/var | 2.5 to 15 in steps of 2.5 | Hex SAD with variable inter-electrode gaps to investigate the effect of geometry on sensor performance |
| 108/MOS | 10 | Hex SAD with an aspect ratio of ~ 200, suitable for characterising MOS films. |
| 123 | 10 | Discrete devices for characterising CP films |
| 125/CP | 10 | Hex SAD compatible with CP microdeposition technique |
| 125/MOS | 10 | Hex SAD for characterising MOS films with the same design as SRL108/MOS |
| 125/XPc | Triple element SAD employing an electrode aspect ratio of 10,000 to characterise XPc films | |
| 125/Dual | | SAD with three dual sensors to investigate long-term drift properties |
| 127/s10<br>127/s50 | 10<br>50 | Discrete device for characterising CP, 4x4 $mm^2$ with co-planar integrated heater |
| 127/110<br>127/150 | 10<br>50 | Discrete device for characterising CP, 4x10 $mm^2$ with co-planar integrated heater |
| 127/b10<br>127/b50 | 10<br>50 | Bridge arrangement for thermal compensation |

## 3.2 Silicon processing – an outline

Engineering of modern microsensors requires inputs from four [3.3] major areas: micromachining, microfabrication, micromechanics, and microelectronics. The use of

silicon planar technology is usually required in the fabrication of microsensors. Silicon planer integrated circuit fabrication generally [3.3] involves the following processes.

- **Crystal growth and epitaxy**

Generally ICs are produced from large single crystals of silicon made through Czechralski crystal pulling or, if very pure silicon is needed, through a float zone process. Si is an easier material (used extensively in ICs production) to process and is more reliable than gallium arsenide, although gallium arsenide has higher carrier mobility. However, recent developments of metal oxides, such as $Ga_2O_3$, are among the most promising [3.2] in sensor applications.

- **Oxidation and film deposition**

A layer of oxide is grown on the silicon surface. This is achieved by placing the silicon wafer in an oven at 1,100°C containing oxygen. The oxygen dissociates, simultaneously reacting with the silicon and diffuses through the growing $SiO_2$ layer.

- **Diffusion or implantation of dopants**

The MOS structure is normally made on a silicon wafer that has been doped [3.3] with n-type or p-type material. Either thermal diffusion or ion implantation controls the measures of dopants, which are introduced into the silicon wafer. In the thermal diffusion method the wafers are placed in a controlled furnace and an inert gas containing the required dopants is passed over them. In the ion implantation method charged ions are accelerated to energies in the range of 10 to 10,000 keV and fired at the silicon surface.

- **Lithography and etching**

The process of imprinting a geometric pattern [3.3] from a mask onto a thin layer (~μm) of a radiation-sensitive material is called lithography. This process generally involves spraying of the radiation-sensitive material on the silicon wafer. A mask is then placed

above it. By applying UV radiation the solubility of the photoresist will change. The next stage of this process is to dissolve away the changed photoresist. This in turn will expose the $SiO_2$ layer, which is then etched away by a HF or an equivalent solution.

- **Metalisation and wire bonding**

A new oxide layer is formed and the required windows for metalisation are exposed lithographically. By using either physical vapour deposition, chemical vapour deposition or sputtering of a ~1μm layer the deposition of the metal is achieved. The metal usually is of a good ohmic contact such as Al or Au. This will be used for pad connections. The produced wafer is thinly diced up using a diamond saw. Finally the IC is mounted onto a package, which could be made of plastics or made of ceramic for higher temperature applications. The connections between the IC pads and the holding package are normally achieved by using ultrasonic welding of thin aluminium or gold wire.

- **Testing and encapsulation**

It is important to protect the ICs from the atmosphere for long term reliability of the ICs. By using photoresist or more frequently a silicon nitride layer a good barrier to water is achieved over the sensitive parts of the IC circuit.

### 3.3 Design of silicon chemoresistive sensor

The design description and properties of a metal oxide semiconductor (MOS) thin film gas sensor is outlined in the following section. This particular sensor package namely the SRL125/MOS was used extensively in this research. This sensor was designed at the University of Warwick Sensor Research Laboratory (SRL) [3.1], and then fabricated at the Institute of microtechnology in Switzerland. The device was used as dual sensor, which can simultaneously operate as a resistive gas sensor and as a microcalorimeter.

The aim was to produce a low cost reliable and to be used in low power applications such as in a hand held electronic nose or in the automotive market.

The design of these sensors was influenced by the choice of gases of interest such as CO, $NO_2$, and volatile organic compounds (VOC). Improved control of composition and morphology of the sensor can lead to a better performance of gas sensitive materials. Another fundamental part of MOS operation is temperature. A resistive heater was therefore incorporated in the design of the SRL125/MOS devices. In order to produce a micro hot plate (MHP) with very low power consumption by using micromachining technique, the use of sensor structure based on silicon was necessary. The other important design requirement of the SRL125/MOS was to improve the poor long-term stability of such sensors.

One on the most important requirements of hand held equipment is low power consumption. Therefore to minimise the thermal losses [3.1] the SRL125/MOS design incorporated a membrane microstructure. A cross section of this is shown in Figure 3.1.

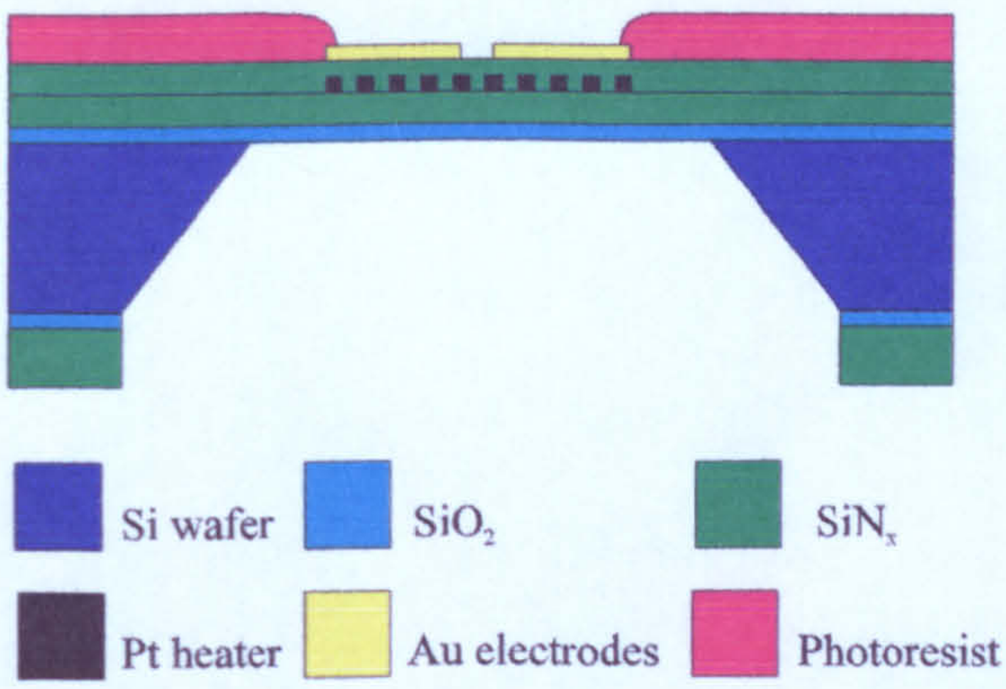


Figure 3.1 Cross-sectional schematic of cell structure in SRL125/MOS before gas-sensitive material deposition.

The structure of the device shown in Figure 3.1 shows the different parts of the SRL125/MOS. However, the actual sensing material is not shown. The MHP structure together with the resistance heater is embedded in a thermally insulating ultra-thin $Si_3N_4$ membrane. The chemoresistor structure, which consists of oxide gas-sensitive material

and gold (Au) electrodes, located on the membrane surface. The MHP provides the operating temperature of the gas-sensitive material. The MHP consists of a Pt thin film resistance heater, which is located between two 0.25 μm layers of low-stress silicon-rich LPCVD and silicon nitride ($SiN_x$). The location of the Pt microheaters and the electrode area which is separated from the chemoresistor by electrically insulating layer of $SiN_x$ this provides a very efficient way to control the temperature of the gas-sensing material.

To achieve a low-power arrangement a low thermal conductivity material ($SiN_x$) was used, which reduces the heat lost to the substrate. Additionally thermal insulation can be improved by increasing the thermal resistance of the membrane, by [3.1] either:

- increasing the membrane area,

or

- reducing the membrane thickness.

A third option is to use oxide rather than nitrate as thermal conductivity is lower. However, in practice, the geometry of the membrane is limited by other physical limitations, such as residual stress and the thermally induced stress in the membrane. To reduce these limitations a low-residual stress $SiN_x$ layer is deposited on an 80 nm thin layer of $SiO_2$. It is vital that the whole microsensor structure is stable mechanically when subjected to thermal cycling. This is attained by maximising adhesion between layers (e.g. using tantalum for Pt and Titanium for Au).

The SRL125/MOS device consists of 6 independent chemoresistive elements, and three MHP structures. Each MHP structure is used to control the temperature of two chemoresistor elements as shown [3.1] in Figure 3.2

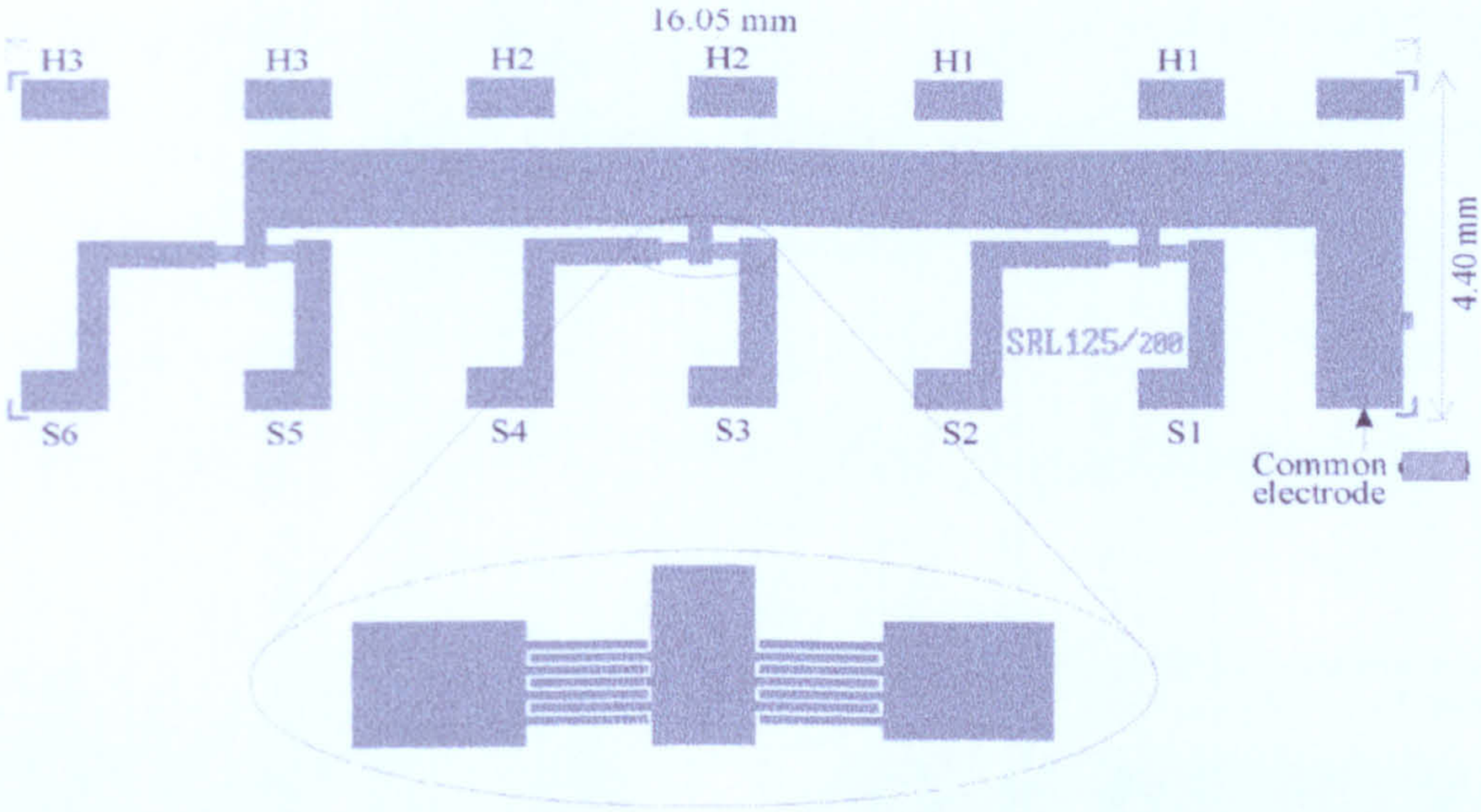


Figure 3.2 Au electrode layout for the MOS chemoresistive sensor. S1 to 6 are one side of the sensors contacts the second set of contacts are common drain electrode. H1-H3 represent the pads of the heating elements, two sensors share each of these.

The SRL125/MOS package consists as mentioned above of six chemoresistors arranged in pairs as shown in Figure 3.3.

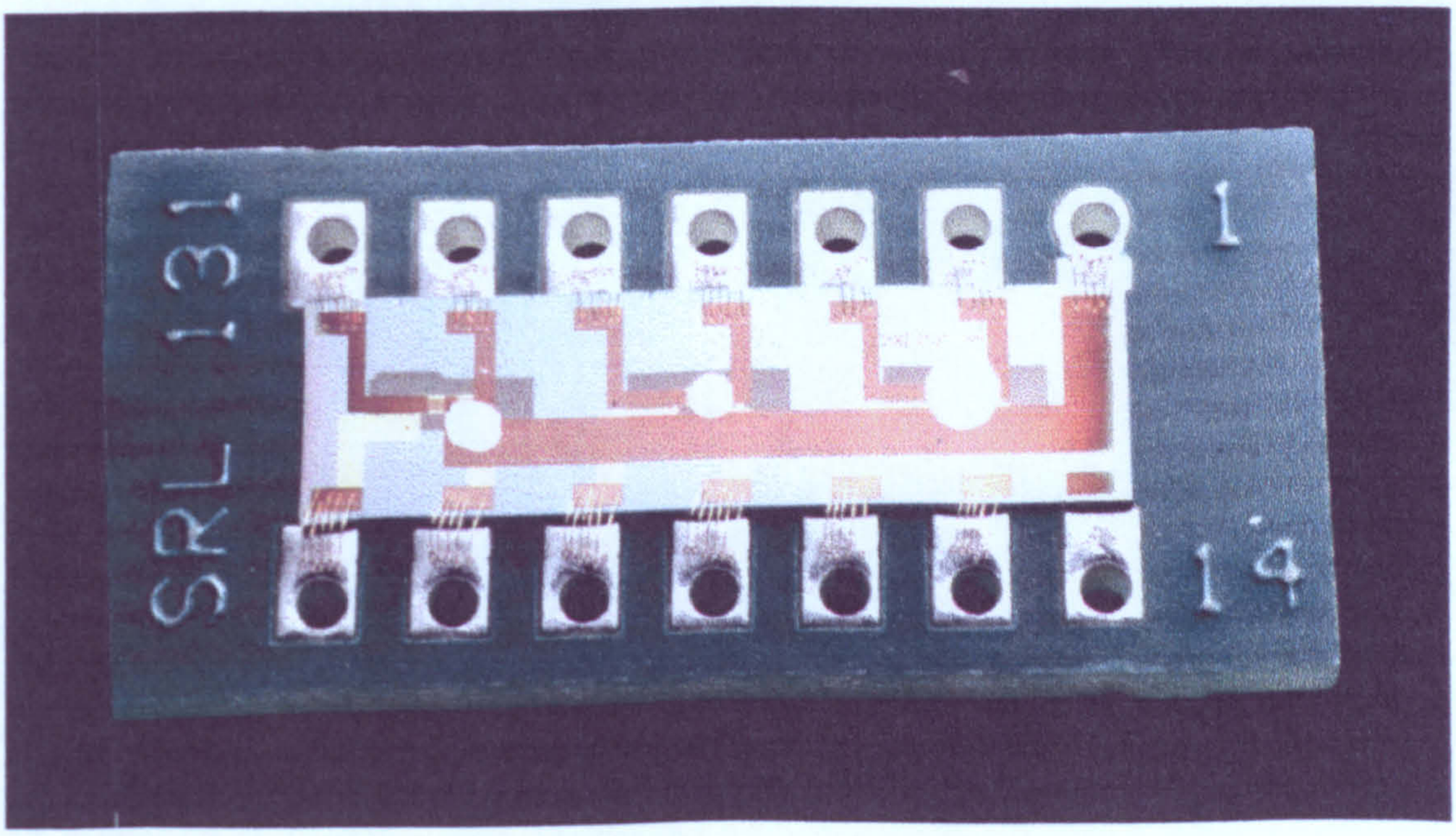


Figure 3.3 Packaged SRL125/MOS hex SAD

Each pair is centred on a membrane with an underlying microheater. One common electrode is connected to all six sensors as shown in Figure 3.2, and by using the common tract, the number of pads has been reduced, which consequently affects the size of the device.

The fabrication procedure steps for the SRL125/MOS are shown in Figure 3.4.

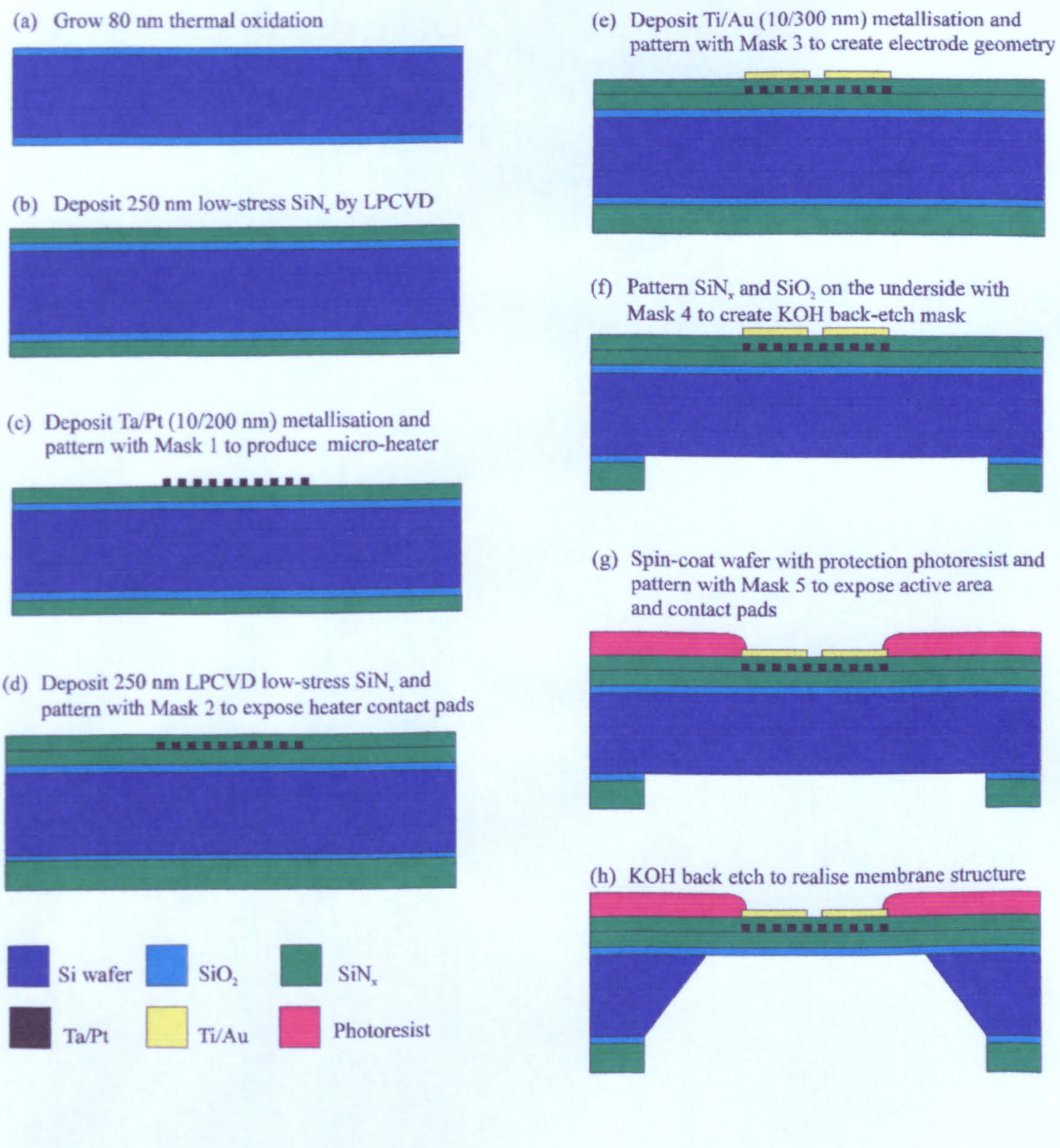


Figure 3.4 Schematic of the wafer processing steps required in fabricating SRL125/MOS.

It is important to note that the impurities [3.2] normally have electrical effects as doping. Minute amount of impurities of a few ppm can have drastic effect on the electrical properties of gas –sensitive materials. Every effort must be taken to prevent contamination. It is not possible to create 100% pure metal oxide. Some unavoidable sources of this may result from the plasma attack on the stainless steel of the containers and the copper target holding plate.

### 3.4 Summary

This chapter outlined the process of design and manufacturing of chemoresistive gas-sensors. The influence of selection of the target gases of interest CO and $NO_2$ has led to the specialised design for the SRL125/MOS chemoresistors. The design criterion of this device was also influenced by the requirement for ultra, low power consumption chemoresistors, to be used in a portable instrument.

### 3.5 References

3.1 A. C. Pike, Design of chemoresistive silicon sensors for application in gas monitoring, *Ph.D. Thesis, University of Warwick, UK, 1996.*

3.2 H. Baltes, W. Göpel, J. Hesse, *Sensors update*, Vol. 2, Wiley-VCH, Germany, 1996.

3.3 J. W. Gardner, *Microsensors*: *Principles and applications*, John Wiley and Sons, Chichester, 1994

# Chapter 4 Theory of thermally – modulated gas sensor

## 4.1 Introduction

Over the last few decades the $SnO_2$-based gas sensors have become the predominant solid-state material used in gas alarm for commercial and industrial applications [4.1]. A large variety of ceramic, thin-film and thick-film have been developed over many years with mostly an empirical ('trial and error') optimisation of their performance [4.2]. The basic sequence of chemical sensing and the influence of contacts and crystalline structure of the $SnO_2$ are not fully understood. This understanding is imperative for their future improvement, which is currently researched by a large number of groups mostly using thin-film technique [4.2]. The well-known advantages of using $SnO_2$ is its low cost and high sensitivity. Its main disadvantage is a lack of long term stability and selectivity [4.4]. To overcome these disadvantages several techniques were used such as operating at different temperatures, by choosing different annealing procedures, catalysts, operating frequencies etc. In conjunction with this, pattern recognition (PARC) and multi-component analysis (MCA) of binary gas mixtures with arrays of non-specific gas sensors are normally used to achieve selectivity. Recently, modulated temperature operation is used as a new approach to enhance the selectivity of sensors. This chapter discusses the background and theory of thermal modelling used in gas identification.

## 4.2 Background and Theory of temperature modulated technique

Gas sensors produced by employing micro-fabrication technology have been of great and on-going interest mainly because of their potential use in array devices with low power [4.1]. Sensors, which are based on a micro-machined hotplate, have the extra advantage of a wide operating temperature range coupled with a rapid thermal time

constant of around 1 ms [4.1]. Microsensors have the advantage of low cost, due to batch fabrication and a low power requirement. The microsensor consists of an integrated heater-thermometer and sensing material. A large part of its production can be achieved by conventional foundries of CMOS chips [4.1].

Earlier attempts have been reported of using dynamic sensor data by pulsing the sensor temperature [4.1]. By operating the sensor dynamically, reaction kinetics on the oxide film surface is changed, yielding a time-varying response mark that is representative of the gas being tested. Periodic alteration between two temperatures has been considered for the improvement of sensitivity and selectivity and to reduce the effect of humidity [4.5]. Hiranka et al. [4.6] outline the use of a single temperature pulse to produce a transient response with a gas–dependant profile time constant [4.6]. The time scale of this temperature modulation is done on time duration of seconds to minutes. The micro-machined devices can be heated typically to around 500° C and then cooled to room temperature in a few milliseconds. This will allow a fast control of the reaction kinetics of the oxide layer, which in turn produces a specific response pattern for a specific gas of interest. The first attempts to investigate the modulated sensor data were carried out on thin film deposited on micromachined substrates or on classical Taguchi sensors. In the case of thin films deposited on micromachined substrate [4.3], the benefit of fast thermal response and lower power consumption is reduced by the lower sensitivity of the thin film. In the example of Taguchi sensors, their high sensitivity is counterbalanced by high power consumption, low thermal response because of their larger substrate, which may induce contortion in the modulated sensor response [4.3]. More recent methods take advantage of the combination of micro-machined substrate and thick film technology [4.3]. In this case the combination of the good response time to temperature modulation of the micro machined substrate and the high sensitivity

property of thick film $SnO_2$ was used to produce an efficient microsensor system. This approach proved that the silicon technology for manufacturing micromachined substrate is compatible with thick film technology for depositing oxide layers. A paper on a constant temperature mode measurement of such devices has already been reported [4.7].

## 4.3 Thermal characteristic and modelling of chemoresistive gas sensor

Growing demands for portable gas and odour instruments have led to an increasing integration in the design of sensor system. One of the essential requirements for such systems is low power consumption in order to achieve a long battery life, e.g. over 12 hours [4.8]. The development of a portable gas system is of interest in automotive, medical, environmental monitoring and other industries as mentioned in previous chapters. However the growth in this area has been limited by the relatively high power consumption of current commercial chemical sensors (e.g. pellistors need 350-850 mW [4.9] and Taguchi gas sensors power consumption 230 – 760 mW [4.10] and high manufacturing costs. The application and use of micromachining coupled with microelectronics may lead to the production of low power, low-cost, reproducible chemoresistor system. For a large number of gas-sensitive materials, the performance of the sensor is improved at higher temperatures e.g. $SnO_2$ are typically sensitive in the range of 250 - 500°C. The utilisation of silicon micro-technology [4.8] enabled the integration of both the sensor and the electrical heating element onto the same chip. Additionally, recent advances in the development of bulk and surface micromachining techniques have allowed a three-dimensional structure to be produced and also to provide better reproducibility in batch processing. A low power CO sensor, which made

use of micromachining techniques, has been reported [4.11], It consists of a planar chemoresistive thin film tin oxide situated on a heated substrate. This type of structure is referred to as a 'micro-hotplate'.

### 4.3.1 Modelling of chemoresistive gas sensors

The use of chemoresistive $SnO_2$ gas sensors as quantitative gas sensors is constrained by its long-term stability and because of such effects as poisoning or ageing [4.12]. This performance deterioration of the sensor is important if the sensors are to be used in safety critical situations as in detection of toxic gases such as CO and $NO_2$. Development of new stable material can improve sensor performance. In attempts to understand and identify the sensor layer mechanism that control performance researchers have proposed physicochemical mechanisms which have led in turn to the development of theoretical models [4.13]. Theoretical models can assist in the selection of pre-processing algorithm [4.14] and improve the accuracy of the gas-sensing device.

The basic structure of a chemoresistive device is show in Figure 4.1.

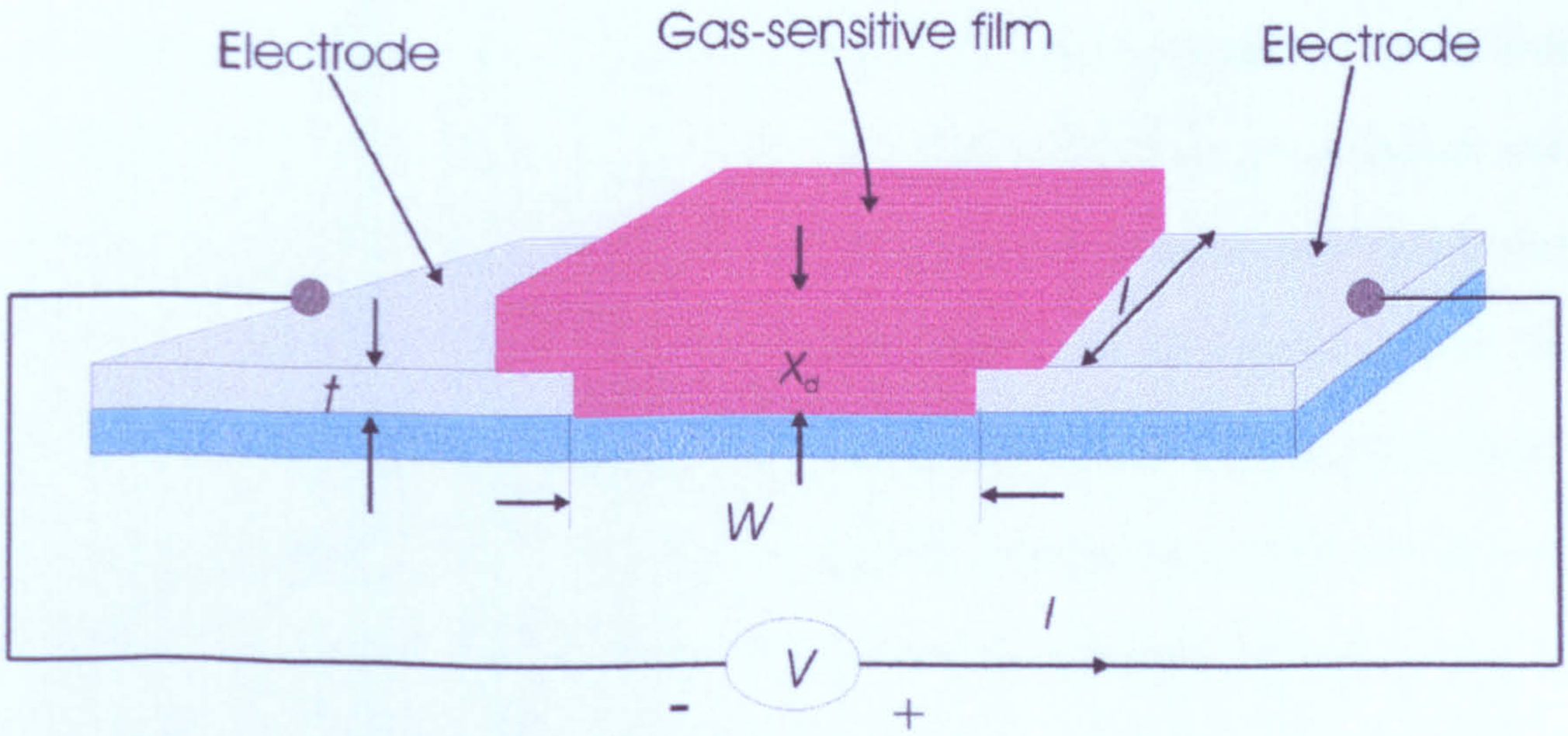


Figure 4.1 Basic structure of a conductometric gas sensor showing the geometrical notation used in modelling. $V$ is the applied voltage, $I$ is the current, $t$ is the electrode thickness, $l$ is the electrode width, $w$ is the inter-electrode gap and $x_d$ is the gas sensitive film thickness.

The dominant sensing mechanism of a chemoresistive device is the interaction of species with surface sites and includes the internal surface of porous sintered oxide layer as described in Chapter Two. A general block diagram [4.8] for different sensing parameters and mechanisms is shown in Figure 4.2.

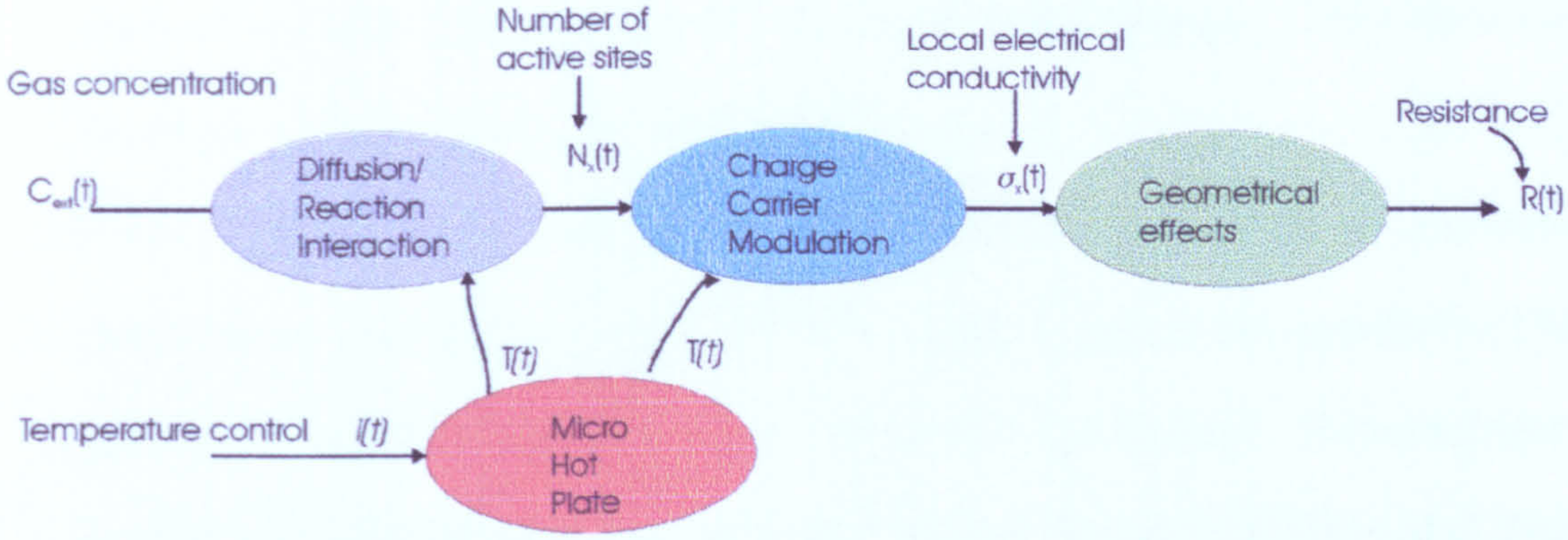


Figure 4.2. Block diagram of general structure of a chemoresistive device, where $C_{ext}$ is the external gas concentration, $N_x$ is the local number of activated internal sites that lead to a change in electrical charge carrier, $\sigma_x$ is the local electrical conductivity, $R$ is the measured sensors resistance, $T$ is the operating temperature, and $t$ is a time variable indicating a dynamic system.

The mechanisms that determine the theoretical models are described for each section in block diagram in Figure 4.2. The first section summarises the diffusion-reaction process that controls the interaction between the external gas concentrations and the internal bonds [4.13]. Porous material is considered here, which allows the gas to diffuse into the bulk. The gas will react with an internal surface to yield an active site. The number of the active local sites, $N_x$ will vary through the depth of the gas-sensitive layer. The subscript $x$ represents the distance through the layer perpendicular to the substrate plane. The micro hot-plate section provides the operating temperature control for the gas-sensitive layer. The charge carrier modulation section represents the change in the electrical conductivity $\sigma_x$ due to the activated surface sites, which relates to the change in the localised charge concentration and carrier mobility. The last section represents the

effect of the geometry of the gas–sensitive layer on the output signal, which in this case is resistance *R*.

In order to simplify the chemoresistive system as shown in Figure 4.2 it has been assumed that there is only one external gas with concentration of $C_{ext}$ in synthetic air and a constant humidity. However, in the absence of the target gas (i.e. $C_{ext}$= 0) and in clean air, constant temperature and humidity, the output resistance of the chemoresistor is referred to as the base-line resistance $R_0$.

It is known that the steady-state response description of MOS to particular gas concentration changes may be described by using a power law expression [4.8]. A quantitative model to describe the response of Taguchi SnO2 chemoresistive with porous sintered pellet structure to reducing gases was derived by Clifford et al. [4.15].

It was shown that the response of CO follows a power law, where

$$R \approx R_o\left(K_{CO}C_{CO}\right)^{-\beta} \qquad (4.1)$$

Where $C_{CO}$ is the CO concentration and $K_{CO}$ is a sensitivity coefficient.

Power law expressions have also been characterised for oxidising gases such as $NO_2$. Hence the increase in resistance with increasing gas concentration produces a positive power coefficient [4.8]. The effect of the operating temperature was characterised by Clifford et al. [4.15], where a straight line was obtained between the logarithm of gas sensitivity coefficients against the inverse temperature.

### 4.3.2 Diffusion and Reaction models

Research into gas sorption in MOS and other material films have led to the material surface to be regarded as a number of immobile locations at which the gas can react

[4.8]. At equilibrium when the surface is exposed to a target gas, certain location of the total number of sites, $N_m$, will be activated according to

$$\theta = \frac{N}{N_m} \tag{4.2}$$

Where $N$ is the number of active sites and $\theta$ is the site occupancy, it is assumed that the distribution of the sites is uniform throughout the film. The steady state relationship between the site occupancy $\theta$ and $C_{ext}$ at constant temperature is referred to as sorption isotherm. The type of this isotherm is decided by the reaction steps that proceed to yield the activated locations, while the kinetic rates control the number of adsorbate $N$. The rate of target gas diffusion in porous materials is a fundamental property in defining the profile of activated sites [4.8]. However, a non uniform gas concentration outline produced when the rate of gas diffusion cannot maintain the rate of gas consumption in an irreversible reaction mechanism such as in combustion of reducing gas (e.g. CO) in MOS films [4.8].

In the diffusion and reaction models the transient characteristics are dependent on the rate of mass transport (diffusion) and the sorption rates [4.8]. The key elements of the diffusion reaction models are shown in Figure 4.3

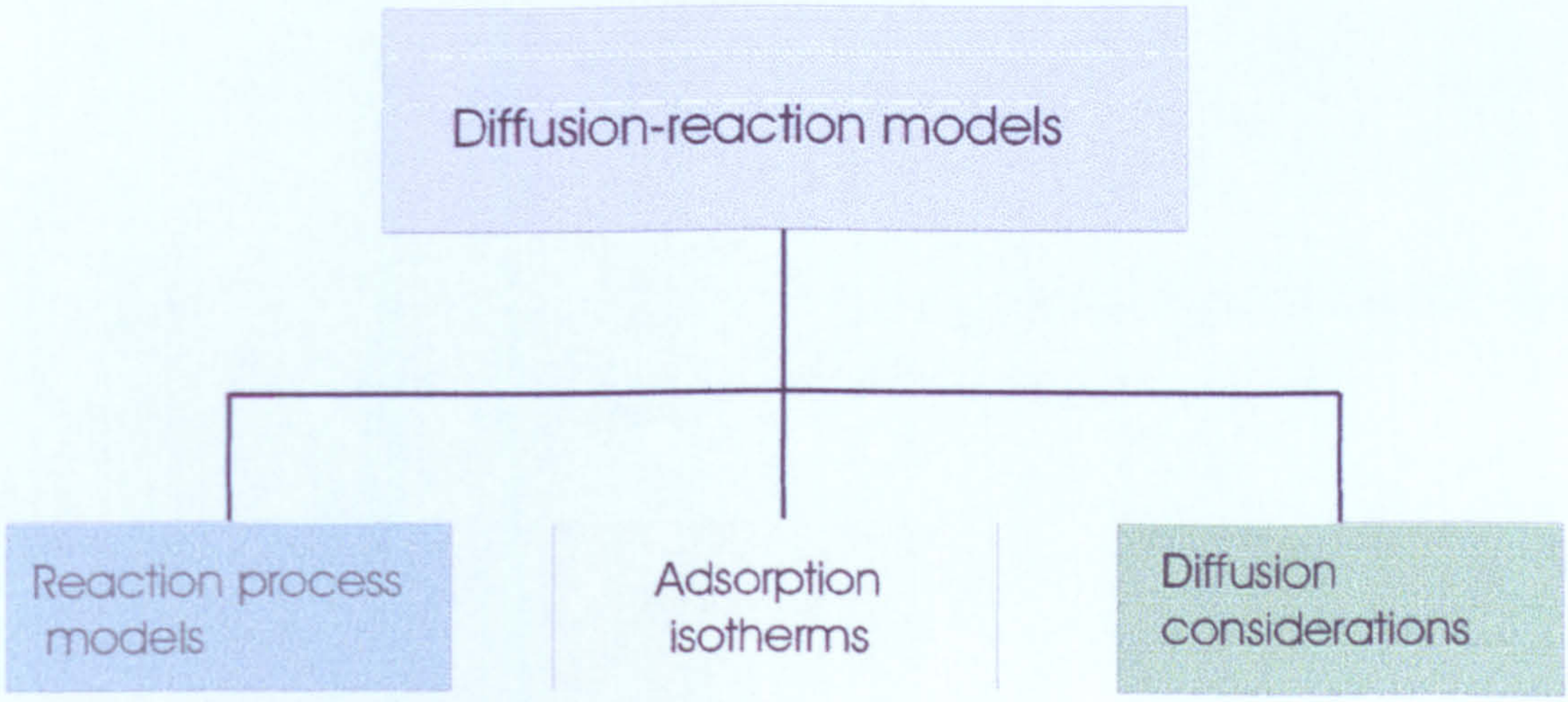


Figure 4.3 Fundamental elements of the diffusion reaction models

### 4.3.2.1 Adsorption Isotherm

To specify an adsorption isotherm the information about the amount of gas adsorbed together with its associated equilibrium concentration will be needed (this is an over simplified model).

The simplest isotherm is the Langmuir isotherm which assumes that every adsorption site, <> is identical and the ability of a gas species *A* to bind on that site is independent of whether or not nearby sites are occupied [4.8].

The dynamic interaction is,

$$A + \text{<site>} \underset{kb}{\overset{kf}{\Leftrightarrow}} \text{<}A\text{>} \tag{4.3}$$

Where <*A*> is the adsorbed gas species formed with $k_f$ and $k_b$ as forward and backward reaction rates, respectively [4.8]. For a an oxide layer with an active volume, *V*, the rate of change of site occupancy is ($d\theta/dt$) because of adsorption is proportional to the concentration of *A* and the number density of vacant sites $N_m(1-\theta)/V$, so

$$d\theta/dt = k_f C N_m (1 - \theta)/V \tag{4.4}$$

Whereas, the $d\theta/dt$ because of desorption is proportional to the number density of adsorbed species, $N_m\,\theta/V$, hence

$$d\theta/dt = k_b N_m \theta/V \tag{4.5}$$

At equilibrium the two rates are equal, and solving for $\theta$ gives the Langmuir isotherm,

$$\theta = N/N_m = KC/1+KC \qquad (4.6)$$

where the reaction-rate coefficient, $K = kf/kb$ [4.8].

For adsorption which happens via a mobile dissociative process, then two surface sites are essential for both adsorption and desorption. The Langmuir isotherm then becomes,

$$\theta = N/N_m = (KC)^{1/2} / 1+ (KC)^{1/2} \qquad (4.7)$$

The importance of the chemical reactions produced during the formation of the activated sites is shown in this modified form of the Langmuir isotherm.

In certain cases, the heat of adsorption decreases as $\theta$ increases, which suggests that the energetically more favourable sites are occupied first, [4.8] e.g adsorbed surface ions may apply an additional electrostatic repulsion which subsequent adsorbants have to overcome. By making an assumption that heat of adsorption falls logarithmically with coverage [4.8], the Freundlich isotherm has been defined [4.16] according to

$$\theta = AC^{\beta} \qquad (4.8)$$

where $A$ is a constant of proportionality and $\beta$ is the power coefficient.

The chemoresistors empirical characteristic can be compared to the adsorption isotherm, assuming that the conductance is directly proportional to the site occupancy [4.8]. Researches to identify the dominant gas sensing mechanism in a film have extensively carried out these comparisons. It is generally accepted that the power law form of a Freundlich adsorption isotherm can be used to model MOS films [4.17].

### 4.3.2.2 Diffusion-Reaction considerations

In the previous section on sorption isothems it was assumed that the gas concentration was constant within the porous film [4.8], that is the number of the activated sites, $N$, was a function of the gas concentration *F(C)*. However, in this case any change in gas mixture will result in a perturbation on *N for* a finite period [4.8]. The time to reach a new equilibrium will depend on the rate of mass transport between the surface and the bulk and the reaction rates of the processes of the activated site [4.8].

It is generally accepted that the reaction mechanism for MOS film with reducing gas (e.g. CO) is through an irreversible reaction [4.18]. Consequently, thick porous MOS films will contain a non-uniform gas concentration and as a result a local site occupancy $\theta_x$ profile.

An expression has been produced by Williams et al.[4.19] for gas concentration profile $C_x(x)$ relating to the consumption of gas species, *A*, as shown in Figure 4.4.

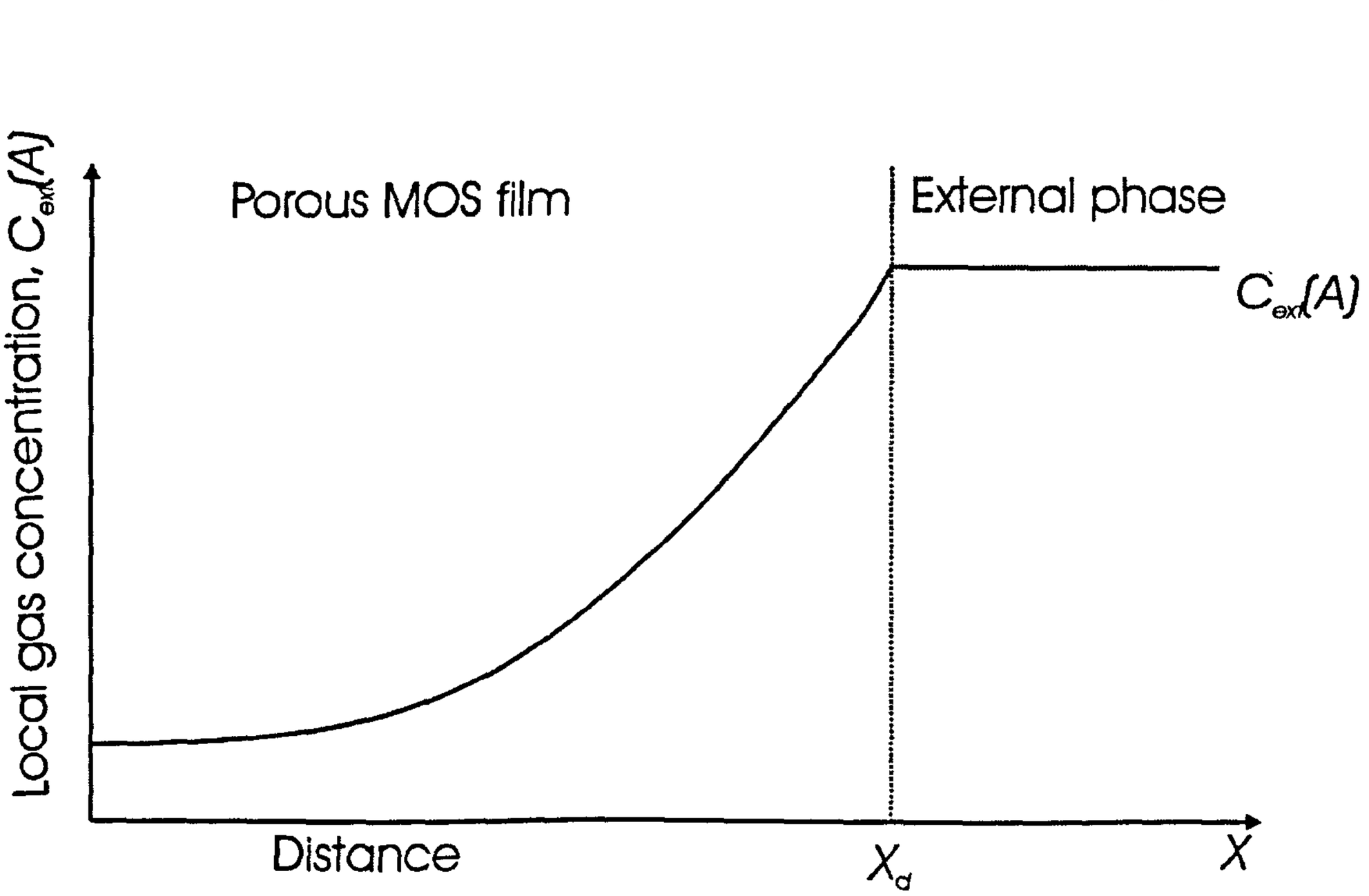


Figure 4.4 Schematic of a reducing gas concentration profile through a MOS film as a result of a constant external gas concentration of $C_{ext}(A)$.

## 4.4 Modelling of film conduction

In this section the relationship between the film conductivity and the activated sites will be described [4.8] The electrical conductivity, σ, of a MOS material is related to the electron and hole concentrations (*n* and *p*, respectively) and their mobilities ($\mu_e$ and $\mu_h$ respectively) by the standard equation

$$\sigma = e\,(n\mu_e + p\mu_h) \tag{4.9}$$

where *e* is the electron and hole charge carriers. Since $SnO_2$ is an n-type semiconductor material the majority carriers are electrons therefor $n>>p$. the equation can be simplified to

$$\sigma_{SnO2} \approx en\mu_e \tag{4.10}$$

It is assumed that the adsorbed gas changes the carrier concentration. If a diffusion-reaction process produces a local gas concentration profile, then a local charge carrier profile is also expected [4.8]. This would create a local conductivity ($\sigma_x$) profile, which would be a function of the gas concentration profile $F(C_x)$ [4.8].

### 4.4.1 Conduction in MOS films

The base-line conductivity, $\sigma_0$, of a $SnO_2$ film in pure air is decided by charge generation from bulk defects in the $SnO_2$ film and the depletion of this charge by adsorbed oxygen at internal surfaces and grain boundaries [4.8]. The depth of the depletion layer, i.e. Debyé length ($L_D$) is [4.20].

$$L_D = \left( \frac{\varepsilon_r \varepsilon_o \kappa T}{e^2 n_b} \right)^{1/2} \tag{4.11}$$

Where $\varepsilon_r$ denotes the relative dielectric permittivity, $\varepsilon_0$ the vacuum permittivity, $k$ Boltzmann's constant, $e$ is the electron charge and $n_b$ is the bulk concentration of electrons. It is known that reducing gases react with bound oxygen sites species such as $O^-, O^{2-}$ and releases electron, which results in reduction in $L_D$ [4.18] as shown in Figure 2.2 and Figure 2.3. However, in general, oxidising gases create more oxidising sites, which leads to a greater depletion layer [4.21] and [4.8].

## 4.5 Modelling Chemoresistor Geometry

Geometrical influence on a chemoresistor conductance is investigated by using an n-type material such as $SnO_2$. The geometrical parameters controlling the electrical properties can be used for modelling [4.8]. This is achieved by integrating the current density, *J*, over a surface bisecting the electrodes to define the device current, *i*,

$$i = \int_0^1 J.ldx' = \int_0^1 \sigma_x E.\, l\, dx' \qquad (4.12)$$

Where x' is $x/x_d$, and *E* is the electric field across the electrodes [4.8]. Gardner [4.22] has produced a model, which investigates the effect of chemoresistors geometry on gas sensor characteristics for different configurations in order to define the optimum performance of the chemoresistors. Two configurations was investigated [4.22] (one

was) a thick film parallel electrode and the (second was) thin coplanar electrodes as shown in Figure 4.7.

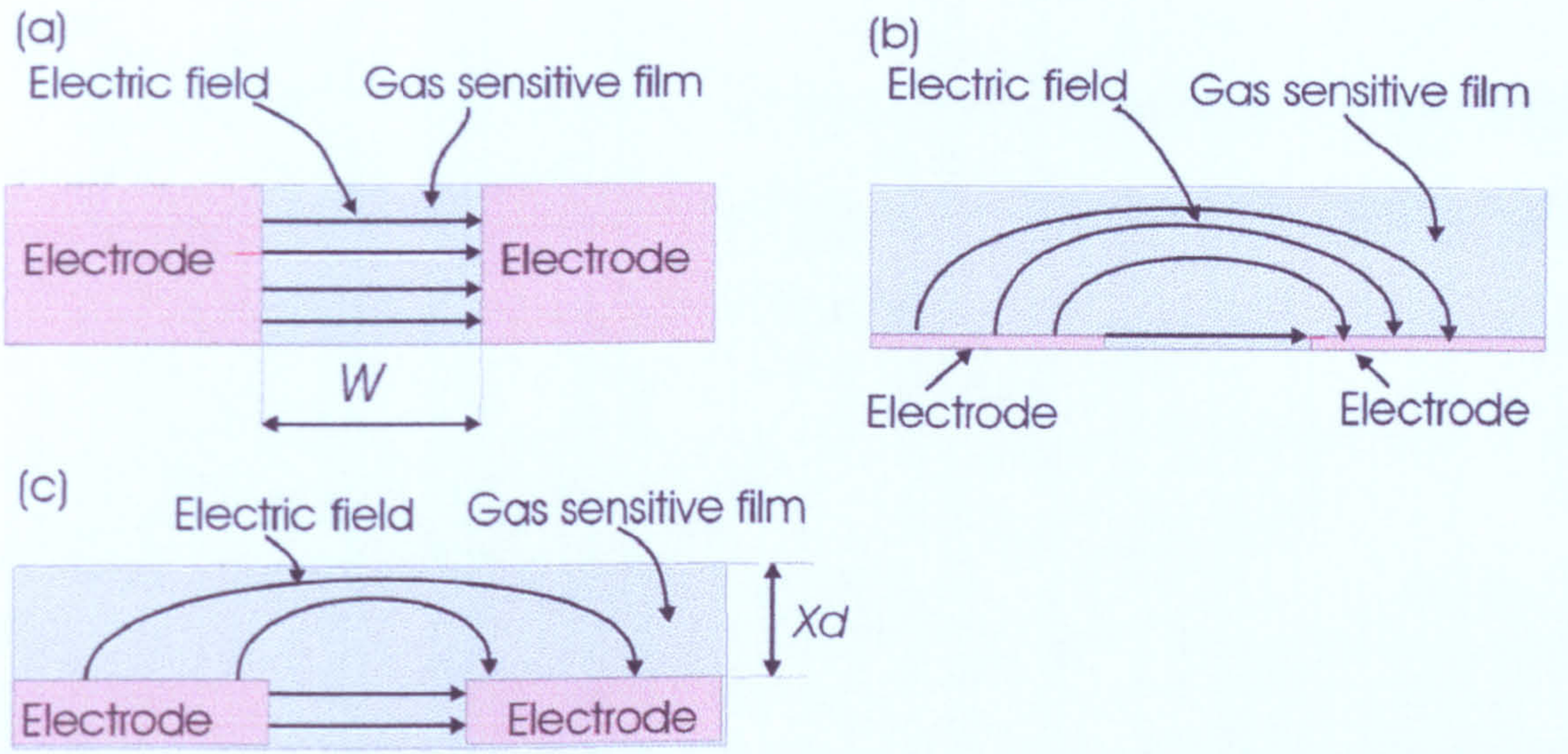


Figure 4.7 Schematic of electrode configuration and associated electric field lines for: (a) thick parallel electrodes, (b) thin coplanar surface electrodes and (c) expected device electrode configuration, combining characteristics from both (a) and (b).

The first configuration consists of two parallel-plate metal electrodes with the gas-sensitive film in between as shown in Figure 4.7 (a). In this arrangement, the electric field equals the applied voltage, $V$, divided by the inter-electrode gap, $w$ that is:

$E = V/W$ and the edge effects are ignored. This equation can be substituted in equation 4.12. To drive the conductance $G$,

$$G = \frac{i}{V} = \frac{\sigma_x x_d l}{w} \tag{4.13}$$

where *l/w* is referred to as the aspect ration of the electrode structure [4.8]using conformal mapping has derived an analytical solution,

$$E(x_d) = \frac{V}{\pi} \left[ X_d^2 - \frac{W^2}{4} \right]^{-\frac{1}{2}} \tag{4.14}$$

The electric field equipotential and flux lines defined by equation 4.14 are hyperbolae and ellipses, respectively [4.22]. If equation 4.14 is substituted into equation 4.12 then the steady-state conductance (*i/v*) in air becomes,

$$G_0 = \frac{\sigma_0 l}{\pi} \ln \left[ 1 + \left( 1 + \frac{w^2}{4x_d^2} \right)^{\frac{1}{2}} \Big/ \frac{w}{2x_d} \right] \tag{4.15}$$

If the thickness of the gas sensitive layer $x_d$ is < the electrode thickness then the electrode arrangement must be considered as having thick parallel electrode structure as shown in Figure 4.5 (a) [4.8]. However, if $x_d$ > the electrode thickness then the electric field would comprise both configurations, as shown in Figure 4.5 (c) [4.22]. The electric field solution to this case is a Jacobean elliptical integral of the third kind with a finite electrode thickness *t* entering equation 4.14.

In general, the thickness of a thick film MOS device is typically around 10 to 100 μm thick [4.8]. The field solution can be approximated to that of thin co-planar electrodes.

## 4.6 Effect of temperature upon resistance of $SnO_2$ gas sensors

### 4.6.1 Background

Resistive sensors have been used for many years to monitor the level of certain combustible atmospheric gases, such as hydrogen and methane. The most successful resistive gas sensor is arguably the Taguchi gas sensor [4.4] which has been sold in its millions. The Taguchi gas sensor consists of a thick-film of porous metal oxide lying on top of interdigitated sensing electrodes supported by a ceramic substrate under which is a platinum resistive heating coil. The sensor is operated at a single temperature, typically between 300 and 500°C. In order to obtain the optimal sensitivity for the target gas, their application has been limited to a simple alarm rather than gas monitors which require a higher level of accuracy.

One way in which the performance of these resistive sensors can be enhanced is to modulate the operating temperature of the gas-sensitive material (e.g. tin dioxide) and then extract more chemical information than possible from a single gas sensor. However, recent advances in microsensor technology have made this technique realisable with silicon planar devices. Reports have already been published of using a silicon micromachined version of the Taguchi gas sensor [4.3], which have much lower power consumption (ca. 50 mW) than the original Taguchi sensors (ca. 800 mW). This does not address the problem of a lack of selectivity of metal oxide resistive sensor, although it does permit both the construction of metal oxide sensors with reasonably low power consumption at lower unit cost [4.23].

A thermal wave resistive microsensor is now a practical proposition because resistive silicon structure can be made with a thermal response time of the order of millisecond [4.8] and run reliably at high temperature (ca. 400°C).

In the earlier attempts to improve the sensitivity of a gas sensor and to reduce the overall power consumption a pulsed temperature operation mode was reported [4.24] where a ceramic $SnO_2$ based thick film were used. The response of $SnO_2$ upon exposure to CO and $NO_2$ separately at different temperature as reported by A Heilig et al. [4.24] is shown in Figure 4.8.

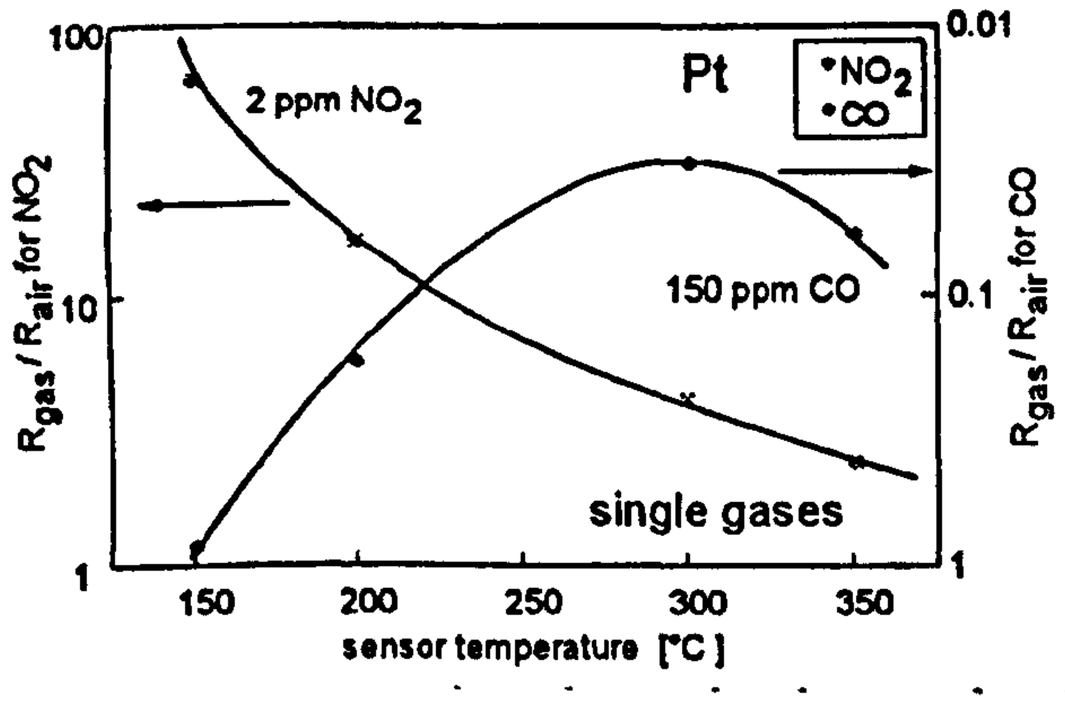


Figure 4.8 Temperature dependence of platinum doped sensor response upon exposure to individual gases. The sensor response was defined as $R_{gas}/R_{air}$.

The response of the sensor was also tested for a mixture of CO and $NO_2$ [4.24] as shown in Figure 4.9

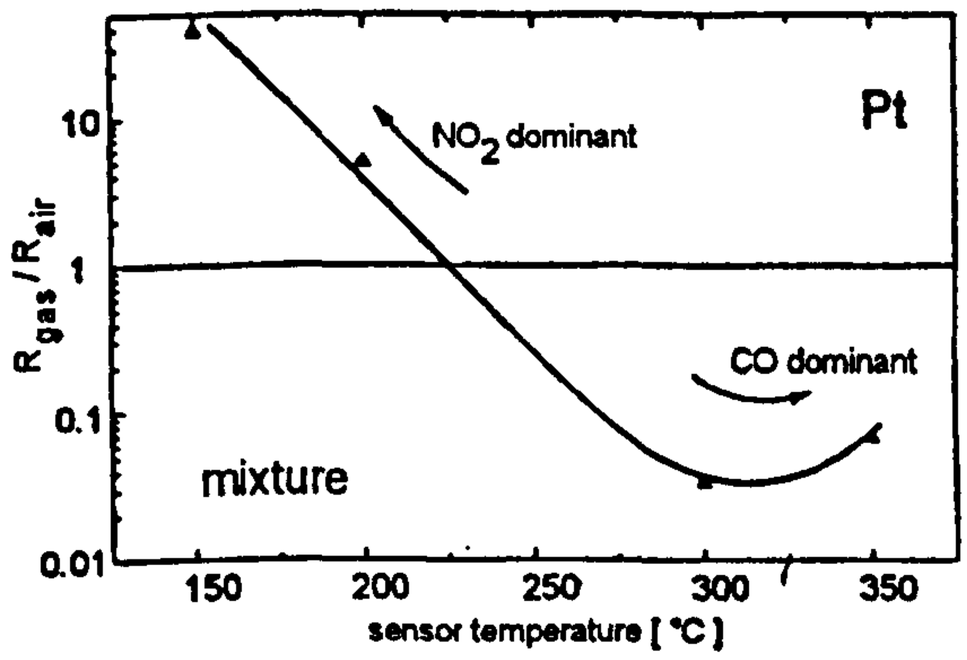


Figure 4.9 Temperature dependence of the sensor response due to the exposure to a binary gas mixture (50 ppm CO and 2 ppm $NO_2$).

It is shown that at low temperatures the response of the sensor to $NO_2$ is dominant while the response of the $SnO_2$ to CO at higher temperature is more dominant [4.24]. This in effect will give information on the composition of CO and $NO_2$ in ambient atmosphere [4.24] so if the sensor resistance decreases at both high and low temperature then only CO is present and also if the response (resistance) from the sensor increases at both temperatures then only $NO_2$ is present. However, if the resistance increases at low temperature and decreases at high temperature then both gases are present in the ambient atmosphere with a certain ratio [4.24]. In order to separate out the response from the sensor to CO and $NO_2$ a temperature pulse (between 150C for 20 minutes and 300C for 5 minutes) was applied and measurement was taken at specific time [4.24]. The response of the sensor to CO and $NO_2$ at high and low temperatures is shown in Figure 4.10 [4.24]

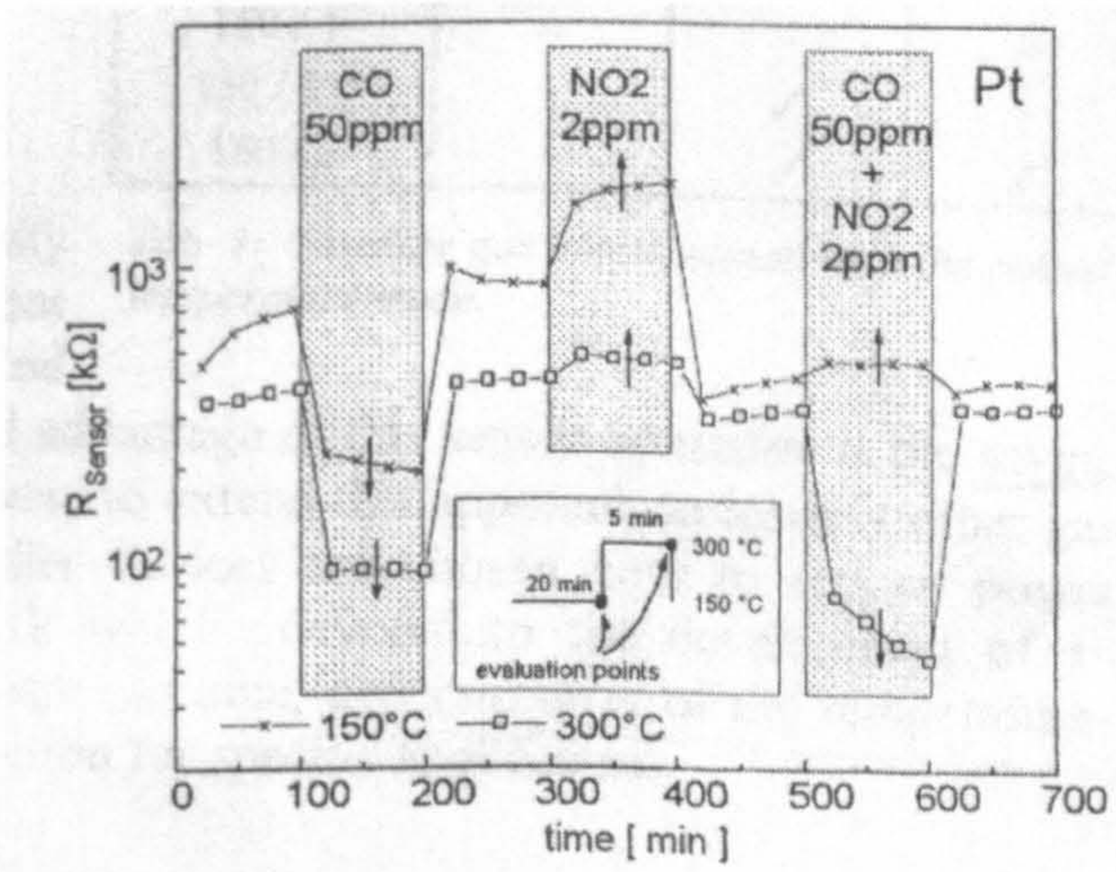


Figure 4.10: Plot of resistance at the evaluation points, i.e. the end of the low and the end of the high temperature period.

The response of the sensor to CO is much larger when subjected to a higher temperature (300°C) than at lower temperature (150°C) as shown in Figure 4.9 [4.24]. One of the

advantages of this method is saving power consumption by using one sensor instead of two sensors, one operating at 150°C, and the other at 300°C. However, power consumption is still high and the duration of the test is very long. This parameter can be improved by using micromachined sensors, which have much lower thermal properties and less power consumption.

An improved sensing system based on the multidimensional information contained in a dynamic non-linear response was reported by Nakata et al. [4.25]. A sinusoidal thermal wave was applied to sensor and the resulting resistance output changes were analysed by Fast Fourier Transformation (FFT). The amplitudes of the higher harmonics of the FFT contains information which relates to chemical structure, concentration and the kinetics of adsorption and reaction of the target gases on the sensor surface [4.25]. By using dynamic non-linear responses of the sensor it was possible to differentiate between gases in a gaseous mixture [4.25].

Nakata et al. [4.25] proposed a model for semiconductor gas response. As shown previously, the conductance of a semiconductor gas sensor depends on temperature and the surface potential barrier. The conductance *G(T)*, is described approximately by the equation 4.16.

$$G(T) \approx G_0 \exp(-eV_s/kT) \tag{4.16}$$

where $V_s$ is surface barrier height, $G_0$ prexponential factor, $e$ electronic charge, $k$ Boltzmann's constant, and $T$ absolute temperature.

The surface barrier height is related to surface concentration of ionosorbed oxygen as shown in equation 4.17

$$Vs = eN_t^2/2k_s\varepsilon_0 N_d \qquad (4.17)$$

where $ks\varepsilon_0$ is the semiconductor permittivity, and $N_d$ is the volumetric density of an electron donor ($N_d = N_{dl} - LN_t$, where $N_{dl}$ is the volumetric density of conductive electron without ionosorbed oxygen and $L$ is a constant) [4.25].

Equations 4.16 and 4.17 indicate that the electron density of the sensor will increase when the reducing gas, $R$, is oxidised by the ionosorbed oxygen and also that the sensor conductance will increase with an increase in temperature [4.25].

By assuming that the gas sensor embodies catalysts such as Pt and Pd, it may be assumed that the reaction on the sensor surface happens in principle by means of the Langmuir-Hinshelwood mechanism. Thus the following reaction schemes are considered [4.25]

$$S + e^- + \tfrac{1}{2} O_2 \underset{k_{-1}}{\overset{k_1}{\Leftrightarrow}} O_s^- \qquad (4.18)$$

$$S + R \underset{k_{-2}}{\overset{k_2}{\Leftrightarrow}} RS \qquad (4.19)$$

$$O_s^- + RS \xrightarrow{k_3} RO + e^- \qquad (4.20)$$

where $S$ represents a surface adsorption site, $e^-$ a free electron, and $RS$ an adsorbed reducing gas that reacts with an oxygen ion. For other types of reducing gases, such as CO, that is not to be adsorbed on Sn [4.25]. In this case the Eley-Rideal mechanism is considered instead of equations 4.19 and 4.20 as shown in equation 4.21 [4.25]

$$O_s^- + R \xrightarrow{k_4} RO + e^- \tag{4.21}$$

The kinetics in the reaction schemes 4.18 to 4.21 may be expressed by equations 4.22 and 4.23 respectively [4.25].

$$d C_{O_s^-}/dt = C_{O_2}{}^{1/2} k_1 (S_0 - C_{O_s^-} - C_{R_s}) - k_{-1} C_{O_s^-} - k_3 C_{O_s^-} C_{R_s} - K_4 C_R C_{O_s^-} \tag{4.22}$$

$$d C_{R_s}/dt = C_R k_2 (S_0 - C_{O_s^-}) - k_{-2} C_{R_s} - k_3 C_{O_s^-} C_{R_s} \tag{4.23}$$

where $S_0$ represents the maximum occupied concentration of the adsorbed gas species, $C_{O_2}$ the concentration of oxygen around the sensor surface, $C_{O_s^-}$ the concentration of oxygen ion adsorbed on the sensor surface ($N_t = C_{O_s^-} / C_{O_s^- 0}$, where $C_{O_s^- 0}$ is the maximum adsorbed concentration of ionosorbed oxygen), $C_R$ the concentration of the reducing gas molecules around the sensor surface, $C_{R_s}$ the concentration of the reducing gas molecules adsorbed on the sensor surface, and $K_n$ (n= -2,-1,1,2,3, or 4) the rate constant. $C_{O_2}$ and $C_{R_s}$ are different from those in the bulk phase because of the effect of external diffusion [4.25]. In equation 4.22 and 4.23,

$$K_n = F_n \exp(-E_n/RT) \tag{4.24}$$

Where $F_n$ represents the rexponential factor (n = -2, -1, 1, 2, 3, or 4), $E_n$ the activation energy (n = -2, -1, 1, 2, 3 or 4), $R$ the gas constant and $T$ the absolute temperature ($K$). It

was apparent that the theoretical model based on kinetic equations 4.22 to 4.24 makes it possible to understand the experimental results as reported by Nakata et al. [4.25].

**4.7 Summary**

In this chapter an overview of models that describe a chemoresistive gas sensor was discussed. The underlying mechanisms for the operation of these models have been described. Also an out-line of gas identification by modulation temperature of $SnO_2$-based gas sensors was detailed. Description of my work on identification of gases in a binary mixture and its related data processing are detailed in chapter 5 and 6. The theoretical models outlined are highly dependent on the operating temperature. In my system the combined analogue temperature and thermometer circuits control this. Detailed descriptions of these are found in chapter 5 and 6.

## 4.8 References

4.1 R. E. Cavicchi, J. S. Suehle, K. G. Kreider, M. Gaitan, and Chaparala, *Optimised temperature pulse sequences for the enhancement of chemically-specific response patterns from micro-hotplate gas sensors,* Conf. Proc. Transducers '95 and Eurosensors IX. P 823-826, Stockholm, 1995.

4.2 W. Göpel, K. D. Schierbaum, *$SnO_2$ Sensors: current status and future prospects,* Sensors and Acuators B 26-27 (1995) 1-12.

4.3 A. Heilig, N. Bârsan, U. Weimar, M. Schweizer-Berberich, J.W. Gardner, W. Göpel, *Gas identification by modulating temperatures of $SnO_2$-based thick film sensors,* Sensors and Actuators B43 (1997) 45 – 51.

4.4 K Ihokura, J Watson, *Stannic Oxide Gas Sensors,* Principles and Applications, CRC Press, Boca Raton FL, 1994.

4.5 V. Lantto, P. Romppainen, T. Rantala, and S. Leppavuori, *Sensors and Actuators* B4, 451 (1991).

4.6 Y.Hiranaka and T. Abe, Transducer 91, (publishing Services, IEEE, NY, San Francisco, CA, 1991), pp157. Seiyama, Surf. Sci. 86, 335 (1997).

4.7 J. W. Gardner, A. Pike, N. F. de Rooij, M. Koudelka-Hep, P. A. Clerc, A. Hierlemann, W. Göpel, *Integrated array sensor for detecting organic solvents*, Sensors and Actuators B 26-27 (1995) 135 – 139.

4.8 A. Pike, J. W. Gardner, *Thermal modelling and characterisation of micropower chemoresistive silicon sensors,*Sensors and actuators B 45 (1997) 19 – 26.

4.9 P T. Moseley, B. C. Tofield, *Solid state Gas Sensors*, Adam Hilger, Bristol, 1987. PP. 17 – 31.

4.10 Figaro Engineering, Figaro Gas Sensors Products Catalogue, April, 1994.

4.11 V. Demarne, A. Grisel, *An integrated low-power thin film CO gas sensor on silicon,* Sensors and Actuators 4 (1991) 539 – 543

4.12 J. W. Gardner, *Intelligent gas sensing using an integrated sensor pair,* Sensors and Actuators B 26-27 (1995) 261-266.

4.13 A. C. Pike, Design of chemoresistive silicon sensors for application in gas monitoring, *Ph.D. Thesis, University of Warwick, UK, 1996.*

4.14 J . W. Gardner, *Detection of vapour and odours from a multisensor array using pattern recognition Part 1. Principal component and cluster analysis,* Sensors and Actuators B, 4 (1991) 109-115.

4.15 P. K. Clifford and D. T. Tuma, *Characterisation of Semiconductor Gas Sensors I. Steady State Response,* Sensors and Actuators, 3 (1982/83) 233-254.

4.16 G. Wedler and D. F. Klemperer, *Chemisorption: An Experimental Approach,* Butterworths, London, 1976.

4.17 J. W. Gardner, A Non-Linear Diffusion-Reaction Model of Electrical Conductance in Semiconductor Gas Sensors, *Sensors and Actuators B,* 1 (1990) 166-170.

4.18 D. Kohl, Surface Processes in the detection of reducing gases with SnO2-Based Devices, *Sensors and actuators*, 18 (1989) 71 – 113.

4.19 D. E. Williams, Conduction and Gas Response of Semiconductor Gas Sensors, In solid State Gas Sensors, P.T. Moseley and B. C. Tofield (eds.), Adam Hilger, Bristol, 1987.

4.20 K. D. Schierbaum, U. Weimar, W. Gopel and R. Kowakowski, Conductance, Work Function and Catalytic Activity of $SnO_2$ –Based Gas Sensors, Sensors and Actuators B, 3 (1991) 205-214.

4.21 S. Chang, Thin-film Semiconductor $No_x$ Sensor, IEEE Trans. Elec. Devices, ED-26 (1979) 1875-1880.

4.22 J. W. Gardner, Electrical Conduction in Solid-State Gas Sensors, Sensors and Actuators, 18 (1989) 373-387.

4.23 S. Al-Khalifa, J W Gardner, J F Craine, *Characterisation of a Thermal Wave Microsensor for the Intelligent Analysis of Atmospheric Gases*, Sensors and their Apllications VIII, Glasgow, 1997.

4.24 A. Heilig, N. Bârsan, U. Weimar, M. Scweizer-Bberberich, W. Gõpel, *Gas identification by means of pulsed temperature operated single SnO2 based-thick film sensors,* Eurosensors, Leuven, 1996.

4.25 S. Nakata, S. Akakabe, M. Nakasuji, K. Youshikawa, *Gas sensing Based on a Nonlinear Response: Discrimination between Hydrocarbone and Quantification of Individual Components in a Gas Mixture*, Anal Chem., 1996.

# Chapter 5 Characterisation of a thermally-modulated gas sensor

## 5.1 Introduction

The sensor array devices (SRL125) as shown in Figures 3.1, 3.2, and 3.3 have integrated resistive heaters to set the chemoresistors to the desired operating temperature. The operating temperature is related to the power dissipated thermally to the environment. The micro-hotplates of the SRL125 are embedded in a thin thermally-resistive membrane to reduce thermal power loss [5.1]. There are three different mechanisms by which thermal power can be dissipated: thermal conduction, convection, and radiation [5.2].

Both the steady-state and transient thermal properties of the micro-hotplate and the $SnO_2$ based SRL125 sensor devices are characterised here. The steady-state calibration of the micro-heater resistance versus temperature is described first. Next the closed loop temperature control of the micro-hotplate is described. The temperature coefficient of resistance (TCR) and the base-line resistance of the heater are calculated, so that the heating element can also be used as a resistive temperature sensor. The computed TCR and the base–line resistance allow the measured heater resistance to be accurately converted to temperature in a closed loop heater-temperature circuit. Finally, the details of the virtual instrumentation required for both DC and AC characterisation are discussed.

## 5.2 Calibration of the embedded heater element

The platinum resistive heater was calibrated over a temperature range of 18°C to about 100°C. The SRL125 sensor array devices have three separate heaters each of which serve two sensors as shown in Figures 3.1, 3.2, 3.3. The devices were

put in a temperature controlled (± 1°C) oven. At each oven temperature (the same temperature as the heater element (for the duration of one hour)) the resistance of the heaters versus temperature was taken as shown in Table 5.1. The resistance of the three micro-heaters on the SRL125 device as a function of temperature is shown in Figure 5.1.

**Table 5.1 at each temperature the resistance of the heaters are recorded.**

| Temperature °C | Heater 1 resistance (Ω) | Heater 2 resistance (Ω) | Heater 3 resistance (Ω) |
|---|---|---|---|
| 24.3 | 192.8 | 191.4 | 190.6 |
| 50 | 200.4 | 199.3 | 198.6 |
| 62 | 204.1 | 203 | 202.2 |
| 78 | 208.8 | 207.6 | 206.7 |
| 86 | 211.4 | 210.1 | 209.3 |
| 98.5 | 214.9 | 213.7 | 212.8 |

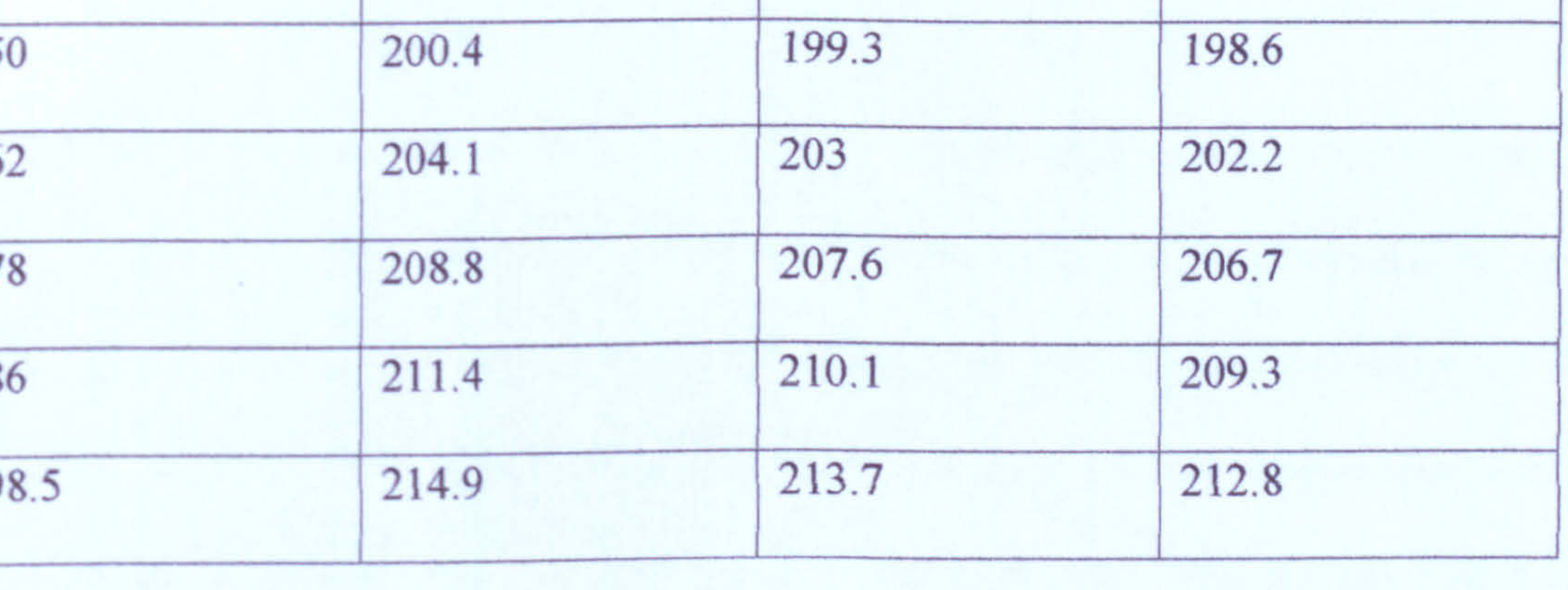


Figure 5.1. Plot of resistance versus temperature for 3 heater elements of a SRL125MOS sensor.

The resistance of the heater element (Pt) was measured as a function of temperature in the oven as described above in order to calibrate the temperature scale. Figure 5.2 shows the heating characteristic of the micro-heater of the SRL125 (Sensor Research Laboratory) after annealing at 5.8 v for 48 hours.

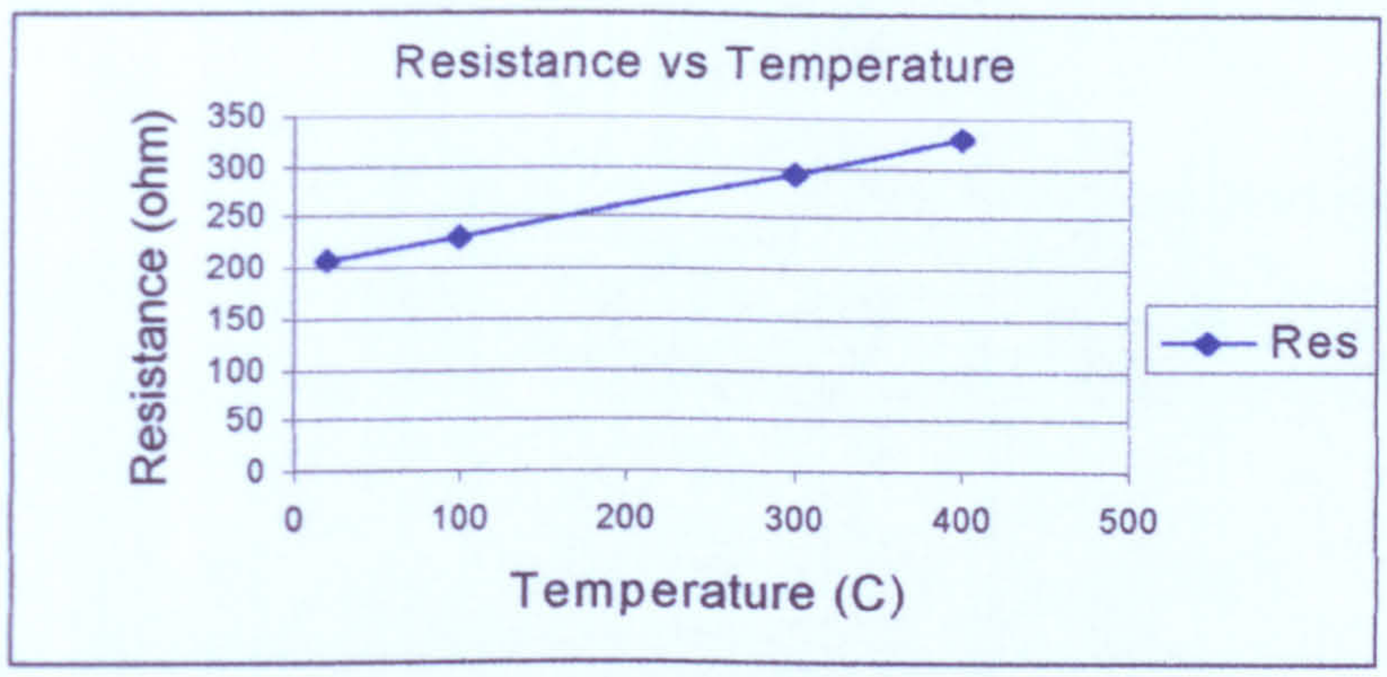


Figure 5.2 Heating characteristics of element of the micro-heater.

It can be seen that the lines are parallel and so the differences in temperature sensitivity are small. However, the large differences in resistance can be attributed to small variations in heater geometry, manufacturing process and material composition. The resistance of the heater element for different voltage steps and the corresponding current are shown in table 5.2. The circuit shown in Figure 5.3 was used for this (the meter resistance was ignored in this case).

Table 5.2 Heater resistance vs applied voltage steps

| Before annealing | | | After annealing (24 hours annealing time at 300°C) | | |
|---|---|---|---|---|---|
| Voltage (v) | Current (mA) | Resistance (ohm) | Voltage (v) | Current (mA) | Resistance (ohm) |
| 0.1 | 0.6 | 166.6 | 0.524 | 2.5 | 209.6 |
| 1.207 | 7.2 | 167.6 | 1.5 | 6.6 | 227.2 |
| 1.7 | 9.6 | 177 | 2.12 | 8.7 | 243.6 |
| 2.1 | 11.4 | 184.4 | 2.67 | 10.4 | 256.7 |
| 3.29 | 15.8 | 207.5 | 3.65 | 12.9 | 282.9 |
| 4.35 | 19 | 228.4 | 4.62 | 15 | 308 |
| 5.31 | 21.5 | 246.5 | 5.04 | 15.9 | 316.9 |
| 6.01 | 23.2 | 256.6 | 6 | 17.6 | 340.9 |

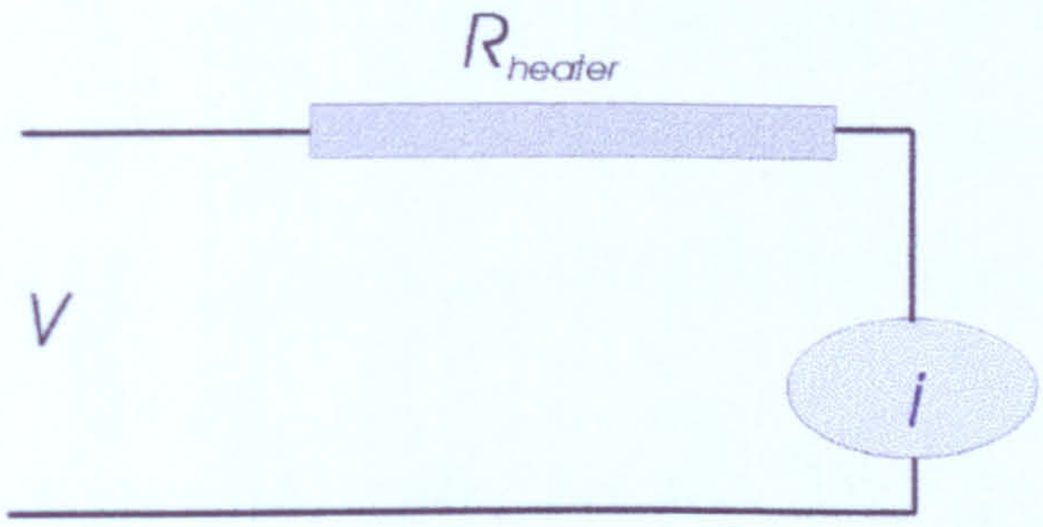


Figure 5.3 Circuit used to measure heater element resistance vs applied voltage

The graph of voltage applied across the heater element versus heater element resistance is shown in Figure 5.4. For accuracy reasons the ameter's resistance should be noted.

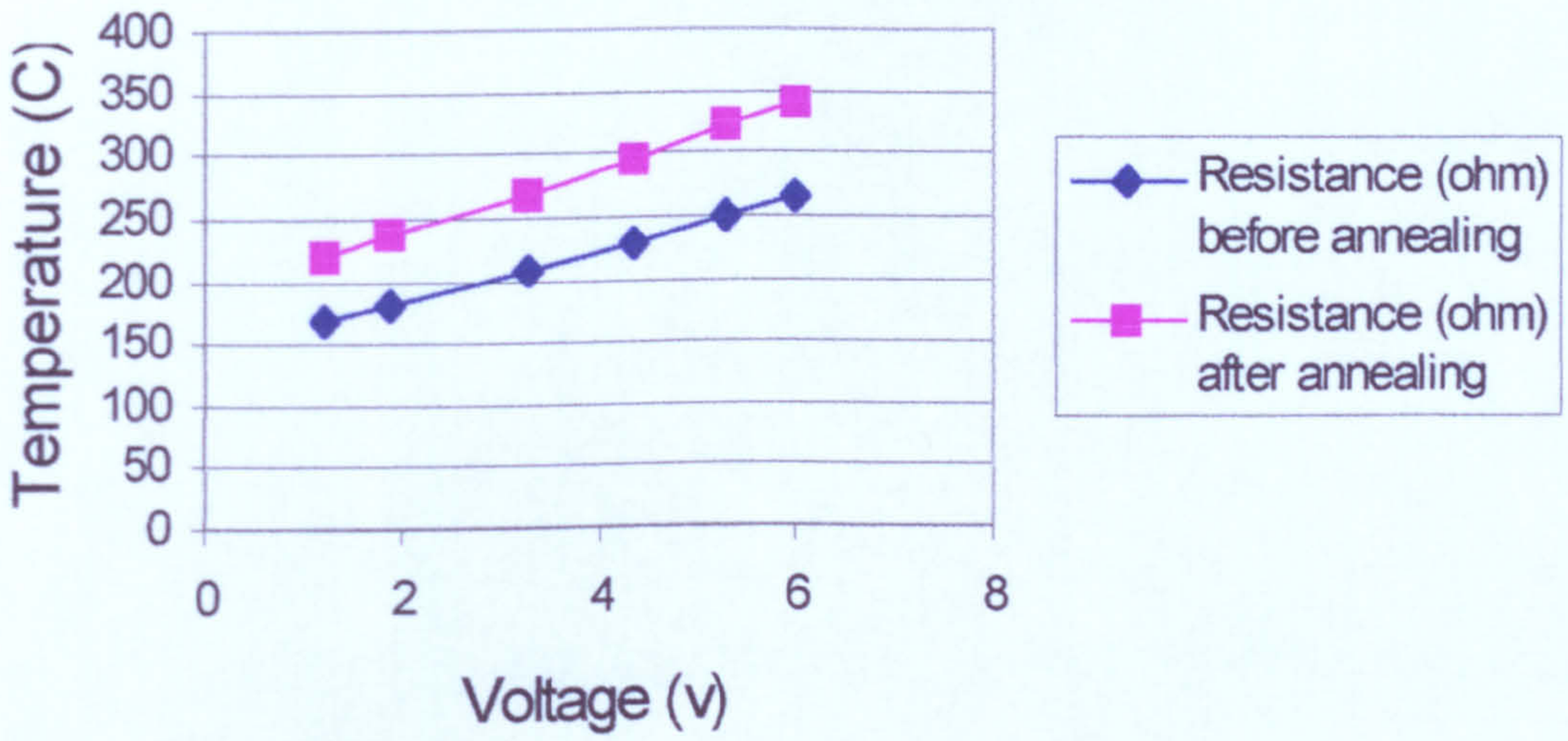


Figure 5.4 Heater element temperature vs applied voltage

## 5.3 Design of front-end analogue circuitry

In order to characterise the response of the resistive sensor to thermal wave, it is essential to have a stable and reliable circuitry which both drives the resistive heater and measures the resistance of the metal oxide coating over a wide dynamic range of both resistance (e.g. 10 Ω to 1 M Ω) and frequency (mHz to KHz). The circuit was designed specifically for this purpose, to characterise the

sensor's response to thermal waves at different levels of target gas concentration and humidity. A simplified version of this block diagram is shown in Figure 5.5. The complete circuit is shown else where in chapter 7.

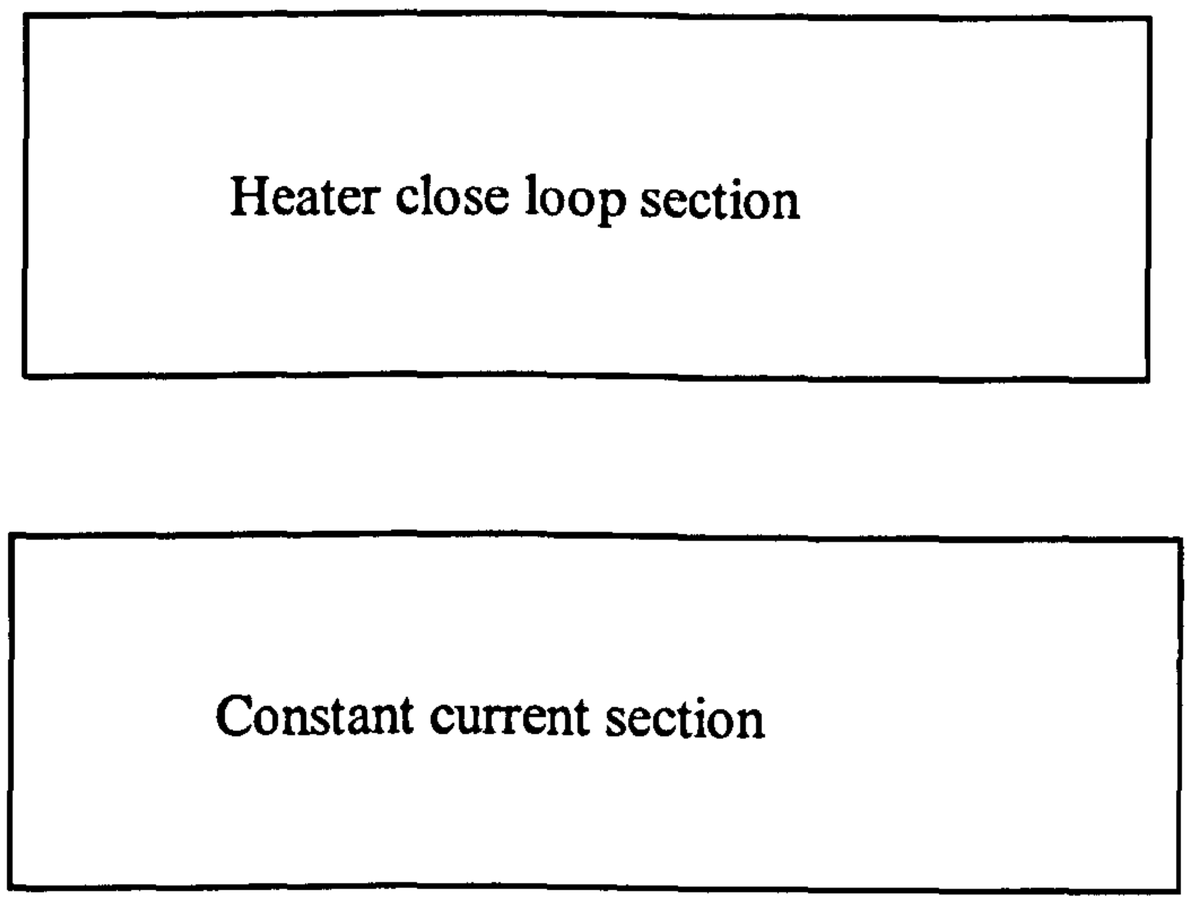


Figure 5.5 Block diagram of heater and sensor circuitry

A virtual instrument was constructed using LabView (National Instruments, US) which runs on a 486-based PC. Figure 5.5 shows the circuit diagram for the measurement system, which allows for setting the d.c. operating temperature of the device (via a bias voltage) and any d.c or a.c. signals, such as a step function, sine wave etc.

### 5.3.1 Constant current circuit

The resistance $R_s$ of gas–sensitive coating is measured using a reference diode based circuit to generate a constant current of $I_s$ with the value set by the choice of precision resistor R6 shown in Figure 5.5. The current was chosen so that the

voltage dropped across the resistive sensor does not exceed 0.1 V and it is ohmic in nature. The $V_s$ output of the sensor is first set close to zero by biassing with a voltage controlled by DAC0 (National Instrument), and then amplified using two programmable gain amplifiers (PGA204 and PGA205, BURR-BROWN)[5.3]. The analogue voltage output is finally fed into the 12-bit ADC (National Instrument) at channel CH0, then filtered, recorded and processed by the virtual instrument (VI). The temperature of the sensing material is assumed to be the same as the Platinum heater because the thermal time-constant through the membrane is less than ca. 2 ms and our thermal modulation is only 1 Hz of less. However, a large number of tests were carried out to investigate the response of the sensor at higher frequencies. These will be discussed later in this chapter. The interface circuitry was then used to characterise step changes and low frequency a.c. temperature modulation of the resistive sensor.

### 5.3.2 Temperature control and thermometer circuits

The voltage across the heater, $V_{heater}$, is set by a 12-bit ADC (Labview PC+, National Instrument), DAC1, with the current $I_H$ is supplied by transistor T1 and flows through the heater RH (ca. 200 Ω) and a precision feedback resistor $R_F$. The heater current, resistance and power can be calculated from the heater voltage and sense voltage $V_{sense}$, as described below.

The test starts by outputting a voltage (see Figure 5.4 for voltage and temperature calibration) $V_{Heater}$ which is controlled by the DAC card (12 bits). $V_{Heater}$ is the same as the voltage across $R_H$ ( Pt Heater element) the voltage at the emitter of transistor T2 is

$$\frac{-R_F}{R_H} \; V_{Heater} \tag{5.1}$$

As $R_H$ warms up, $R_H$ increases ( $V_{Sense}$ $\alpha$ $\frac{1}{T}$ approximately).

$$\text{voltage across } R_F \text{ is } = \frac{R2}{R_3} \; V_{Sense} \tag{5.2}$$

Since the current in $R_F$ = the current in $R_H$.Therefore

$$I_{Heater} = \frac{R_3 V_{sense}}{R_2 R_F} \tag{5.3}$$

$$P_{Heater} = I_{Heater} \; V_{Heater} \tag{5.4}$$

The voltage applied under software control controls the power in the heater element and therefore the sensor temperature. The heater resistance is calculated from the following equation:

$$V_{Sense} = -\frac{R_2}{R_3} \text{ x } -\frac{R_F}{R_H} \; V_{Heater} \tag{5.5}$$

Therefore

$$R_H = R2 \text{ x } R3 \; \frac{V_{Heater}}{R_3} \; / V_{Sense} \tag{5.6}$$

The heater temperature is calculated from the following equation

$$R_H = R_0 ( 1 + \alpha ( T - T_0)) \tag{5.7}$$

$$T = T0 + \frac{R_H - R_0}{\alpha R_0} \tag{5.8}$$

Where $T$ is the heater element (and the sensor) at any temperature, $T_0$ is the room temperature, $R_0$ is the resistance of the heater element at temperature $T_0$, and $\alpha$ is

the temperature coefficient (constant up to at least 900°C). Equation (5.8) was used to calibrate the heater and then the temperature was computed with the virtual instrument, as shown in Figures 5.6 and 5.7.

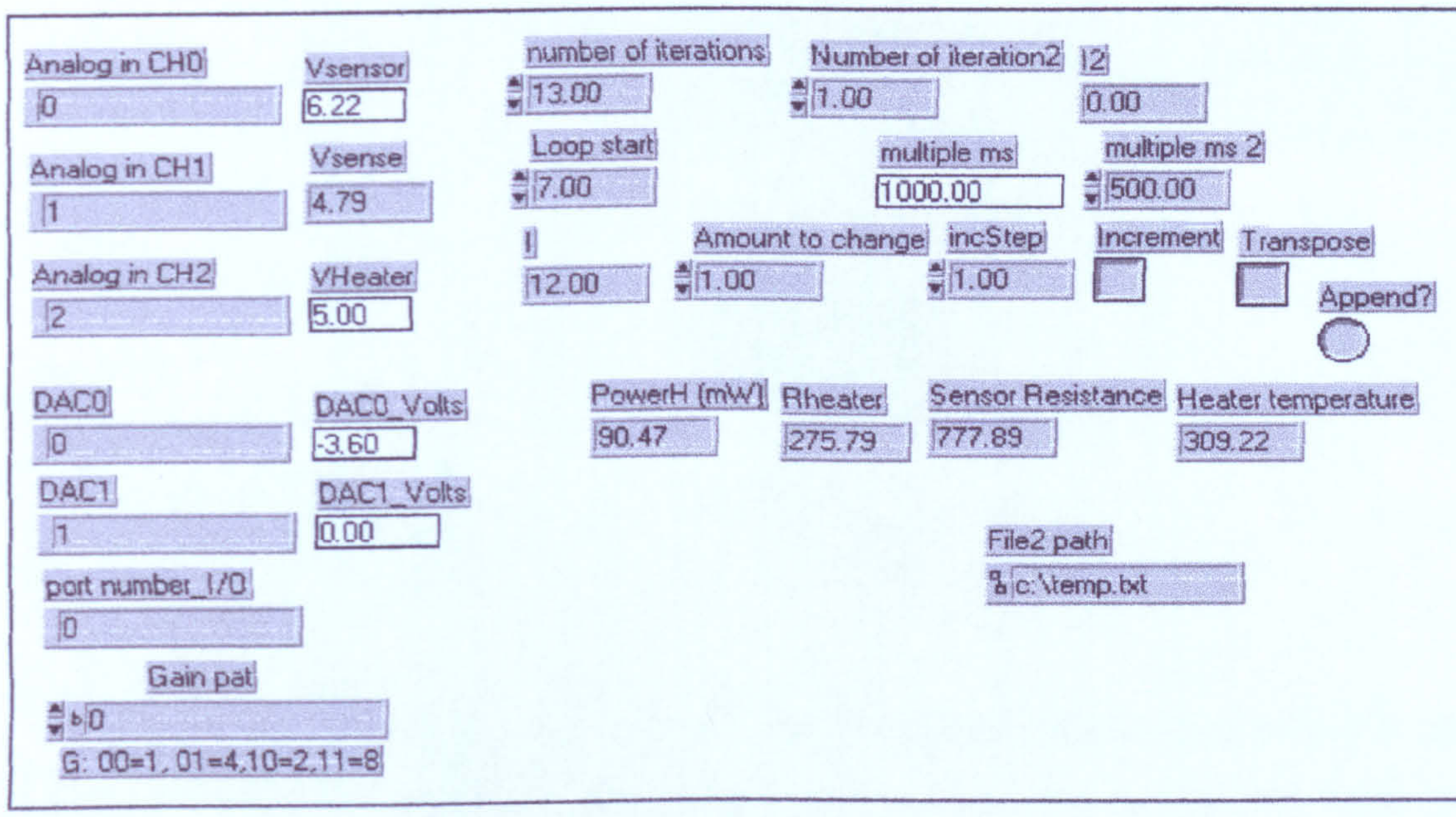


Figure 5.6 Virtual instrument front panel for controlling the sensor and heater element circuits.

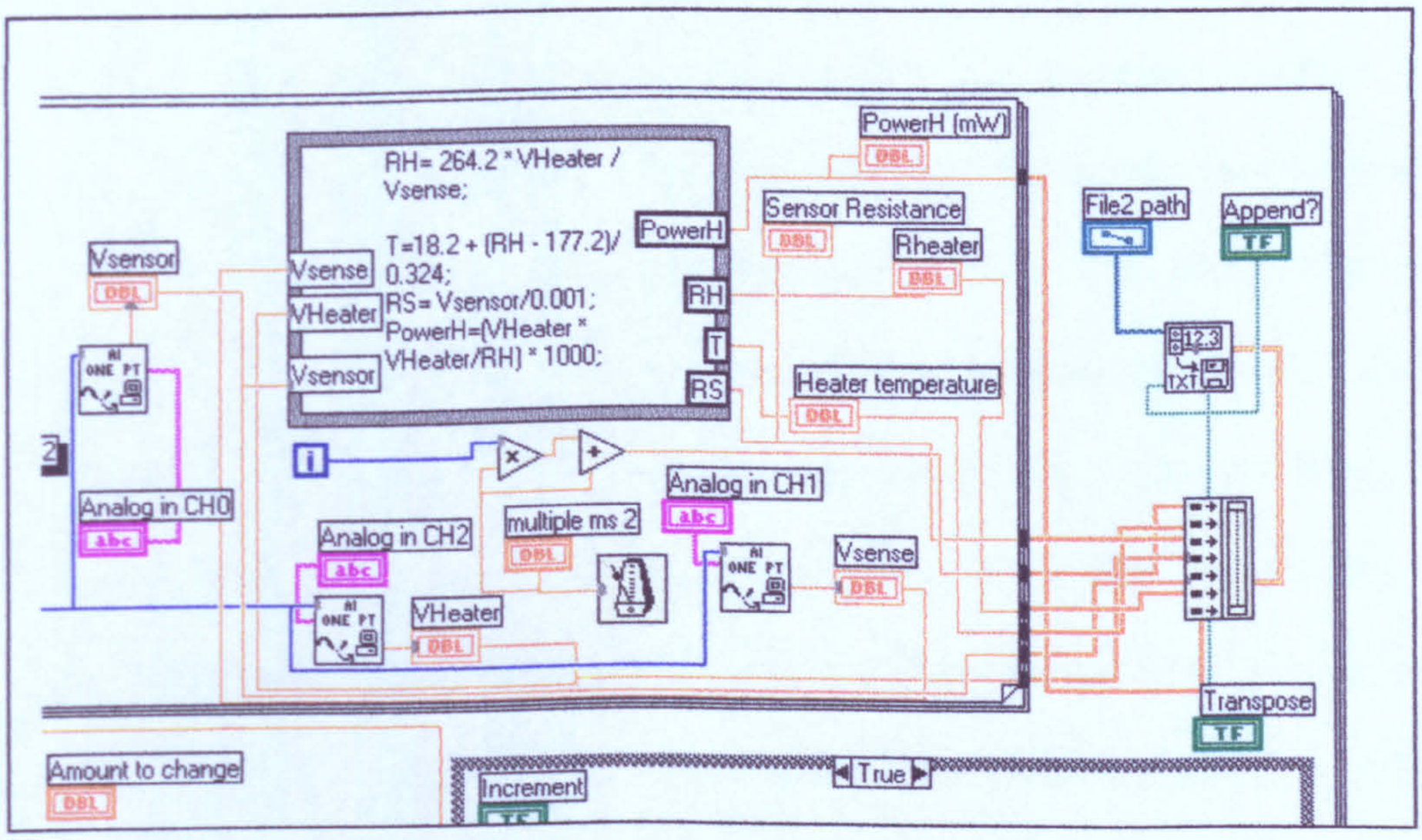


Figure 5.7 Part (too large to fit one screen) of the Virtual instrument circuit

## 5.4 Virtual instrumentation design I – DC measurement

The complete test system is comprised of several sub systems as show in Figure 5.8.

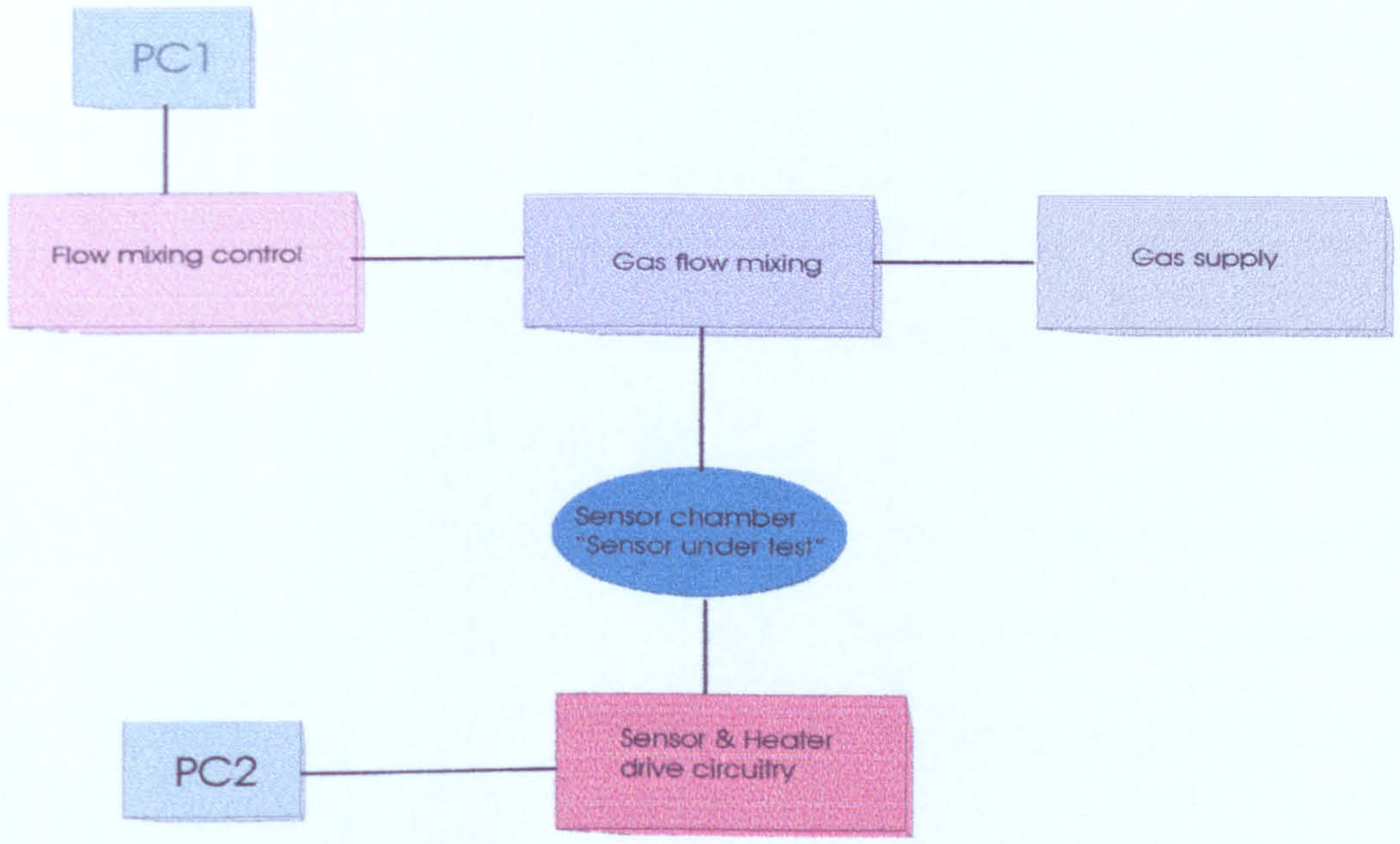


Figure 5.8 Block diagramme of the test and control system for characterising the sensors and the target gases.

The gas flow system is fully automated, PC1 provides a menu driven user interface which allows the user to input the gas exposure duration, gas concentration in ppm, amount of relative humidity (rh) and the flow volume of gas (or gas mixtures) in millilitre per minute (ml/min). PC1 drives four mass flow controllers (MFCs) that are used to set the gas concentrations and humidity. The gas supplies are filtered upstream from the MFCs to prevent particulate matter accumulating in the MFCs aperture [5.1]. One way check valves are positioned at various points in the system to direct the gas flow. To achieve a constant air flow temperature independent of the flow-rate, the brass blocks (housing the sensors) are mounted in a Dri-block® heater. The gas upon entering the inlet fitting is directed through a heat exchanger, which is a meandering

channel machined into the brass block. The heat exchanger ensures that even for the maximum flow rates the gas temperature still acquires the brass block temperature [5.1].

The system operates by controlling the flow of the required target gas concentration through the sensor chamber for a required period, this is controlled by PC1 as shown in diagram 5.8. PC2 then control the sensor temperature, length of temperature steps, amplitude and frequency of the heat wave modulation signal as inputted by the user. The virtual instrument controls these parameters through its front panel as shown in Figure 5.6 as well as logging the response of the sensor in real-time for later processing. The front panel as shown in Figure 5.6 also displays the resistance change of the sensor and also the temperature [5.5].

The test starts by checking that the sensor and the heating element are behaving as expected, as shown in Figure 5.9.

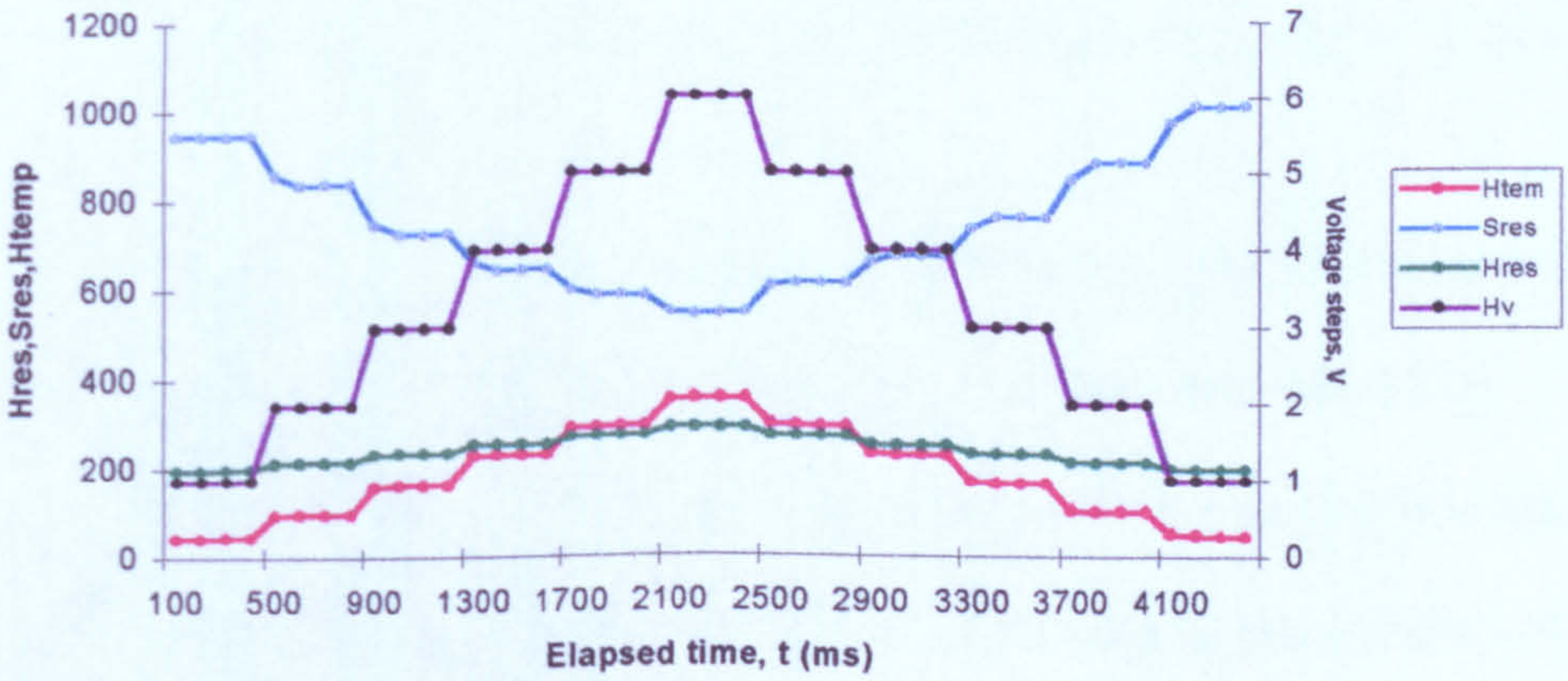


Figure 5.9 Plot of sensor response (blue) to voltage steps (black) which control the heater (and sensor) temperature (red) and heater element resistance (green)

This test starts by outputting a voltage step (black) across the heater element (these voltages and its related temperatures were calibrated as shown earlier on in this chapter) the $SnO_2$ coating resistance (blue) will decrease as the temperature increases (red). The heater element resistance increases (green) as the temperature increases. The process is shown to be reversible as shown in Figure 5.9.

The next test was to check the response of the sensor to CO at different CO (ppm) concentrations, 350 °C, and 25%rh as shown in Figure 5.10.

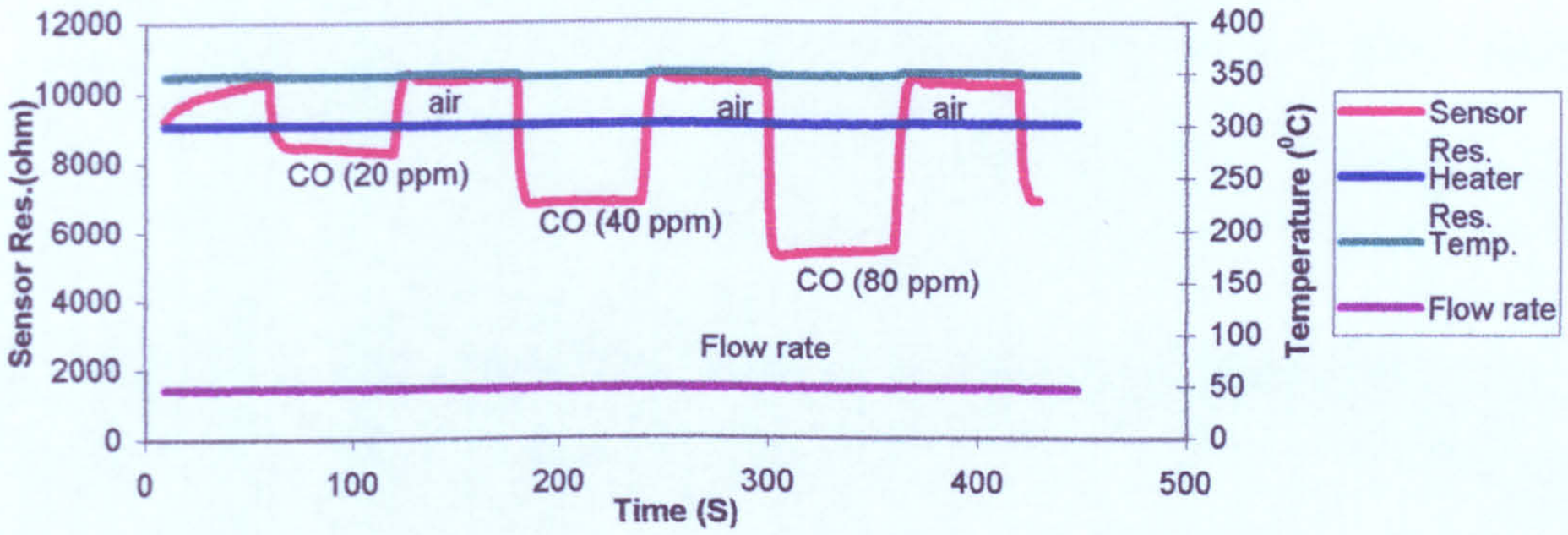


Figure 5.10 Response of $SnO_2$ (Pd doped) sensor to different CO concentrations at 350 °C and 25% rh.

This test starts by elevating the sensor temperature to 350 °C and keeping it at this temperature for the duration of the test. The flow-rate (black line in Figure 5.10) of the target gas (CO in this case) was monitored during the whole test period and found to be constant as shown. After purging the system with clean air for a period of one hour at 150 ml/min, the target gas (CO) at 20 ppm was passed through the system to the sensor chamber for 50 seconds. At the end of this period the target gas was switched off and only clean air was moved through the system, this was repeated with target gas concentrations of 40 and 80 ppm

and clean air. As expected the sensor response (red) to CO exposure resulted in a decrease in the sensor resistance. The catalyst in the $SnO_2$ sensor such as palladium (Pd) principally determines the height of the potential barrier of the $SnO_2$ by attracting electrons from the $SnO_2$. However, when Pd receives electrons from CO it would be more electron negative thus releasing electrons to the $SnO_2$. This effect will decrease the height of the Schottky barrier and consequently reduce the $SnO_2$ resistivity as shown in Figure 5.10.

**5.5 Virtual instrumentation design II – AC measurement**

I have constructed a virtual instrument for controlling the AC measurement and characterisation of the SnO2 based SRL125 sensor devices. The virtual instrument comprised of a front panel as shown in Figure 5.11, block diagram and icons and connectors as shown in Figure 5.12.

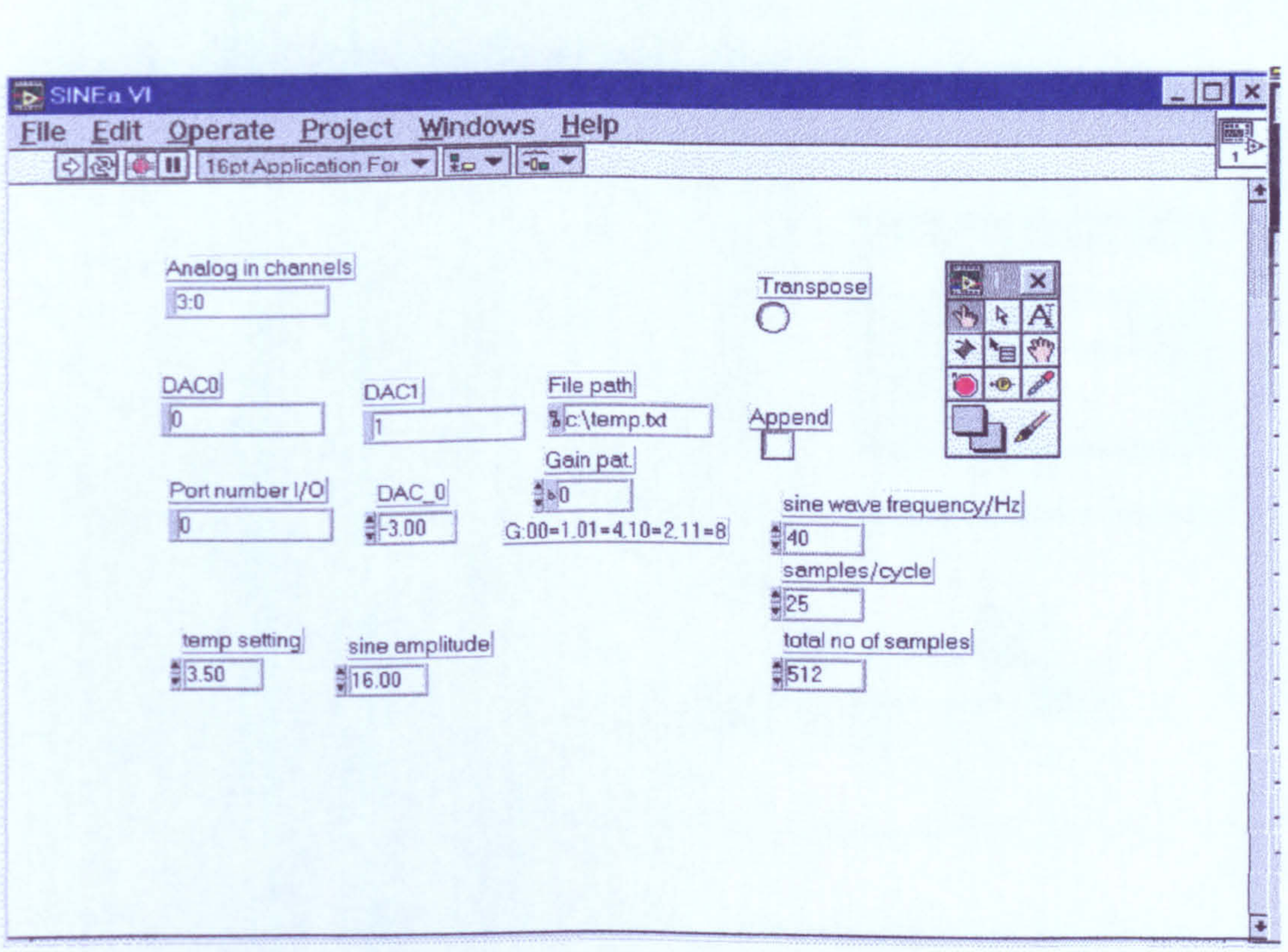


Figure 5.11 virtual instrument front panel for AC measurement

The front panel of the virtual instrument consists of control and measurement boxes. The test starts by setting the temperature (e.g. 3.5 V equivalent to 350ºC), next the frequency of the sinusoidal drive wave is set up in Hertz as shown in sine wave frequency/Hz box in Figure 5.11. The front panel allows also setting the number of samples per cycle as well as the total number of samples. The data from the test are logged in a file (c:\temp.txt) for later processing. The block diagram as shown in Figure 5.12 also contains a formula node that can be used for entering algebraic formulas directly into the block diagram. For example once the $R_H$ (heater element resistance) is calculated from $V_{Heater}$ (voltage across heater element) and $V_{sense}$ (see equation 5.6), then the temperature of the sensor can be calculated as shown in Figure 5.12.

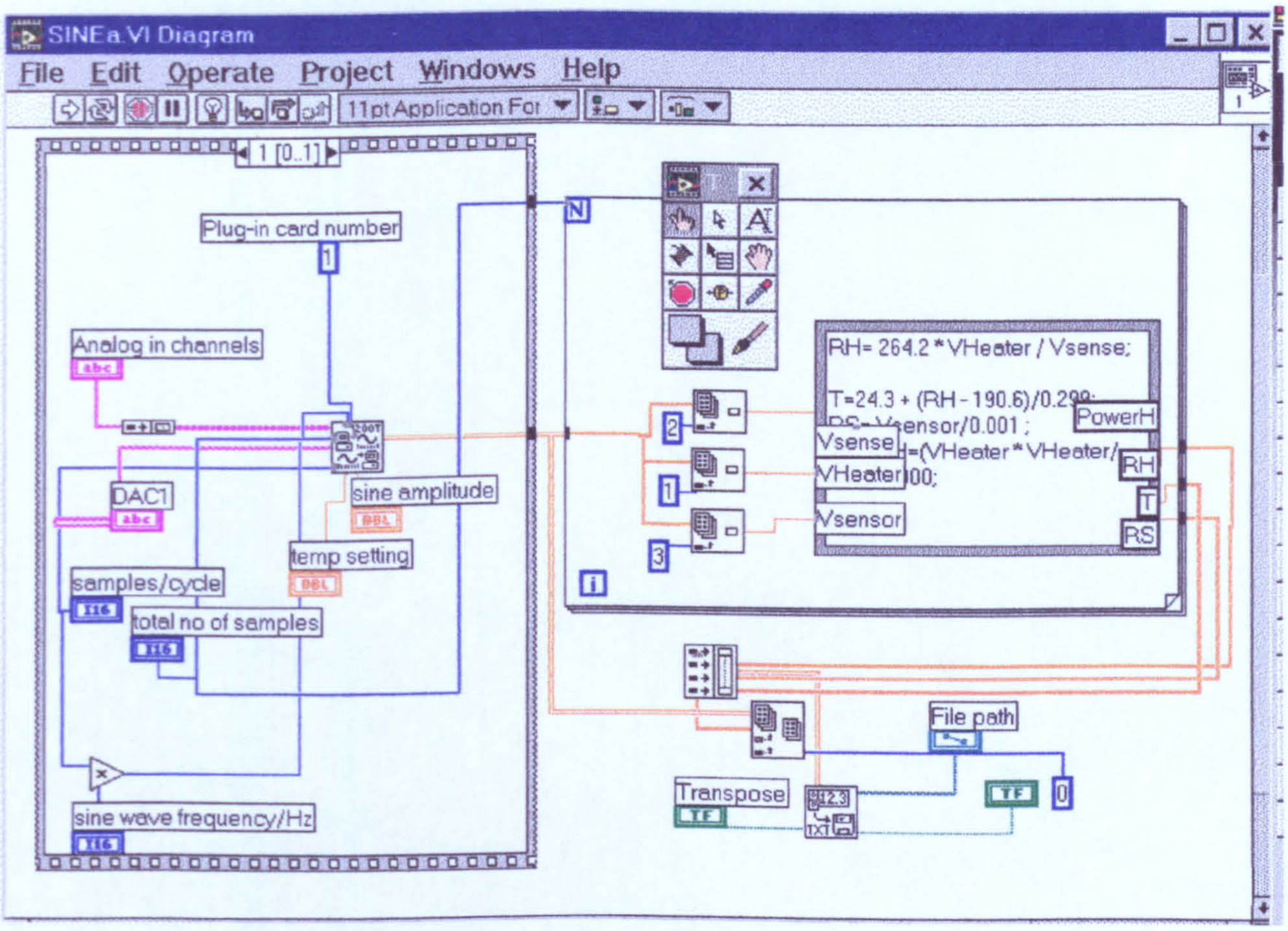


Figure 5.12 Virtual instrument block diagram for AC measurement

### 5.5.1 Experimentation

The experimentation started by characterising the sensor response to a sinusoidal heat wave modulation. Table 5.3 shows the test parameters.

Table 5.3 Test parameters for sinusoidal modulation

| | |
|---|---|
| Logged file name | Cosin3c1.txt |
| Sensor type | Pd doped $SnO_2$ |
| Virtual instrument name | Flow3.vi |
| Sine amplitude | 1.45 V this gives a swing of temperature between 243°C and 405°C |
| Temperature setting | 325°C |
| Signal frequency | 50 mHz |
| Total number of samples | 9000 |

The first 50 readings from the sensor was ignored, this is to let the sensor achieve stability. The sensor response to the parameters set up as listed in Table 5.3 is shown in Figure 5.13.

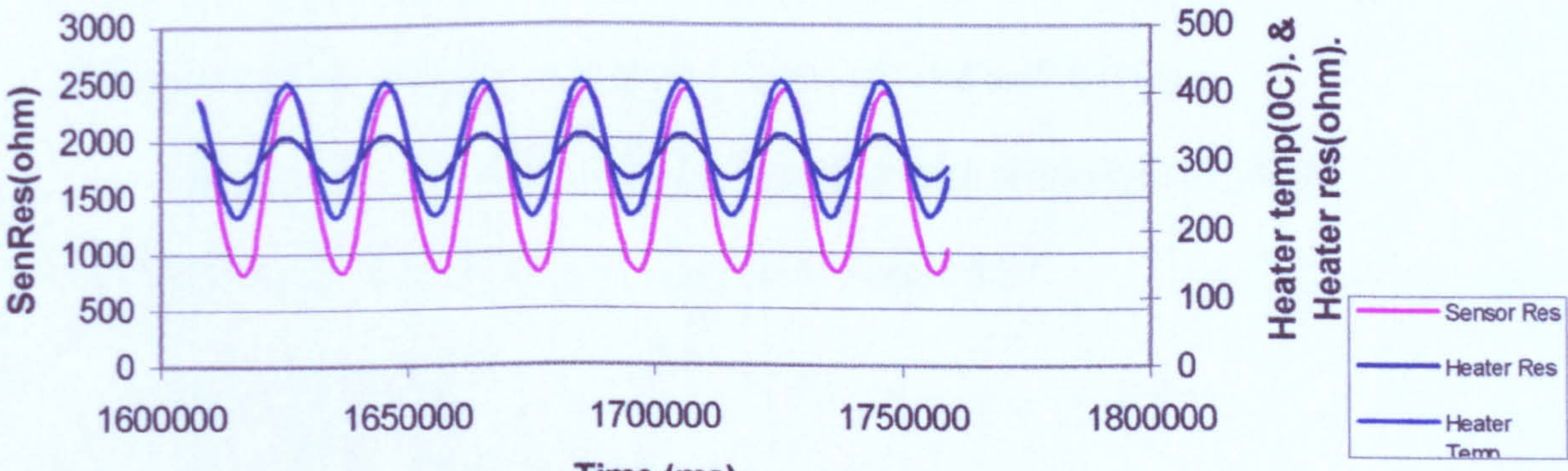


Figure 5.13 Plot of sensor response (magenta) to sinusoidal temperature modulation of 50 mHz (blue) and heater element resistance response (black) to the same temperature modulation, at 325°C.

The sensor response is basically sinusoidal and repeatable in this test. Next the response of the sensor to four different target gas (CO) concentration was tested and the resulting responses for the sensor is shown in Figure 5.14.

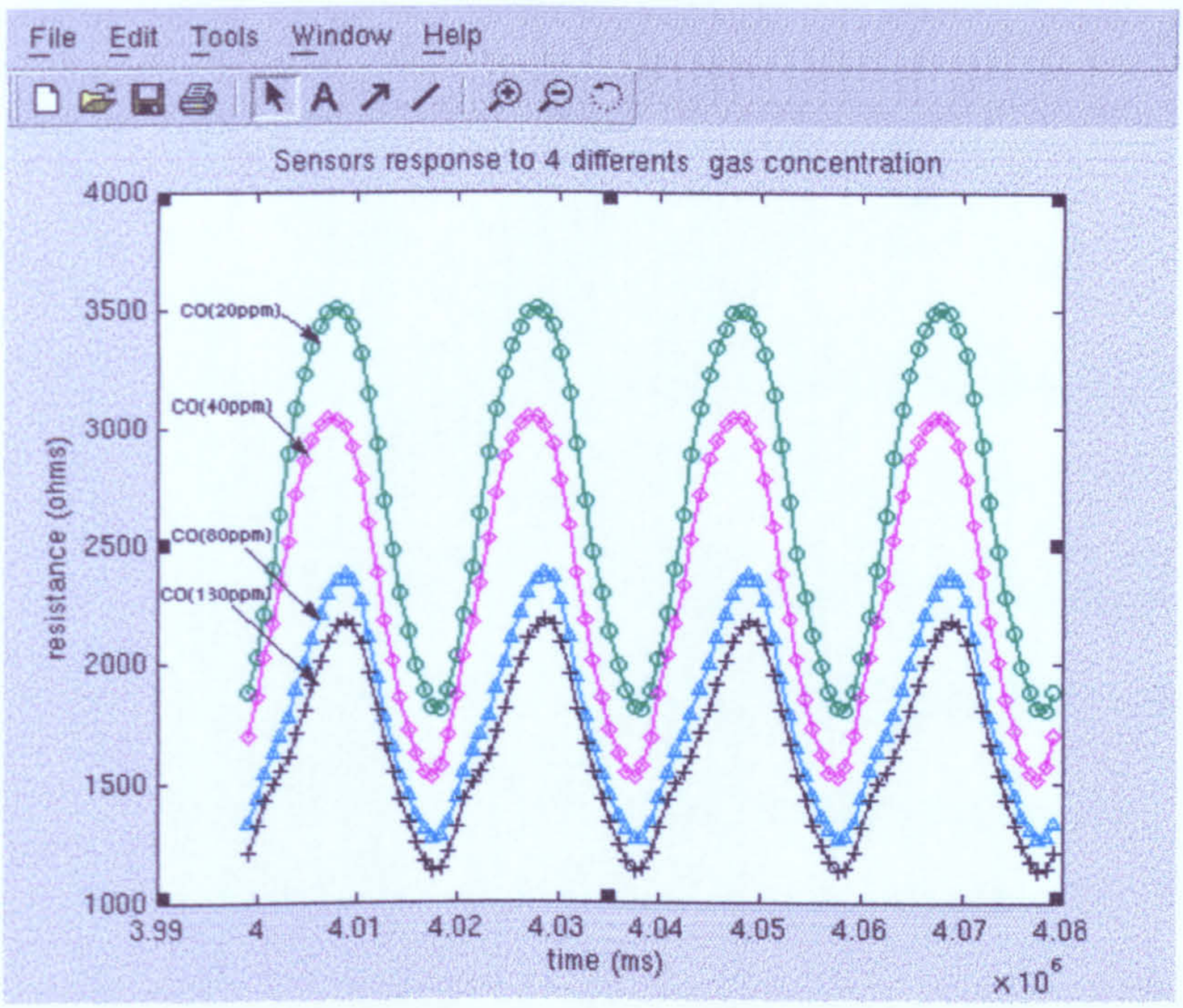


Figure 5.14 Plot of sensor response to 20, 40, 80, 130 ppm at temperature modulation of 200°C and 25%rh.

The sensor resistance decreased as the target gas (CO) concentration increased at 25% rh and average temperature modulation of 350°C the heat wave modulation is 50 mHz. The sensor response appears sinusoidal and well-behaved.

The response of pd doped $SnO_2$ sensor at four different temperatures to four $NO_2$ concentrations at 25% rh is shown in Figure 5.15.

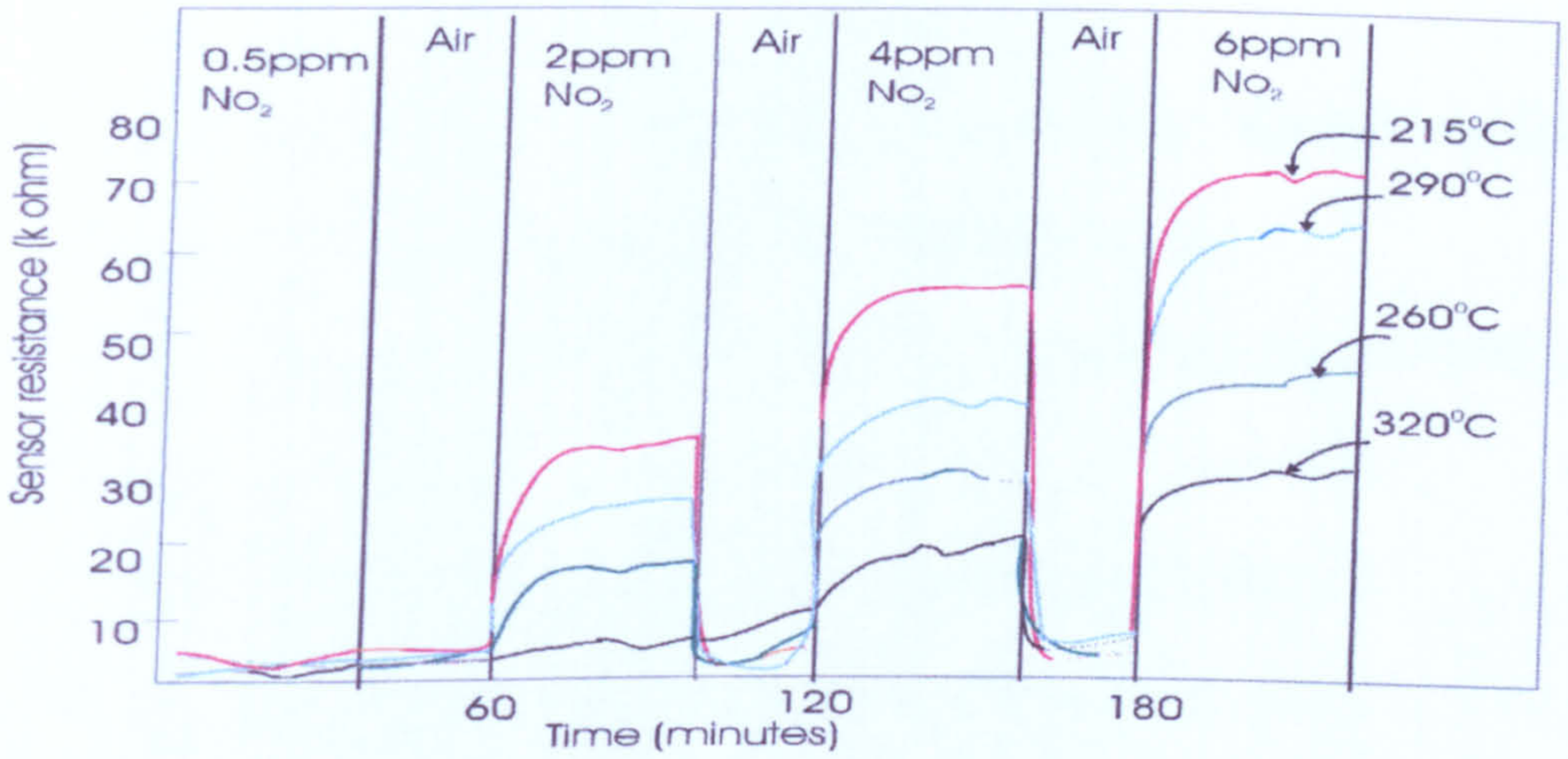


Figure 5.15 Response of Pd doped SnO2, sensor at four different temperature to four different $NO_2$ gas concentrations at 25% rh.

As can be seen in Figure 5.15, the Pd doped $SnO_2$ chemoresistor gave a large response at lower temperatures. However, commercial devices are usually run hotter to improve response time and reduce humidity sensitivities.

**5.6 Summary**

The resistive $SnO_2$ microsensor was characterised for both step and a.c. thermal wave modulations. The temperature/thermometer circuit were described. This proved to be an accurate and repeatable system. Virtual instrumentation for controlling both the sensor temperature and sensor response was designed and tested.

## 5.7 References

5.1 A. Pike, *Design of chemoresistive silicon sensors for application in gases monitoring. Ph.D. Thesis*, University of Warwick, UK, 1996.

5.2 A. J. Chapman, *Heat Transfer 4th Edition*, (1984), Macmillan Publishing Company, New York.

5.3 PGA204 and PGA205, BURR-BROWN, data sheets, 1994.

5.4 Labview, National Instrument, data sheets, 1997.

5.5 S. Al-Khalifa, J W Gardner, J F Craine, Characterisation of a Thermal Wave Microsensor for the Intelligent Analysis of Atmospheric Gases, Sensors and their Applications VIII, Editors A. T. Augousti and N. M. White, Institute of Physics Publishing, Bristol and Philadelphia, 1997.

# Chapter 6 Signal and data processing

## 6.1 Introduction

The main objective of this chapter is to describe the processing of the sensor signal, extraction of signal features and to process the data.. Single gas identification of CO and $NO_2$ in air is discussed first of all. Next and more interestingly, identification of a binary gas mixture (CO and $NO_2$) is fully discussed using one $SnO_2$ coating sensor. The sensor signals are first analysed by applying an FFT the resulting FFT coefficients studied. The higher harmonics FFT coefficients were analysed and discussed this was then normalised and prepared for input to the neural networks for further analysis. The data processing and classification was performed by using MATLAB with its NEURAL NEWTWORKS tool box software. MATLAB is an interactive mathematical and analysis program to help solve engineering and scientific problems. Its basic data element is a matrix, which does not require dimensioning. NEURAL NETWORKS is a complete and comprehensive multi-paradigm prototyping and development system. It is used here to design, build, train and deploy neural networks to solve the signal component and binary gas mixture identification problem..

## 6.2 Data preparation

As shown in chapter 5 data collections are achieved by using the fully automated virtual instrument (vi), the data are then saved in a temporary file for later processing. For each file saved there are attributes related to that particular test, an example of these is shown in Table 6.1.

Table 6.1 An example of parameters associated with a particular test file.

| | |
|---|---|
| Test file name | Cosin5N1.txt, N is for $NO_2$ |
| VI used | Flow4.exe |
| Sensor | Pd doped $SnO_2$ |
| Heater room temperature value to be entered in vi' formula node | 189 Ω |
| Heater sine wave modulation | 1.45 this will give a temperature swing from 405°C to 243°C, i.e. ± 80°C |
| Heat wave modulation frequency | 50 mHz |
| Total number of samples | 9000 |

After each test the data points are saved in a file with a suitable name for subsequent processing. The data saved in a file structure as shown in table 6.2.

Table 6.2 The structure of test files for later processing.

| Time (ms) | Heater element resistance (Ω) | Sensor resistance (Ω) | Temperature (°C) |
|---|---|---|---|
| … | … | … | … |
| 9000 readings | 9000 readings | 9000 readings | 9000 readings |

Matlab was used to pre-process the data sets from the $SnO_2$ sensor response. The Fast Fourier transformation function was used to extract the Fourier coefficient.

The Fourier series is a mathematical expression for a periodic function [6.1] The theorem associated with this series states that any periodic function $f(t)$ can be written in the form

$$f(t) = a_0 + a_1 \cos(\omega t) + a_2 \cos(2\omega t) + a_n \cos(n\omega t) + b_1 \sin(\omega t) + b_2 \sin(2\omega t) + b_n \sin(n\omega t) \quad (6.1)$$

Where $\omega$ is the fundamental angular frequency or $2\pi$ times the natural frequency of the original periodic wave *f*. The term $a_0$ is the average ordinate or the d.c. component of the wave. The coefficient $a_0$ is the average value of *f(t)* and is

$$a_0 = \frac{1}{T}\int_0^T f(t)dt \qquad \text{where T= time period } (2\pi(\omega)) \qquad (6.2)$$

The term

$$a_1 \cos(\omega t) + b_1 \sin(\omega t) \qquad (6.3)$$

is the fundamental component and has the same frequency and period as the original wave. The remaining terms, taken as pairs of the form

$$a_n \cos(n\omega t) + b_n \sin(n\omega t) \qquad (6.4)$$

give the nth-harmonic component of the function.

### 6.2.1 Fourier coefficient extraction

The MATLAB function for FFT was applied to the data. The following is an example of such operation.

1. Data file was loaded in to MATLAB

Load testsin9.dat

2. Perform FFT on file testsin9 data from 1 to 512 of column 2 (sensor resistance in this case)

3. Plot the absolute value of ftrans. The plot of this is shown in Figure 6.1.

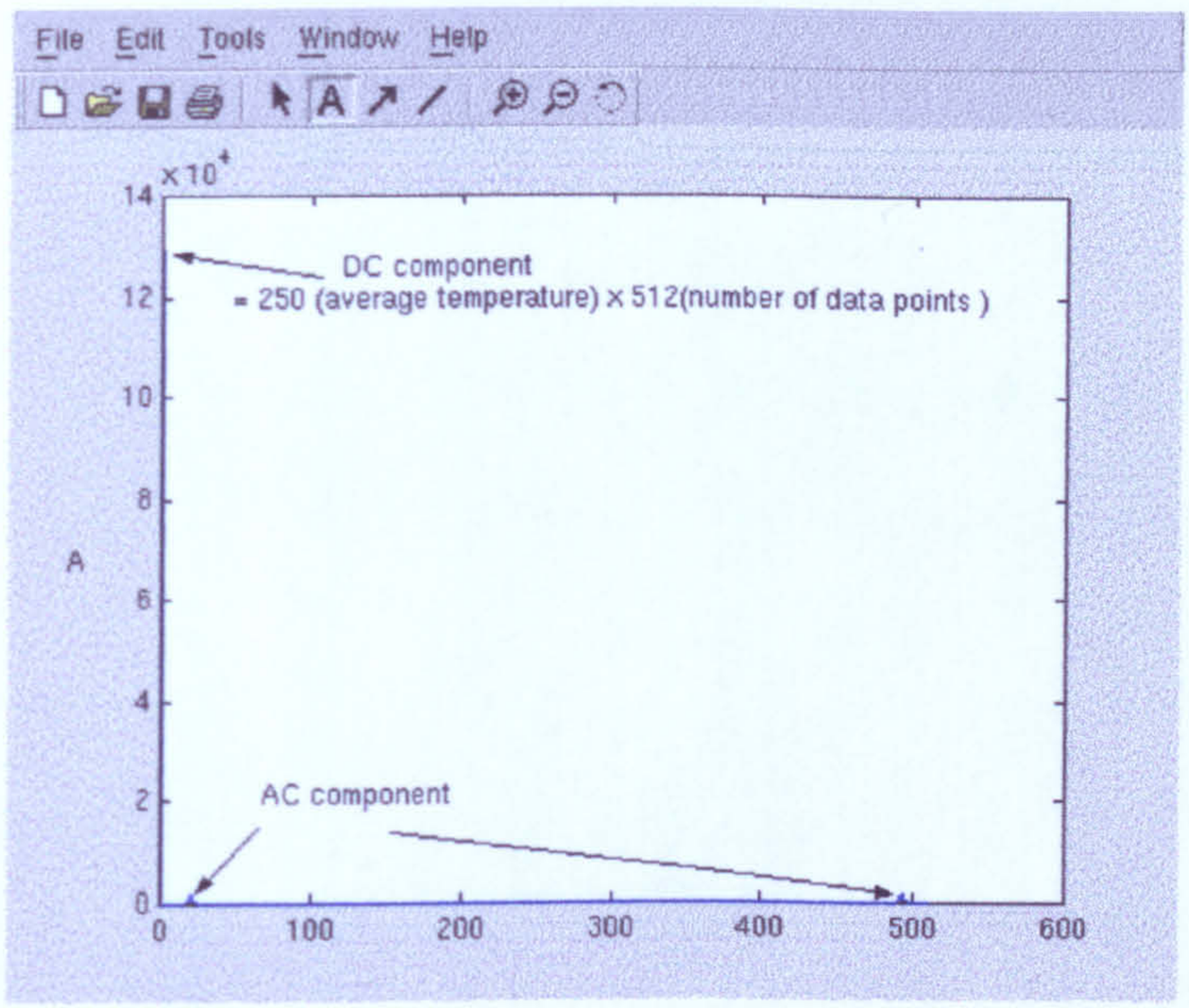


Figure 6.1 Plot of absolute values of the amplitude vers period. The DC components represent the Sum of all average (512 cycles) DC temperature.

ftrans is the sum of all average value. To remove the DC part the following was carried out

$$ftrans(1) = 0 \tag{6.5}$$

The plot of absolute ftrans without the DC component is shown in Figure 6.2.

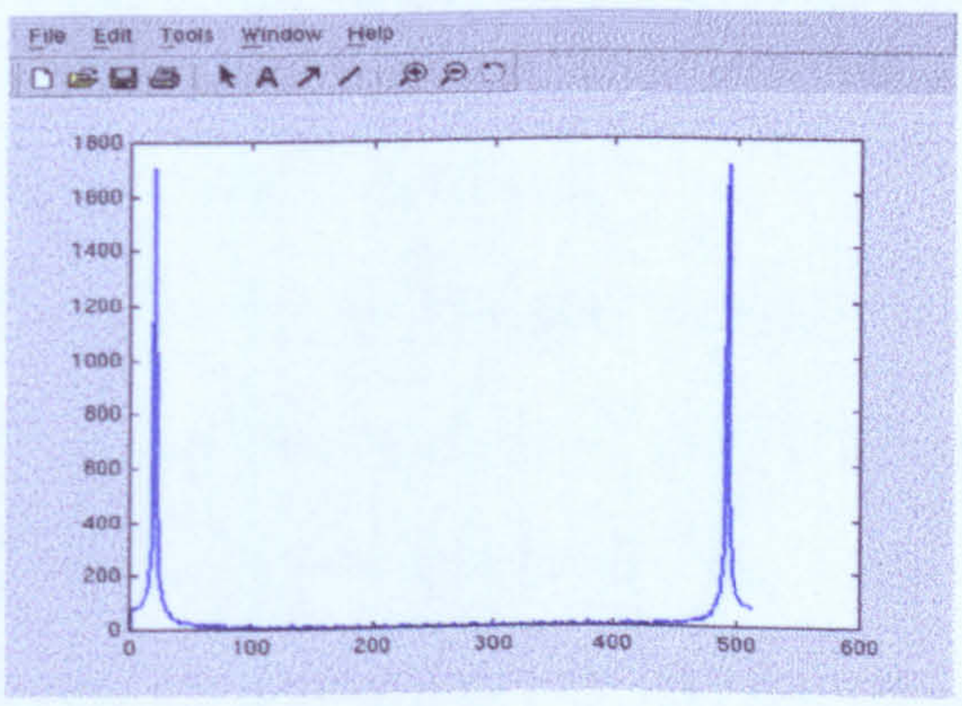


Figure 6.2 plot of AC component

### 6.2.2 Fourier coefficient initial analysis

A large number of tests (over 300 tests) were carried out on the $SnO_2$ sensor at different gas concentrations (CO and $NO_2$), heater drive frequencies and humidity in order to optimise the sensors and study the responses.

The amplitude of the fundamental frequency was shown to increase by increasing the sinusoidal heating modulation of the sensor as shown in Figure 6.3.

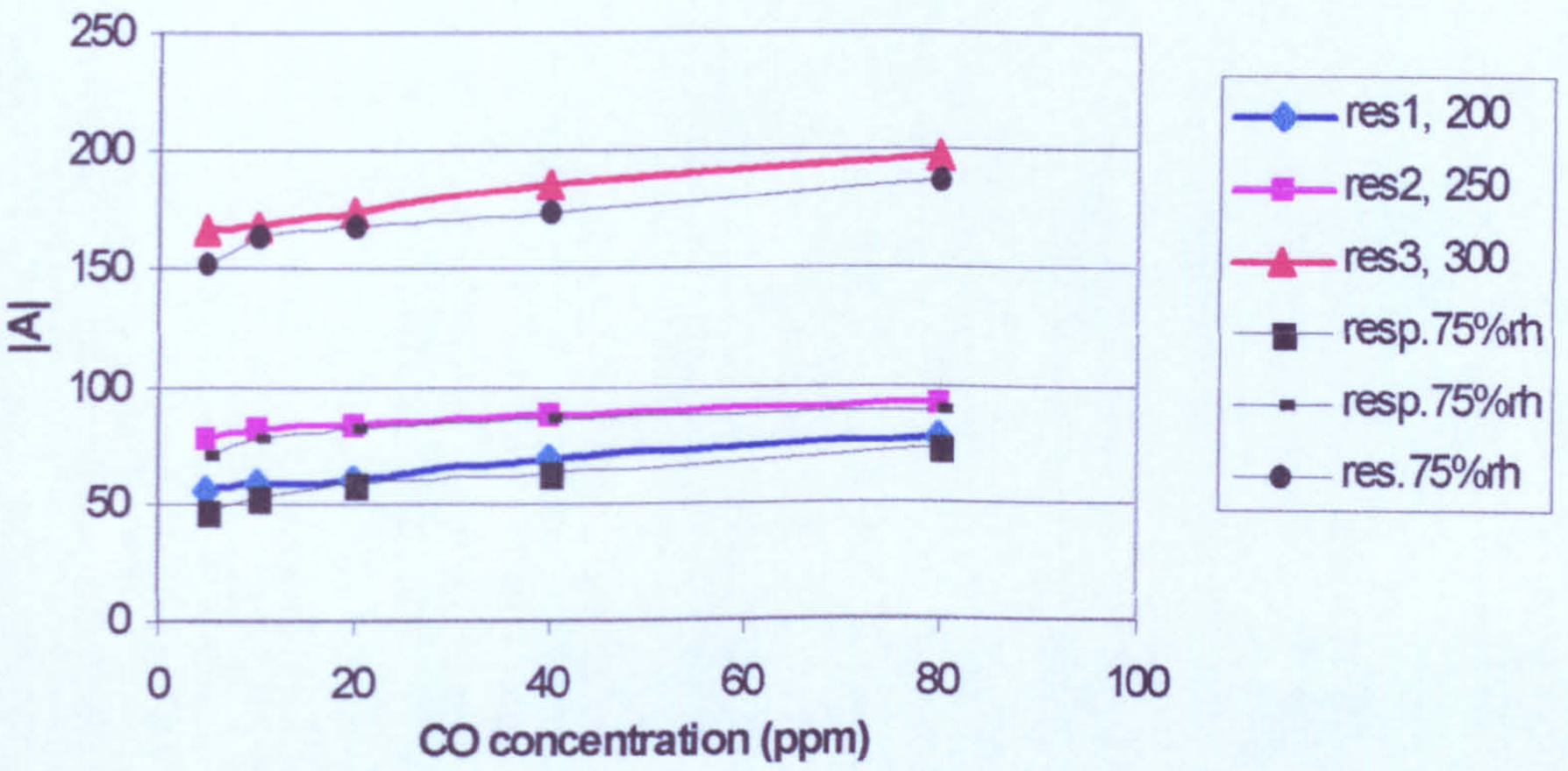


Figure 6.3 Plot of amplitude of fundamental frequency ($a_1$) vs CO concentration (ppm) at three different temperatures and two relative humidity, blue (200°C, 25% rh) and black square (200°C, 75% rh), magenta (250°C, 25% rh) and black rectangle (250°C, 75% rh) red (300°C, 25% rh) and black circle (300°C , 75% rh) and all at 1 Hz modulation.

The effect of an increase in humidity is shown to decrease the amplitude of the fundamental frequency as shown in Figure 6.3.

The relationship between the first ($a_0$), second ($a_1$), and the third ($a_2$) Fourier coefficients for a test with parameters shown in Table 6.3 is shown in Figure 6.4.

The testing process was started by collecting data from 10 identical tests of CO concentration at 20 ppm; this was repeated for CO concentration of 40, 80, 130 ppm.

The first three Fourier coefficients were extracted for each test (i.e. 10 coefficients for each of the four CO concentrations).

Table 6.3 an example of test parameters for extracting Fourier coefficients

| | |
|---|---|
| Test file names | Cosin1a.txt, CO 20 ppm (10 off)<br>Cosin2a.txt, CO 40 ppm (10 off)<br>Cosin3a.txt, CO 80 ppm (10 off)<br>Cosin4a.txt, CO 130 ppm (10 off) |
| VI used | Flow2.exe |
| Sensor | Au doped $SnO_2$ |
| Heat wave modulation frequency | 50 mHz |
| Heater room temperature resistance value to be entered in vi' formula node | 192Ω |
| Heater sine wave modulation | 1.45 this will give a temperature swing from 405°C to 243°C, ± 80 °C |
| Total number of samples | 9000 |

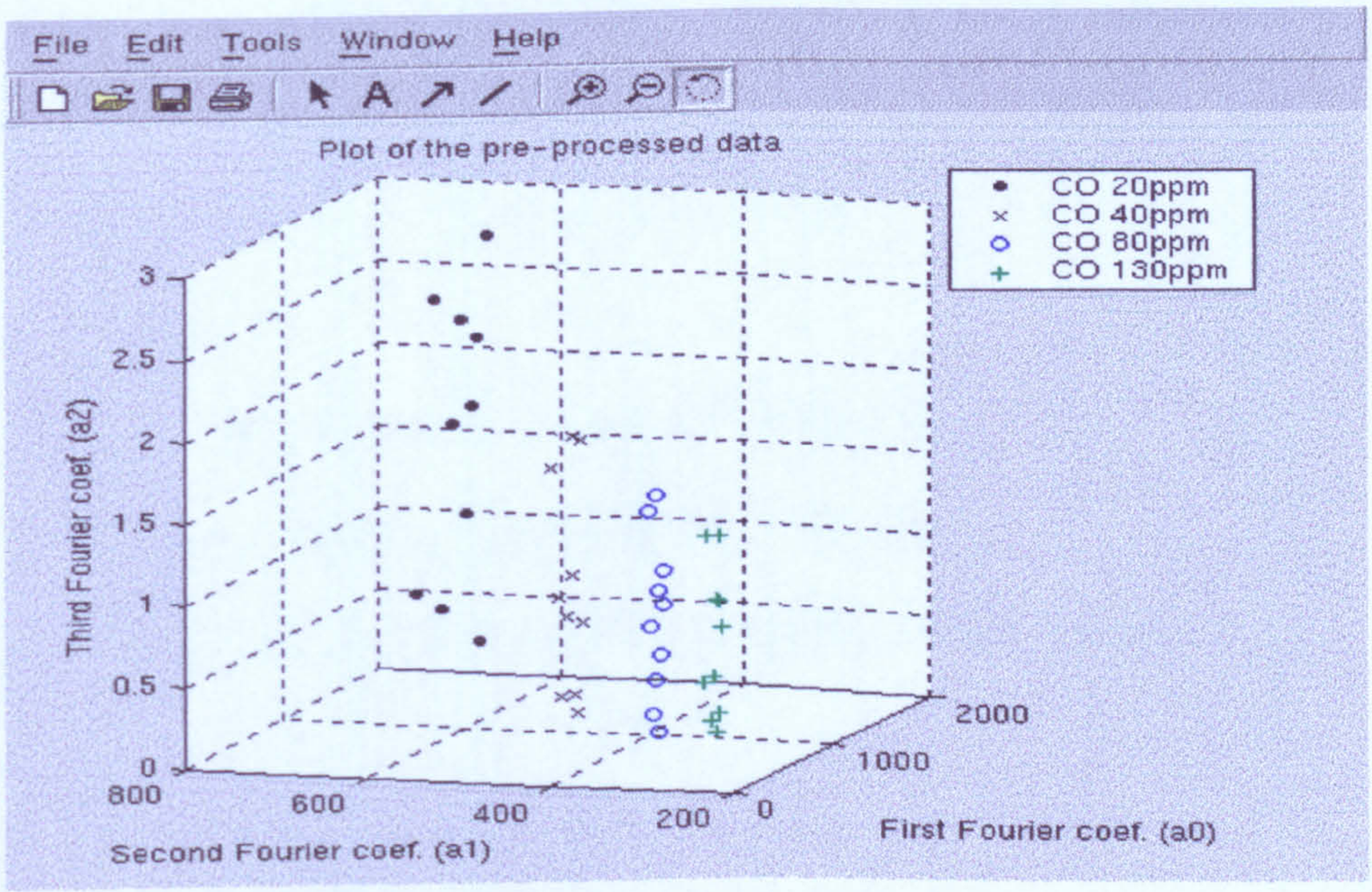


Figure 6.4 Plot of Fourier coefficients $a_0$, $a_1$ and $a_3$ extracted from these sets of 10 tests at 20, 40,80, 130 ppm of CO with 25% rh.

### 6.2.3 Normalisation

Normalisation of the data sets has been used to improve the classification performance.

The pre-processing normalisation algorithm used for each data *i* is,

$$x_i^{\text{normalised}} = 2 * \frac{x_i - x_{\min}}{x_{\max} - x_{\min}} - 1 \qquad (6.6)$$

where the normalised array parameter $x_i^{\text{normalised}}$ lies in the range of $\pm 1$ although $\pm 1$ normalisation was used on the data set other types of normalisation are also available for application on my MATLAB program such as

- Autoscaling $$x^{\text{normalised}} = \frac{x - mean}{stddevia\theta} \qquad (6.7)$$
- Autoranging $$x^{\text{normalised}} = \frac{x - \min}{\max - \min} \qquad (6.8)$$

However, setting the range to $\pm 1$ maps well onto the back-propagation network used later on.

### 6.2.4 Target allocation for gas concentration

**A. CO gas**

CO concentrations of interest are the following:

0 (no gas), 20 ppm, 40 ppm, 80 ppm, 130 ppm.

The target value was assigned by using the following equation

$$\text{Target} = \left[\frac{2c}{C_{\max}} - 1\right] \qquad (6.9)$$

Where $C$ is concentration of interest, $C_{max}$ is the maximum CO concentration in ppm e.g. 130 ppm. From this equation the target gas concentrations are computed as shown in Table 6.4.

Table 6.4 Target Gas concentrations of CO and target output values.

| CO concentration (ppm) | Target value |
|---|---|
| 0 (no gas) | -1 |
| 20 | -0.69 |
| 40 | -0.38 |
| 80 | 0.23 |
| 130 | +1 |

The plot of the ± 1 normalisation of the CO target concentration is shown in Figure 6.5.

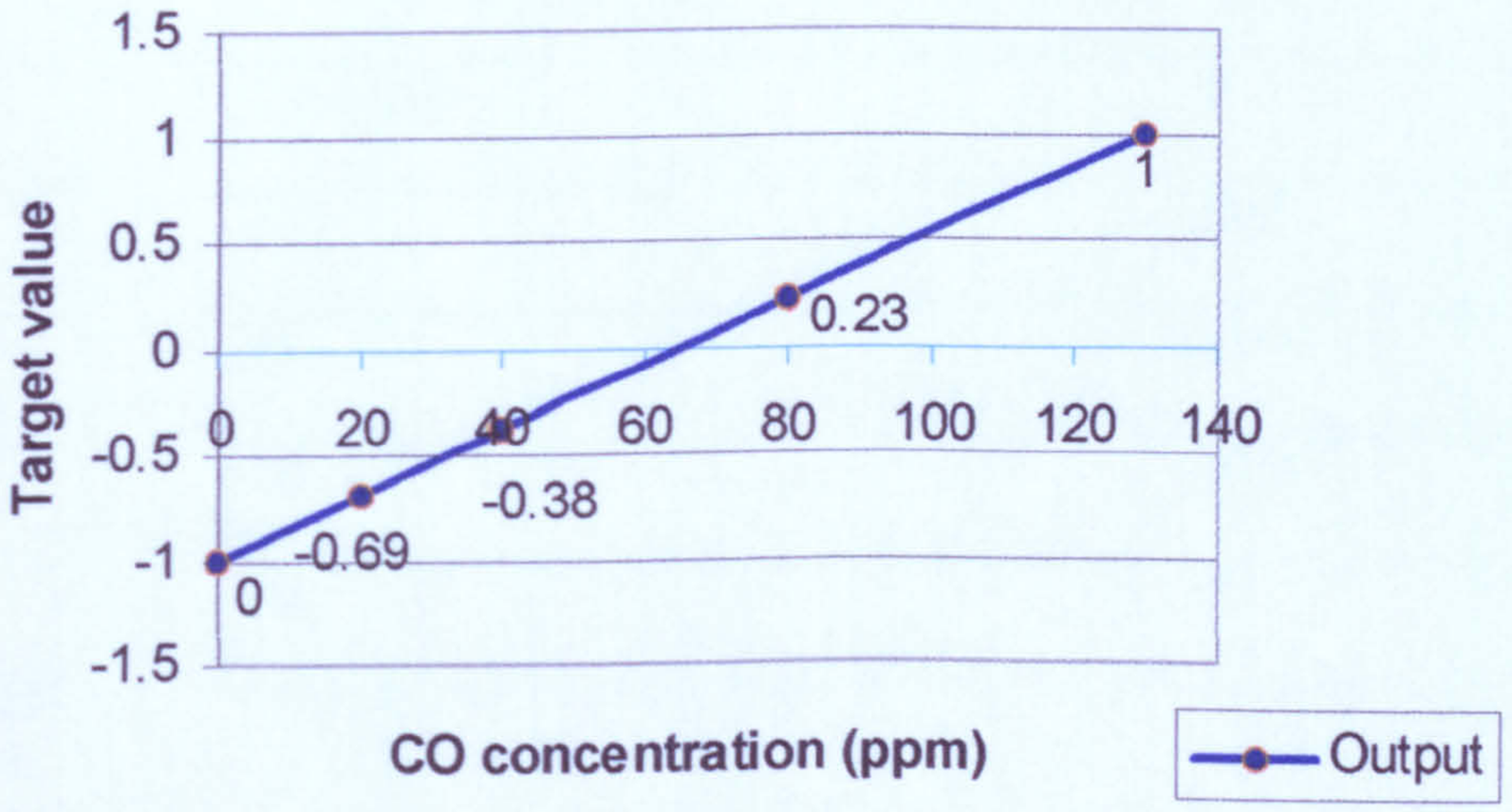


Figure 6.5 Plot of target values vs CO concentration in ppm

Figure 6.5 shows the target allocation for each of CO concentration of interest (e.g. 130 ppm of CO is set to (+1); no CO present setto (0) and so on as shown).

**B. $NO_2$ gas**

$NO_2$ concentrations of interest are the followings:

0 ( no $NO_2$ present), 10 ppm, 20 ppm, 40 ppm, 60 ppm. Target values was allocated by using the following equation

$$\text{Target value} = \left[\frac{2C}{C_{\max}} - 1\right] \tag{6.10}$$

where $C$ is $NO_2$ gas concentration , $C_{max}$ represents the maximum $NO_2$ concentration, i.e. 60 ppm. From this equation the target gas concentrations are calculated from equation 6.10 and the results are shown in Table 6.5.

Table 6.5 Target gas concentration for $NO_2$.

| $NO_2$ concentration (ppm) | Target value |
|---|---|
| 0 (no gas) | -1 |
| 10 | -0.67 |
| 20 | -0.33 |
| 40 | +0.33 |
| 60 | +1 |

The plot of the ± 1 normalisation of $NO_2$ target concentration is shown in Figure 6.6.

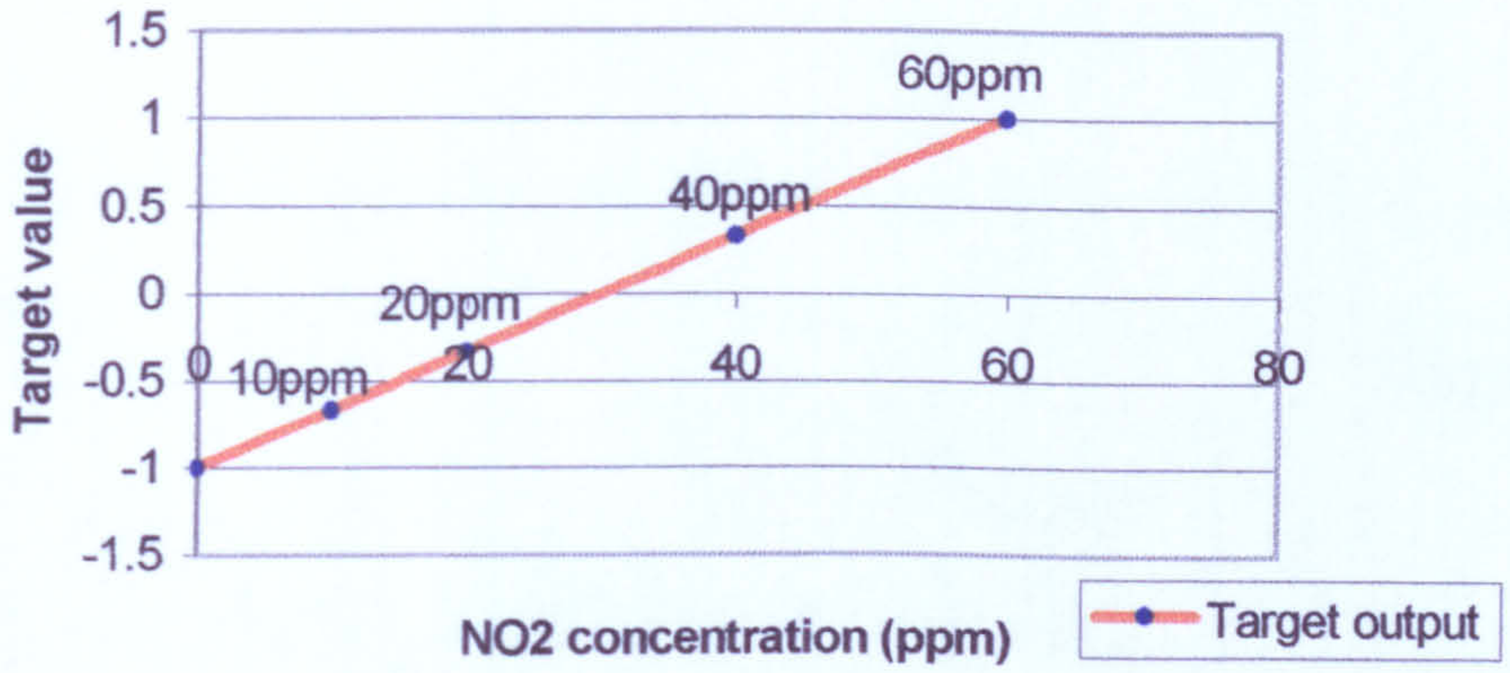


Figure 6.6 Plot of target values vs $NO_2$ concentration in ppm

**C. Binary gas target allocation**

The concentrations of the binary mixture (CO and $NO_2$) are the following:

20 (CO) and 10 ($NO_2$), 40 (CO) and 20 ($NO_2$), 80 (CO), 40($NO_2$) , 130 (CO) and 60 ($NO_2$). These are arranged together with the target value as shown in Table 6.6.

Table 6.6 Binary gas mixture and the corresponding target values.

| Binary gas mixture (CO and $NO_2$) | Target values x and y |
|---|---|
| 0 (no gas) | - 1 , - 1 |
| 20 ppm (CO) 10 ($NO_2$ ) | - 0.69, - 0.67 |
| 40 ppm (CO) 20 ($NO_2$ ) | -0.38 , - 0.33 |
| 80 ppm (CO) 40($NO_2$) | 0.23, 0.33 |
| 130 ppm (CO) 60 ($NO_2$) | 1, 1 |

The normalised binary data and target values are shown in Figure 6.7

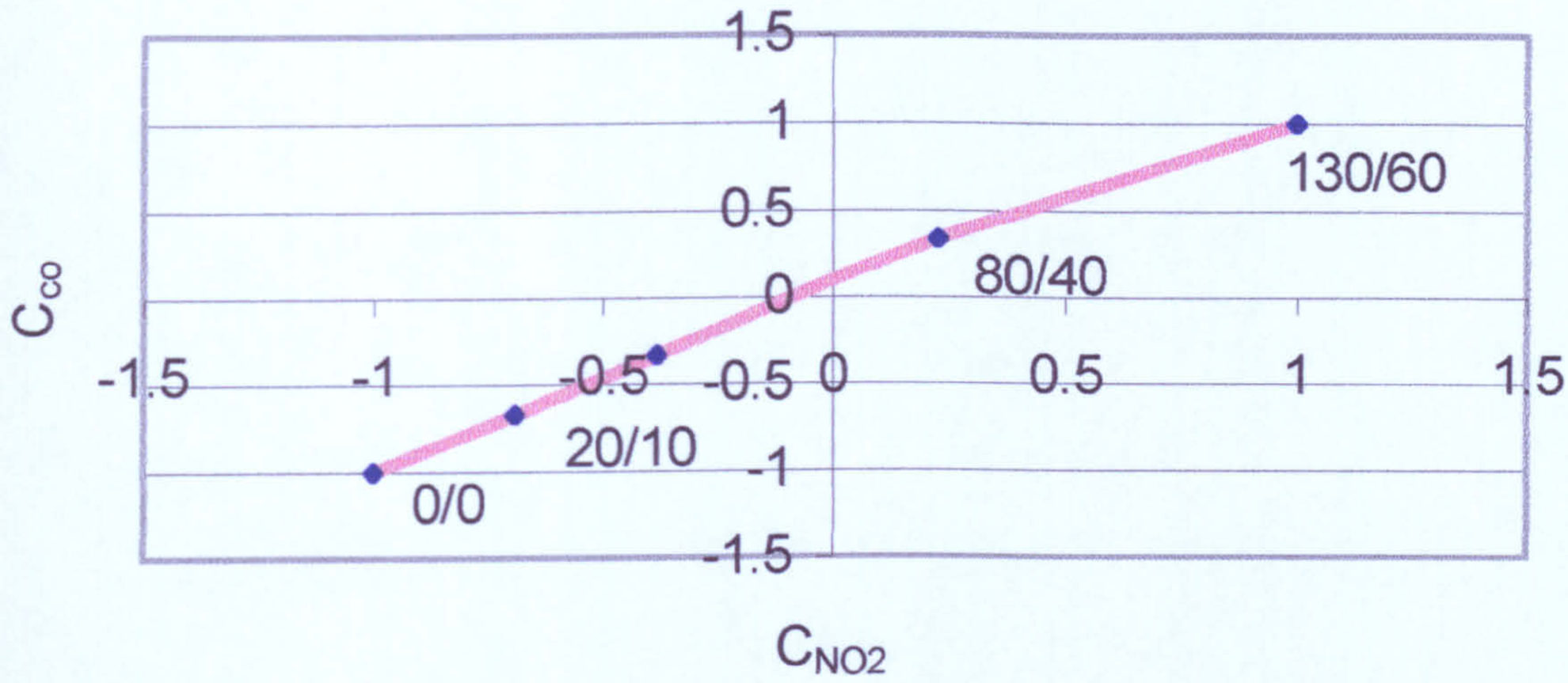


Figure 6.7 Plot of binary gas concentrations vs target values.

The ±1 normalised data for both CO and $NO_2$ are allocated target values as shown in the previous sections and summarised in Table 6.6 is then used in further analysis using Neural Networks.

Table 6.7 Summary of CO, $NO_2$ and binary gas mixture and its target values

| Gas concentration (ppm) | Target X | Target Y |
|---|---|---|
| CO @ 20 ppm | -0.69 | -1 |
| CO @ 40 ppm | -0.38 | -1 |
| CO @ 80 ppm | 0.23 | -1 |
| CO @ 130 ppm | 1 | -1 |
| $NO_2$ @ 10 ppm | -1 | -0.67 |
| $NO_2$ @ 20 ppm | -1 | -0.33 |
| $NO_2$ @ 40 ppm | -1 | 0.33 |
| $NO_2$ @ 60 ppm | -1 | 1 |
| CO/ $NO_2$ 20/10 | -0.69 | -0.67 |
| CO/ $NO_2$ 40/20 | -0.38 | -0.33 |
| CO/ $NO_2$ 80/40 | 0.23 | 0.33 |
| CO/ $NO_2$ 130/60 | 1 | 1 |
| No gas | 1- | -1 |

For each gas concentration (i.e. CO at 20, 40, 80, 130 ppm, $NO_2$ at 10, 20, 40, 60, and CO/ $NO_2$ 20/10, CO/ $NO_2$ 40/20, CO/ $NO_2$ 80/40, CO/ $NO_2$ 130/60) there are ten data sets, which are conducted under the same test conditions. These data points are then used as input to the Neural Networks as described next.

## 6.3 Artificial Neural Network

Artificial Neural Networks (ANNs) have been widely used in engineering applications where the problem is not linear [6.2]. ANNs have been widely used in the application of electronic nose systems. The technique usually used here (electronic

nose) is Multilayer Perceptrons (MLP) ANNs trained using the back-propagation (BP) technique. ANNs which mimic the architecture of the biological olfactory system do not require an explicit description of how the problem is to be solved [6.3]. This type of ANN learns from the data and usually configures itself during a training period. One of the main advantages of using this technique is coping with highly non-linear data and therefore can be used with noisy or drifting sensor data [6.4].

### 6.3.1 Neurone as Model

A typical artificial neurone with $R$ inputs schematic is shown in Figure 6.8. This figure describes the various elements that constitute the model of an artificial neurone.

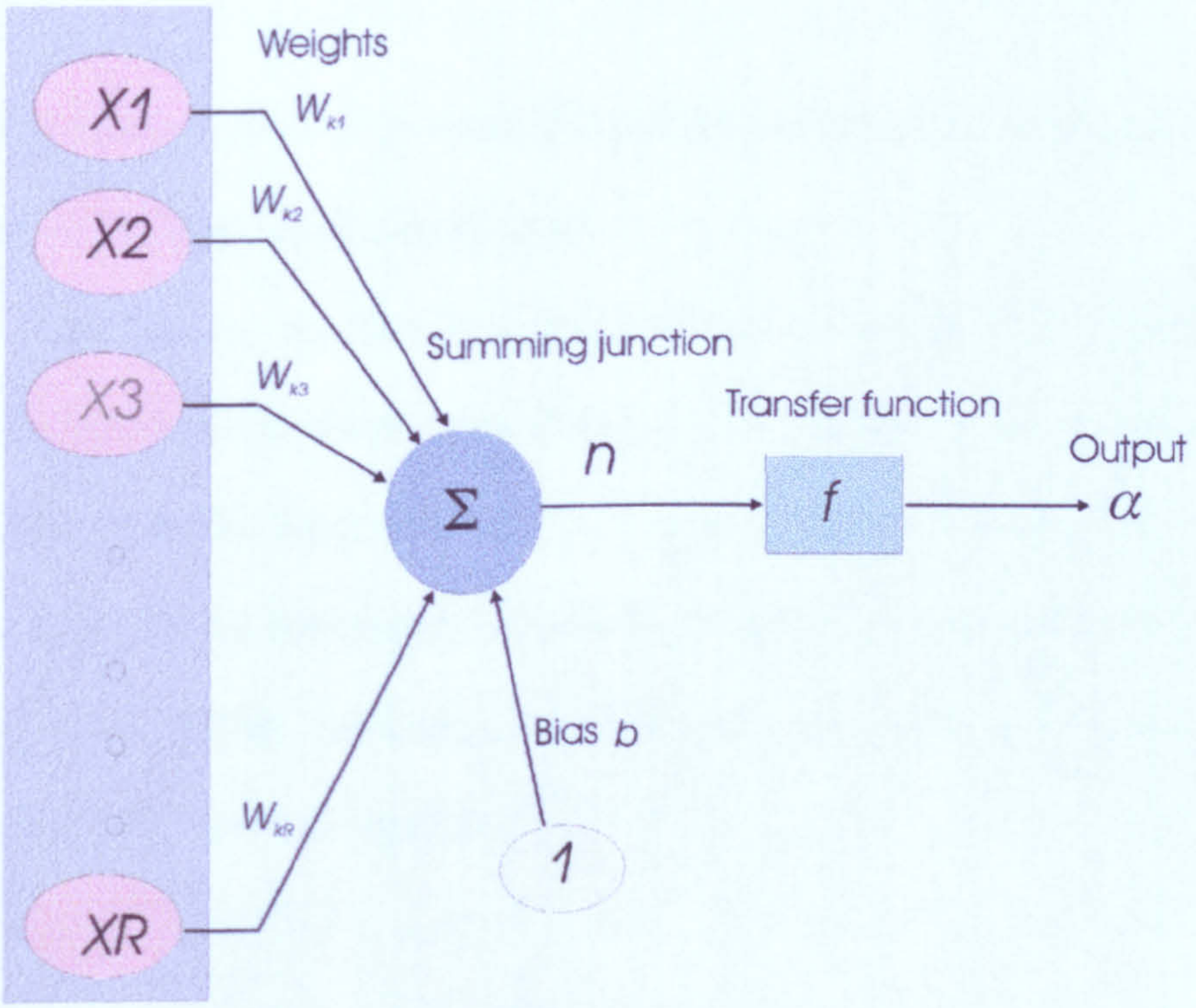


Figure 6.8 Schematic diagram of an artificial neurone

The neurone has a bias $b$, which is summed with the weighted inputs to form the net input $n$.

$$n = \sum_{i=1}^{R} w_{ki} x_i + b \tag{6.11}$$

The neurone output can be written with respect to $n$ as

$$\alpha = f(n) \tag{6.12}$$

The output depends on the particular transfer function that is chosen e.g. sigmoidal function. Each inputs has an associated adjustable coefficient called the weight $w$, which represents the strength of each input connected to the neurone. Bias $b$ is similar to a weight except that it has a fixed input (e.g. 1). The bias gives the network an extra variable and so the network with biases is more powerful than those networks without bias [6.6].

The bias has the effect of lowering the net input of the transfer function although, the bias can be omitted in a certain neurone.

The transfer function is usually chosen to satisfy some specification of a particular problem that the neurone attempting to solve [6.7]. An example of this is the log-sigmoid transfer function which is commonly used in multilayer networks, when trained using the backpropagation algorithm. It sets the output into a 0 to 1 range and defined as a strictly increasing function that shows smoothness and asymptotic properties. This can be defined by

$$\alpha = \frac{1}{1 + e^{-n}} \tag{6.13}$$

where n is the net input of the neurone. Several other functions are used such as linear, hyperbolic tangent sigmoid (used later in neural network calculation) and competitive transfer functions. Hyperbolic tangent sigmoid function, which is similar to the log-sigmoid function, changes the outputs into a range of $\pm 1$. The range of output is important as it improves the training qualities of the neural network. The expression of hyperbolic tangent sigmoid can be shown as

$$\alpha = \frac{e^{n} - e^{-n}}{e^{n} + e^{-n}} \tag{6.14}$$

A single neurone has very limited capability as a device for solving problems. Processing elements can be combined to make a layer of nodes and be interconnected. Therefore, an artificial neural networks is able to solve complicated problems, which require more intricate decision areas to a group of data. A single layer of neurones can be set to a different transfer function by combining neural networks in parallel.

### 6.3.2 Multi layer perceptron (MLP)

The multi-layer perceptron (MLP) is one of the most commonly used neural network architecture and is suited to a wide range of applications [6.2]. It consists of a set of sensory units that constitute the input layer, one or two hidden layers, and an output layer. Figure 6.9 shows how a fully connected three-layer MLP network, with 14 weights to train. This type of network may be referred to as a 3-2-2 network. Input and output were considered as layers, which constitute the network architecture. All outputs from a previous layer are inputs to the next layer, each layer has its own weight, and bias as well as a net input and an output. Adding one or more hidden layers to the network will be able to extract higher-order statistics.

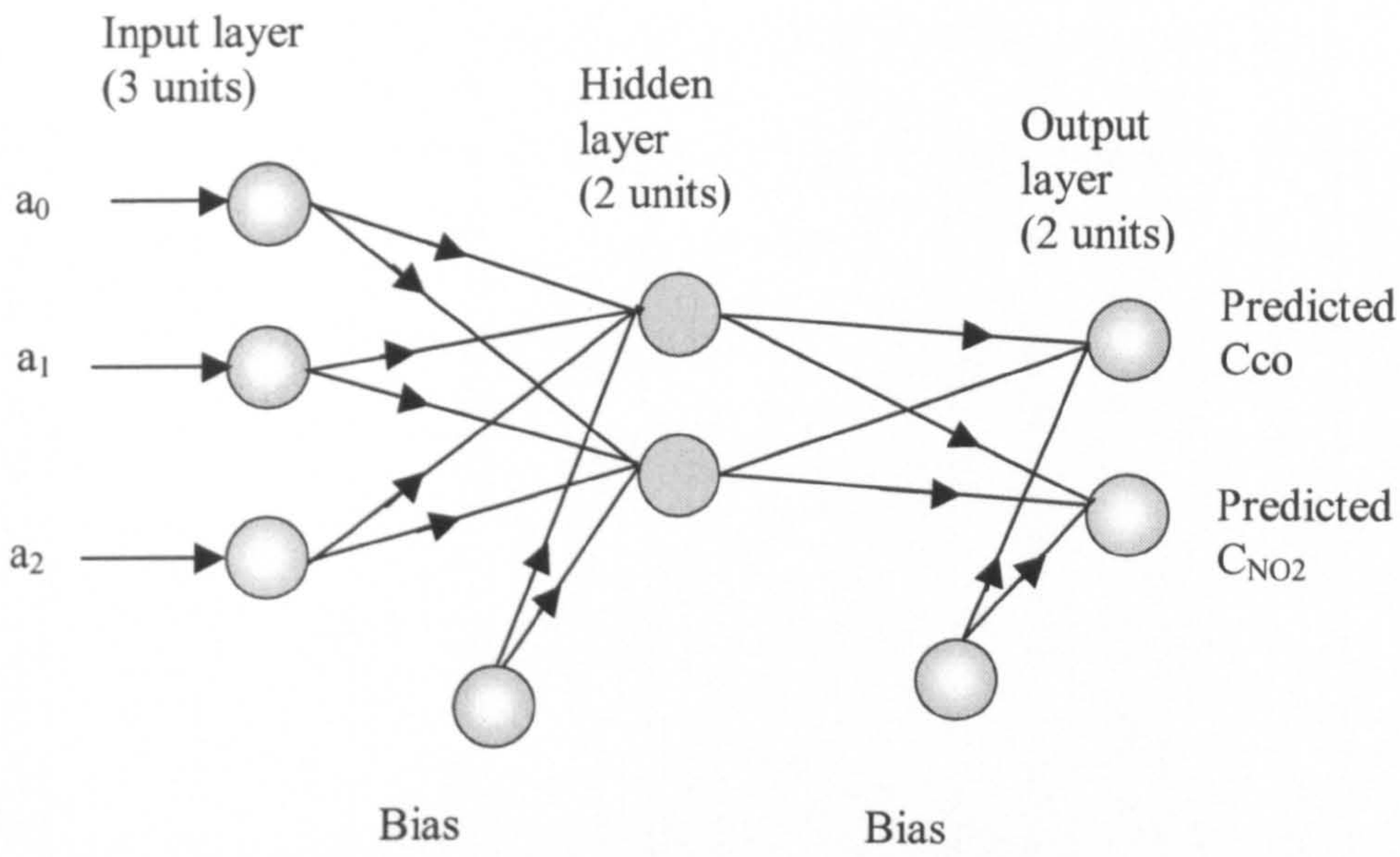


Figure 6.9 Schematic diagram of a fully connected three layers MLP with 3 inputs, 2 hidden neurones, and 2 outputs.

There are a number of training algorithms for training a neural network. One of the most powerful techniques is supervised training, where for each input vector, the target output vector is known [6.8]. In this technique, changes in weights and biases are due to the intervention of any external assignment, which provide output target. Back propagation (BP) is commonly used supervised training algorithm and MLP are usually trained using BP. The BP technique performs a gradient descent within the solution's vector space toward a global minimum along the steepest vector of the error space. The global minimum is a theoretical solution with the lowest possible error [6.8]. In most problems, the solution space is very irregular that may cause the network to settle down in local minima and not the best global solution. Figure 6.10, illustrates the possibility of converging to a local minimum in weight space [6.8]. If a local minimum *Z1* is reached, the error at the network outputs may still be unacceptably high. Various

technique exist to find global rather than local minima but that is behind the scope of this thesis. The BP algorithm employs a method of gradient descent, where the neural network in initialised and its error can be visualised at random co-ordinates on the error surface as in Figure 6.10. The error signal ($\delta_{pk}$) at the output of kth at the nth training vector is defined by

$$\delta_{pk} = y_{pk} - o_{pk} \qquad (6.15)$$

where $y_{pk}$ is the target value and $o_{pk}$ is the actual output from the kth output unit.

The sum of the squared errors for all output units can be written as:

$$E_p = \Sigma(y_{pk} - o_{pk})^2 = \Sigma\, \delta^2_{pk} \qquad (6.16)$$

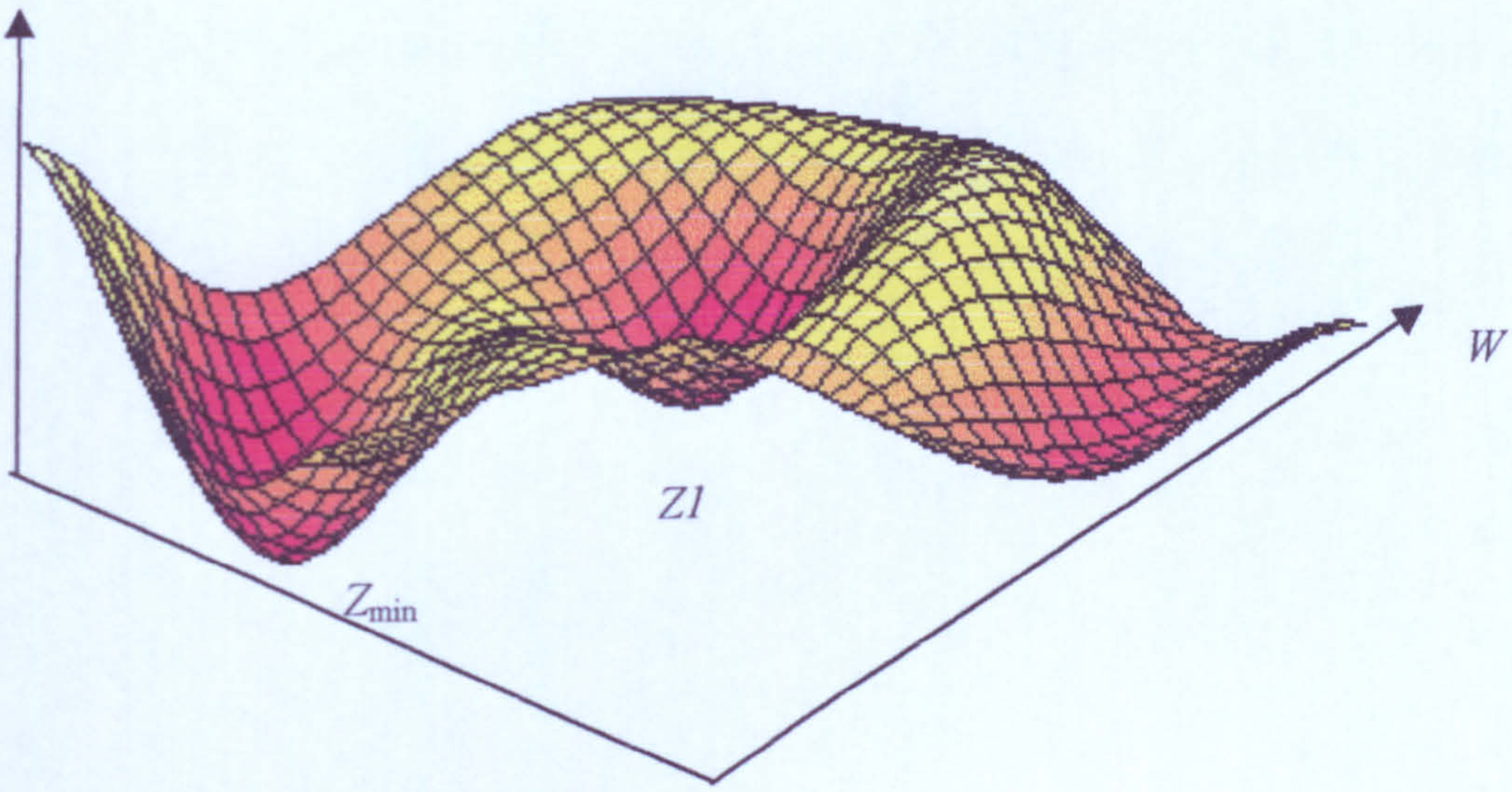


Figure 6.10 Hypothetical surface in weight space, point $Z_{min}$ is called the global minimum and the second minimum point, *Z1*, is called a local minimum.

The main objective of the BP training is to minimise the difference between the actual network output and the target output (i.e. the error space) and to find an appropriate set of weights. Weights should be initialised to small, random values, often in the range of ±0.5. The gradient descent vector is calculated such that the steepest negative gradient of $E_p$ is the path followed by the network error. The values of the weights are then adjusted in order to reduce the total error. From the derivative of Equation (6.16) with respect to the weights, $w_{kj}$, the weights on the output layer are updated according to a simple learning rule, e.g.

$$w_{kj}(t+1) = w_{kj}(t) - \eta\Delta_p \qquad (6.17)$$

where $\Delta_p$ is the gradient descent vector component for weight $w_{kj}$ and the factor $\eta$ is called the learning-rate parameter that determines the magnitude of the change in the weightings [6.8]. Also $w_{kj}(t)$ is the weight value between hidden perceptron $k$ and output perceptron $j$ at time $t$. The process is continually repeated for the number of iterations until the final error between the target values and the actual output values is acceptably low. Many other learning rules exist but the simplest has been used in these expriments. The error that this process minimises is the total squared sum

$$E=\sum_{p=1}^{P} E^2{}_P \qquad (6.18)$$

where $p$ is the number of patterns in the training set.

## 6.4 Data analysis and results

A MATLAB program was designed in order to facilitate data processing, plotting and applying Artificial Neural Networks. The user interface of this program is shown in Figure 6.11. The general description of the program is as follows:

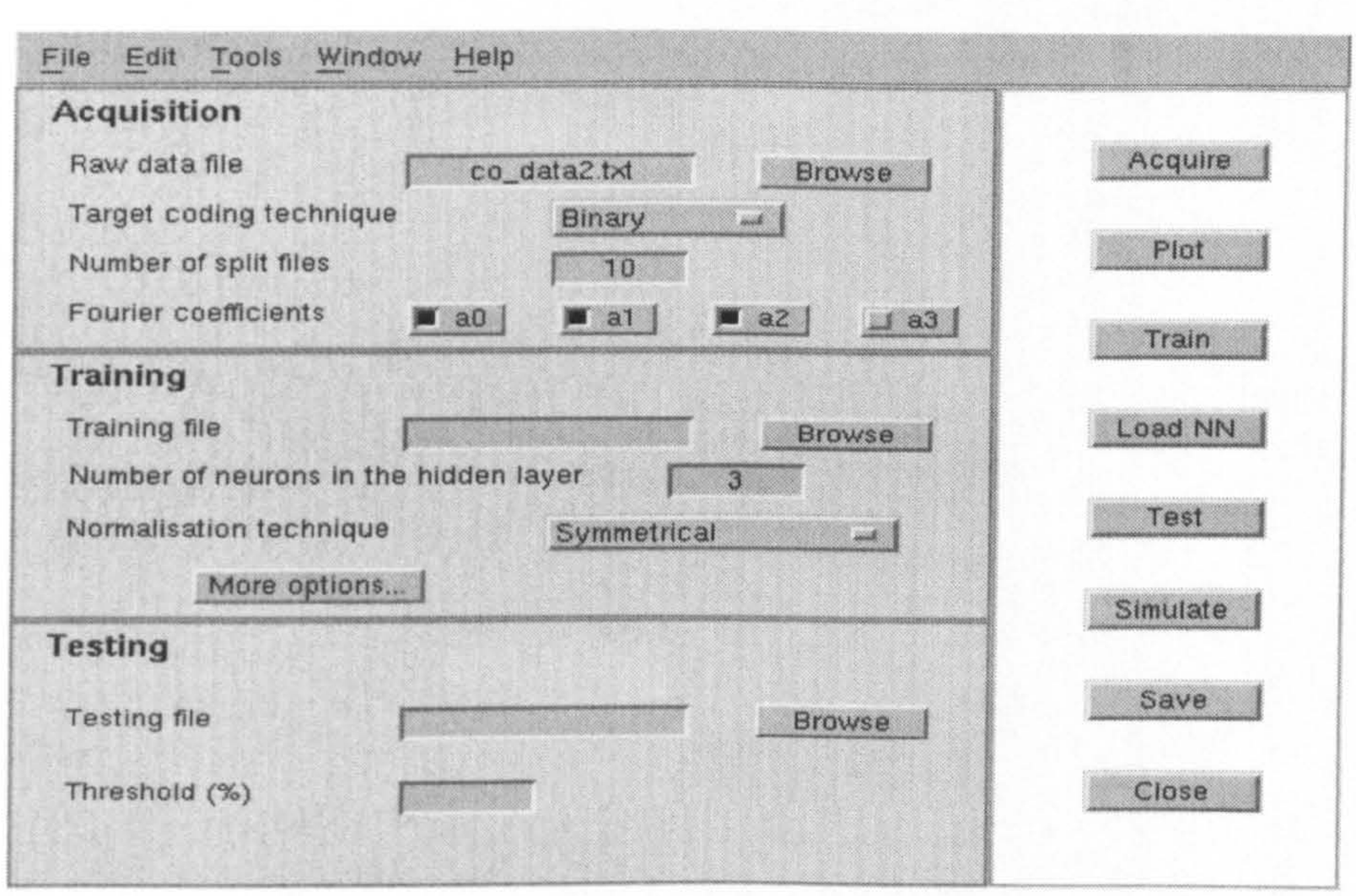


Figure 6.11 User interface. For data analysis using MATLAB.

The user interface is divided into three sections. The first section is the data acquisition area. In this part the raw data is entered this consists of 4 large files each e.g with 4 different gas concentrations. The target coding technique allocation is set (e.g. binary) and also the required Fourier coefficient is set (up to 4 Fourier coefficients). Once this section is filled then the Acquire button is pressed, which will produce the values of the required number of Fourier coefficients. At this stage a plot of the coefficients can be produced. In the Training section the output file from the first section is entered and the number of the neurones in the hidden layer is chosen. The normalisation technique is also entered in this section ( e.g. No normalisation, or Symmetrical [-1, +1] or sensor normalisation [0, 1] or Autoscaling ). The output of this section is the training classifications (i.e. how well the data was trained). In the More option, the transfer

function is chosen (e.g. Tansig, logsig). In the testing section the program will test a data set and produces the predicted results.

### 6.4.1 Neural networks algorithm used

The method used to train and test the data sets is as follows (10-fold validation):

1. Remove 10% of the data set at random for later testing.
2. Train on the remaining 90%
3. Test on the previously removed 10% of the data.
4. Output classification results

The following example describes a simplified version of testing the data .The neural network uses the Leave one out algorithm and tansig for transfer function. The data set in this case consists of 25 data points for each CO gas concentration (i.e. 25 data points for 20 ppm, 25 for 40 ppm, 25 for 80 ppm and 25 for 130 ppm) as shown in Table 6.8.

Table 6.8 number of data for each gas concentration

| Gas concentration 20 ppm | Gas concentration 40 ppm | Gas concentration 80 ppm | Gas concentration 130 ppm |
|---|---|---|---|
| Number of data points in this class 25 | Number of data points in this class 25 | Number of data points in this class 25 | Number of data points in this class 25 |

The neural networks will remove 10% of the data and train with the remaining 90%. When the training process finishes the neural networks will test the 10%. At the end of this process the network will produce a vector of 10 outputs (an example of one of the actual outputs is (0.9, -0.8). This will be compared with target values as shown in Table 6.9.

Table 6.9 an example of one (out of 10 in this case) of the test result and the target values for CO.

| Vector from test result | Targets |
|---|---|
| (0.9, -0.8) | (1, -1) |
| | (0.23, -1) |
| | (-0.38, -1) |
| | (-0.69, -1) |

The next step is to process these vectors (10 off in this example) as shown below to produce the right classification.

$$\sqrt{(0.9-1)^2+(-0.8-(-1))^2}=0.22$$

$$\sqrt{(0.9-(0.23))^2+(-0.8-(-1))^2}=0.69$$

$$\sqrt{(0.9-(-0.38))^2+(-0.8-(-1))^2}=1.29$$

$$\sqrt{(0.9-(-0.69))^2+(-0.8-(-1))^2}=1.6$$

The process will find the shortest distance between these vectors and the targets. Since 0.22 is the smallest value therefore this data belongs to the class of 130 ppm CO and so on. However, if 9 out of 10 of this data falls in this category then the data is 90% from a 130 ppm CO class.

### 6.4.2 Single gas identifications

By using the above program the plot of trained and predicted CO gas concentrations versus the actual CO gas concentration was produced as shown in Figure 6.12.

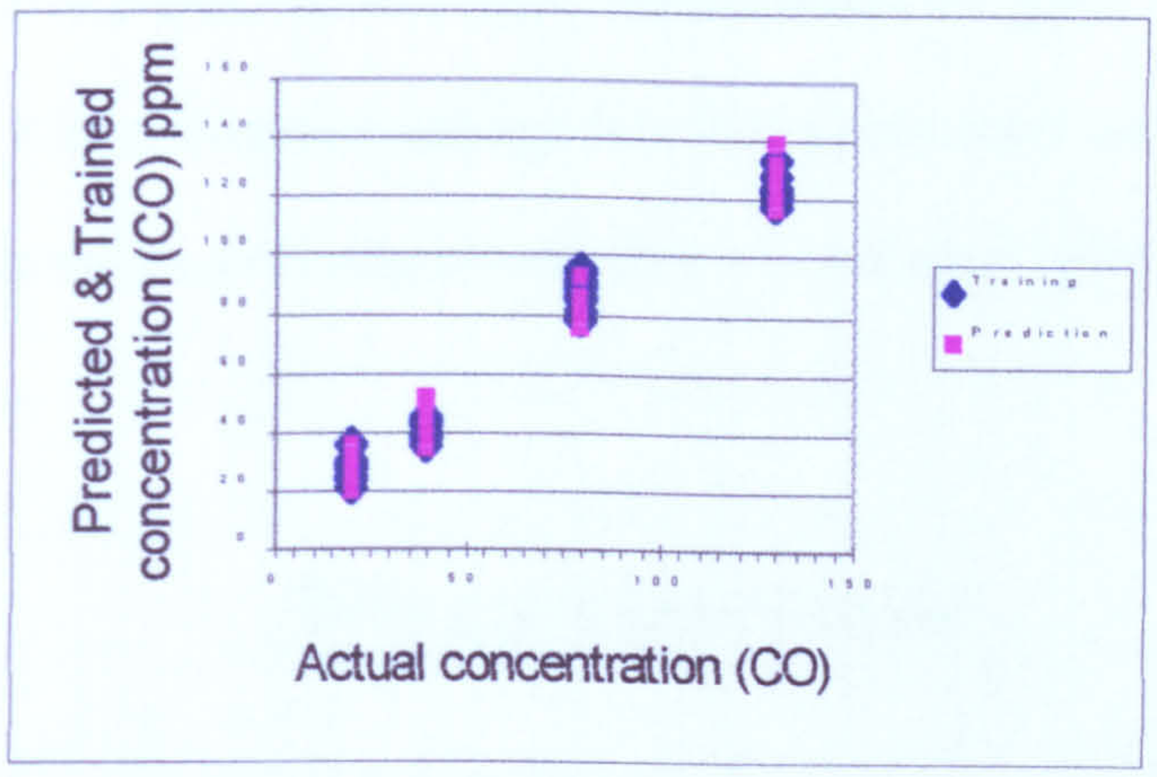


Figure 6.12 Plot of trained and predicted (tested) data vs actual CO concentrations

The same plot was produced for $NO_2$ as shown in Figure 6.13.

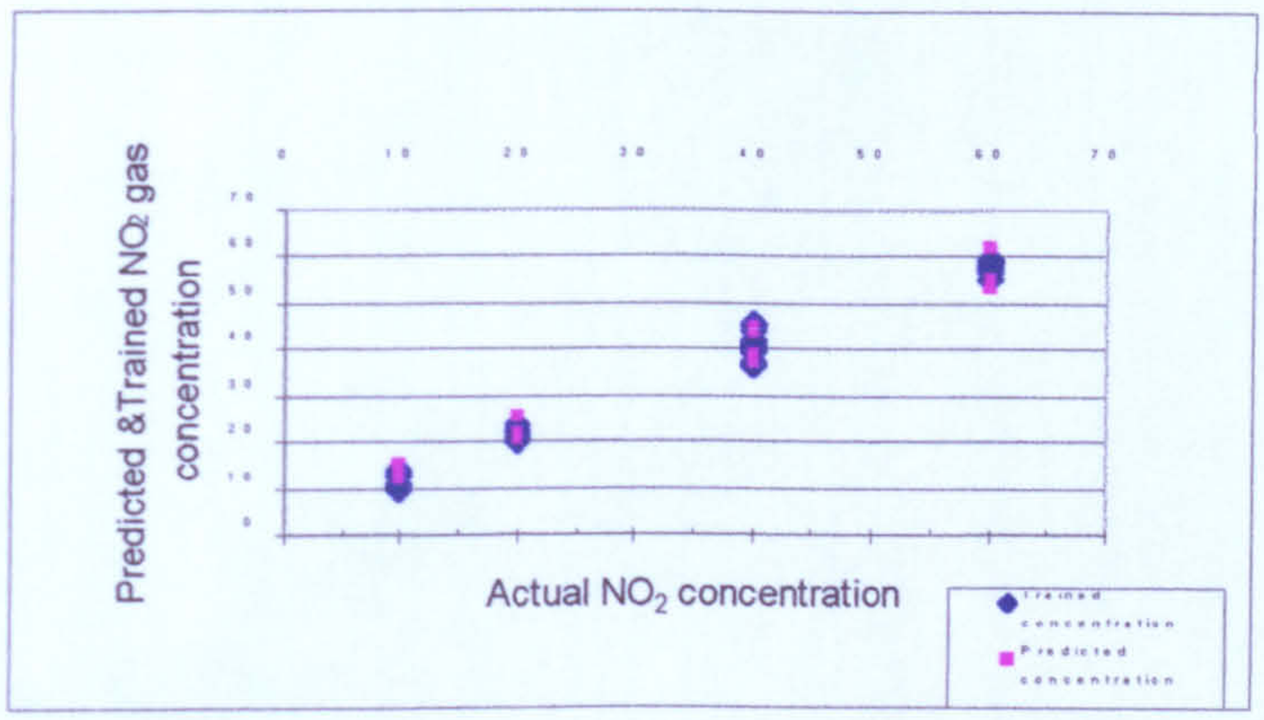


Figure 6.13 Plot of predicted (tested) and trained data vs actual $NO_2$ gas concentration (ppm), the trained data is well behaved and very close to the predicted data, this prove that the system is capable in classifying the untrained data.

### 6.4.3 Binary gas identifications

A binary gas data is produced by a test mixing controlled amounts of CO and $NO_2$ concentrations. This binary gas data is then fed into neural networks to be trained and tested as described in the previous sections.

Figure 6.14 shows plot of $NO_2$ gas concentration in ppm versus CO gas concentration in ppm. The calibrated (training) data looks reasonable and is close to the target points. The predicted (tested) values were also well behaved. This result

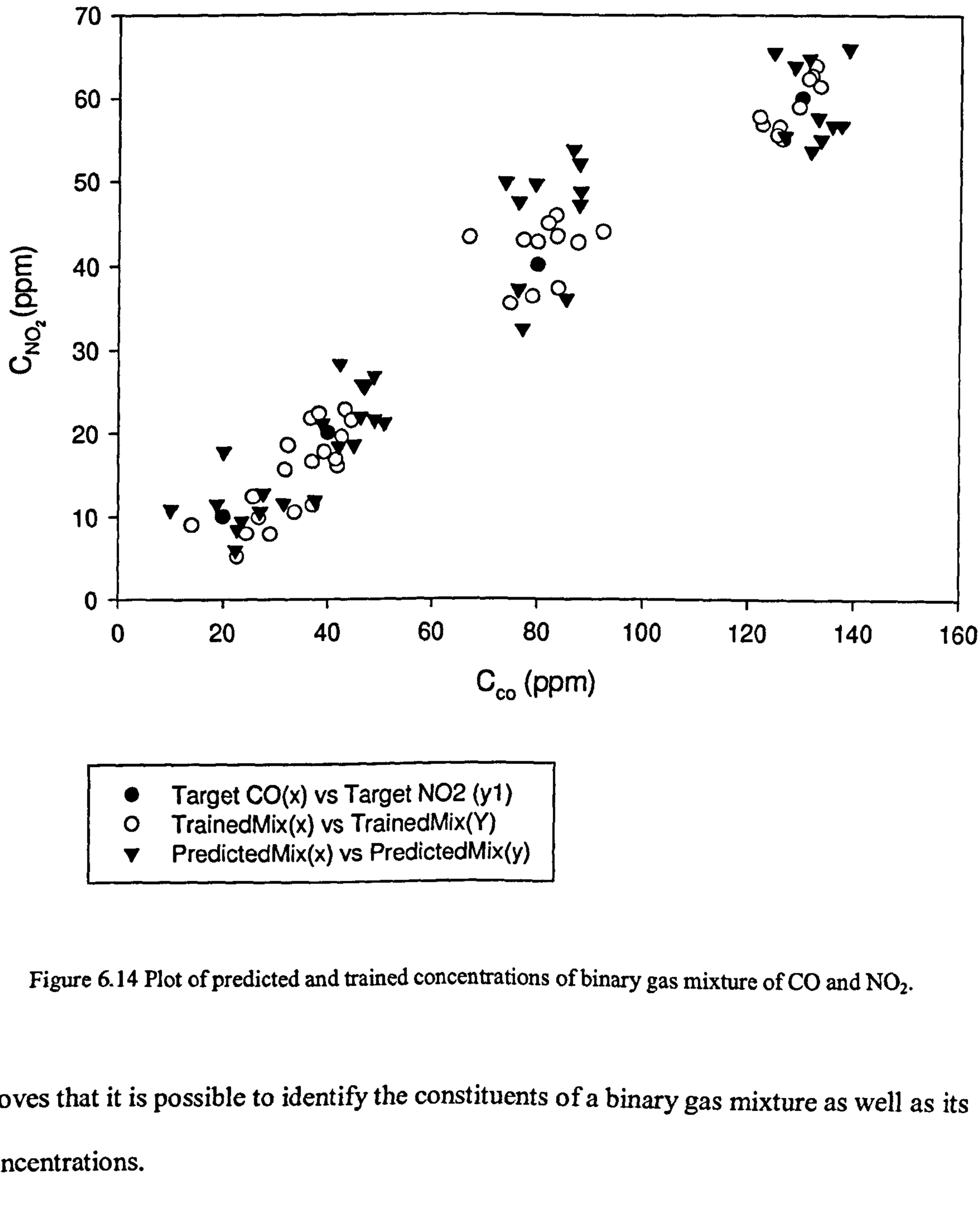


Figure 6.14 Plot of predicted and trained concentrations of binary gas mixture of CO and $NO_2$.

proves that it is possible to identify the constituents of a binary gas mixture as well as its concentrations.

## 6.5 Summary

In this chapter, signal and data processing techniques have been discussed. The extraction of Fourier coefficients is described in detail then the initial Fourier coefficients were identified for several experimental runs. The amplitude of fundamental frequency was shown to increase with operating temperature because of the reactions of the $SnO_2$ coating with the atmospheric gases. The same amplitude was shown to decrease slightly with higher humidity as shown in Figure 6.3. Target neural values were allocated to CO and $NO_2$ gas concentrations. Data analysis (MLP) and results were then discussed next. By using neural networks in MATLAB environment, concentrations were predicted accurately in both single component gas detection as well as gas identifications in a binary gas mixture. Thus, it has been shown that a single doped $SnO_2$ resistive sensor can be used to classify binary gas mixtures in air.

## 6.6 References


6.1 Fitzgerald, Grabel, Higginbotham, *Basic Electrical Engineering*, McGraw-Hill Kogakusha, 1967.

6.2 M. T. Hagan, H. B. Demuth, M. Beale, *Neural network Design*, PWS publishing company, 1996.

6.3 A Carling, *Introducing Neural Networks*, SIGMA PRESS, Wilmslow, UK, 1992.

6.4 R Hecht-Nielson, *Neurocomputing*, Addison Wesley, 1990.

6.5 R Beale, T Jackson, *Neural computing an introduction*, IOP publishing Ltd 1990.

6.6 S Haykin, Neural Networks: A comprehensive foundation, Macmillan Publishing company, 1994.

6.7 H. W Shin, *A Hybrid Electronic Nose system for Monitoring the quality of Potable Water,* PhD thesis, University of Warwick, 1999.

6.8 J. A. Freeman, and D. M. Skapura, *Neural Networks: Algorithm, Applications, and Programming Techniques*, Addison-Wesley Publishing Company, 1992.

# Chapter 7 Design of hand-held gas monitor

## 7.1 Introduction

This chapter describes in detail the design of a novel type of hand-held microcontroller based instrument for use as a $CO/NO_2$ gas monitor. The instrument utilises the Philips XA micro-controller [1]. The design uses low power electronic components with power saving facilities in order, to maximise battery life. The microcontroller controls a number of input output devices such as DAC, ADC, non-volatile memory as well as controlling the sensor heating element and supplying a constant current to the resistive sensor, see Figure 7.1. The instrument is divided into a number of sub-systems and each sub-system uses 5 V low power CMOS components, many of which have either hardware or software shutdown facilities that are described in detail later.

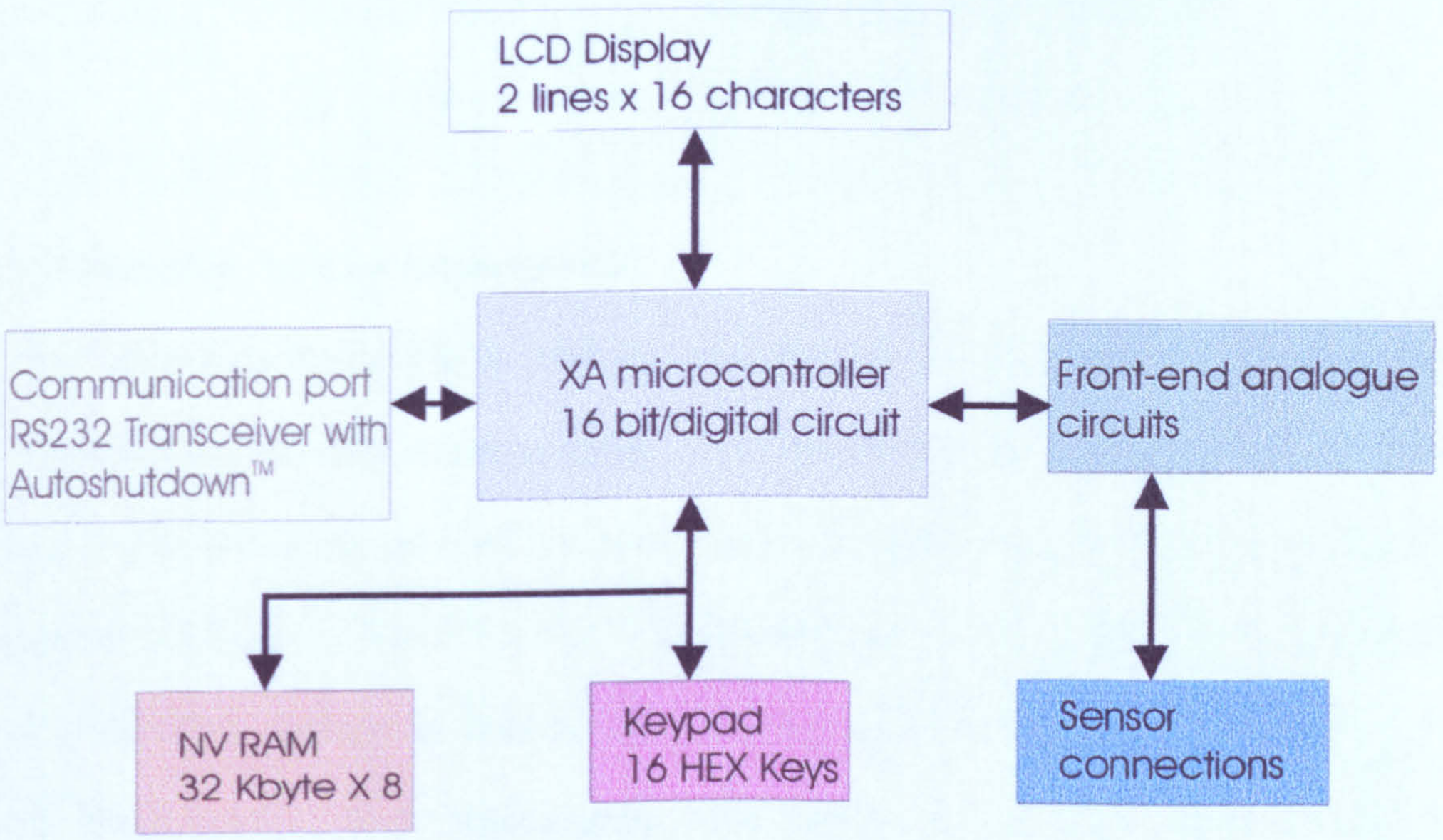


Figure 7.1 Instrument: general block diagram

A 3 V system was considered for reasons of maximum power efficiency, but due to the non-availability of a 3 V LCD display unit a 5 V system was chosen. However, certain sub-system components can be powered by either 3 or 5 volts. Additionally, the

controlling software is written in a high-level language (C). However, some of the software modules are written in assembly language when a high-speed input output communication is required. The use of an in-circuit emulator (ICE) is utilised in the development of the software. The controlling software was divided into modules. These modules were initially used to test individual hardware modules using XA-G3 simulator. The hardware is divided to two sub-systems, one is the analogue controlling section and the other is the digital system. A block diagram of the basic system is shown in Figure 7.2.

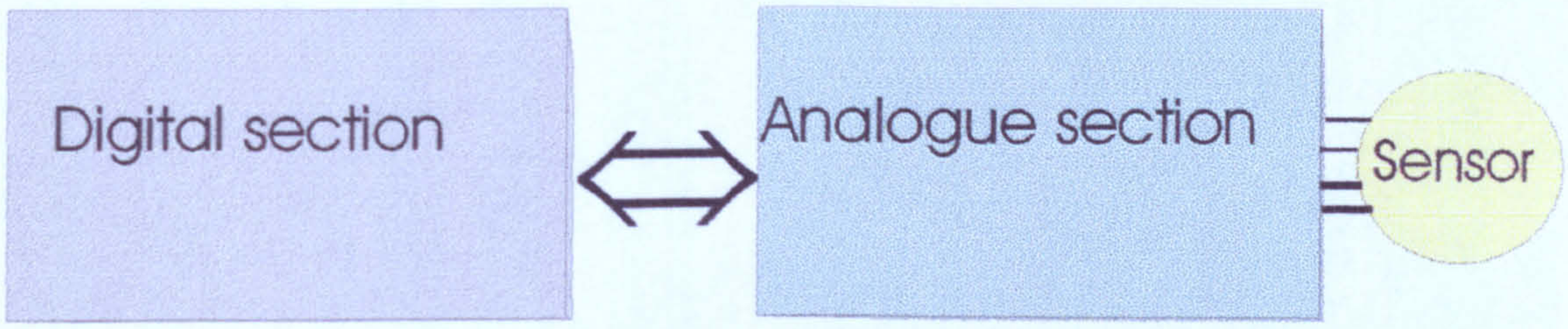


Figure 7.2 general block diagram of the system

## 7.2 Hardware systems requirements

The hardware is designed to be used as a hand-held instrument were the final size of the package should be able to accommodate all the circuitry, battery and be of a reasonable size to be held in the palm of one hand. This is achieved by using an "off the shelf" package as shown in Figure 7.3. The power consumption is very important in the design of a hand-held instrument, therefore the devices used in this design were chosen with the lowest possible power consumption. More details on this are provided later on in this chapter.

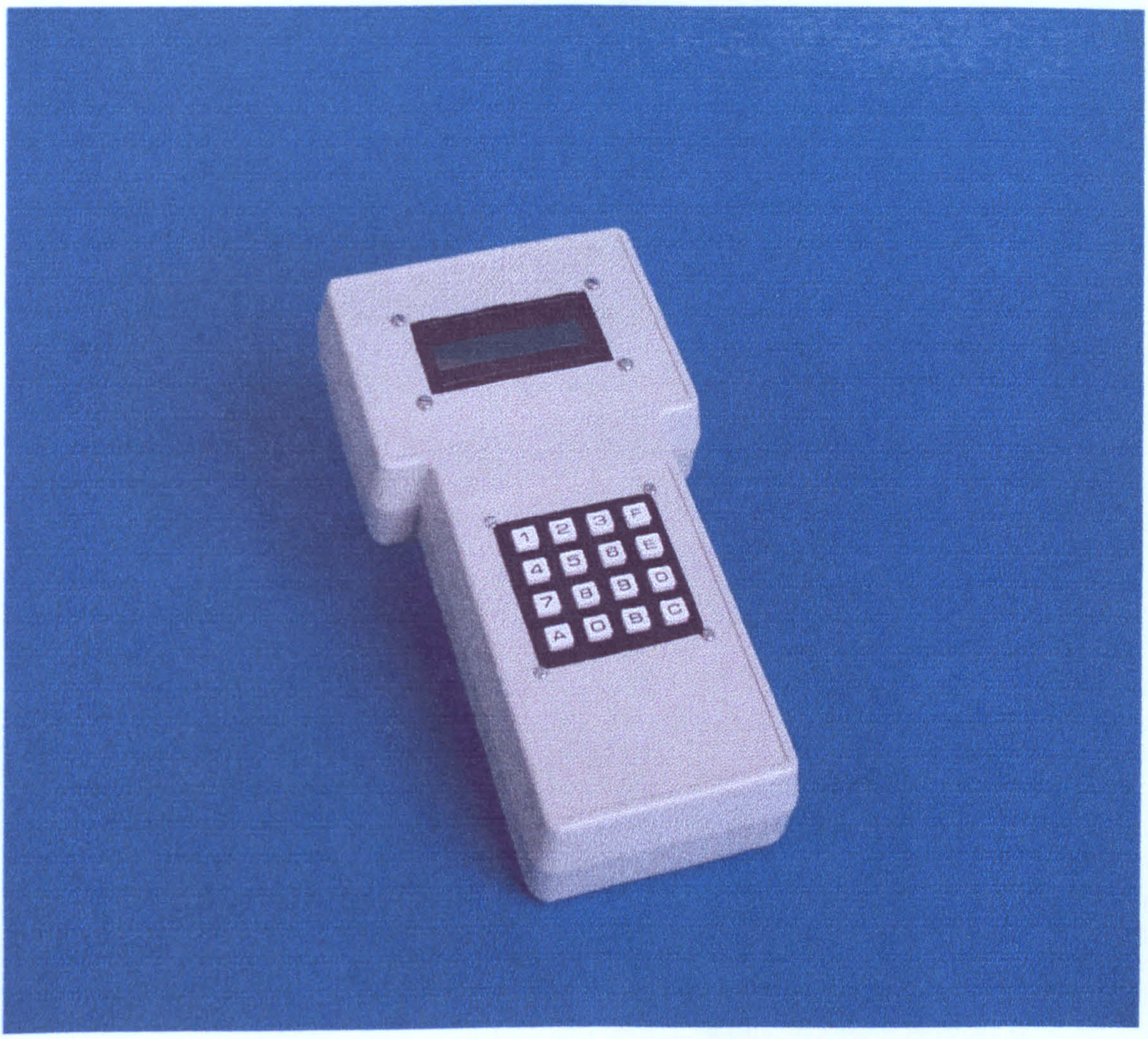

Figure 7.3 The prototype hand-held instrument

## 7.3 Systems design

The control system consists of two distinct sections analogue and digital as noted above.

The precision analogue circuitry as shown in Appendix B was designed on the outset of this research.

This proved to be a stable and reliable circuit by repeatedly testing it with known parameters. This circuit was used both to generate thermal waves in an integrated platinum resistive heater and to monitor the oxide resistance. The analogue circuit was connected to a PC running LabView virtual instrument software as described in chapter 4. The general configuration is shown in Figure 7.5. The second section of this system is the digital area. This is based on a microcontroller and a number of peripheral devices for controlling a number of functions as will be discussed in detail in the following sections of this chapter.

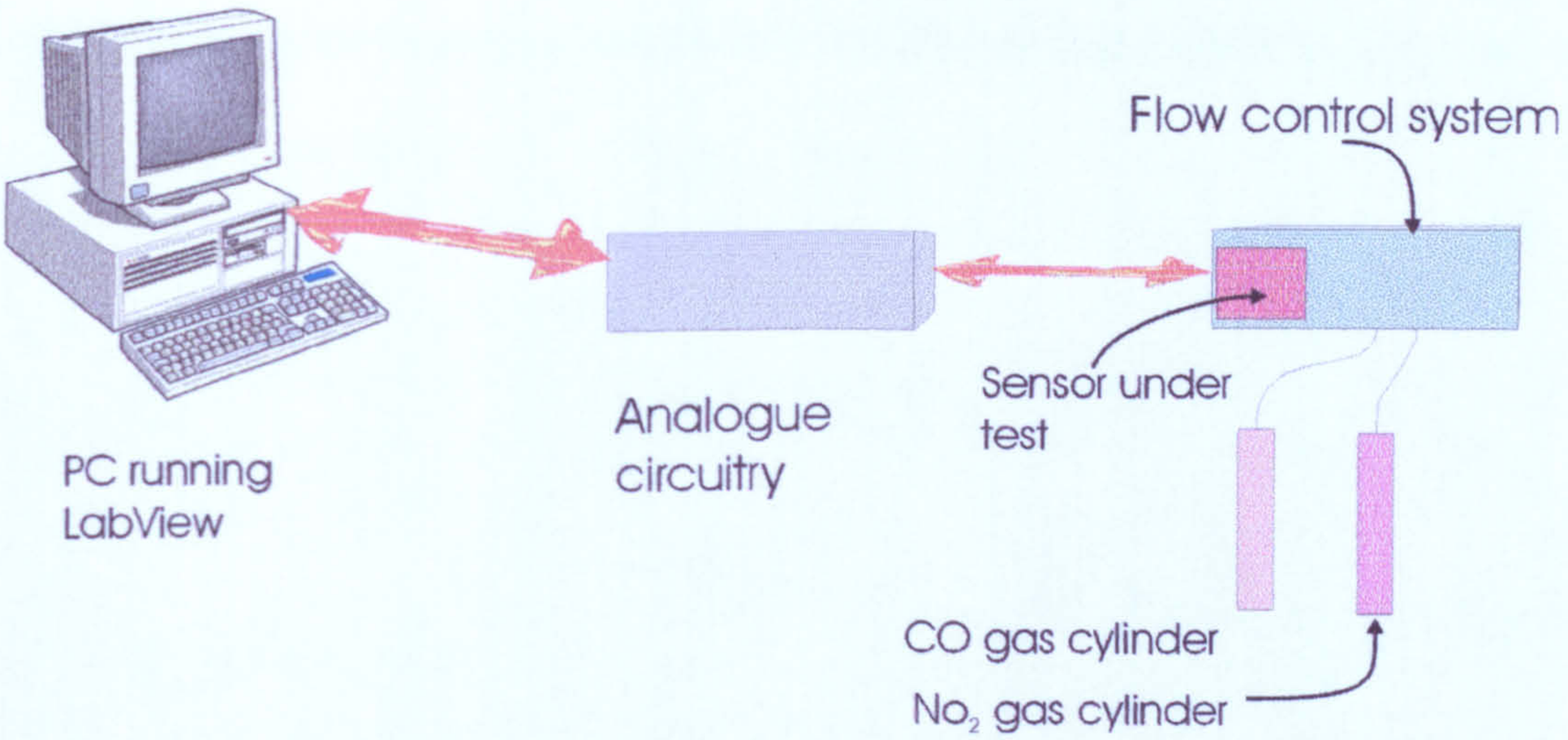


Figure 7.5 PC LabView controlled testing system

### 7.3.1 Analogue front end circuitry

In order to characterise the response of the resistive sensor to thermal waves, it is essential to have stable and reliable circuitry which both drives the resistive heater (nominally 100 Ω) and measures the resistance of the metal oxide coating over a wide dynamic range of both resistance (e.g. 10 Ω to 1 MΩ) and frequency (mHz to kHz). A circuit has been specifically designed, see Figure 7.4, to characterise the sensor's response to thermal waves at different levels of target gas concentration and relative

humidity. The analogue circuit contains four distinct parts; constant current, temperature control, humidity and ambient temperature circuits. These are discussed next.

### 7.3.1.1 Constant current circuitry

The resistance $R_S$ of the gas-sensitive coating is measured using a reference diode based circuit to generate a constant current of $I_S$ with the value set by the choice of the precision resistor $R_6$ shown in Figure 7.6. The current is chosen so that the voltage dropped across the resistive sensor does not exceed 0.1 V and it behaves in an ohmic manner with no self-heating. The voltage $V_S$ output of the sensor is first set close to zero by biasing with a voltage controlled by DAC0, and then amplified using two

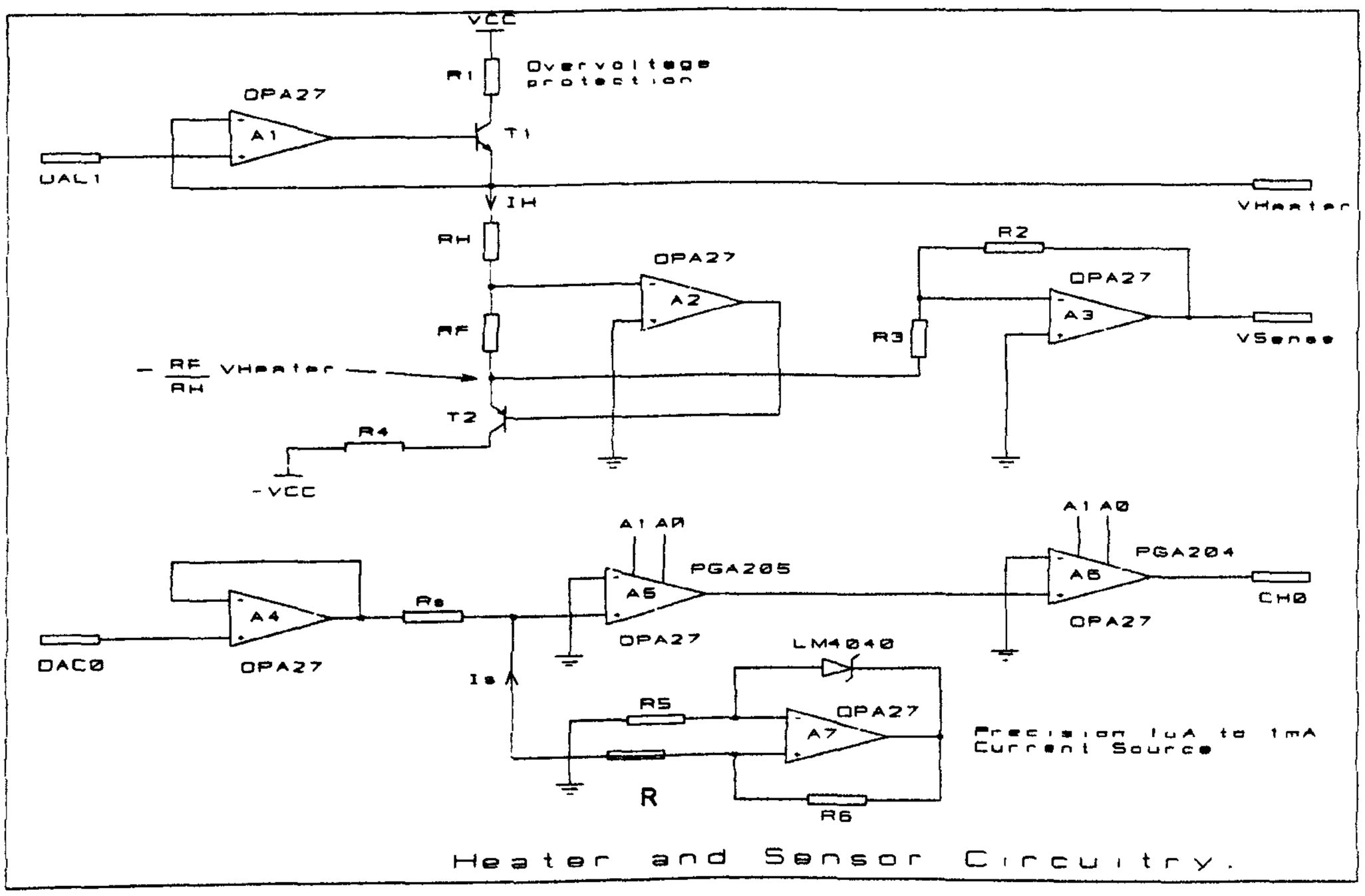


Figure 7.6 Schematic of heater and Sensor circuitry

programmable gain amplifiers (PGA204 & PGA205). The analogue voltage output is finally fed into the 12-bit ADC as channel CH0, then filtered and recorded by the VI.

The temperature of the sensing material is assumed to be the same as the platinum heater because the thermal time-constant of the membrane is *ca.* 2 ms and our thermal modulation frequency is only 1 Hz or less. This interface circuitry was then used to characterise step changes and low-frequency a.c. temperature modulation of the resistive sensor.

### 7.3.1.2 Temperature control circuit

The voltage across the heater, $V_{Heater}$, is set by a 12-bit ADC (Labview PC$^+$), DAC1. The current $I_H$ is supplied by the transistor T1 and flows through the heater $R_H$ (*ca.* 200 Ω) and a precision feedback resistor $R_F$. The heater current, resistance $R_{Heater}$ and power $P_{Heater}$ can be calculated from the heater voltage and sense voltage $V_{sense}$, whence,

$$I_{Heater} = \frac{R_3 V_{Sense}}{R_2 R_F} \;;\; R_H = \frac{R_2 R_F V_{Heater}}{R_3 V_{Sense}} \text{ and } P_{Heater} = I_{Heater} \times V_{Heater} \qquad (7.1)$$

These values were computed in a VI running on the PC. The resistance of the platinum heater is accurately related to its temperature $T$ in a linear manner and given by,

$$R_{Heater} = R_0\left(1 + \alpha(T - T_0)\right) \qquad (7.2)$$

where $R_0$ and $T_0$ are the resistance and temperature of the heater at a fixed temperature, here 21°C. For a platinum resistance heater, the temperature coefficient α is constant up to at least 900°C and the linear model is accurate to about 0.1 %. Equation (7.2) was used to calibrate the heater and then the temperature computed with the VI.

### 7.3.1.3 Humidity circuit

The humidity circuit is controlled by the Panasonic's MiniCap2 [2] as shown in Figure 7.7. This device is a low cost, general-purpose thin film polymer capacitive type relative humidity sensor.

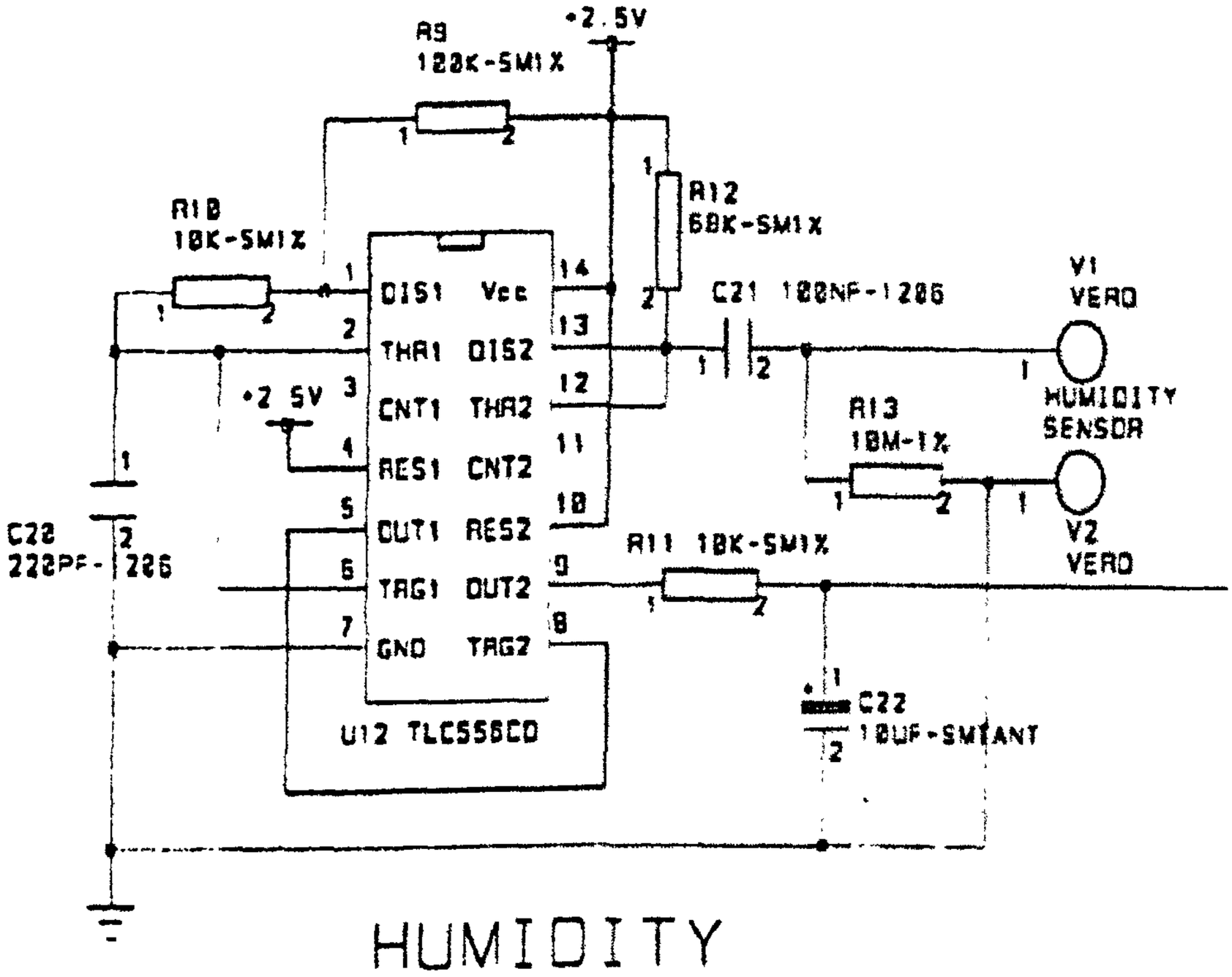


Figure 7.7 Humidity control circuit

The dielectric constant of the polymer thin film changes with humidity, resulting in a change in capacitance changes. The relative humidity is then computed from the operating temperature and known dew point.

### 7.3.1.4 Ambient temperature circuit

The ambient temperature monitor is controlled by the LM35DZ [3] a precision integrated-circuit temperature sensor as shown in Figure 7.8

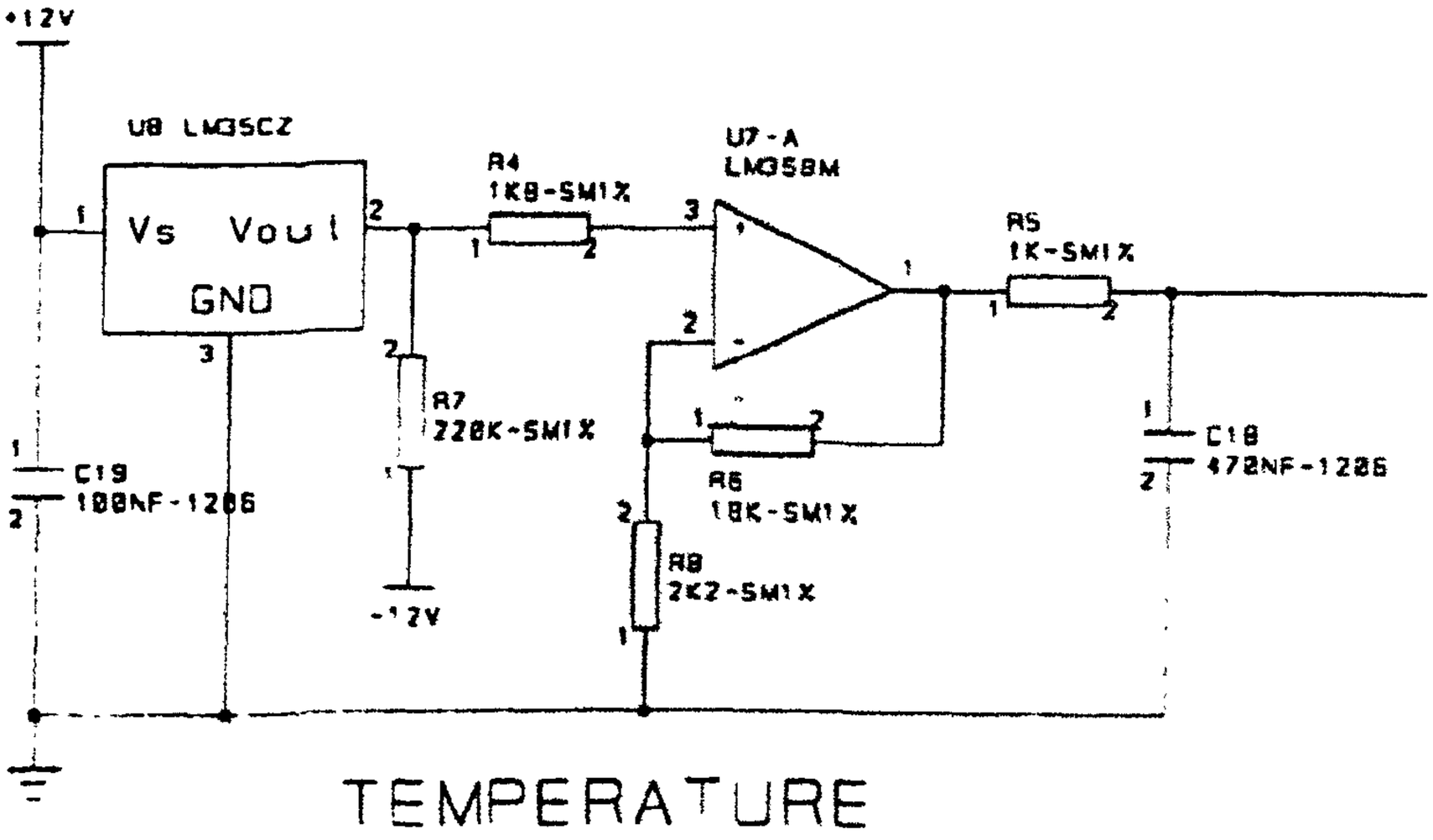


Figure 7.8 Ambient temperature monitor circuit

### 7.3.2 Digital circuitry Specification

Hardware module specifications are as follows:

- LCD Display- minimum of 2 by 16 alpha numeric required because a human-computer interface is required for hand held application.
- Keypad – minimum 4 by 4 – this is used for menu selection
- NV-RAM – If the system is used as a hand held gas monitor as well as a data logger, it must have non-volatile memory (NV), because when the system is powered down, logged data should not be lost. NV-RAM could also be used in applications where "look-up" tables are required.
- RS232 port – The controller will require a connection to the external systems, particularly workstations. It is therefore that the RS232 function was included in the system.

- Battery power management system – The controller will frequently be powered by batteries, and therefore efficient use of the power source is essential. Typically the system should "draw" no more than 150 mA, when all subsystems are enabled.
- Analogue Interface – Multi-channel DAC and ADC functions was included
- Micro-core – a C –compiler and ICE system should be available for this
- Digital ports – these are required to communicate and control programmable gains and provide handshaking with other sub-systems.
- Memory – sufficient memory should be available to the code and data.

The complete digital circuit is shown in Appendix B9.

### 7.3.2.1 The microcontroller

There are many microcontrollers and microprocessors available on the market today. Initially a number of microcontrollers were considered for the system design, such as Motorola 68000 microprocessor and Motorola 6811. However, after consideration the Philips 8051XA 16 bit microcontroller was used in the system. The main reason was the availability of an ICE (In Circuit Emulator) and a simulator for the XA microcontroller. The other reason was the availability of a C-compiler for this microcontroller. The 8051XA is a relatively new microcontroller although any software written for the 8051 microcontroller can be converted directly into the 8051XA code. The 8051XA is evolved from the original INTEL 8051 series microcontrollers. The core of the XA is partially pipelined. When executing instructions via the Execution unit, the fetch unit 'pre fetches' the next instruction(s) and puts them in a 7 byte queue, meaning the execution unit will not have to wait for the next instruction to be fetched when ready to execute a new instruction. If a branch instruction is executed the queue is flushed, and the next instruction is fetched from memory. This operation results in fast instruction executions. The power requirements of the XA-G3 microcontroller are as follows:

- maximum supply current operating at 5 V, 30 MHz is 100 mA
- maximum idle mode supply current at 5 V, 30 MHz is 25 MA
- maximum power-down current at 5V, 3V is typically 5 μA.

#### 7.3.2.1.1 Core registers

XA core contains several important Special Function Registers (SFR), which directly affect the operation of the device. These are:

- SCR - System Control Register
- PSW - Program Status Word

- DS - Data Segment Register, CS (Code Segment Register), ES (Extra Segment Register)
- SSEL - Segment Select Register
- PCON- Power Control Register

The Segment Registers are used in systems with large memory (greater than 64K)

**7.3.2.1.2 Register File**

Unlike the standard 8051, the register file is in a totally independent address space to all other XA memory spaces. There are twenty 16 bit registers in the XA-G3 derivative (R0 to R7), with R0 to R3 banked to provide access to 8 out of 20 registers at any one time. The active bank is dependent upon the Program Status Word. Register R7 is the Stack Pointer, and points to either the system or the user stack, dependent on the contents of the program status word. All registers in the Register File are bit addressable, which is useful if memory is low and single bit is required as flags as shown in Figure 7.10.

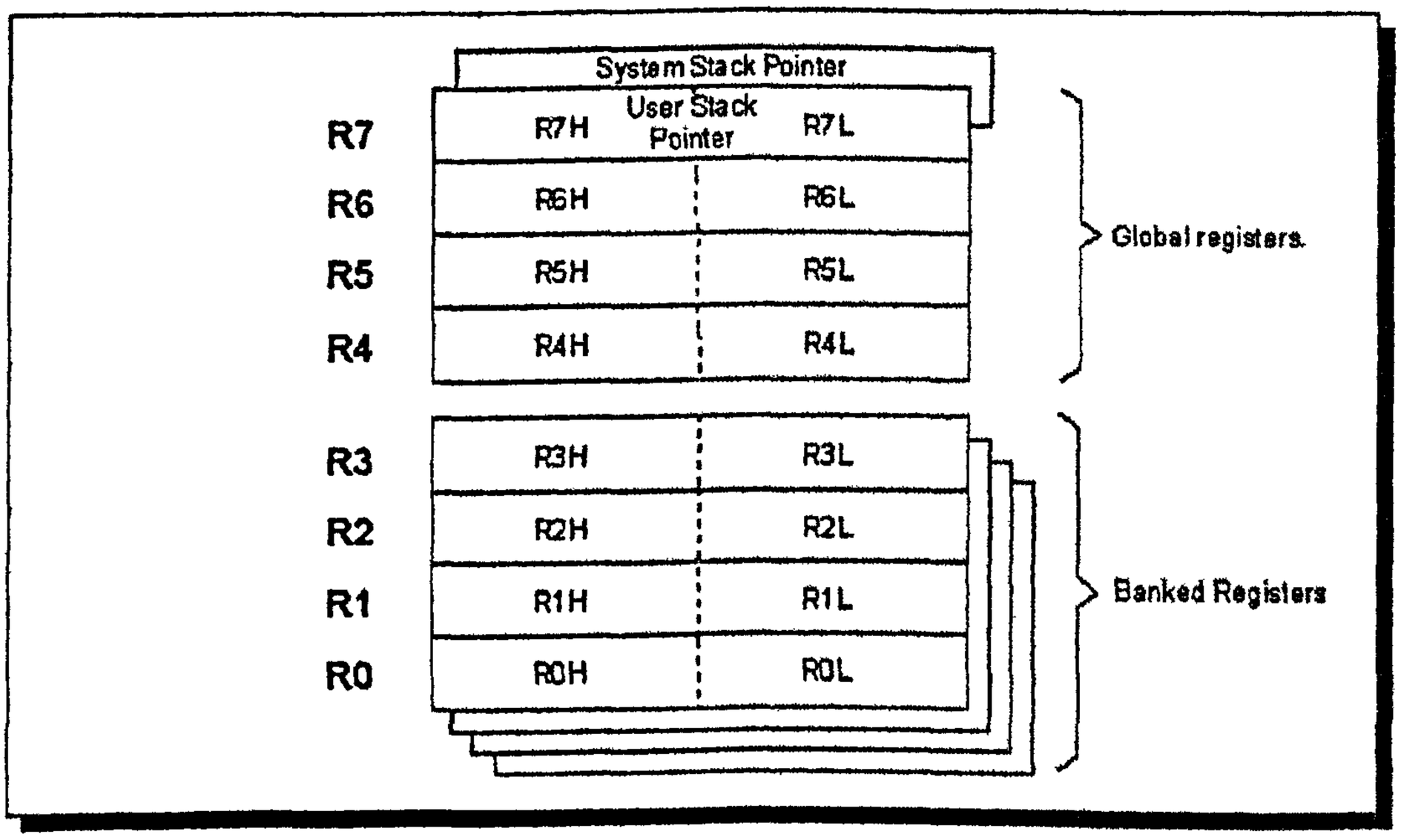


Figure 7.10 The register file

#### 7.3.2.1.3 Memory

The XA memory space is configured as a Harvard architecture, i.e. the code and data space are logically separated. The XA architecture is capable of using 24 address lines, providing an addressable memory space of 16 Mbytes of code and data. However, the XA-G3 derivative is capable of using only 20 address lines, and contains 512 bytes of on-chip RAM and 32 Kbytes of on-chip ROM. Additionally, a logically separate area of registers called Special Function Registers (SFR) are used. These provide access to on-chip 'peripheral' functions such as the UARTs, ports, timers etc. In the design of the system the XA is configured in a 'single-chip' mode and the EA input is connected to '1'. Therefore, only the internal memory can be accessed.

#### 7.3.2.1.4 Systems configuration registers

The program status word as shown in Figure 7.11 is the most important SFR on the XA. The register is divided into 2 separately addressable bytes (PSW high) and (PSW Low).

| SM | TM | RS1 | RS0 | IM3 | IM2 | IM1 | IM0 |
|---|---|---|---|---|---|---|---|
| C | AC | - | - | - | V | N | Z |

Figure 7.11 Program status word

PSWH, is used by the programmer to set the XA operating mode:

- SM – set when XA is in system mode, clear when in user mode
- TM – set when XA is in trace mode, for normal operations
- RS1-RS0 – select register bank
- IM0-IM3 – interrupt masks, setting the priority of the code currently executing.

The contents of the SM bit determines which stack is used i.e. system or user stack, and which privilege code is currently executed. Multitasking system would exploit this function. The XA in this design is run in system mode. PSWL, contains flags to indicate the results of operations. The systems configuration register as shown in Figure 7.12, is a single byte SFR, that sets the XA's global operating mode. For normal operation, the register should only be written to once, during the "boot-code" of an application.

| - | - | - | - | PT1 | PT0 | CM | PZ |
|---|---|---|---|---|---|---|---|

Figure 7.12 System configuration Register

PT1, PT0 – Many 'on-chip' peripherals, such as the Times, use a clock (peripheral timing clock or PTC) derived from the main clock. The frequency of the clock is determined via bits PT1 and PT0.

CM – The XA can be operated in one of two modes (Native or compatibility mode). Compatibility mode, enables code written for generic 8051 to re-assembled/compiled and ran without significant alterations. This is achieved by "emulating" the 8051 8bit architecture within the XA. However, if the XA is used in compatibility mode, the XA architecture is not fully exploited. For this research the Native mode was used by clearing the CM bit.

PZ – The XA can be forced to use one of two memory models (large memory model or page zero memory model). Basically, with the PZ bit clear, the XA core uses 24 bit addresses (large model) and with PZ set (page zero model), the XA core uses 16 bit addresses. The merits of the page 0 mode are detailed next, because this is the mode the software was compiled for. The Page Zero Mode the XA, uses only a 16 bit address. This means that only 64K of code and 64K of data memory can be addressed. Operating XA in a Page Zero mode provides a significant performance increase. When

addresses are pushed onto the stack, only 16 bit need "pushing" as opposed to 24 bits. This not only saves stack space, but also increases the speed of Function and ISR calls.

For bus configuration, the external data bus can be configured in many different ways. For example, 8 bit data bus and 12 addresses lines or 16 bit data bus and 20 address lines, amongst other can be selected. Figure 7.13 shows bus control register.

| | | | | | | | |
|---|---|---|---|---|---|---|---|
| - | - | - | Waited | Busd | BC2 | BC1 | BC0 |

Figure 7.13 Bus control register

When the 'Busd' is set, the external bus facilities are permanently disabled. This feature is useful when using the XA in 'single chip' mode, because it ensures the external bus is never activated.

**7.3.2.1.5 Power control**

The XA is ideal for low power applications, because it provides two reduced power modes: idle and power down mode. Each power saving mode can be initialised by setting the relevant bit in the power control register (PCON) as shown in Figure 7.14.

| | | | | | | | |
|---|---|---|---|---|---|---|---|
| - | - | - | - | - | - | PD | IDL |

Figure 7.14 Power Control Register

The XA can minimise power consumption, by running in idle mode, which reduces the supply current from approximately 90mA to 25mA (operating at 30Mhz with 5 volt supply). This is achieved by setting the idl bit in the PCON SFR. Once the XA is in idle mode, program execution is halted, but the oscillator continues to run. Since the oscillator is still running, all on chip peripheral can still run. This means that the XA can

be returned to active mode, by any event or exception interrupt. This particular power saving mode is useful if the XA is not highly loaded, because the XA can execute code rapidly and then idle. For example, it could send data to a PC via the on chip UART, then idle, awaiting a replay. When data is received, the UART would generate an interrupt returning the XA to active mode. Further power can be saved, by moving into power down mode, which reduces the supply current to approximately 5 μA (operating at 30Mhz with 5 volt supply). This is achieved by setting the PD bit in the PCON SFR. Once in the power down mode, the on-chip oscillator is halted, thus all on-chip peripherals are inactive. Therefore, the XA can only returned to active mode by either a reset exception interrupt, or external event interrupt (if enabled). The power down mode is ideal for situations where the system is awaiting an action from its user for extended periods. In such a case, the Xa could be "powered-down" and re-activated by external event interrupt, generated by e.g a keypad.

### 7.3.3 SPI bus

The serial port interface (SPI) bus system is used in this design to connect a number of peripheral devices in order to reduce the number of CPU pins required for such connections. The SPI bus is a MOTOROLA development, and is designed primarily as a method of connecting multiple peripheral to a 3 wire bus. In addition to the 3 connections, chip select connections are required as shown in Figure 7.15. As can be seen, the number of connections required is significantly less than if an 8 or 16 bit parallel bus were used.

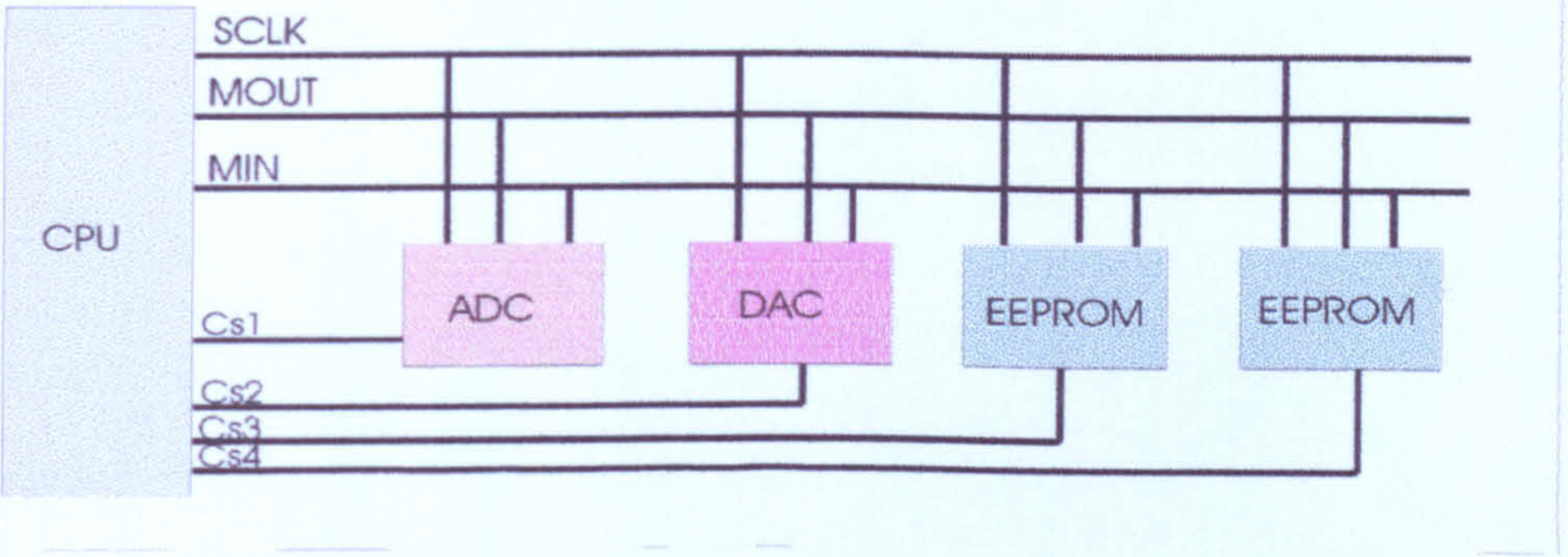


Figure 7.15 SPI Bus block diagram

The master system (typically a microcontroller) controls all data transfer and therefore called 'master'. The peripherals are controlled by the CPU (master), and are therefore called 'slaves'. A typical data transfer operation is as follows:

- A data transfer is started by selecting a slave (CS low )
- On each positive edge of SCLK, the data on MOUT (Master out) is shifted into a receive register on the slave device.
- On each negative edge of SCLK, the data on the MIN (MASTER IN) pin, is shifted into a register on the master device.
- Once the data transfer is completed, the master de-select the slave (CS high). The SPI protocol can be achieved by hardware, software or a mixture of both. In this design the peripheral have dedicated SPI ports, but the XA-G3 does not have an SPI port, and therefore the SPI protocol is emulated in software.

### 7.3.4 NV – RAM subsystem

The NV- RAM subsystem is implemented using two 16 Kbyte SPI interface EEPROM. The X25128 [5] has the highest bit density to standby current (1μA) ratio of any serial EEPROM on the market, and can be powered from 2.7V to 5V, therefore an ideal

choice for a hand held instrument. The EEPROM1 and 2 are connected as shown in Figure 7.16.

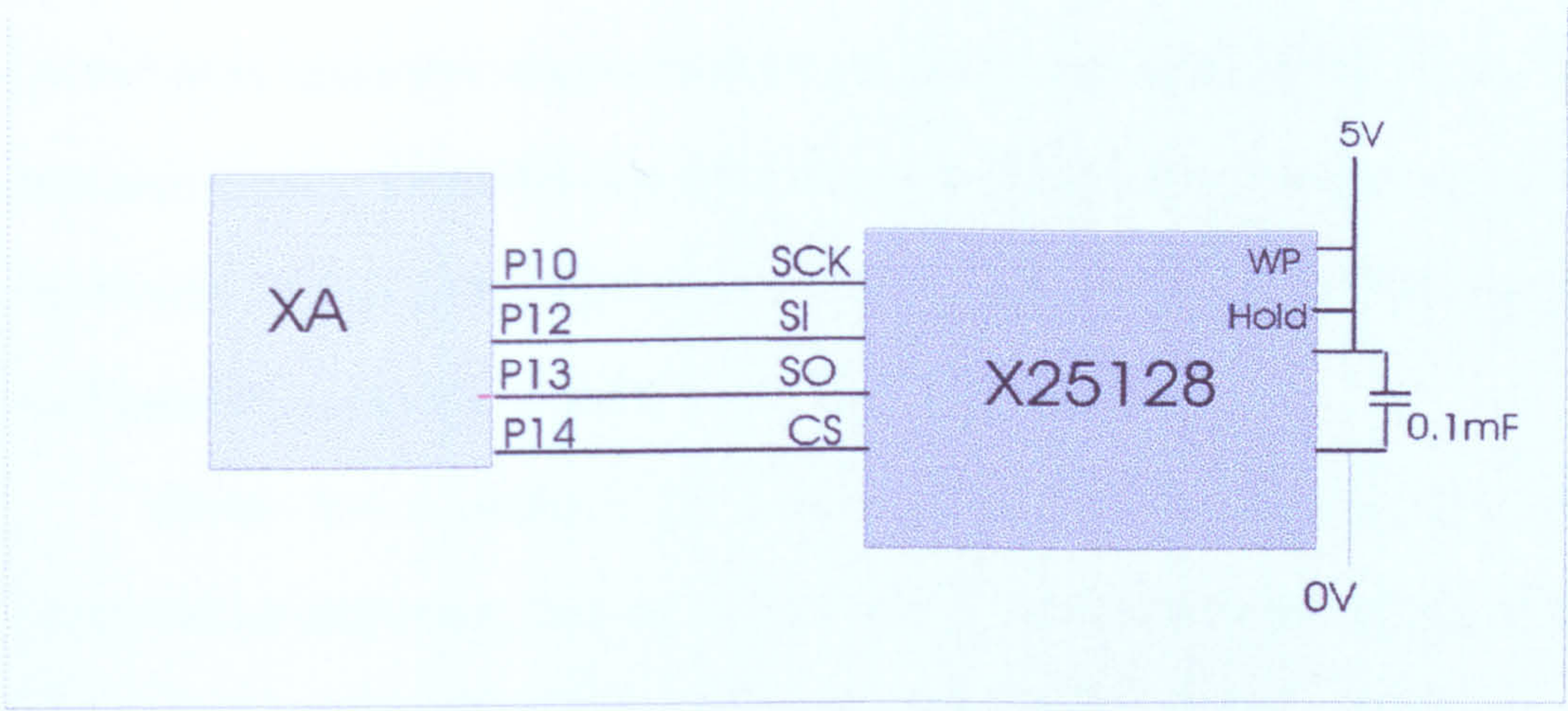


Figure 7.16 NV-RAM connection

The WP and Hold pins are strapped high, therefore the write protect and hold facilities are disabled, thus all areas of the memory arrays can be written to. The capacitor is there for de-coupling purposes to ensure noise introduced onto the supply lines is limited. The X25128 contains an 8bit instruction register, accessed via the SPI interface used to receive the instructions as shown in Table 7.1.

Table 7.1 EEPROM instruction registers

| Instruction Name | Instruction Format* | Operation |
|---|---|---|
| WREN | 0000 0110 | Set the Write Enable Latch (Enable Write Operations) |
| WRDI | 0000 0100 | Reset the Write Enable Latch (Disable Write Operations) |
| RDSR | 0000 0101 | Read Status Register |
| WRSR | 0000 0001 | Write Status Register |
| READ | 0000 0011 | Read Data from Memory Array beginning at selected address |
| WRITE | 0000 0010 | Write Data to Memory Array beginning at Selected Address (1 to 32 Bytes) |

Additionally, an 8-bit status register is provided, that can be used to check the status of the device and configure it. To read data from the EEPROM CS is pulled low and then the READ instruction is transmitted by the XA via the SPI software module. After the

READ instruction has been sent, the 16 bit address is sent and starting on the next negative SCLK edge, the EEPROM outputs the data byte. The read sequence is completed by returning CS high after reading a single data byte. Alternatively, data can be read from sequential memory locations by providing further SCLK pulses. To read the status register, the RDSR instruction is sent to the EEPROM, and the status register received by the XA, in the same manner as data byte is read. The RDSR instruction is used typically to poll the WIP bit, to see if the device is busy.

Before data is written to the memory array, the XA must first send a WREN (write enable) instruction, then the WRITE instruction and a 16 bit address of the first data byte to be written, followed by the data bytes as shown in Figure 7.17.

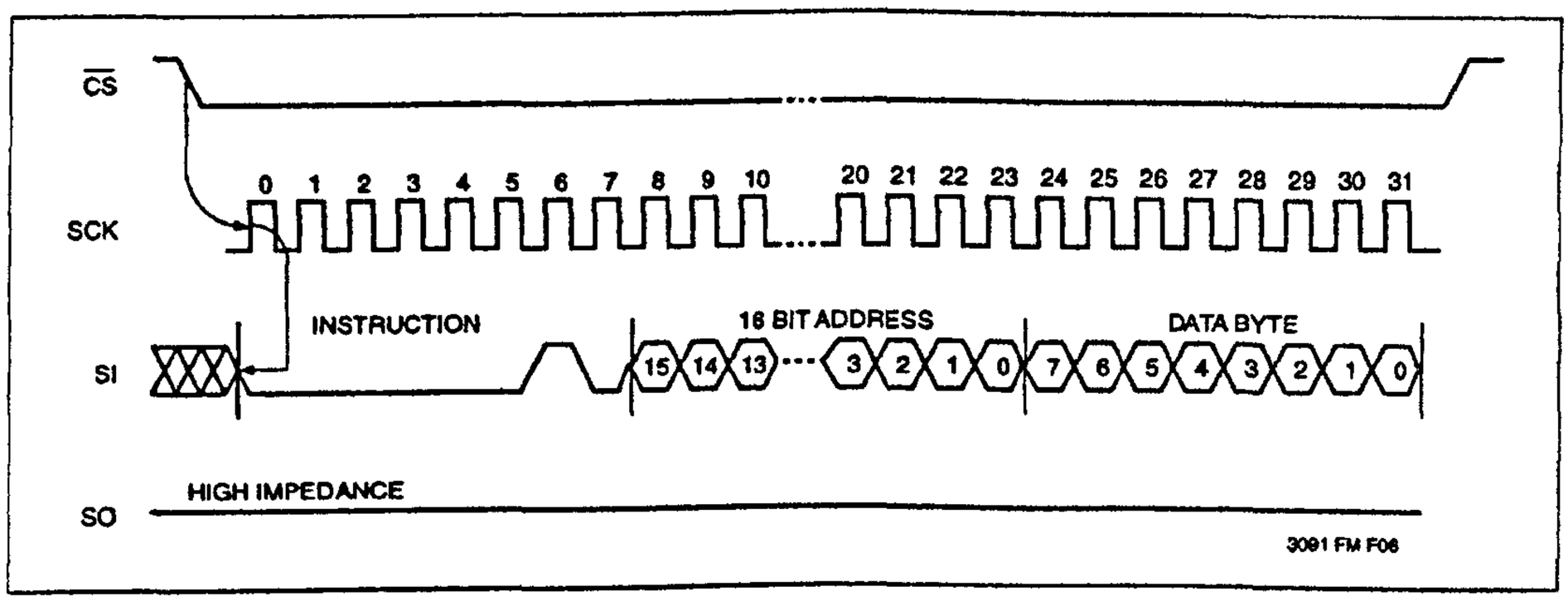


Figure 7.17 Write sequence waveform

Once again, the XA must take the CS pin low for the duration of the write sequence. Additionally, up to 32 bytes of data can be sequentially written to the device by providing further SCLK pulses. When the EEPROM detects the CS return high at the end of the write sequence, it sets the WIP bit in the status register. The WIP bit remains set whilst the memory array is programmed, which takes approximately 5 ms regardless of the number of bytes to be programmed.

### 7.3.5 ADC sub- systems

The chosen ADC subsystem is the MAX 147[6]. It combines an 8 channel multiplexer, track and hold analogue input, SPI interface and 12 bit successive approximation ADC and can be operated from 2.7 V to 5.25 V supply. In operating mode it draws only 0.9 mA and when shutdown only 1 μA and therefore ideal for hand-held instrument use.

The device is connected as shown in Figure 7.18.

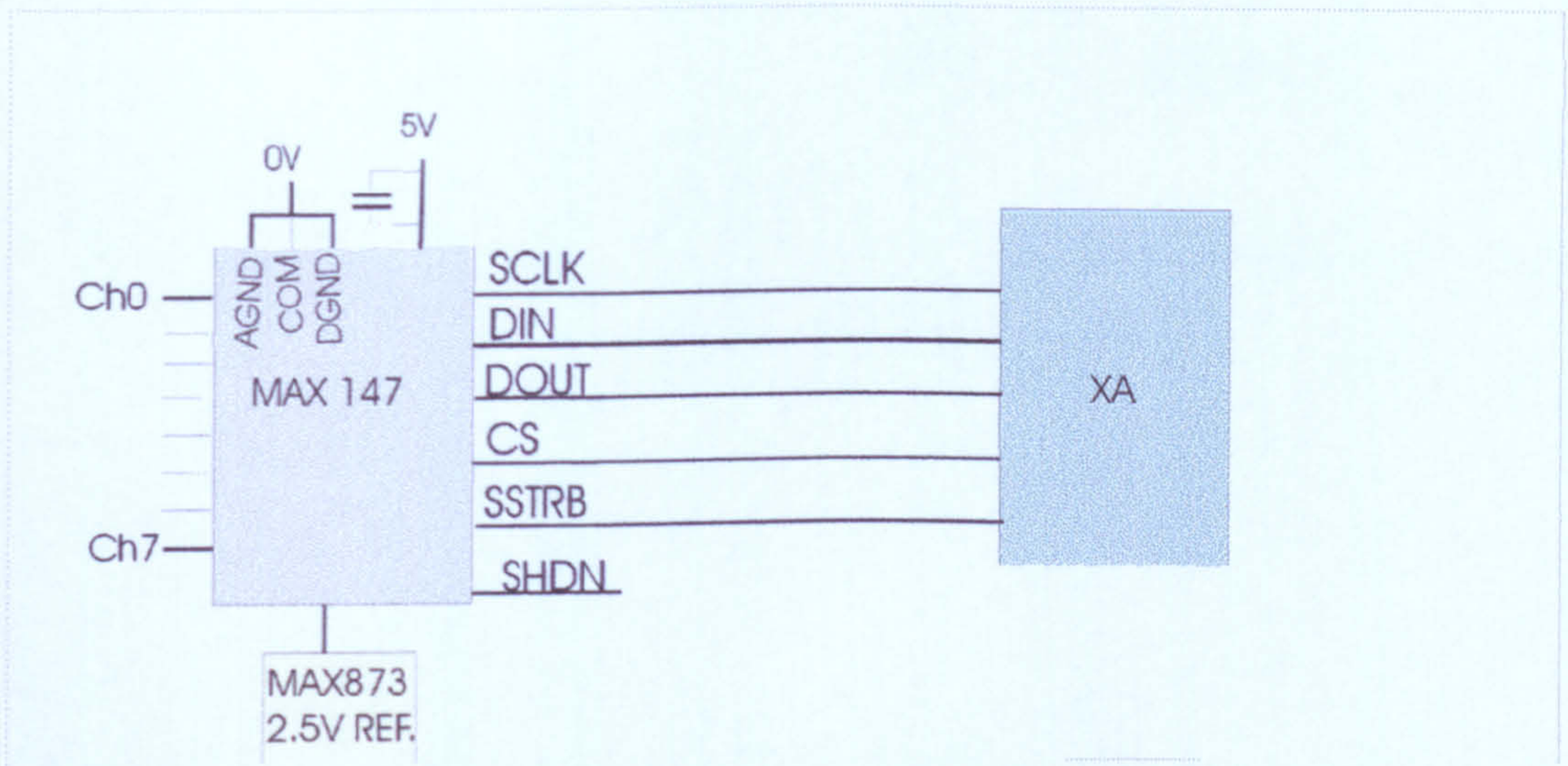


Figure 7.18 ADC connections

The ADC can be locked in two different modes, selected by the shutdown pin (SHDN) and the control byte. To generate a 12 bit conversion the XA needs to take the CS line low, then output a control byte as shown in Figure 7.19

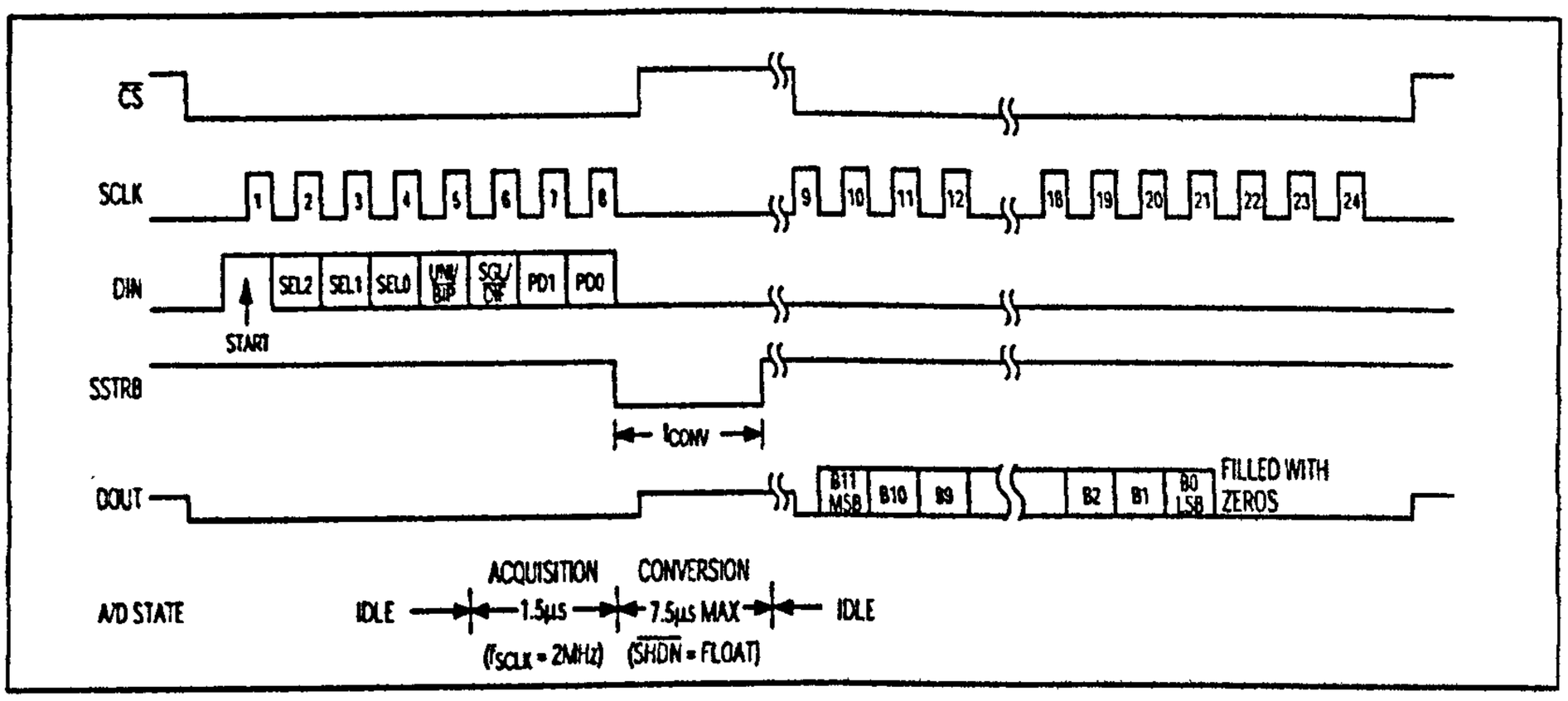


Figure 7.19 Communicating with the MAX 147

The control byte is outputted using the SPI bus and is shifted into the ADC on each positive edge of SCLK. On the following negative going edge of the 5th SCLK pulse, the acquisition period begins i.e. the ADC's track/hold system moves into the track position. The $C_{hold}$ capacitor is then charged from the selected input channel, until the falling edge of the 8th SCLK pulse. The acquisition period requires a minimum of:

$$T_{ACQ} = 9 * (R_S + R_{IN}) * 16\ pF \tag{7.3}$$

Therefore, this should be taken into consideration when the input signals source impedance is high, i.e. as $R_S$ increases a longer acquisition time must be allowed. With an internal clock frequency of 1.8Mhz, the conversion takes a maximum of 7.5μS, during which time the SSTRB pin is held low. Once the conversion is complete the 12 bit conversion can be shifted out of DOUT, on each negative edge of SCLK. To complete the conversion process CS is returned high.

### 7.3.6 DAC sub-system

The DAC sub-system is implemented using a MAX 525[7] device. It combines an SPI interface, four 12 bit channels each with a separate precision OpAmp output stage and a software shutdown facility. While in operation, it draws typically only 0.85 mA and when shutdown only 10 μA and is therefore ideal for hand-held instrument use. The system is connected as shown in Figure 7.20, using only three processor connections. The power down lockout PDL and Clear (CL) pins are strapped to 5 V, thus enabling the software shutdown facility, and disabling the asynchronous clear DAC register facility. All OpAmp output stages are connected as voltage followers, by connecting the OpAmp output directly to their inverting

inputs (OUT and FB) as shown in Figure 7.20. Two separate voltage references can be used, such that DAC's A and B are connected to one and DAC's C and D to the other. All DACs are effectively uni-polar, and therefore the output voltage is calculated as below:

$$\text{AOUT} = \text{VREF}\left(\frac{DACregister\_contents}{4096}\right) \tag{7.4}$$

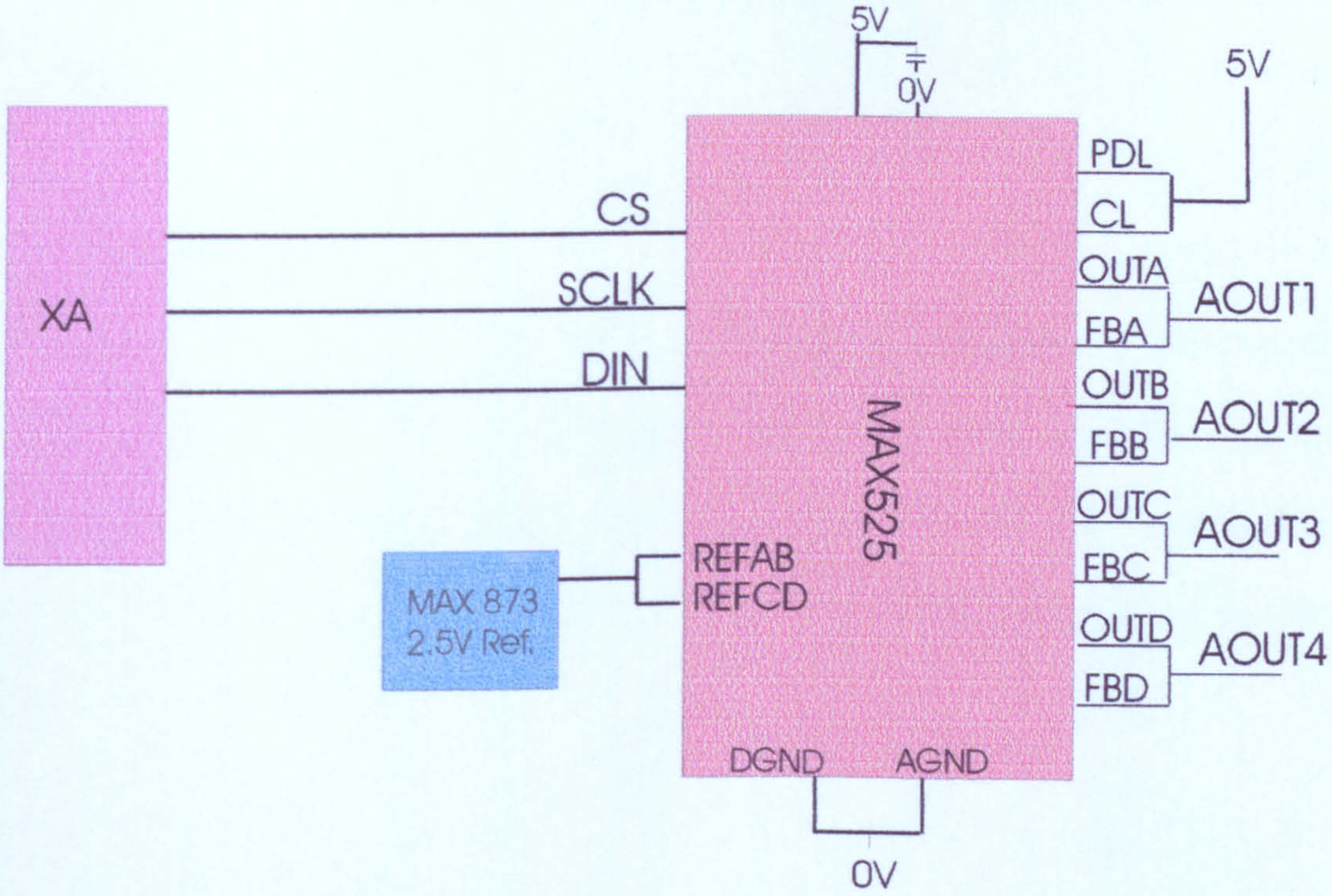


Figure 7.20 DAC connections

For communicating with the DAC, two registers are provided for each DAC (INPUT and DAC registers). The contents of the registers can be updated by sending data packets over the SPI bus, using software modules. A data packet is a 16 bit word that consists of two address bits, identifying the DAC that the data is associated with, followed by two control bits and 12 bit of data as shown in Figure 7.21.

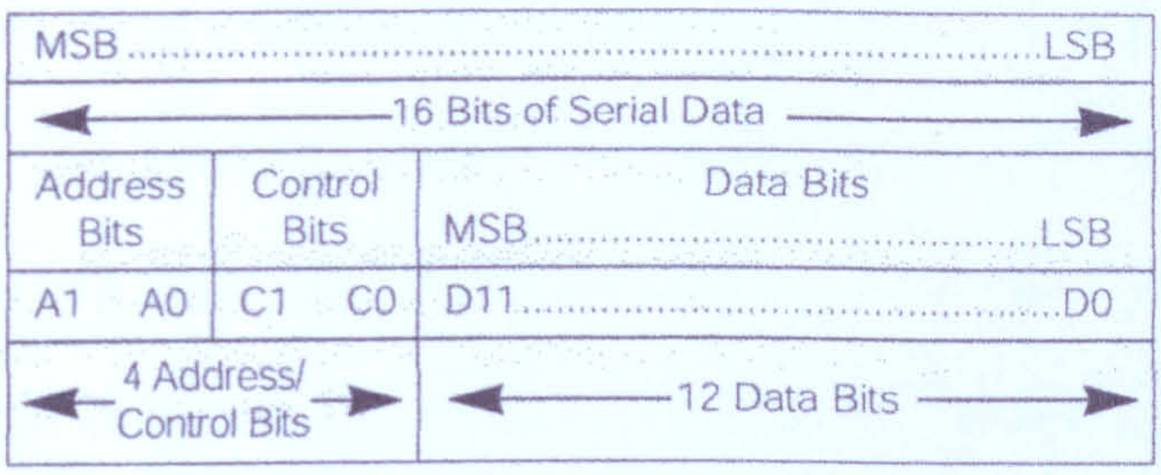


Figure 7.21 DAC Data packet Format

Many different data packets are possible, ranging from shutting the device down, to updating all DAC registers.

### 7.3.7 Display unit

The LCD display sub-system is implemented using an intelligent LCD display, the Hitachi LM016L [8]. It can be interfaced to either an 8 bit or 4 bit data bus, and requires only 3 additional control lines. The hand-held instrument therefore only requires 7 ports connections as shown in Figure 7.22 to communicate with the LCD unit.

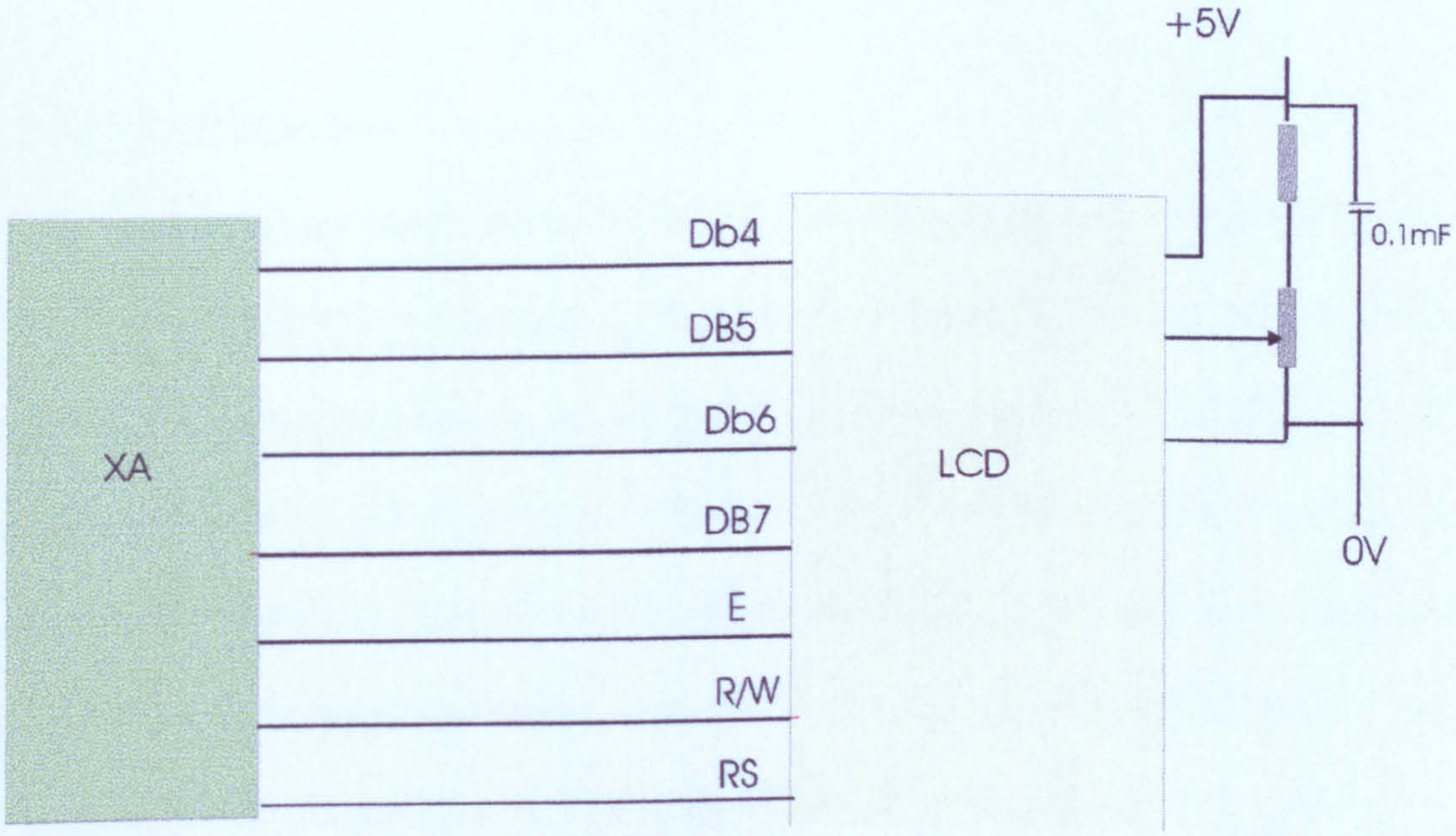


Figure 7.22 LCD XA inter-connections

The LCD is accessed by sending data to either instruction or data register, which is selected by the RS (register select) line, high data register or low instruction register. Additionally, data can be read from the LCD display, to inspect the busy flag. The LCD display contains 80 byte DD (display data) RAM, that is used to contain ASCII codes for the characters displayed. Additionally a register (ADD) is used to store the address where the next received character 'id' to be stored. Only 32 characters can be displayed on the LCD at any time, therefore the contents of only 32 bytes of the DD RAM are displayed. DD RAM addresses 1 to 39 decimal correspond to the top line and 40 to 79 decimal to the bottom line. Since the instrument uses only four data lines, characters are sent to display by setting the RS line, clearing the R/W line and then sending the upper nibble of the byte, followed by the lower nibble. Each nibble is latched into the data register by pulsing the strobe line. Alternatively, to send an instruction, the above procedure is used but the RS line is held low.

### 7.3.8 The RS232 port

The hand-held instrument has a RS232 port, which comprises a UART located on the XA and a RS232 transceiver. The transceiver used, is the MAX3223, which provides a voltage conversion facility so that CMOS voltage levels (0 and 5 V) can be converted to RS232 voltage levels (typically ± 12 V). This is a low power device that can be shutdown using either auto shutdown facility or software shutdown, and draws only 1 μA when shutdowns. A single 5 volt supply is used. If the RS232 port is not required, the transceiver should be shutdown by taking the FON pin low i.e. writing a '0' to XA port thus saving power. The hardware connection is shown in Figure 7.23.

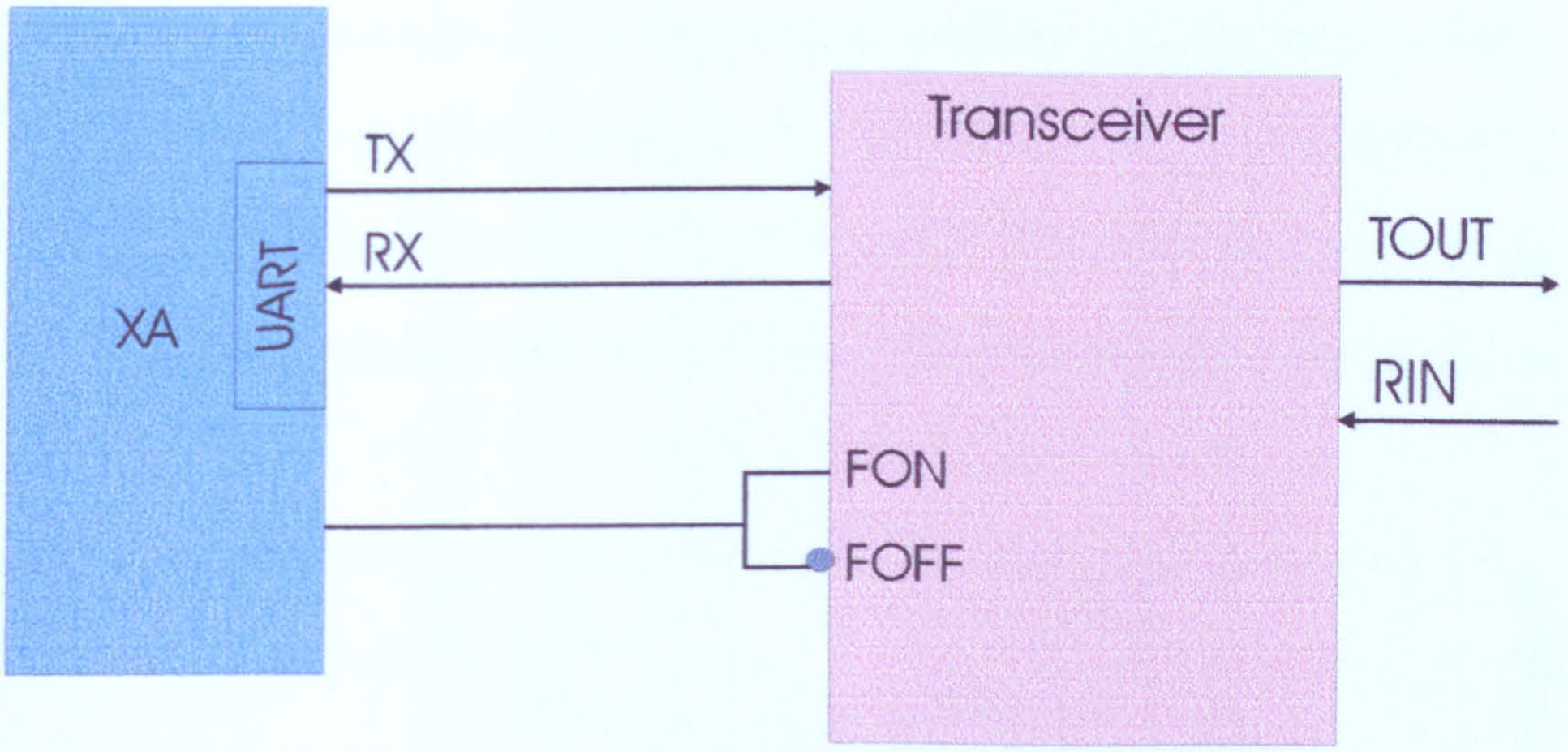


Figure 7.23 –RS232 port connections

### 7.3.9 Keypad sub-system

The keypad section of the system utilises a National Semiconductor keypad encoder (MM74C922) as shown in Figure 7.24.

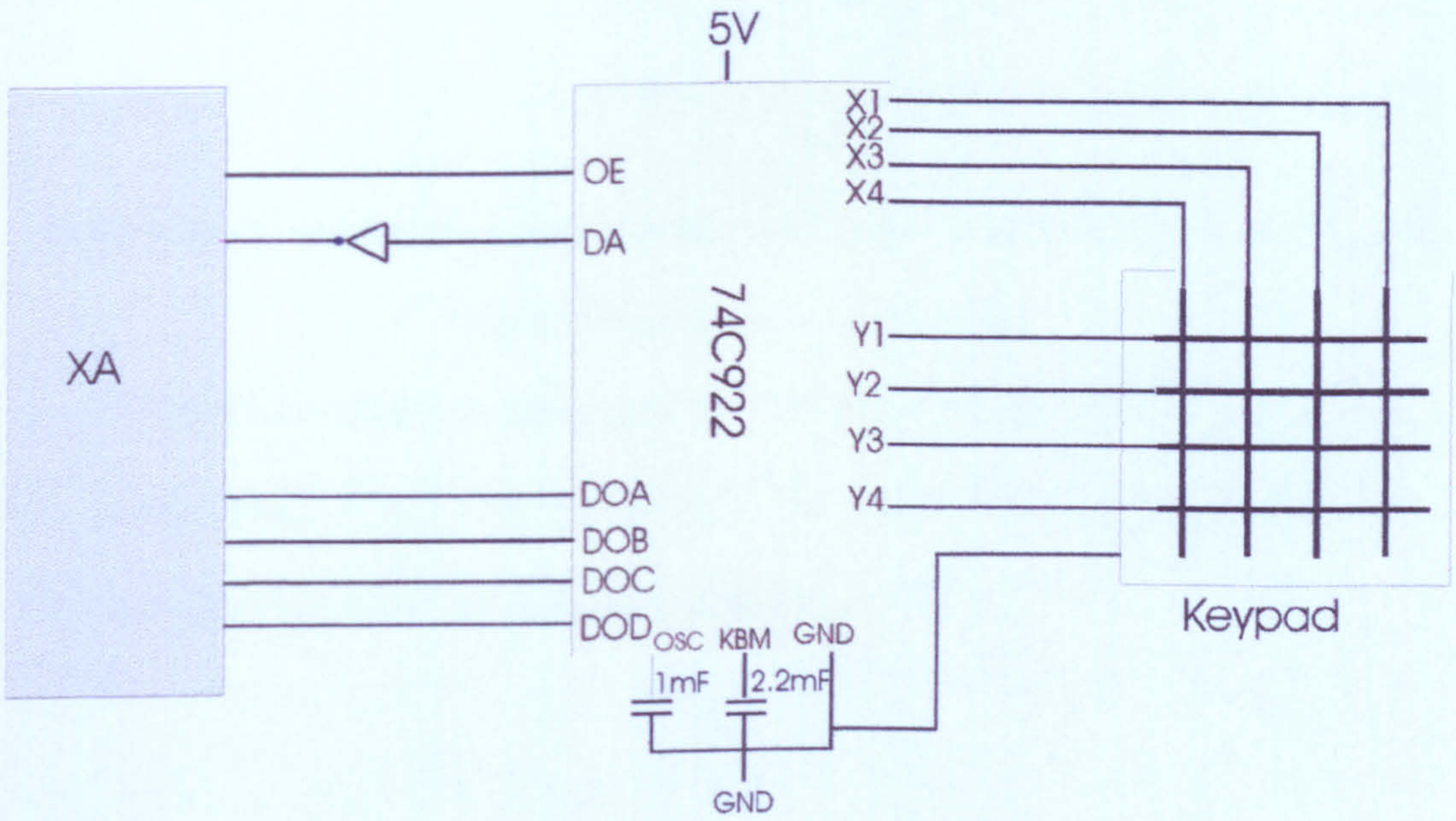


Figure 7.24 Keypad connections

The Keypad is scanned by the decoder at a frequency determined by the capacitor $C_{OSC}$. With a 1μF capacitor, the scan frequency is 30 Hz. When a key is pressed, a key-debounce time is started, which is clocked at a frequency determined by the capacitor $C_{KBM}$. A 2.2μF will provide a period of around 20ms allowed for key

bounce, which is adequate for the keypad used, which has a typical bounce period of 10ms. After the key-debounce period, the key scan code is latched, and the data available (DA) output taken high. This result in the INTO line being taken low thus produces a negative edge, hence generating a processor interrupt as shown in Figure 7.25

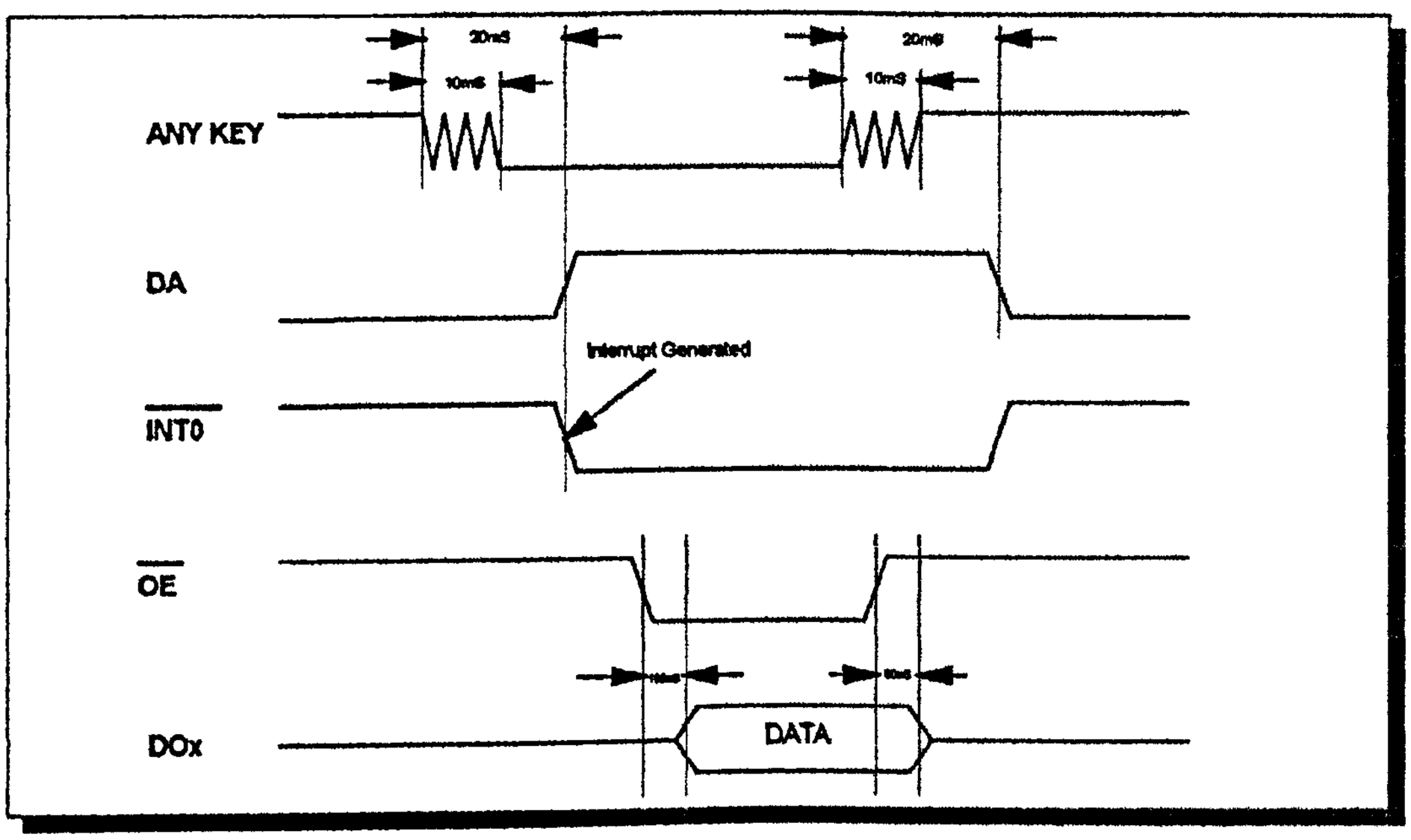


Figure 7.25 Keypad system waveform

The XA interrupt handler can then take the OE pin of the encoder low, and read in the key scan code. When a key is pressed, a 4 bit binary code is placed on DOA – DOD and each key has a unique code to identify it.

### 7.4 Summary

This chapter described the design of the hardware for the gas monitoring instrument. The hardware was divided into two separate parts: digital and analogue circuits. The analogue circuitry was tested fully and proved to be precise and stable. The digital circuitry was fully designed and built, except for a few surface mount capacitors. However, some suggested improvements in the different sections of the digital circuits are noted below.

The only protection for the ADC analogue inputs is currently provided by the MAX147 itself, via internal protection diodes. These diodes only offer protection between (AGRND – 0.3 V) and (VDD +0.3 V). This limitation could be solved in a number of ways. A fixed low pass filter (with a higher input protection) could be used, but this would not be suitable for all possible sampling frequencies. Alternatively a programmable active filter such as MAX261 or MAX270 could be used. However, such programmable filters generally provide only a $2^{nd}$ order response. To achieve higher order responses clock programmable filters can be used such as MAX280, but then varying clock frequencies need to be generated and so divider circuits would be required. Alternatively, a single chip analogue interface circuit (AIC), such as the Texas Instruments TLC3202 could be used. This device provides a 2 channel 14 bit ADC, single 14 bit DAC, $6^{th}$ order anti-aliasing filter and an SPI interface. The device can be powered down "drawing" only 100μA when powered down, and is therefore ideal for a hand-held instrument.

The DAC circuit is currently powered from a 5 V supplies. If a 3.3 V system is required then the MAX525 DAC can be replaced by the pin to pin compatible MAX5253.

Currently, the LCD is a 2 line x 16 alpha-numeric display. It has no shutdown facility, and can only be powered by a 5 V supply therefore continuously "draws" approximately 2 mA of current.

The communications interface is the RS232 serial interface. A significant enhancement could therefore be the addition of a CAN (control area network) interface, that would enable communication rates of up to 1 Mbits/s as opposed to a maximum of 115.2 Kbits/s provided by the RS232. Such an interface would increase the viability of the hand-held instrument being used in control applications, where many "hand-held" instruments could be controlled remotely via the CAN network. Philip has released an XA derivative with a CAN on chip interface (the XA-C3).

The hardware met the initial specification for the design of a low power and low cost gas-monitoring instrument. Table 7.2 shows the power requirements for the hardware components.

Table 7.2 Systems power requirements

| Device | Current requirement/ conditions |
|---|---|
| LCD | 2 mA |
| XA-G3 microcontroller | 60 mA at 30 MHz or < 20 mA at 10 MHz<br>idle mode supply current: or 8 mA.<br>Power down current: 5 µA |
| RS232 Transceiver | 1.6 mA operation.<br>Autoshutdown : 1 µA |
| DAC MAX525 | Supply current 0.85 mA<br>Supply shutdown 10 µA |
| ADC MAX147 | Operating mode, full scale input 0.9 mA<br>Shutdown : 1 µA |
| Sensor SRL125 | ~ 20 mA |
| Total average current<br>Total power | < 50 mA (XA operation at 10Mhz)<br>~ 250 mW for 5 V or ~ 90 mW for 3 V system. |

## 7.5 References


1. 16-bit 80C51XA Microcontrollers, Philips Semiconductors, 1997.
2. MiniCap 2, Relative Humidity Sensor,
3. Precision Centigrade Temperature Sensors, National Semiconductors, July 1999.
4. SPI bus, Motorola data sheets, 1998.
5. XICOR data book, XICOR INC, 1996.
6. MAXIM 147 data sheet, Maxim Integrated Products, 1996.
7. MAXIM 525 data sheet, Maxim integrated Products, 1996.
8. RS Data sheet, Alpha Numeric Display, RS components, 1997.
9. MAXIM 3223 data sheet, Maxim Integrated Products, 1998.
10. National Semiconductors data sheet, MM74C922 16-key encoder, National Semiconductors Corporation, 1994.

# Chapter 8

# Conclusion and future work

## 8.1 Conclusion

The primary objective of this research was to investigate the use of a single doped $SnO_2$ resistive sensor to classify an atmospheric binary gas mixture. A thermal sinusoidal modulation technique was developed in which the first 3 Fourier coefficients were extracted. These coefficients were then used as inputs to a feed-forward neural network to determine individual gas concentrations.

A number of gas sensor technologies, signal processing and neural networks were investigated. The response of two prototype research-based silicon devices, SRL125 and IDC 10 were characterised with an automated gas sensor test system. The results were encouraging with respect to the detection of CO, $NO_2$ and using low-power consumption microheaters, 78 mW (SRL 125/MOS) and 66 mW (IDC 10) at 350 °C. These devices have a fast thermal response (~ 5 ms), which permits the use of pulsed-mode, or sinusoidal thermal modulation, which reduces the average power consumption of the heater of around ca. 1 mW. These silicon devices offer a low-cost option due to the use of a standard silicon fabrication technique, which lends itself for use in a hand-held instrument. The gas flow system including solenoid valves and flow meters were controlled using a PC software package, LabVIEW (National Instrument Inc). The software was constructed with a main virtual instrument (vi) capable of controlling the sub VIs.

The sensor signals are first analysed by applying an FFT with the resulting FFT coefficients studied. These were then normalised and prepared for input to the neural networks for further analysis. The data were trained and later a new set of data was tested with this trained network. The result was encouraging as the networks correctly classified the gas type and concentration as discussed in chapter 6. It is important to note that the humidity and the ambient temperature are of importance as these will affect the output signals of the sensors and it is for this reason that the hand-held instrument contain circuits to detect both these factors. This objective was realised as discussed in chapters 5 and 6.

The secondary objective of the research was to design a microcontroller based hand-held gas-monitoring instrument. The design of this instrument was divided into two major parts. The first part was to design the front-end analogue circuitry as detailed in chapter 7. This work involved designing stable and reliable circuitry that both drives the platinum resistive heater (nominally 200 Ω) and measures the resistance of the metal oxide sensing element over a wide dynamic range of both resistance (e.g. 10 Ω to 1 MΩ) and frequency (mHz to kHz). This circuitry was specifically designed to characterise the sensor's response to thermal modulations at different levels of target gas concentration and relative humidity. It was used extensively during the course of the research and proved to be both stable and reliable. This circuit was connected to PC via LabView virtual instrument (National Instrument,USA). The principle requirement as far as the hardware configuration is concerned was for the designed precision analogue circuit to be used with a PC. Once the characterisation, signal processing and data analysis were completed, then the analogue circuit would be incorporated in the hand-held instrument.

The second part was the digital section. This was designed and developed as described in chapter 7.

This research has shown that it is possible to produce an instrument for real-time analysis, including on-line monitoring of atmospheric gases such as CO and $NO_2$. This is of importance in applications for monitoring the natural environment. Although the research was concentrated on the detection of CO and NO2 mixture in air, it is feasible to apply the technique to other different gas mixtures.

The sinusoidal method has the advantage over the step voltage as the speed of the test is faster and it is in the region of a few seconds. The step voltage method takes about 20 minutes per step [2.24]. Also in this research the humidity effect was taken into account while in a similar research the $H_2O$ was removed from the test [4.25]. Additionally, a novelty factor in the hardware design was to design a close loop temperature/thermometer circuit.

## 8.2 Future work

Future work can be outlined as follow:

- Use of custom made ASICS devices for both the analogue and digital circuitry this will result in a smaller size and more reliable instrument.
- Development of a low cost general purpose gas monitoring or electronic nose instrument with a dedicated "calibration" software package for different gases or aromas. This "calibration" software could be downloaded by using the RS232 interface of the instrument and installed in the EEPROM.
- Development of novel neural network to improve the classification of a combination of gas mixture.

# Appendix A

## Parts list

SMART SENSOR SYSTEM - DIGITAL BOARD

| PART NO. | DESCRIPTION | QTY | NAME |
|---|---|---|---|
| LCD-16X2 | 16X2 DISPLAY | 1 | DISP1 |
| KEYPAD-16 | 4X4 KEYPAD | 1 | KP1 |
| 1M-SM1% | 1206 0.125W 1% RESISTOR | 1 | R1 |
| 12K-SM1% | 1206 0.125W 1% RESISTOR | 1 | R2 |
| 20K-3142 | 3142W SERIES SMD POT | 1 | R3 |
| 1K8-SM1% | 1206 0.125W 1% RESISTOR | 1 | R4 |
| 1K-SM1% | 1206 0.125W 1% RESISTOR | 1 | R5 |
| 18K-SM1% | 1206 0.125W 1% RESISTOR | 1 | R6 |
| 220K-SM1% | 1206 0.125W 1% RESISTOR | 1 | R7 |
| 2K2-SM1% | 1206 0.125W 1% RESISTOR | 1 | R8 |
| 100K-SM1% | 1206 0.125W 1% RESISTOR | 1 | R9 |
| 10K-SM1% | 1206 0.125W 1% RESISTOR | 2 | R10-11 |
| 68K-SM1% | 1206 0.125W 1% RESISTOR | 1 | R12 |
| 10M-1% | 0.6W MRS25 METAL FILM RESISTOR | 1 | R13 |
| 10K-SIL7 | 0.2W 7 COMMON SIL PACK | 2 | RP1-2 |
| 100NF-1206 | 50V Y5V NICKEL BARRIER CAPACIT | 10 | C1-2<br>C6<br>C10<br>C12<br>C14-15<br>C19<br>C21<br>C23 |
| 10UF-SMTANT | 16V TANTULUM CAP SMD | 2 | C3<br>C22 |
| 22PF-1206 | 100V NPO NICKEL BARRIER CAPACI | 2 | C4-5 |
| 2U2F-SMTANT | 16V TANTULUM CAP SMD | 5 | C7<br>C17<br>C24-26 |
| 1UF-SMTANT | 16V TANTULUM CAP SMD | 3 | C8-9<br>C16 |
| 4U7F-SMTANT | 16V TANTULUM CAP SMD | 2 | C11<br>C13 |
| 470NF-1206 | 25V X7R NICKEL BARRIER CAPACIT | 1 | C18 |
| 220PF-1206 | 100V NPO NICKEL BARRIER CAPACI | 1 | C20 |
| XA-G3 | 16BIT CMOS MICROCONTROLLER | 1 | U1 |
| X25128S | EEPROM SERIAL SMD | 1 | U2 |
| MAX525BCAP | 12BIT QUAD DAC | 1 | U3 |
| MAX147BCPP | 12BIT 8CH ADC | 1 | U4 |
| 74HC04M | HEX INVERTERS SMD | 1 | U5 |
| 74C922 | DARLINGTON DRIVER LOW SIDE | 1 | U6 |
| LM358M | DUAL OP AMP SMD | 1 | U7 |
| LM35CZ | TEMPERATURE SENSOR (TO92 PACKA | 1 | U8 |
| MAX3223CPP | RS232 TRANSCEIVER | 1 | U9 |
| KF50BD | 5.0V 150MA REGULATOR SMD | 1 | U10 |
| LP2966-25 | 2.5V 100MA REGULATOR SMD | 1 | U11 |
| TLC556CD | DUAL CMOS TIMER SMD | 1 | U12 |
| 29MHZ | 12MHZ CRYSTAL HC49 PACKAGE | 1 | X1 |
| 2W-JP | 2W JUMPER LINK | 1 | J1 |
| VERO | VERO PIN CONNECTION | 9 | V1-9 |

SMART SENSOR SYSTEM - ANALOGUE BOARD

| PART NO. | DESCRIPTION | QTY | NAME |
|---|---|---|---|
| SENSOR | SENSOR HEAD 14PIN DIL | 1 | U13 |
| MAX305CSE | PROG GAIN AMPLIFIER | 2 | U14-15 |
| LM318M | SINGLE OP-AMP | 1 | U16 |
| LMC6062IM | DUAL OP AMP CMOS PRECISION SMD | 1 | U17 |
| LM4040DIZ25 | PRECISION VOLTAGE REG 2.5V | 1 | U18 |
| OP27GS | SINGLE OP AMP LOW NOISE SMD | 4 | U19-22 |
| PGA205AP | PROG GAIN AMPLIFIER | 1 | U23 |
| PGA204AP | PROG GAIN AMPLIFIER | 1 | U24 |
| 22PF-1206 | 100V NPO NICKEL BARRIER CAPACI | 1 | C28 |
| 1UF-SMTANT | 16V TANTULUM CAP SMD | 14 | C29-42 |
| 100NF-1206 | 50V Y5V NICKEL BARRIER CAPACIT | 20 | C43-62 |
| 100K-3142 | 3142W SERIES SMD POT | 1 | R15 |
| 10K-3142 | 3142W SERIES SMD POT | 4 | R16-19 |
| 1M-3142 | 3142W SERIES SMD POT | 2 | R20-21 |
| 270K-SM1% | 1206 0.125W 1% RESISTOR | 1 | R22 |
| 4K7-SM1% | 1206 0.125W 1% RESISTOR | 1 | R23 |
| 20K-RN | 0.1% RN SERIES FILM RESISTOR | 1 | R24 |
| 100K-RN | 0.1% RN SERIES FILM RESISTOR | 2 | R25-26 |
| 49K9-RN | 0.1% RN SERIES FILM RESISTOR | 1 | R27 |
| 24K9-RN | 0.1% RN SERIES FILM RESISTOR | 1 | R28 |
| 4K99-RN | 0.1% RN SERIES FILM RESISTOR | 1 | R29 |
| 2K49-RN | 0.1% RN SERIES FILM RESISTOR | 1 | R30 |
| 68R-PRO2 | 2W PRO2 RESISTOR | 1 | R31 |
| 47R-PRO2 | 2W PRO2 RESISTOR | 1 | R32 |
| 1K-RN | 0.1% RN SERIES FILM RESISTOR | 1 | R33 |
| 681R-RN | 0.1% RN SERIES FILM RESISTOR | 1 | R34 |
| BD131-A | NPN TO126 POWER TRANSISTOR | 1 | Q1 |
| BD132-A | PNP TO126 POWER TRANSISTOR | 1 | Q2 |
| 2W-JP | 2W JUMPER LINK | 1 | J2 |
| 6WDIP-SMD | 6W DIL SWITCH SMD | 1 | SW1 |
| R-PLUG | PLUGGABLE RESISTOR | 1 | RPLG1 |

# Appendix B

**Schematic diagram and printed circuit layout**

HUMIDITY

TEMPERATURE

| | | | |
|---|---|---|---|
| DRAWING TITLE | | .DB REF | IG2072 A |
| SMART SENSOR SYSTEM - DIGITAL BOARD | | REV | ISSUE 1 |
| IG2072A1 CSD | | DATE | OCT 99 |

| | |
|---|---|
| DESIGNED BY | S AL-KHALIFA |
| DRAWN BY | IAN GRIFFITI |
| SHEET NO | 1 OF * |

0V TO -3V
SET VOLTAGE

CONSTANT CURRENT

SENSOR
INPUT
SOCKET

| | | | |
|---|---|---|---|
| DRAWING TITLE | JOB REF | IG2072 B | DESIGNED BY | S AL-KHAIFA |
| SMART SENSOR SYSTEM ANALOGUE BCARD | ISSUE | 1 | DRAWN BY | I GRIFFITH |
| IG2072B1 CSD | DATE | NOV 99 | SHEET NO | 1 OF 1 |

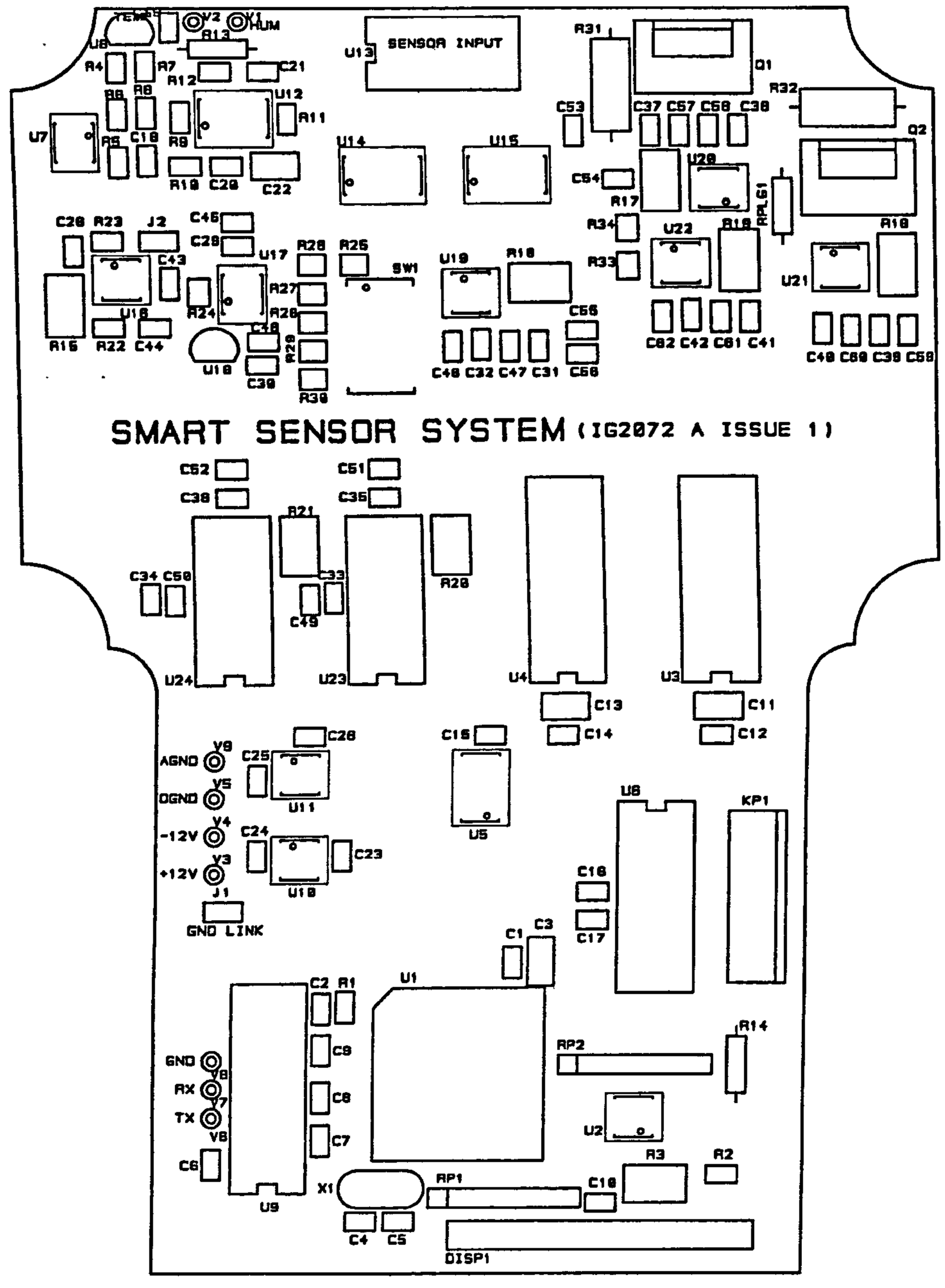
TEMP
V2
V1
HUM
U8
R13
R4
R7
R12
C21
U13
SENSOR INPUT
R31
Q1
R32
Q2
C53
C37 C57 C58 C38
R8
R8
U12
R11
U7
R5
C18
R9
U14
U15
C54
U20
R17
RPL61
R34
U22
R18
R33
U21
R18
R19
C20
C22
C26
R23
J2
C45
C28
U17
R28
R25
SW1
U19
R18
C43
R27
R24
R26
U16
C48
R29
C55
R16
R22
C44
U18
C39
R30
C40 C60 C38 C58
C62 C42 C61 C41
C48 C32 C47 C31 C56
SMART SENSOR SYSTEM (IG2072 A ISSUE 1)
C62
C38
C51
C35
R21
C34 C50
C33
C49
R28
U24
U23
U4
U3
C13
C11
C14
C12
V9
AGND
C28
C25
U11
C15
U5
V5
OGND
V4
-12V
C24
C23
V3
+12V
U18
J1
GND LINK
U8
KP1
C16
C17
C1
C3
U1
C2
R1
C9
C8
C7
GND
V8
RX
V7
TX
V6
C6
U9
RP2
R14
U2
R3
R2
X1
RP1
C10
C4
C5
DISP1

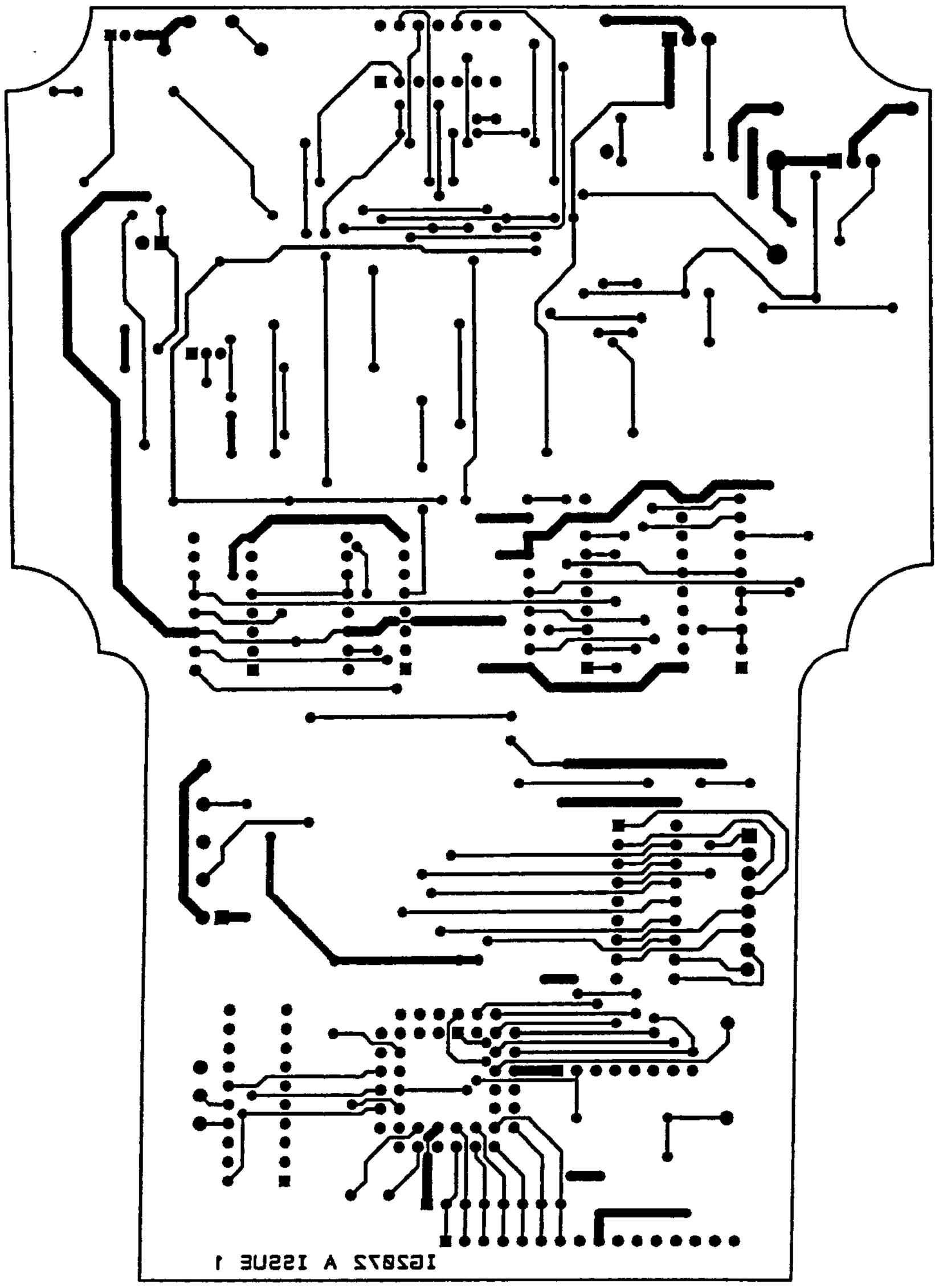
IE2872 A ISSUE 1

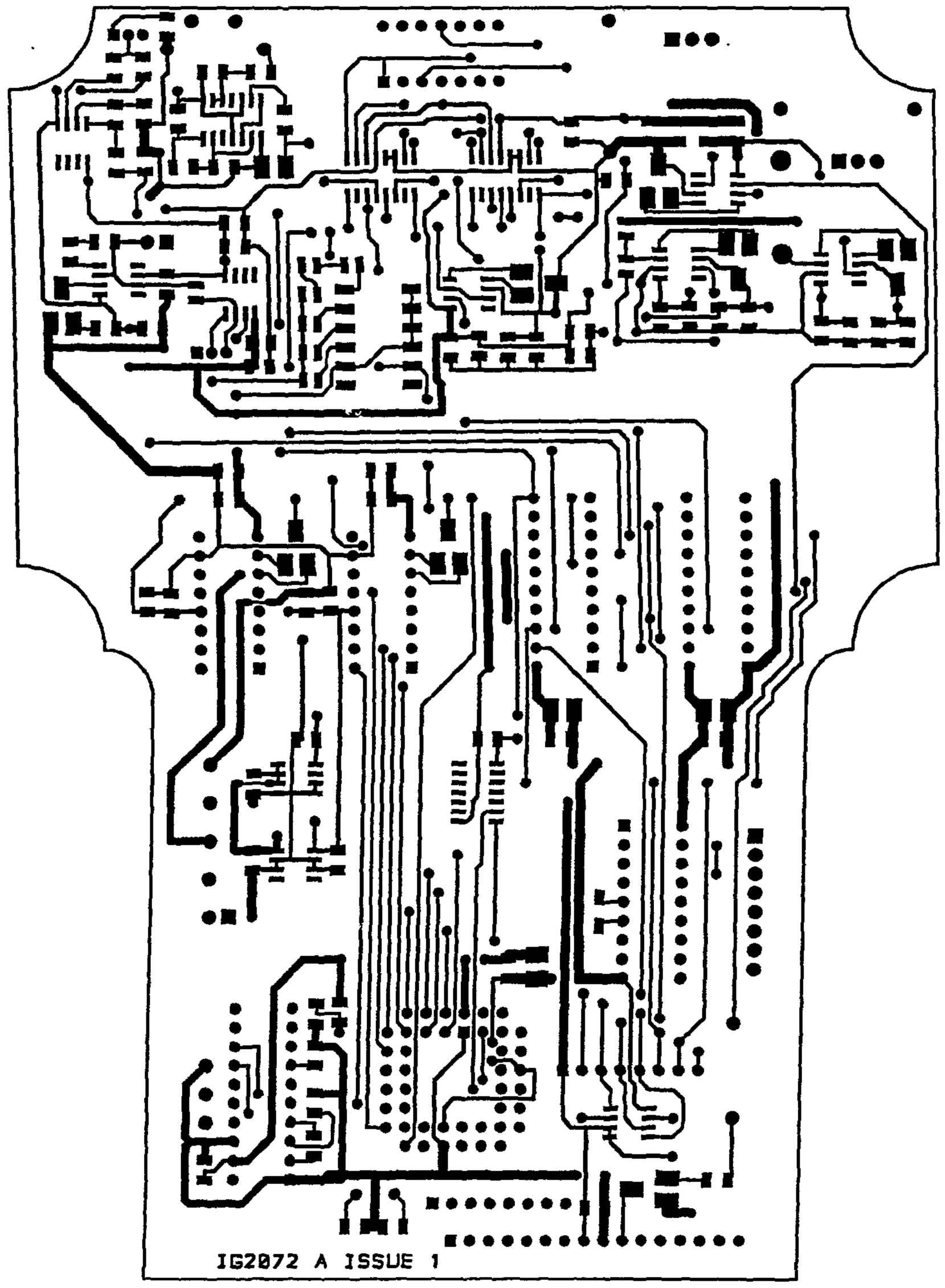
IG2072 A ISSUE 1

# Appendix C

Papers published or submitted for publication

# Characterisation of a thermal wave microsensor for the intelligent analysis of atmospheric gases

S Al-Khalifa, J W Gardner, J F Craine

Department of Engineering, University of Warwick, Coventry CV4 7AL, UK.

**Abstract.** This paper describes the characterisation of a metal oxide resistive gas sensor when subjected to d.c. and a.c. thermal fluctuations. The measurement system comprises precision analogue circuitry both to generate thermal waves in an integrated platinum resistive heater and to monitor the oxide resistance, and a virtual instrument running on a 486-based PC. Response of the microsensor to ppm levels of CO are reported with a typical operating temperature of 300°C and 10°C thermal oscillations at frequencies of up to 1 Hz. Thermal wave gas sensors are of potential application in the field of environmental monitoring because they do not require a zero-gas to define a baseline signal and can discriminate between several gases employing only one non-specific gas-sensitive coating.

## 1. Introduction

Resistive sensors have been used for many years to monitor the levels of certain combustible atmospheric gases, such as hydrogen and methane. The most successful resistive gas sensor is arguably the Taguchi gas sensor [1] which has been sold in its millions by companies such as Figaro Engineering (Japan), FiS (Japan) and more recently in a planar thick-film form by Capteur Ltd (UK). The Taguchi gas sensor consists of a thick-film of porous metal oxide lying on top of interdigitated sensing electrodes supported by a ceramic substrate under which is a platinum resistive heating coil (or film in the case of Capteur Ltd). The sensor is operated at a single temperature, typically between 300 and 500°C, in order to obtain the optimal sensitivity for the target gas. Despite the large number of Taguchi sensors sold, their application has been somewhat limited to simple alarms rather than gas monitors which require a higher level of accuracy.

One way in which the performance of these existing resistive sensors can be enhanced is to modulate the operating temperature of the gas-sensitive material (e.g. tin dioxide) and thus extract more chemical information than possible from a single gas sensor. This idea is not new and was discussed some ten years or more ago by Jones [2]. However, recent advances in microsensor technology have made this technique realisable with silicon planar devices. Reports have already been made of using a silicon micromachined version of the Taguchi gas sensor, for example see [3,4], which boast a much low power consumption (*ca.* 50 mW) than Taguchi sensors (*ca.* 800 mW). Of course this does not address the problem of a lack of specificity of the metal oxide resistive sensor, although it does permit both the construction of metal oxide sensors with a reasonably low power consumption at lower unit cost and sensor arrays running with different operating temperatures and/or catalytic materials.

A thermal wave resistive microsensor is now a practical proposition because resistive silicon sensor structures can be made with a thermal response time of the order of milliseconds [4] and run reliably at high temperatures (*ca.* 400°C). We report on the design and implementation of a measurement system required to characterise a thermal wave

microsensor. The basic structure of the microsensor is shown in Figure 1(a) with a typical membrane thickness of about 0.6 μm and an area of 250 μm by 500 μm. The operating principle is illustrated in Figure 1(b), basically, the heater element $R_{Heater}$ is electrically driven and its effect on the metal oxide resistive element $R_S$ is sensed using a constant current circuit.

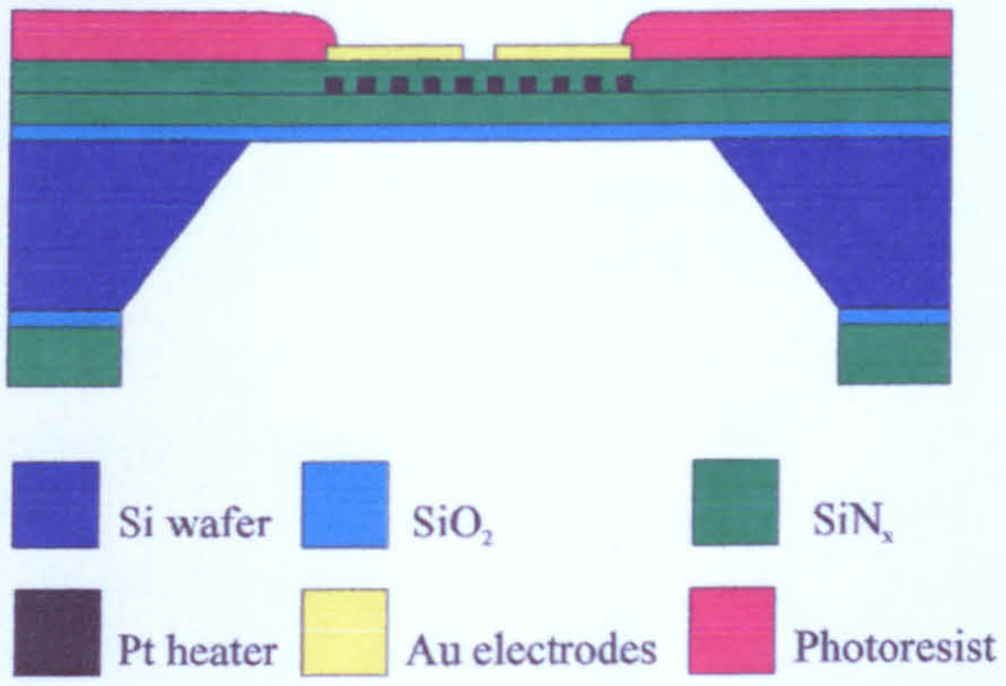


**Fig. 1(a)**: Structure of microsensor.

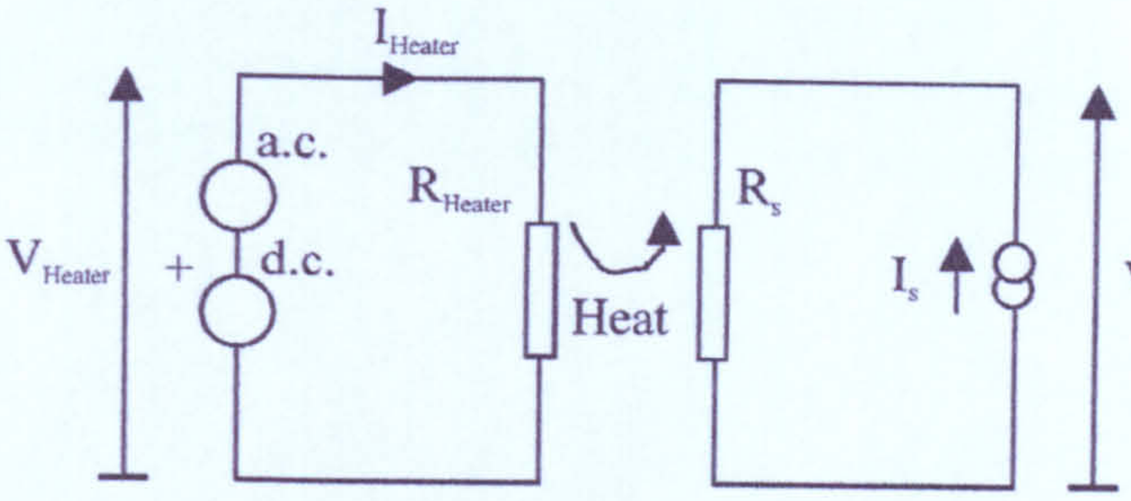


**Fig. 1(b)**: Basic measuring principle.

## 2. Design of heater drive and sensing circuitry

In order to characterise the response of the resistive sensor to thermal waves, it is essential to have stable and reliable circuitry which both drives the resistive heater (nominally 100 Ω) and measures the resistance of the metal oxide coating over a wide dynamic range of both

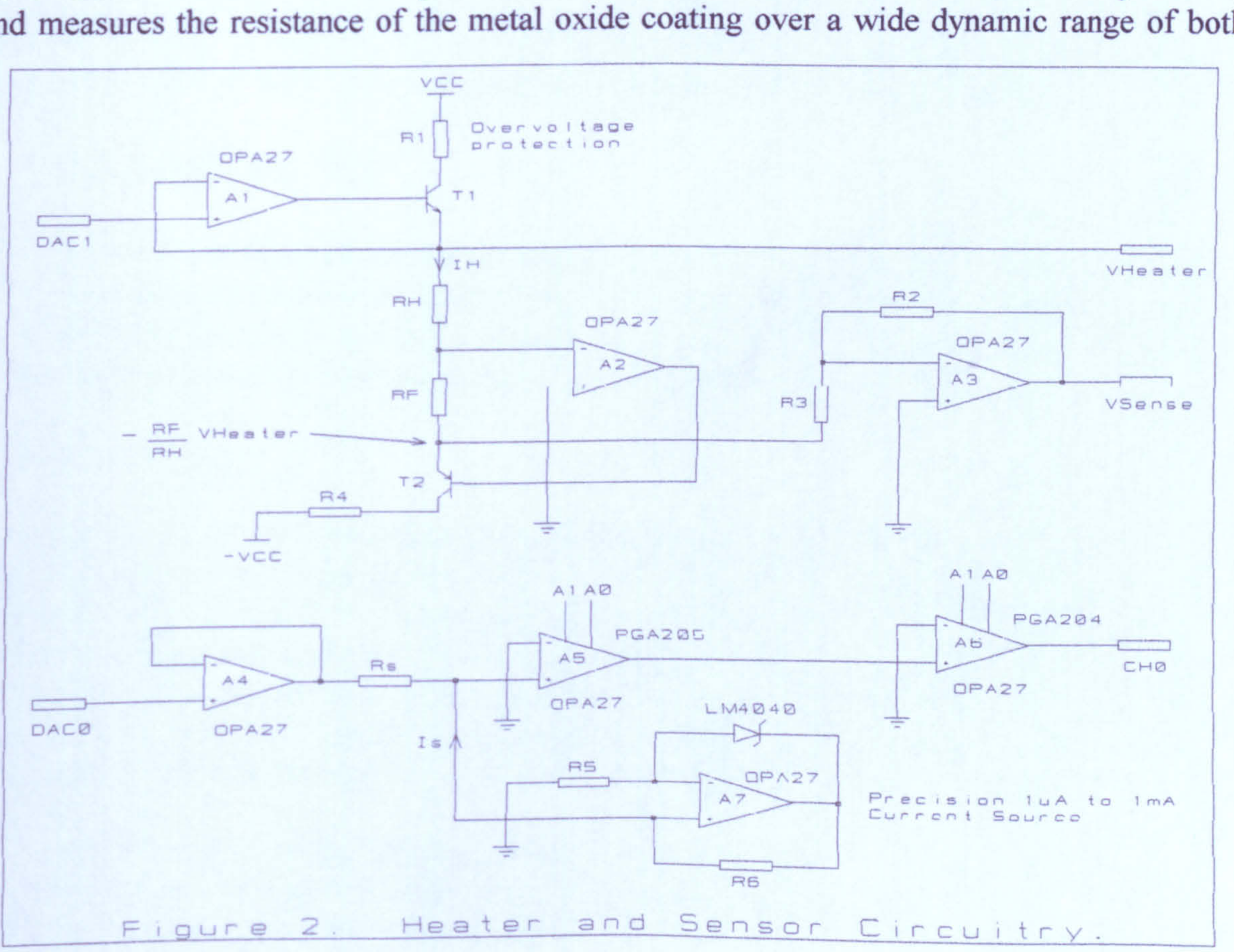


Figure 2. Heater and Sensor Circuitry.

resistance (e.g. 10 Ω to 1 MΩ) and frequency (mHz to kHz). A circuit has been specifically designed, see Figure 2, to characterise the sensor's response to thermal waves at different levels of target gas concentration and relative humidity.

In the first instance we have constructed a virtual instrument using LabView (National Instruments, USA) which runs on a 486-based PC. Figure 2 shows the circuit diagram for the measurement system which allows us to set the d.c. operating temperature of the device (via a bias voltage) and any a.c. signal, such as a step function, sine wave etc. This system can drive the heater at frequencies of up to 1 Hz and this is suitable for probing the response of resistive microsensors coated with materials with a chemical reaction time of less than 1 Hz (e.g. metal oxides).

## 3. System specification

### *3.1 Resistive heater*

The voltage across the heater, $V_{Heater}$, is set by a 12-bit ADC (Labview PC$^+$), DAC1, with the current $I_H$ is supplied by the transistor T1 and flows through the heater $R_H$ (*ca.* 200 Ω) and a precision feedback resistor $R_F$. The heater current, resistance $R_{Heater}$ and power $P_{Heater}$ can be calculated from the heater voltage and sense voltage $V_{sense}$, whence,

$$I_{Heater} = \frac{R_3 V_{Sense}}{R_2 R_F} \;;\; R_H = \frac{R_2 R_F V_{Heater}}{R_3 V_{Sense}} \text{ and } P_{Heater} = I_{Heater} \times V_{Heater} \qquad (1)$$

These values were computed in a VI running on the 486. The resistance of the platinum heater is accurately related to its temperature T in a linear manner and given by,

$$R_{Heater} = R_0\left(1 + \alpha(T - T_0)\right) \qquad (2)$$

where $R_0$ and $T_0$ are the resistance and temperature of the heater at fixed temperature, here 21°C. For a platinum resistance heater, the temperature coefficient α is constant up to at least 900°C and the linear model is accurate to about 0.1 %. Equation (2) was used to calibrate the heater and then the temperature computed with the VI.

### *3.2 Sensor resistance*

The resistance $R_S$ of the gas-sensitive coating is measured using a reference diode based circuit to generate a constant current of $I_S$ with the value set by the choice of precision resistor $R_6$ shown in Figure 2. The current is chosen so that the voltage dropped across the resistive sensor does not exceed 0.1 V and it is ohmic in nature. The voltage $V_S$ output of the sensor is first set close to zero by biassing with a voltage controlled by DAC0, and then amplified using two programmable gain amplifiers (PGA204 & PGA205). The analogue voltage output is finally fed into the 12-bit ADC as channel CH0, then filtered and recorded by the VI.

The temperature of the sensing material is assumed to be the same as the platinum heater because the thermal time-constant of the membrane is *ca.* 2 ms and our thermal modulation frequency is only 1 Hz or less. This interface circuitry was then used to

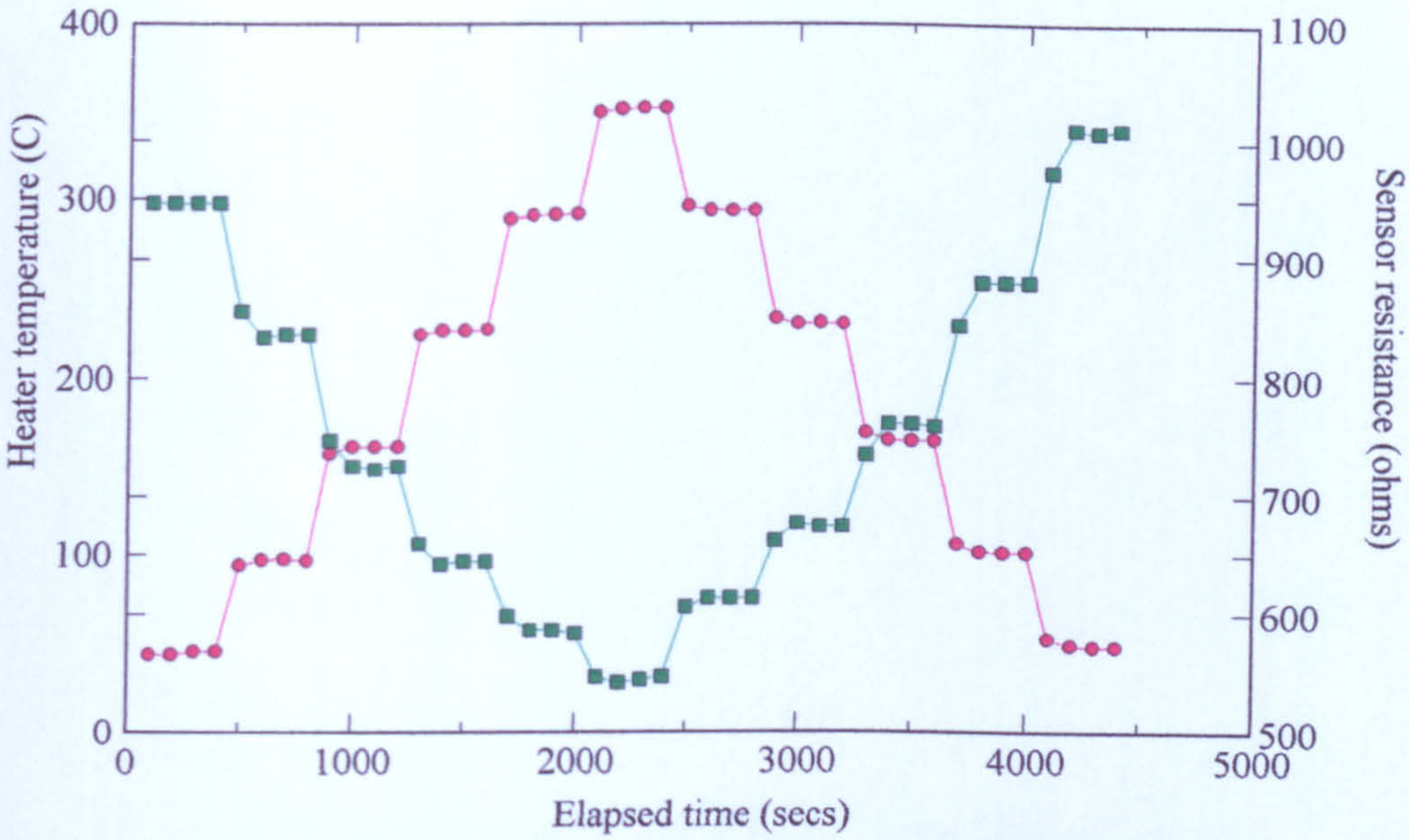


**Fig. 3**: Response of sensor resistance (squares) to step changes in heater temperature (circles).

characterise step changes and low-frequency a.c. temperature modulation of the resistive sensor. Firmware implementation is relatively straightforward because it is possible to generate the C code for this program and down-load it to a microcontroller.

## 4. Results

### *4.1 DC experiments*

Figure 3 shows a typical response of a tin oxide doped resistive sensor to a series of step increases and decreases of the heater temperature. It is evident that there is a strong correlation between the d.c. resistance of the sensor and the heater temperature and that the effect is reversible. The measurements were made in clean air with a relative humidity of 25% and a temperature of 20°C.

### *4.2 AC experiments*

Figure 4 shows the typical response of the sensor when driven at two different CO concentrations: 5 ppm of CO and 80 ppm of CO in clean air at 25% rh. The average sensor resistance falls as expected with increasing concentration and at this average operating temperature, the sensor resistance also appears sinusoidal and well-behaved.

A Fourier analysis of these signals has been carried out and Figure 5 shows a plot of the amplitude of the fundamental frequency against the CO concentration. It shows that the a.c. signal is a similar function of the CO concentration as the d.c. (base-line) signal. It has been observed previously that different spectra occur for different gases, such as $NO_2$, as well as concentrations and that these may be used to analyse multicomponent mixtures [5]. However, it is evident here that the fundamental frequency also depends upon the relative

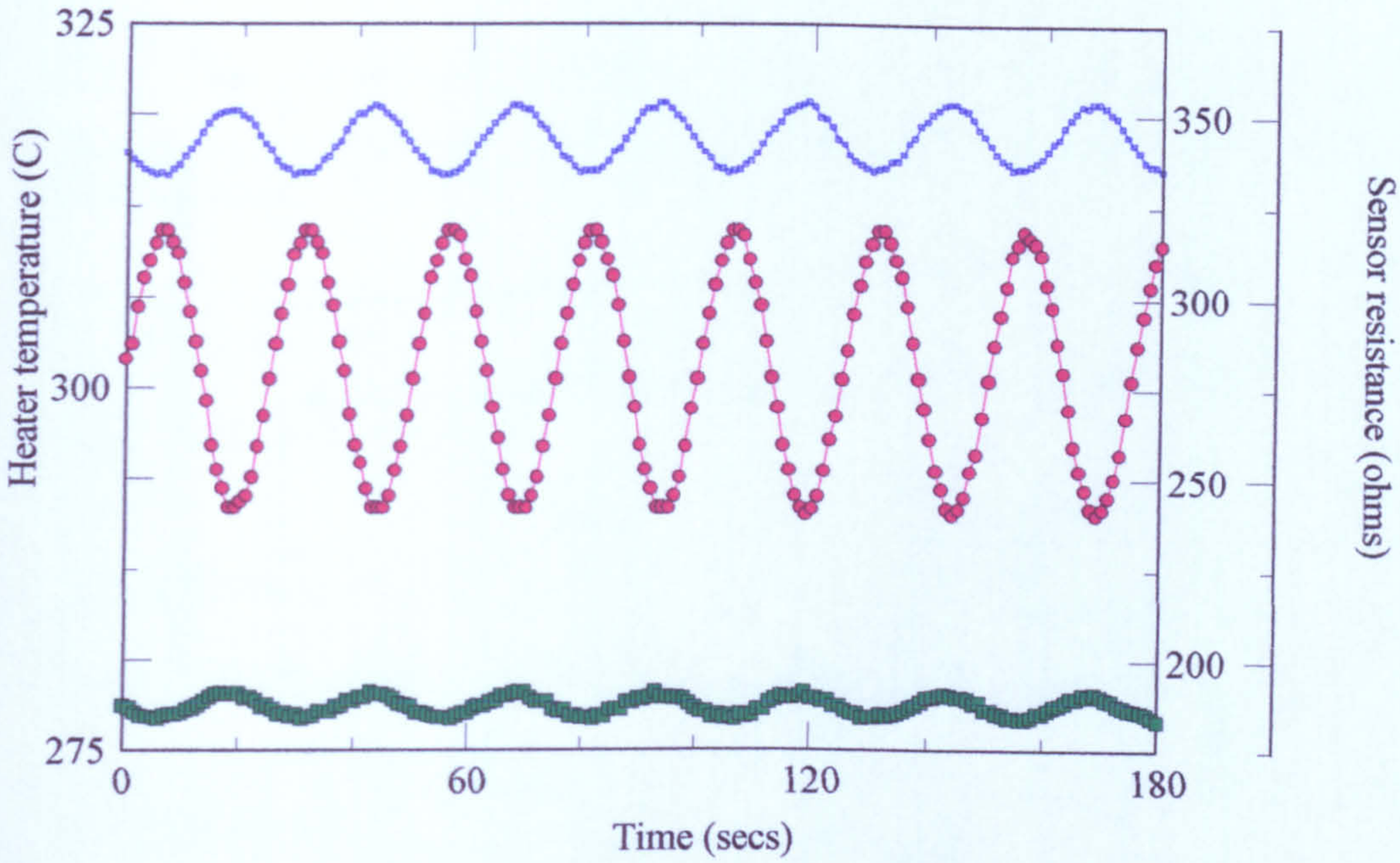


**Fig. 4:** Response of device to a.c. temperature wave (open squares) in 5 ppm (solid squares) and 80 ppm (circles) of CO in clean air at 25% rh.

humidity of the ambient air (as r.h. is increased to 75%) and so some form of signal compensation may be necessary.

## 5. Conclusion

We have designed and implemented a programmable measurement system to characterise a thermal wave microsensor for detecting CO and other atmospheric gases. A stable and versatile front-end circuitry was produced to test sensors under different parameters such as temperature, gas concentration, humidity. This system is controlled by a VI on a PC in software but the C-code can be generated and downloaded to run considerably faster on a microcontroller. The response of a metal oxide gas sensor to ppm levels of CO and $NO_2$ have been made with thermal oscillations of around 10°C at frequencies up to 1 Hz. Initial studies of the a.c. signals using Fourier analysis demonstrate an ability to discriminate between different gas types and concentrations, for example with a back-propagation neural network [5]. Further studies are being carried out to investigate the regime in which the chemical reaction kinetics are no longer in equilibrium ($f > 1$ Hz).

**Acknowledgements**

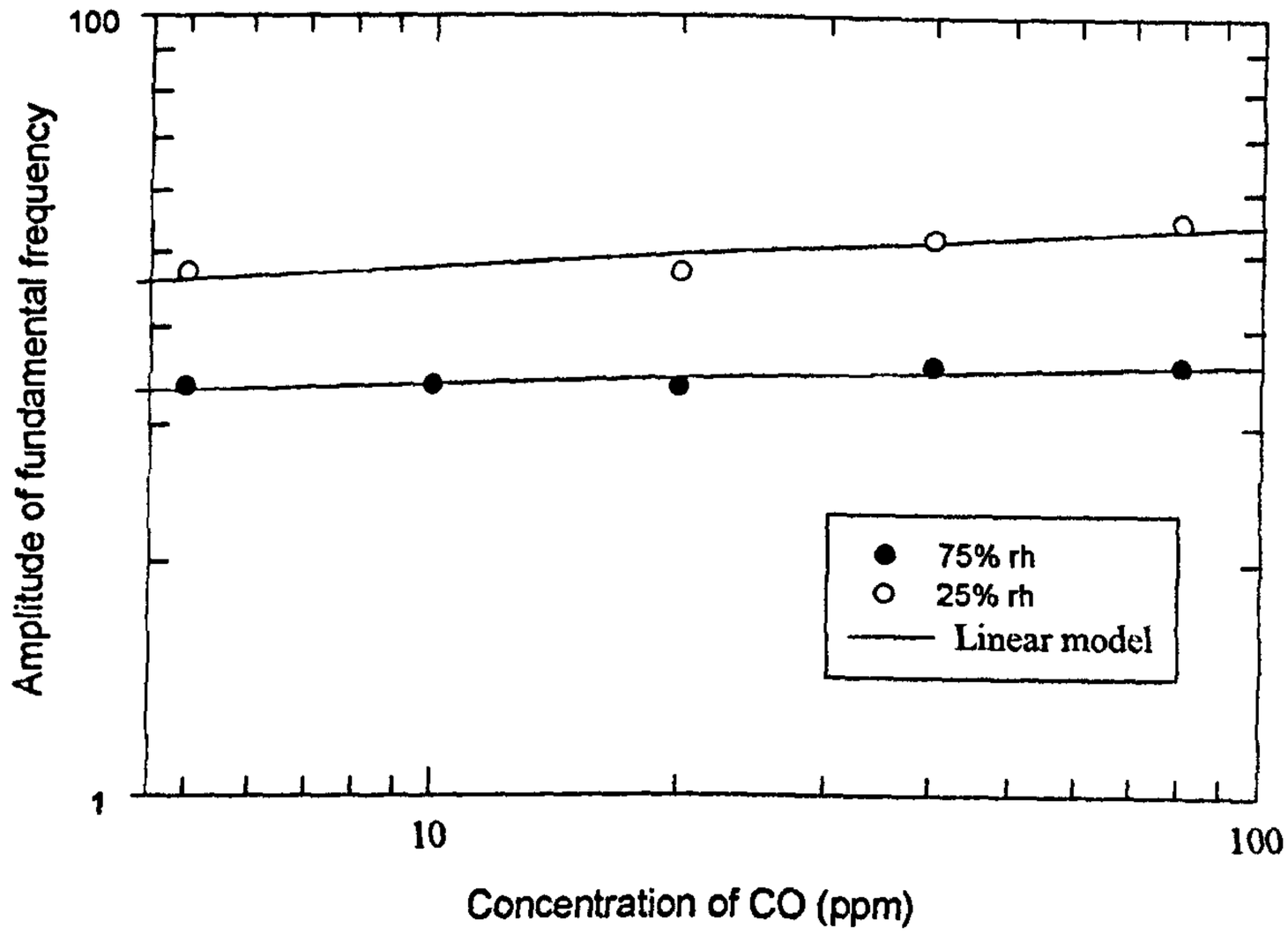


**Fig. 5**: Effect of CO concentration on the fundamental frequency of the response of resistive sensor with an average operating temperature of 250°C and ambient air at 25% and 75% rh.

The authors wish to thank Dr. Nicolae Barsan (Tuebingen University) for depositing the doped tin oxide films onto the silicon structures, and Dr. Andy Pike for work on the microsensor design.

## References

[1] K. Ihokura and J. Watson, *The stannic oxide gas sensor*. Florida: CRC Press Inc., 1994.
[2] A. Jones, Health & Saftey Executive, Sheffield, *Private communication*, 1988.
[3] J. W. Gardner, A. Pike, N. F. de Rooij, M. Koudelka-hep, P. A. Clerc, A. Hierlemann, and W. Goepel, "Integrated array sensor for detecting organic materials," *Sensors and Actuators B*, vol. 26-27, pp. 135-167, 1995.
[4] A. C. Pike, "Design of microresistive silicon sensors for application in gas sensing," in *Engineering*. Coventry: Warwick, 1996, pp. 268.
[5] A. Heilig, N. Barsan, U. Weimar, M. Schweizer-Berberich, W. Goepel amd J. W. Gardner, "Gas identification by modulating temperatures of tin dioxide based thick film gas sensors, *Eurosensors X, Leuven, Belgium, 9-11 September 1996.*

**1. Title:**

Identifying atmospheric CO and $NO_2$ using a single thermally modulated resistive microsensor.

**2. Submitted to:**

***IEE – Sci. Meas. Technol.***

**3. Authors:**

Sherzad Al-Khalifa[a], Julian W. Gardner[a], Nicolae Bârsan[b]

**4. Affiliations:**

[a]School of Engineering
University of Warwick
Coventry CV4 7AL,
United Kingdom
[b]Institute of Physical Chemistry
University of Tübingen,
Auf der Morgenstelle 8
72076 Germany

**5. Address for correspondence:**

Prof. Julian W. Gardner
Sensors Research Laboratory
School of Engineering
University of Warwick
Coventry, CV4 7AL
United Kingdom

Tel: +44 (0) 24 76 523695
Fax: +44 (0) 24 76 418922
E-mail: J.W.GARDNER@WARWICK.AC.UK
Web: www.eng.wrwick.ac.uk/SRL

Date: July 2000
File: IEE_MST_tms 3.doc

# Identifying atmospheric CO and $NO_2$ using a single thermally modulated resistive microsensor

Sherzad Al-Khalifa[a], Julian W. Gardner[a1], Nicolae Barsan[b]

[a]*School of Engineering, University of Warwick, Coventry CV4 7AL, UK.*
[b]*Institute of Physical Chemistry, University of Tübingen, Auf der Morgenstelle 8 72076, Germany*

**Abstract**

This paper describes a novel method of identifying the binary mixture of CO and $NO_2$ gases in air from the response of a single thermally modulated resistive tin dioxide gas sensor. The measurement system comprises precision analogue circuitry and a virtual instrument running on a PC - both to generate a thermal wave via an integrated platinum resistive micro-heater and to measure the resulting a.c. resistive signal. Responses of the microsensor to ppm levels of CO and $NO_2$ are measured with the average operating temperature set to 300°C and the amplitude and frequency of the thermal oscillation set to 100°C and 50 mHz, respectively. The first three Fourier components of the response are fed into a trained back-propagation neural network for concentration prediction. This thermally modulated gas sensor is particularly attractive for monitoring hazardous levels of pollutants in air because it does not require a stable baseline signal and can identify several gases using only a single gas sensor.

**Key words:** Gas sensors, microsensors, CO detection

---

[1] Author to whom all correspondence is addressed.

## 1. Introduction

Over the last two decades tin dioxide ($SnO_2$) has become the predominant solid-state material to be used in low-cost gas alarms for commercial and industrial applications [1]. A large variety of different thin-film and thick-film metal oxide have been researched over the past ten years with usually an empirical ('trial and error') optimisation of their performance [2]. The well-known advantages of using resistive-type $SnO_2$ gas sensors are their low cost and high sensitivity. Their main disadvantage is a lack of long term stability and relatively poor specificity [3]. In order to overcome these disadvantages, several approaches have been made with limited success, such as operating at different temperatures, choosing different annealing procedures, adding catalytic metals etc. An alternative approach has been to constructs an array of non-specific gas sensors coupled with a pattern recognition (PARC) technique in order to enhance the gas specificity or detect mixtures of gases. Here the approach is quite different, namely to modulate the operating temperature of a single gas sensor to use exploit differing reaction kinetics. Even the relationship between the steady-state response of a tin oxide gas sensor and temperature is a complex and non-linear. Consequently, no attempt is made here to determine an analytical solution to the problem. However, a detailed discussion of the problem is provided in reference [7] while it is assumed here that small perturbations in temperature could be approximated with a linear model.

The basic structure of our micro-machined planar resistive gas sensor is shown in Figure 1(a) with a membrane thickness of about 0.6 μm and an active (hot) area of 250 μm by 500 μm.[2] The operating principle is illustrated in Figure

[2] The device was fabricated at the Institute of Neuchatel, Switzerland.

1(b), in which the heater element of resistance $R_{Heater}$ is electrically driven and its effect on the resistance of the metal oxide film $R_S$ is sensed using a constant current circuit [4].

We report here on this novel approach to detect the composition of a binary gas mixture; a technique that could equally be applied to conventional (e.g. TGS [3]) as well as micromachined gas sensors.

## 2. Design of heater drive and sensing circuitry

In order to characterise the response of the resistive sensor to thermal modulation, it was essential to design a stable and reliable circuitry that both drives the resistive heater (nominally 200 Ω) and measures the resistance of the metal oxide coating over a wide dynamic range of both resistances (e.g. 100 Ω to 1 MΩ) and frequencies (e.g. mHz to kHz). We have already reported at a conference the details of the precision op-amp circuitry shown in Figure 2 [4] and the construction of a virtual instrument using LabView (National Instruments, USA), which runs on a PC. Here we present the results of our main experiments.

## 3. Virtual instrument design

A programmable virtual instrument (VI) was designed using the commercial software Labview (National Instruments) for controlling the frequency and amplitude of the thermal modulation of the platinum micro-heater, the total number of samples taken per cycle of the resistive film, and the temperature setting. The front panel is shown in Figures 3 and 4 with the DACs setting the inputs seen in Figure 2.

## 4. Experimentation

A layer of Pd-doped $SnO_2$ was deposited using a micro-pipette onto the surface of the silicon sensor and subsequently annealed. Full details of this work have been published elsewhere [6]. The tin dioxide microsensor was exposed to a controlled gas mixture of CO and $NO_2$ and raw data were collected using LabView in a file with all the related attributes, such as sensor type, frequency, and temperature setting. Initially the sensor was tested for its response to single components of CO, and then $NO_2$. It was then shown that the sensor was behaving as expected. A typical sample response to CO is shown in Figure 5. The sensor's d.c. resistance is seen to fall as the target gas (CO) concentration increases at 25% rh with a thermal modulation of 100 °C at 50 mHz. The sensor response appears sinusoidal and behaves as expected for a normal d.c. device.

## 5. Fourier analysis of signals

The first three Fourier coefficients were extracted using the software MATLAB and the function FFT. The amplitude of the first coefficient has been plotted in Figure 6 against the concentration of CO in air at 25% rh. The effect of increasing the r.h. to 75% can also be seen. Numerous experiments were made to determine the effect of the thermal modulation frequency and amplitude upon the CO and $NO_2$ Fourier coefficient isotherms and to optimise the settings. Further details may be found in reference [7].

## 6. Single and Binary gas target allocation

The actual concentrations of the CO and $NO_2$ concentrations in the single and binary mixtures and the analogue target values used in the neural computation are

given in Table 1a and 1b. The target value for the concentration was assigned by using the following equation

$$\text{Target} = \left[\frac{2c}{C_{\max}} - 1\right]$$

Where $C$ is concentration of interest, $C_{max}$ is the maximum CO concentration in ppm e.g. 130 ppm. From this equation the target gas concentrations are computed as shown in Table 1. The single gas and binary mixture data and the target values are plotted in Figures 7a and 7b and lie on a straight line.

## 7. Neural network analysis and results

A MATLAB program was designed in order to facilitate data processing, plotting and applying the back-propagation neural network. The user interface of this program is shown in Figure 8.

The three Fourier coefficients obtained from the tests for each binary CO and $NO_2$ gas mixture as described earlier were used as the input to a two-layer perceptron neural network, see Figure 9. The output later consists of two analogue processing elements, one for each gas type. 10% of the data set was first removed randomly for later testing. The remaining 90% of the data were then used to train the network using the delta learning rule and back-propagation algorithm. Finally, the unknown 10% of the data-set was entered as the input into to the trained network for cross-validation. The output of the neural networks can then be used to compute the predicted gas concentrations.

## 8. Identification of binary gas mixtures

The gases were produced by a fully automated test mixing controlled amounts of CO and $NO_2$ concentrations [7]. The binary gas data was then fed into the neural network to be trained and tested as described in the previous section. Figure 10 shows that the predicted concentration of CO only is quite accurate in a single component. A similar result was observed for NO (not shown). Figure 11 shows a plot of $NO_2$ gas concentration in ppm against the CO gas concentration in ppm. The calibrated (training) binary mixture data are well behaved and found to lie reasonably close to the target points. The predicted (tested) values are also well behaved. These preliminary results show that it is possible to identify the constituents of a binary gas mixture as well as its concentrations with an accuracy of about 10%.

## 9. Conclusion

In this work our results show it is possible to identify the constituents of a binary gas mixture of CO and $NO_2$ using only a single $SnO_2$ gas sensor and a linear frequency (FFT) decomposition technique.

Large numbers of gas sensing array systems has been developed for the field of artificial olfaction – so-called electronic noses [8]. There is some possibility that this approach could be applied to the discrimination of simple odours. However, there may be a problems in certain applications of the complexity of the quantitative relationship between chemical composition and sensor response. The main problem is due to non-linearity of the response of the sensor to the constituent gases. However, our approach may be improved upon for more challenging applications through the use of a *non-linear* signal/data processing technique that replaces the fourier transform, such as wavelet theory or time series methods.

## References

[1] R. E. Cavicchi, J. S. Suehle, K.G. Kreider, M. Gaitan and Chaparala, 'Optimised temperature pulse sequences for the enhancement of chemically-specific response patterns from micro-hotplate gas sensors', Conf. Proc. Transducers' 95 and Eurosensors IX 1995 Stockholm. pp 823-826

[2] W. Göpel, K. D. Schierbaum. '$SnO_2$ Sensors: current status and future prospects', Sensors and Actuators B 26-27 (1995) pp 1-12

[3] K Ihokura, J Watson.: 'Stannic Oxide Gas Sensors, Principles and Applications' (CRC Press, Boca Raton FL, 1994)

[4] S, A-Khalifa, J. W. Gardner, J. F. Craine. 'Characterisation of a Thermal Wave Microsensor for Intelligent Analysis of Atmospheric Gases'. Sensors and their Applications VIII, 1997 Glasgow, pp. 89-94

[5] S. Nakata, S. Akakabe, M. Nakasuji, K. Yoshikawa, 'Gas sensing based on a non-linear response', Anal. Chem., 1996, pp2067-2072

[6] N. Barsan and U. Weimar, Proceedings of Eurosensors, Southampton, 1999.

[7] J. W. Gardner, P. N. Bartlett, Electronic noses: principles and applications, Oxford University Press, 1999.

[8] S. Al-Khalifa, PhD thesis, University of Warwick (submitted).

Table 1a. Single gas and its corresponding target values.

| CO concentration (ppm) | Target value |
|---|---|
| 0 (no gas) | -1 |
| 20 | -0.69 |
| 40 | -0.38 |
| 80 | 0.23 |
| 130 | +1 |

Table 1b. Binary gas mixture and the corresponding target values.

| Binary gas mixture (CO and $NO_2$) ppm | Target |
|---|---|
| 0 (no gas) | (-1, -1) |
| 20 (CO) 10 ($NO_2$ ) | (0.69, -0.67) |
| 40 (CO) 20 ($NO_2$ ) | (-0.38, –0.33) |
| 80 (CO) 40($NO_2$) | (0.23, 0.33) |
| 130 (CO) 60 ($NO_2$) | (1, 1) |

**Captions to Figures:**

Figure 1 (a) Cross-section of the silicon micro-machined resistive gas sensor (the tin oxide layer is not shown). (b) Basic circuit design: a heater drive voltage $V_{heater}$ modulates the temperature of the tin oxide film. Its resistance $R_s$ being measured in a constant current $I_s$ circuit.

Figure 2 Schematic layout of the op-amp circuitry for the thermally modulated resistive gas sensor.

Figure 3 Virtual instrument front panel showing the circuit parameters that can be set manually.

Figure 4 Virtual instrument wiring circuit diagram for the thermally modulated resistive gas sensor.

Figure 5 Plot of response of the Pd-doped $SnO_2$ gas sensor to 20, 40, 80, 130 ppm of CO at an average temperature modulation of 310°C (varying from 410 °C to 240 °C).

Figure 6 Plot of the amplitude of the fundamental frequency |A| against CO concentration (ppm) at three different temperatures and two relative humidity's, diamond (200°C, 25% rh) and large square (200°C, 75% rh), small square (250°C, 25% rh) and small dash (250°C, 75% rh) triangle (300°C, 25% rh) and circle (300°C, 75% rh) and all at 1 Hz modulation.

Figure 7 Plot of (a) single gas and (b) the binary gas concentrations against the target values.

Figure 8 User interface for data analysis using MATLAB software.

Figure 9 Schematic diagram of a fully connected three layers MLP with 3 inputs, 2 hidden neurones in a single hidden layer, and 2 output neurones.

Figure 10 Plot of the concentrations of CO in a single component gas calculated from the training (known) data set and test (unknown) data set. Perfect classification would results in all the points lying upon a straight line.

Figure 11 Plot of the concentrations of CO and $NO_2$ in a binary mixture calculated from the training (known) data set and test (unknown) data set. Perfect classification would results in all the points lying upon a straight line.

Figure 1

(a)

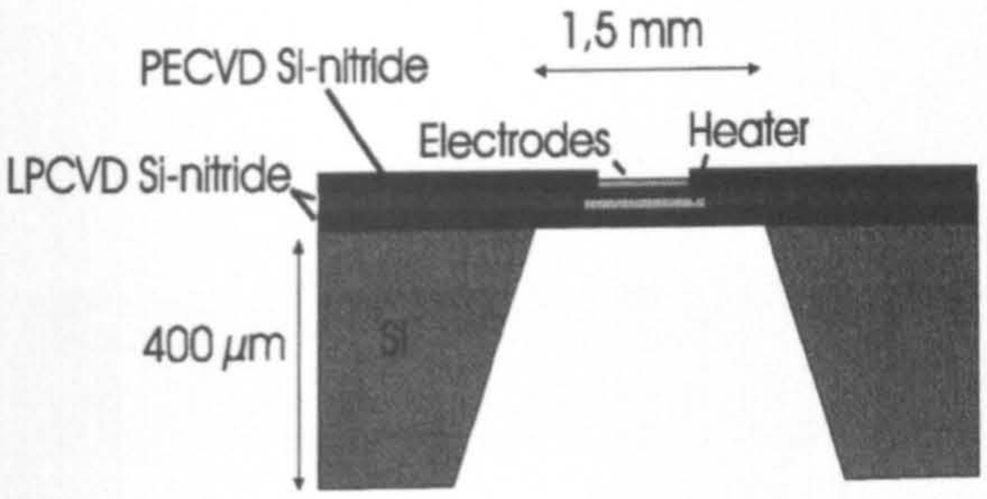
1,5 mm
PECVD Si-nitride
Electrodes
Heater
LPCVD Si-nitride
400 μm
Si

(b)

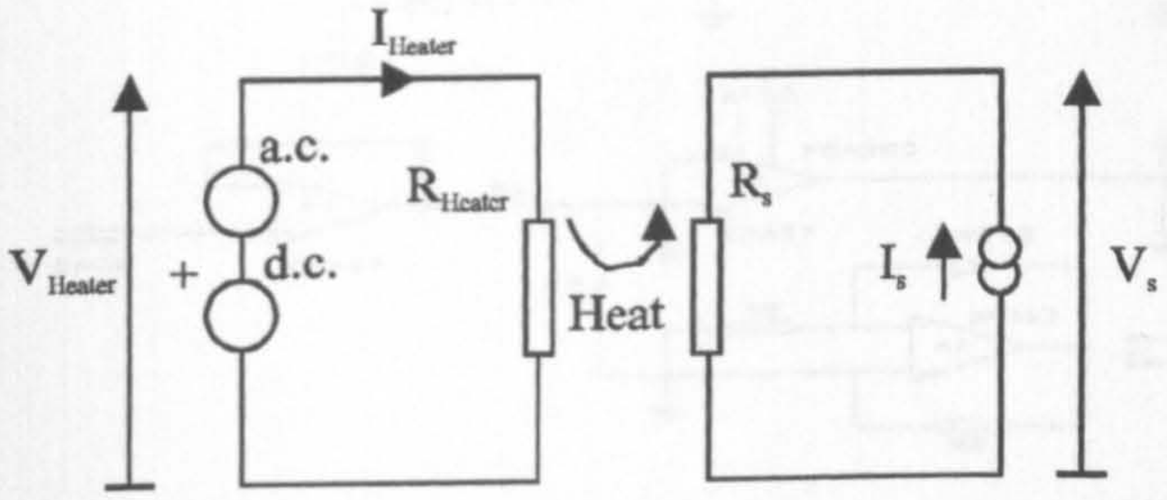
I Heater
a.c.
R Heater
V Heater
+
d.c.
Heat
R s
I s
V s

Figure 2

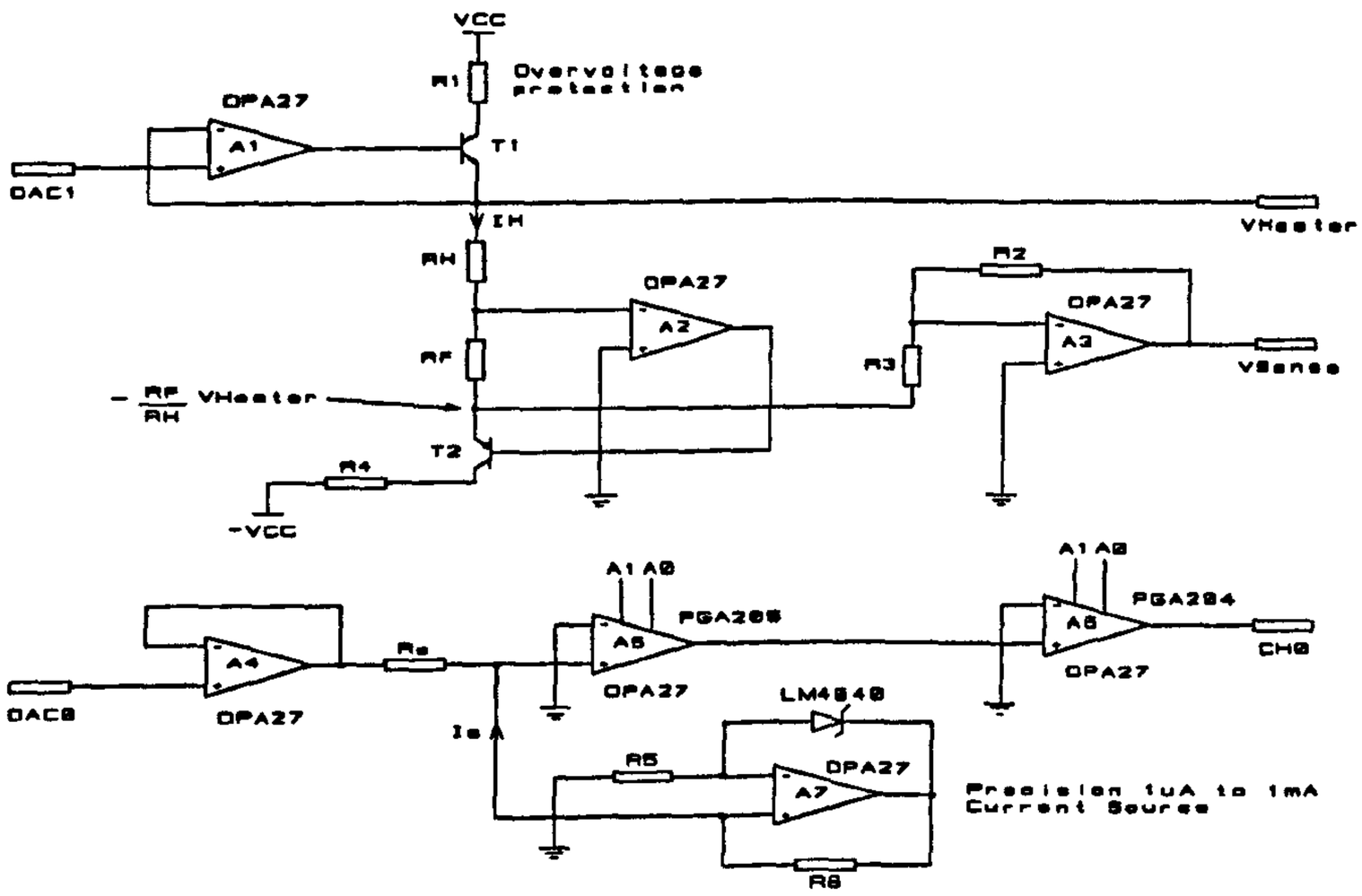
VCC
R1
Overvoltage protection
OPA27
A1
T1
DAC1
IH
VHeater
RH
OPA27
A2
RF
R2
OPA27
A3
R3
VSense
- RF/RH VHeater
T2
R4
-VCC
A1 A0
PGA206
A4
Rs
A5
OPA27
OPA27
DAC0
OPA27
LM4040
Is
R5
OPA27
A7
Precision 1uA to 1mA Current Source
R6
A1 A0
PGA204
A6
OPA27
CH0

Figure 3

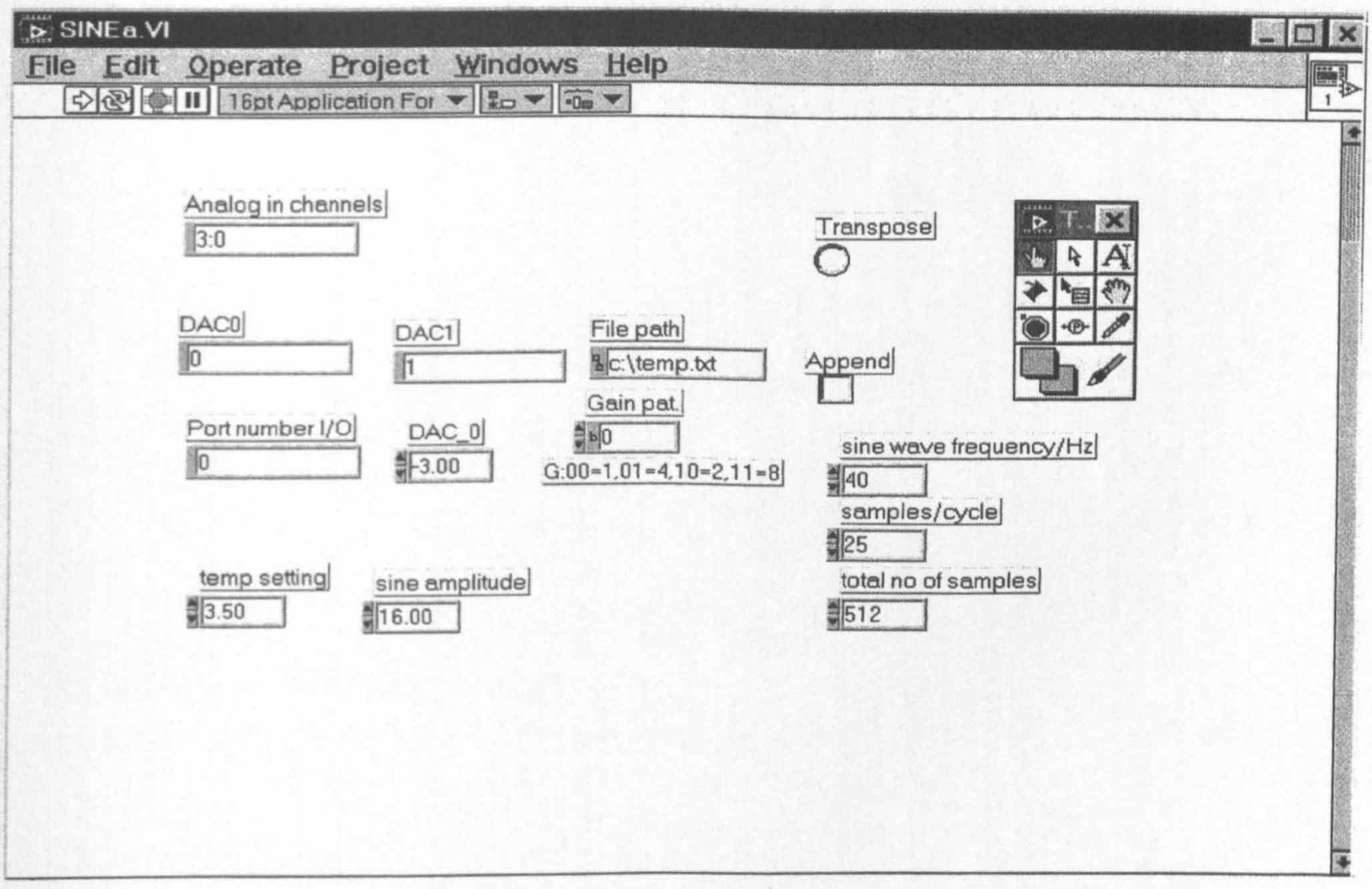
SINEa.VI
File Edit Operate Project Windows Help
16pt Application For
Analog in channels
3:0
Transpose
DAC0
0
DAC1
1
File path
c:\temp.txt
Append
Gain pat.
Port number I/O
0
DAC_0
-3.00
0
G:00=1,01=4,10=2,11=8
sine wave frequency/Hz
40
samples/cycle
25
temp setting
3.50
sine amplitude
16.00
total no of samples
512

Figure 4

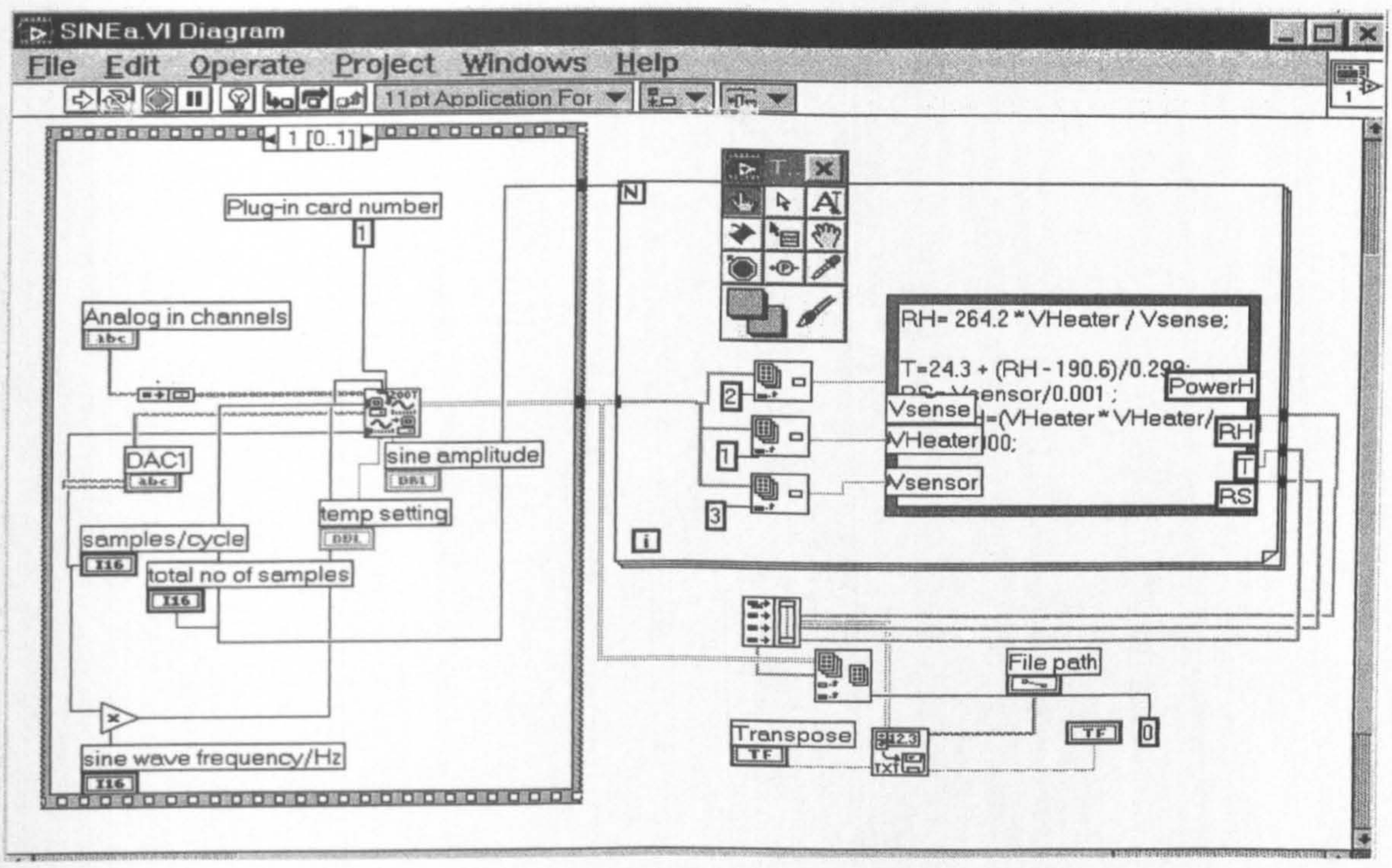
SINEa.VI Diagram
File Edit Operate Project Windows Help
11pt Application For
1 [0..1]
Plug-in card number
Analog in channels
DAC1
sine amplitude
temp setting
samples/cycle
total no of samples
sine wave frequency/Hz
RH= 264.2 * VHeater / Vsense;
T=24.3 + (RH - 190.6)/0.29
Vsense
VHeater
Vsensor
PowerH
RH
T
RS
File path
Transpose
TF

**Figure 5**

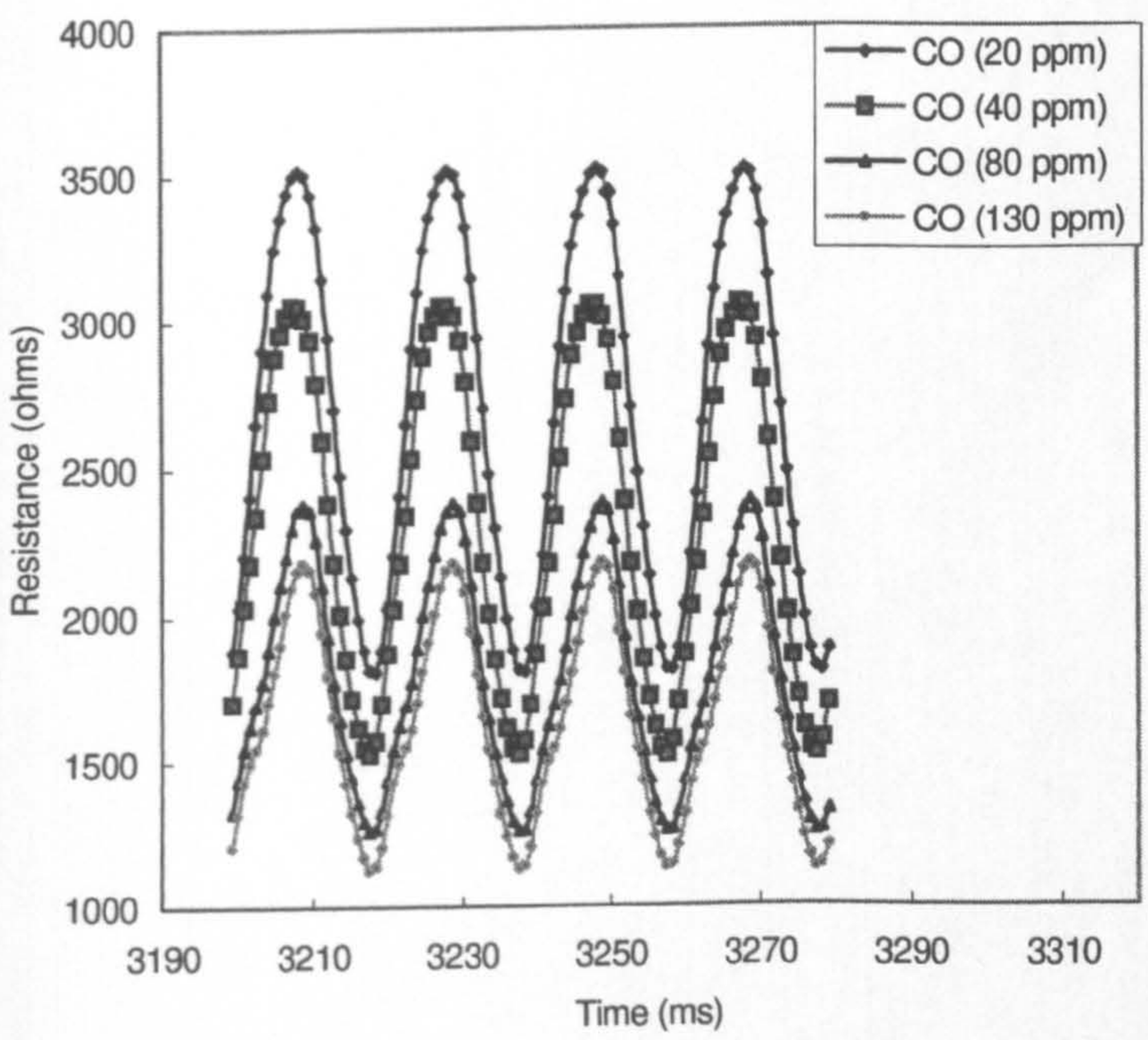
CO (20 ppm)
CO (40 ppm)
CO (80 ppm)
CO (130 ppm)
Resistance (ohms)
4000
3500
3000
2500
2000
1500
1000
3190
3210
3230
3250
3270
3290
3310
Time (ms)

**Figure 6**

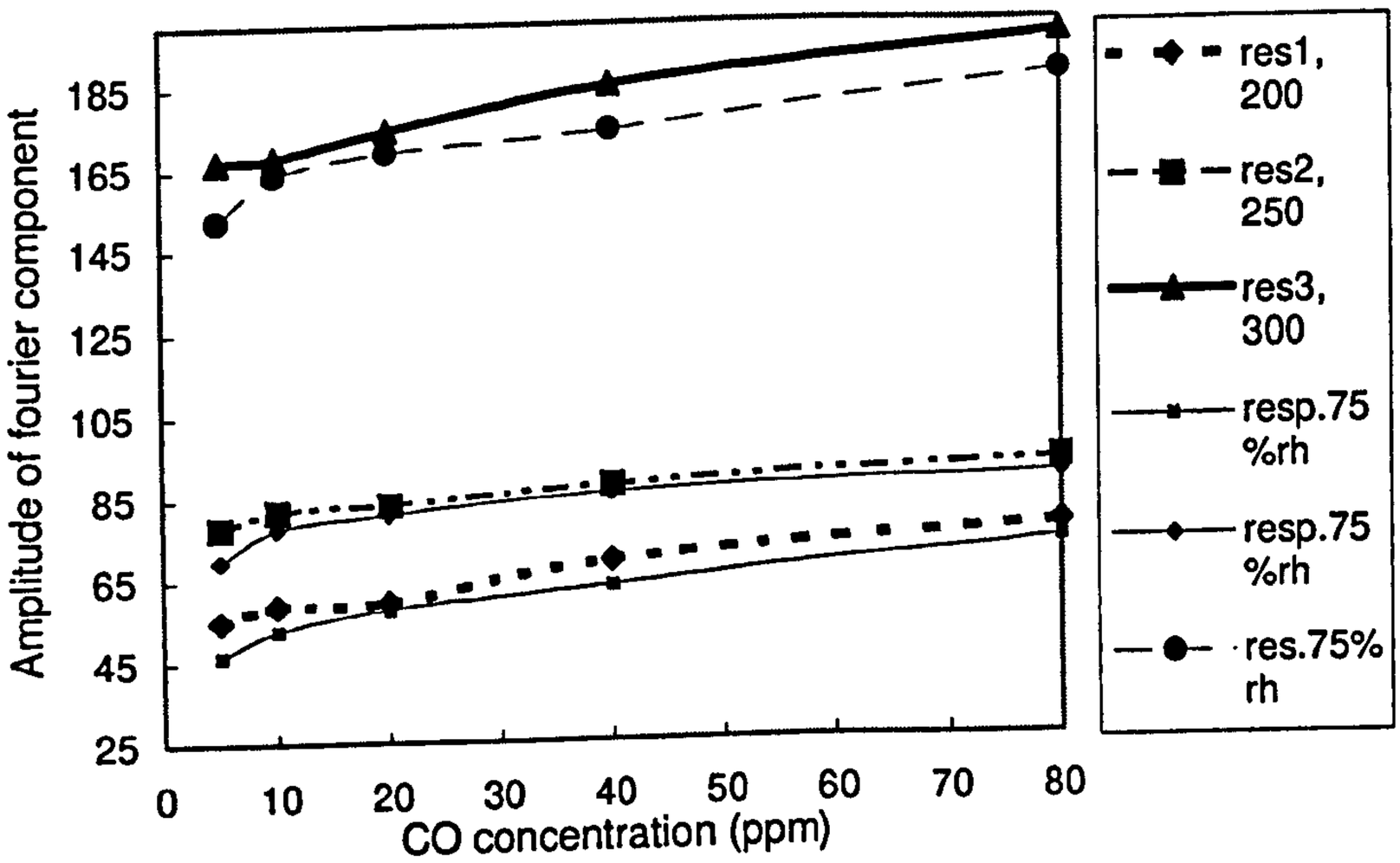
Amplitude of fourier component
185
165
145
125
105
85
65
45
25
0
10
20
30
40
50
60
70
80
CO concentration (ppm)
res1, 200
res2, 250
res3, 300
resp.75 %rh
resp.75 %rh
res.75% rh

Figure 7

(a)

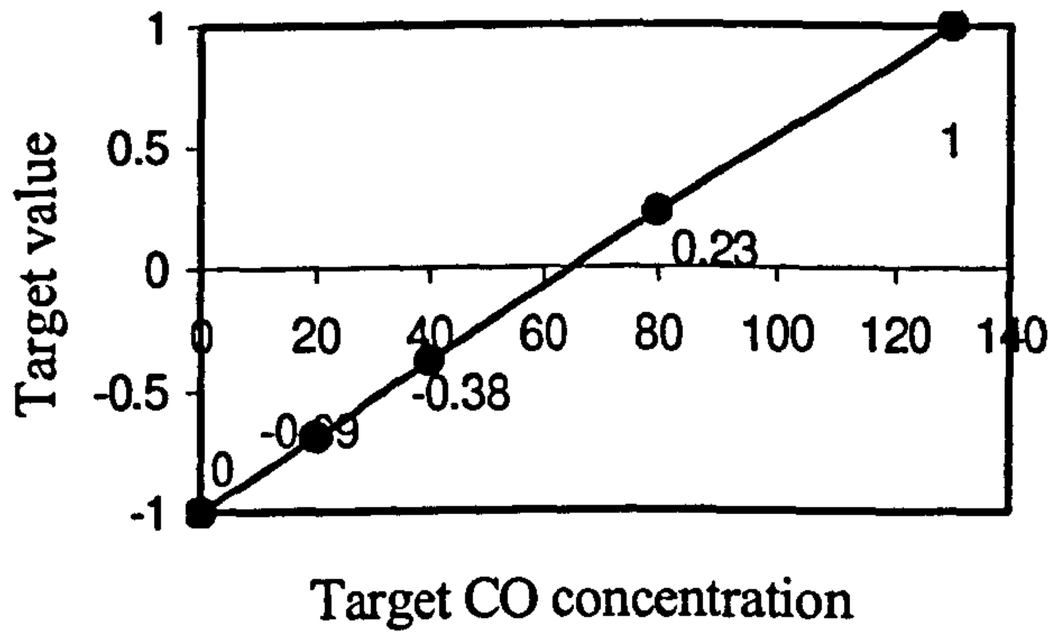
1
0.5
0
-0.5
-1
0
20
40
60
80
100
120
140
0
-0.09
-0.38
0.23
1
Target value
Target CO concentration

(b)

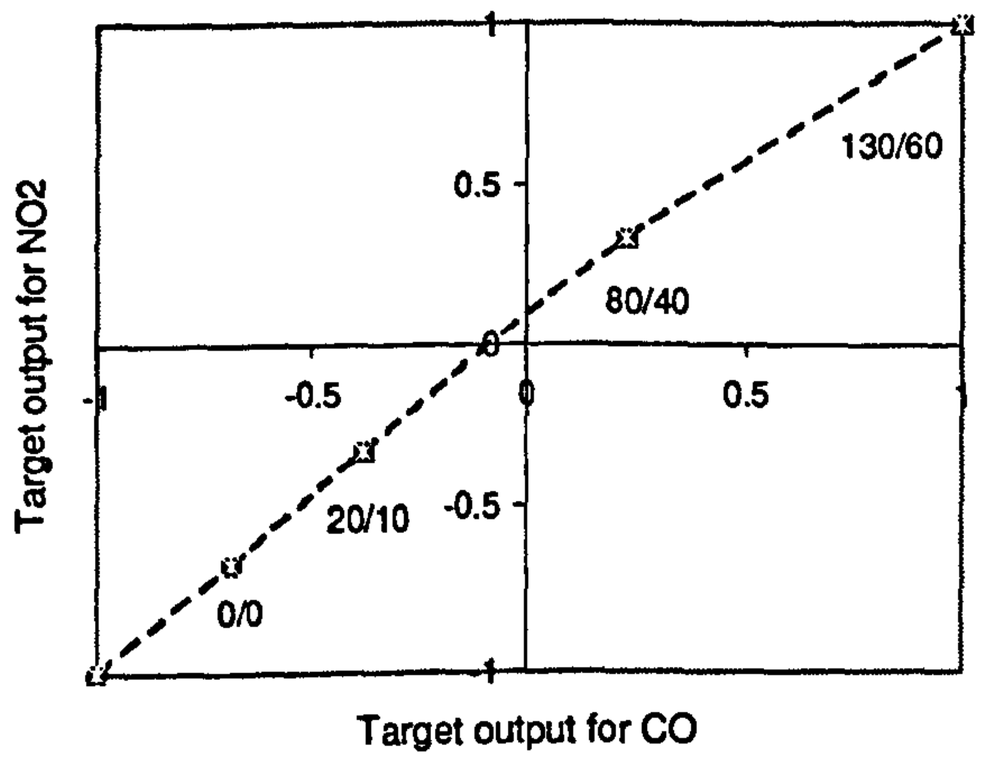
1
0.5
0
-0.5
-1
-0.5
0
0.5
1
0/0
20/10
80/40
130/60
Target output for NO2
Target output for CO

**Figure 8**

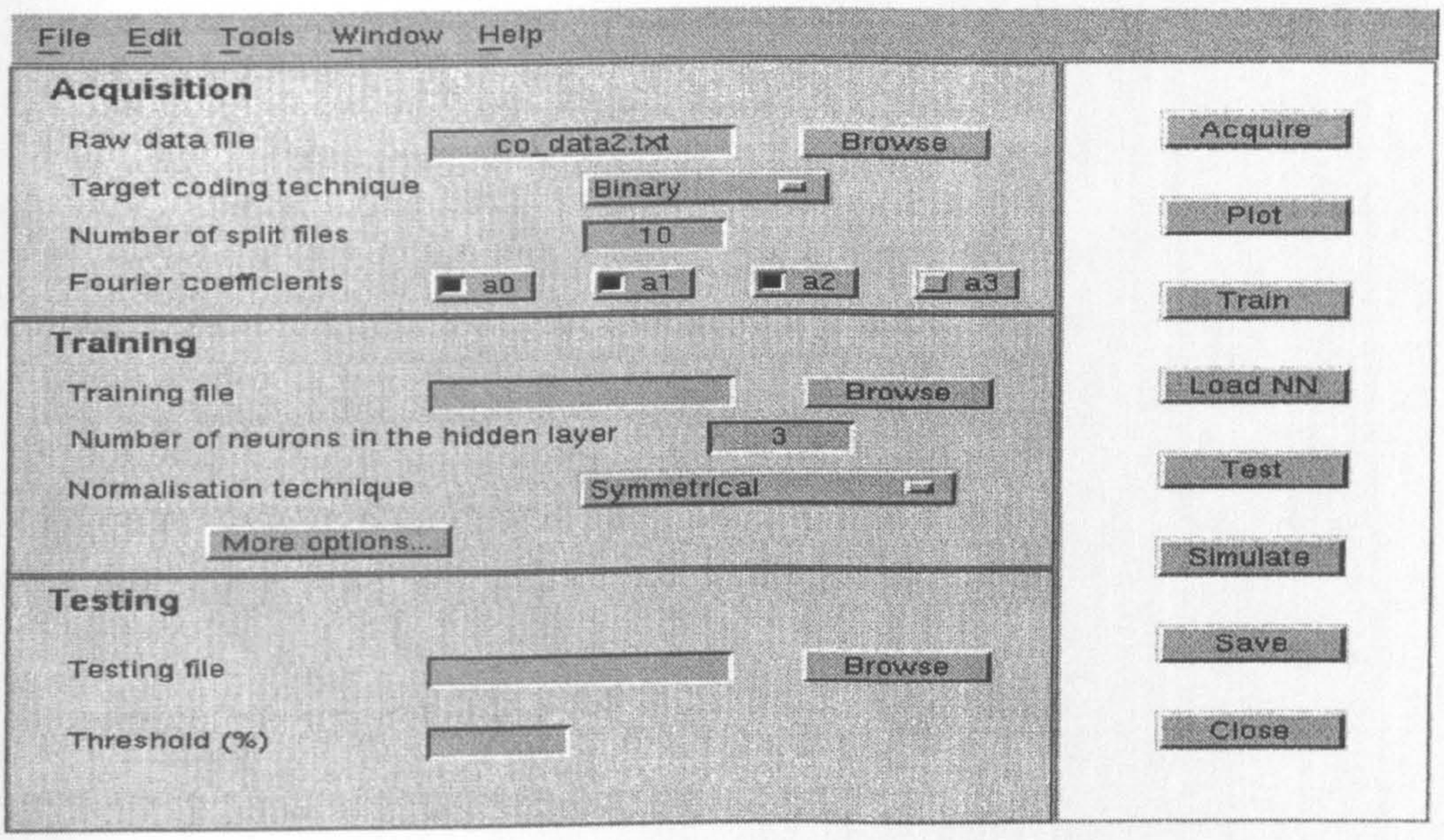
File Edit Tools Window Help
Acquisition
Raw data file
co_data2.txt
Browse
Target coding technique
Binary
Number of split files
10
Fourier coefficients
a0
a1
a2
a3
Training
Training file
Browse
Number of neurons in the hidden layer
3
Normalisation technique
Symmetrical
More options...
Testing
Testing file
Browse
Threshold (%)
Acquire
Plot
Train
Load NN
Test
Simulate
Save
Close

Figure 9

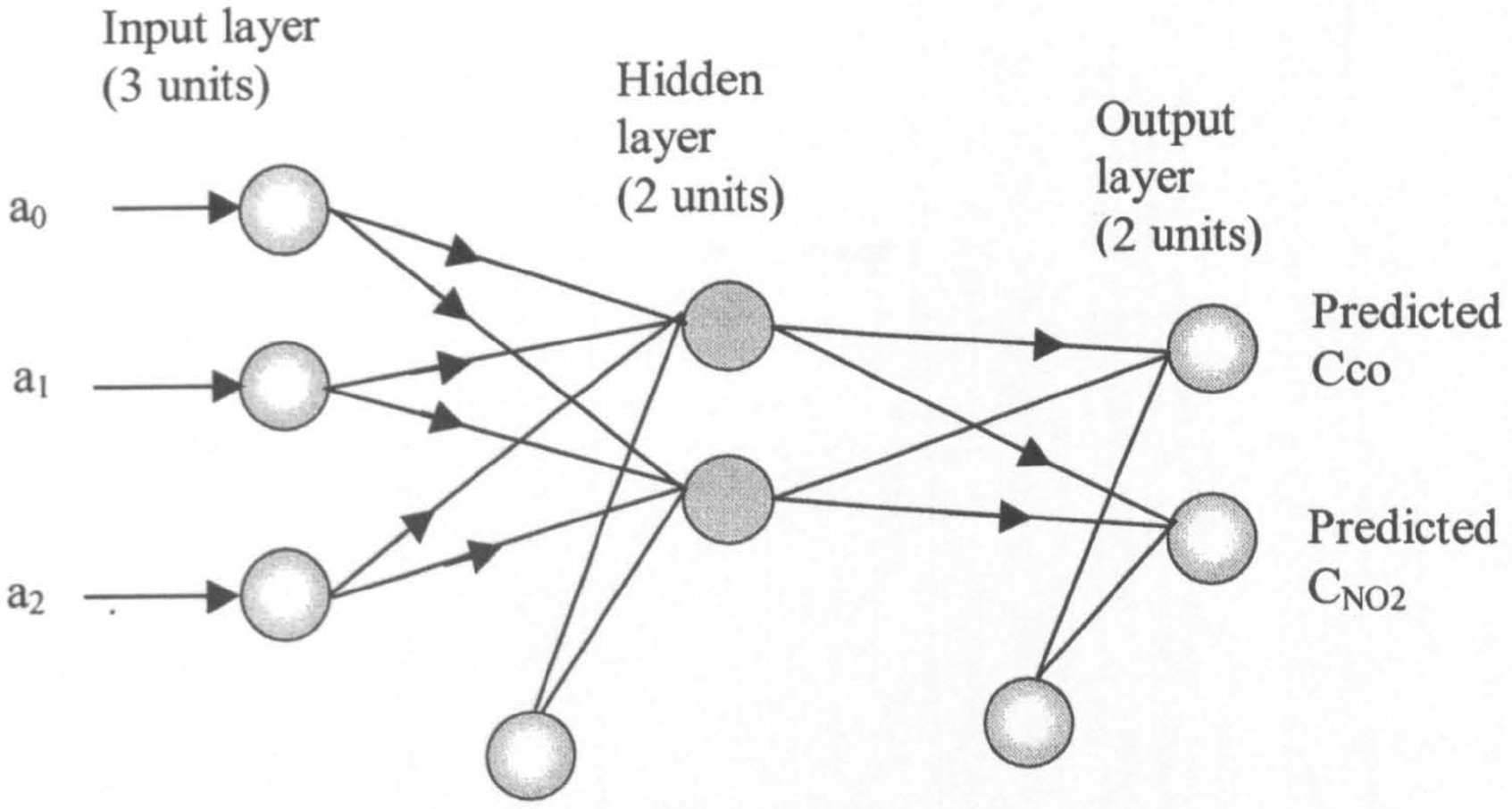
Input layer
(3 units)
Hidden
layer
(2 units)
Output
layer
(2 units)
$a_0$
$a_1$
$a_2$
Predicted
Cco
Predicted
$C_{NO2}$
Bias
Bias

Figure 10

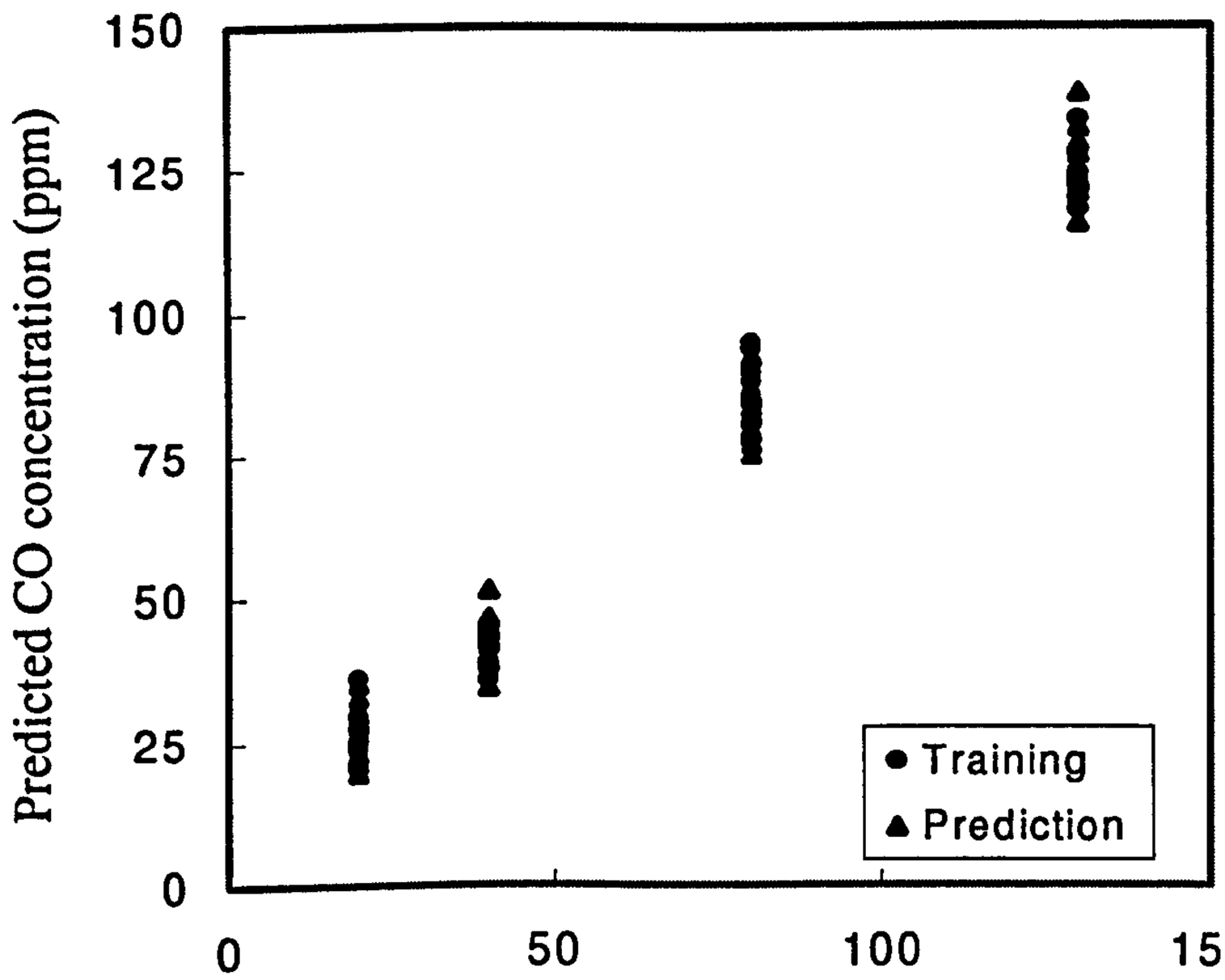
Predicted CO concentration (ppm)
150
125
100
75
50
25
0
0
50
100
150
True CO concentration
Training
Prediction

Figure 11

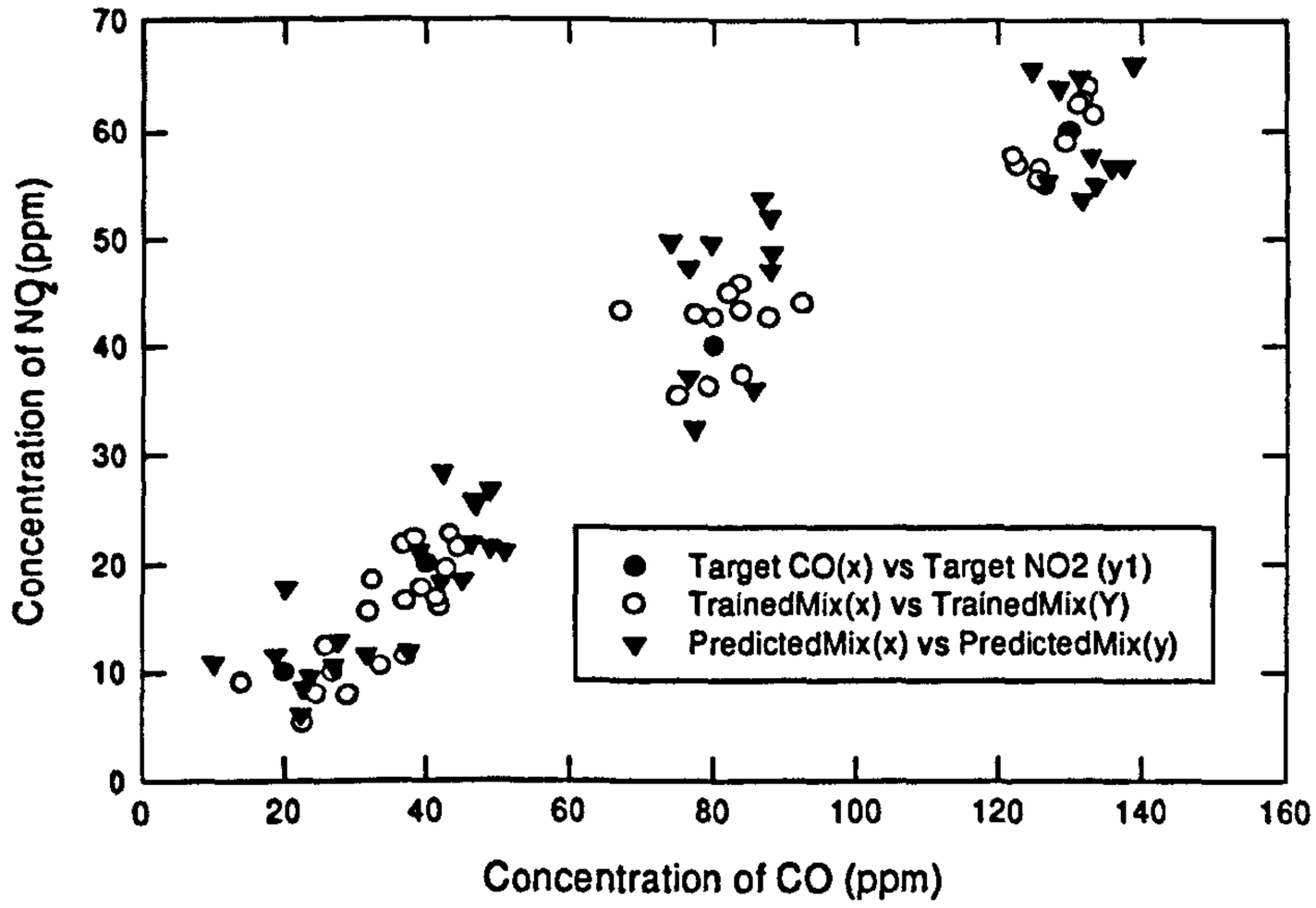
Concentration of NQ (ppm)
Concentration of CO (ppm)
0
10
20
30
40
50
60
70
0
20
40
60
80
100
120
140
160
Target CO(x) vs Target NO2 (y1)
TrainedMix(x) vs TrainedMix(Y)
PredictedMix(x) vs PredictedMix(y)

# Appendix D

LabView control circuits

108H3_2.VI
1/05/96 04:49 PM

Analog in CH0
0

Vsensor
0.38

number of iterations
13.00

I
12.00

Analog in CH1
1

Vsense
1.31

Loop start
7.00

Number of iteration2
1.00

Loop Parameter
7.00

Analog in CH2
2

VHeater
1.00

multiple ms
1000.00

multiple ms 2
500.00

Append?

DAC0
0

DAC0_Volts
0.00

Amount to change
1.00

Increment

Transpose

PowerH (mW)
4.97

DAC1
1

DAC1_Volts
0.00

incStep
1.00

File2 path
c:\temp.txt

Rheater
201.72

Heater temperature
61.48

port number_I/O
0

Gain pat
b 0

Sensor Resistance
378.42

G: 00=1, 01=4,10=2,11=8

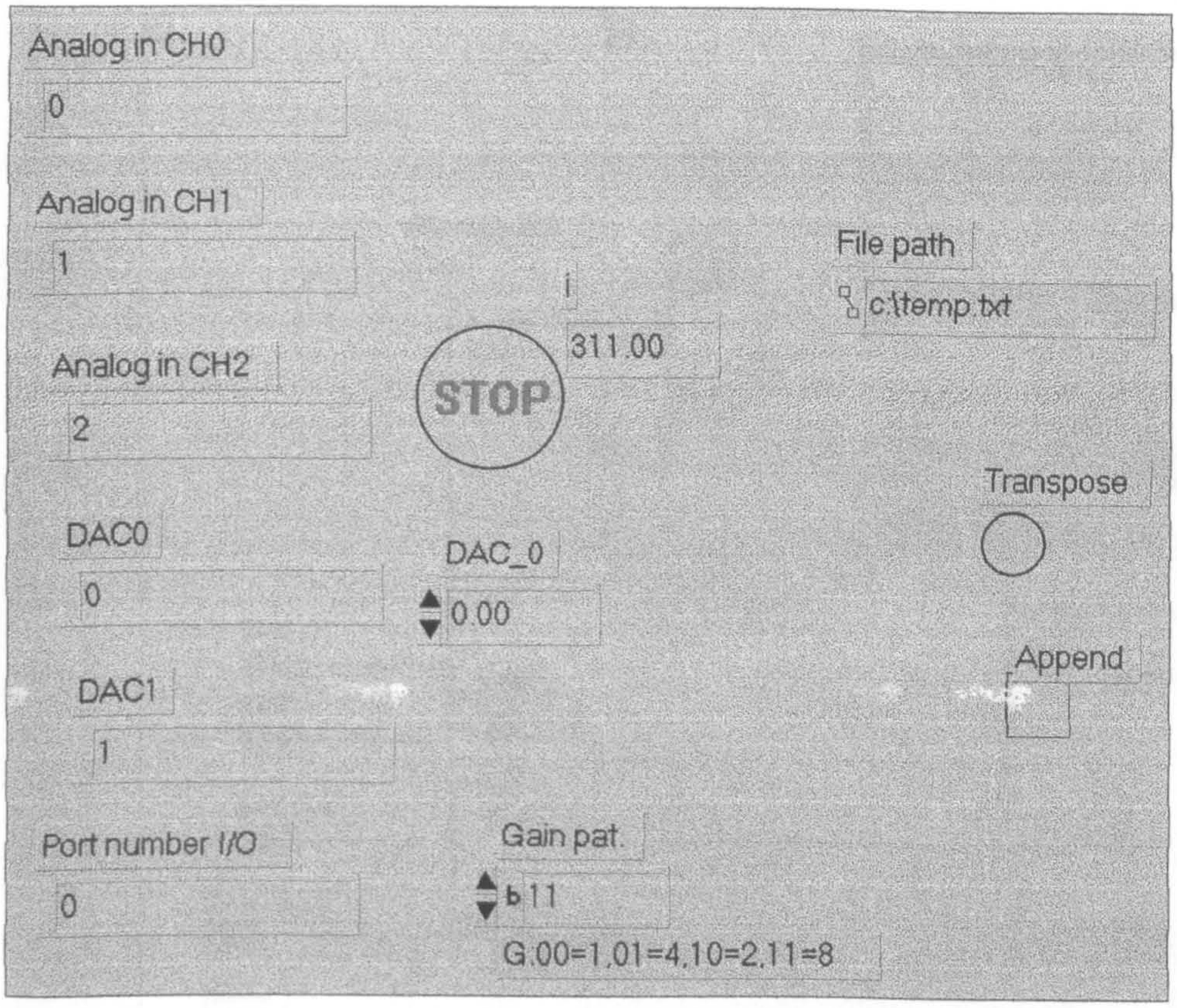
Analog in CH0
0
Analog in CH1
1
Analog in CH2
2
STOP
i
311.00
File path
c:\temp.txt
Transpose
DAC0
0
DAC_0
0.00
Append
DAC1
1
Port number I/O
0
Gain pat.
b 11
G:00=1,01=4,10=2,11=8

S108H3_2.VI
1/05/96 04:49 PM

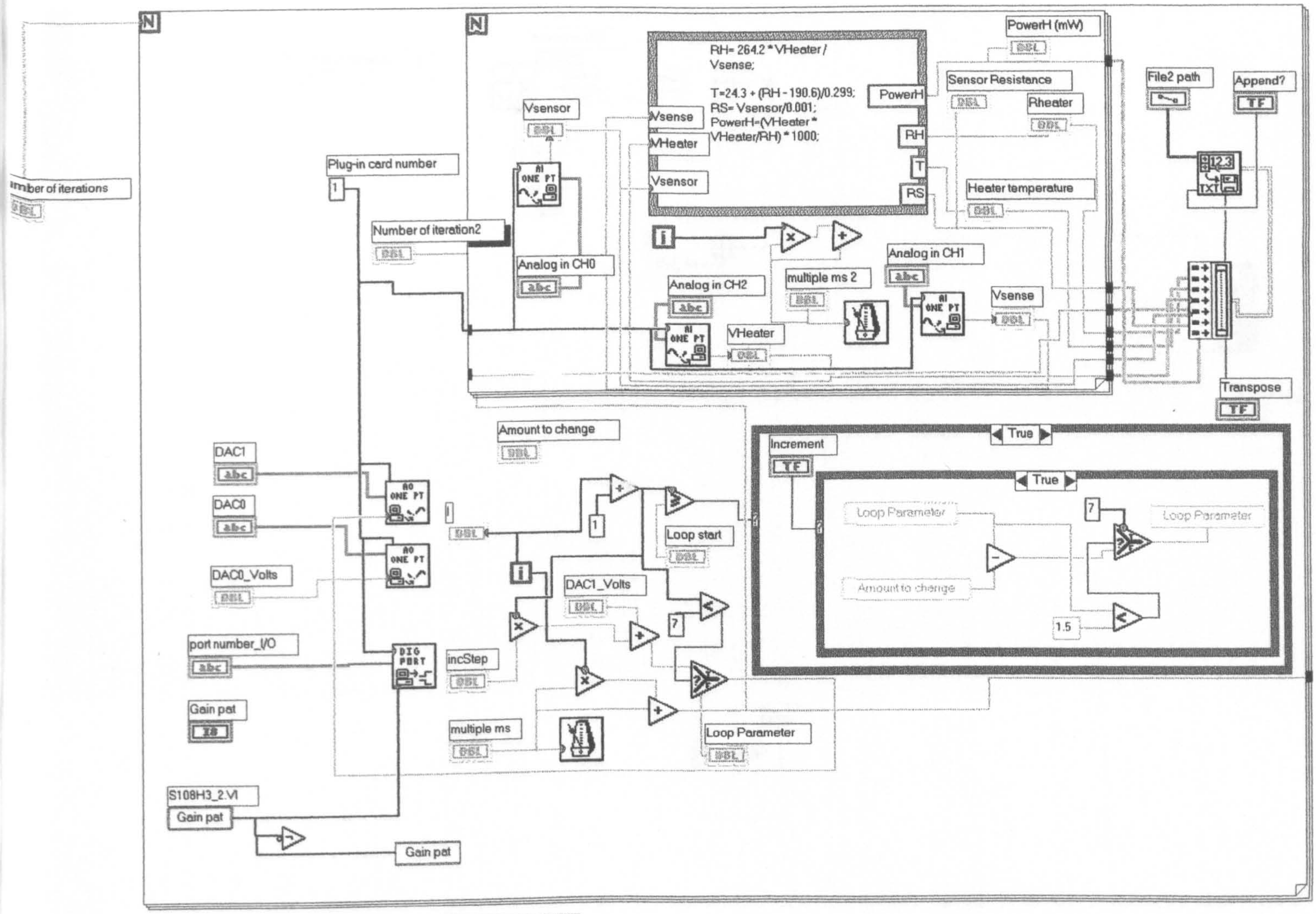

108H3T1.VI
5/07/99 11:39 AM

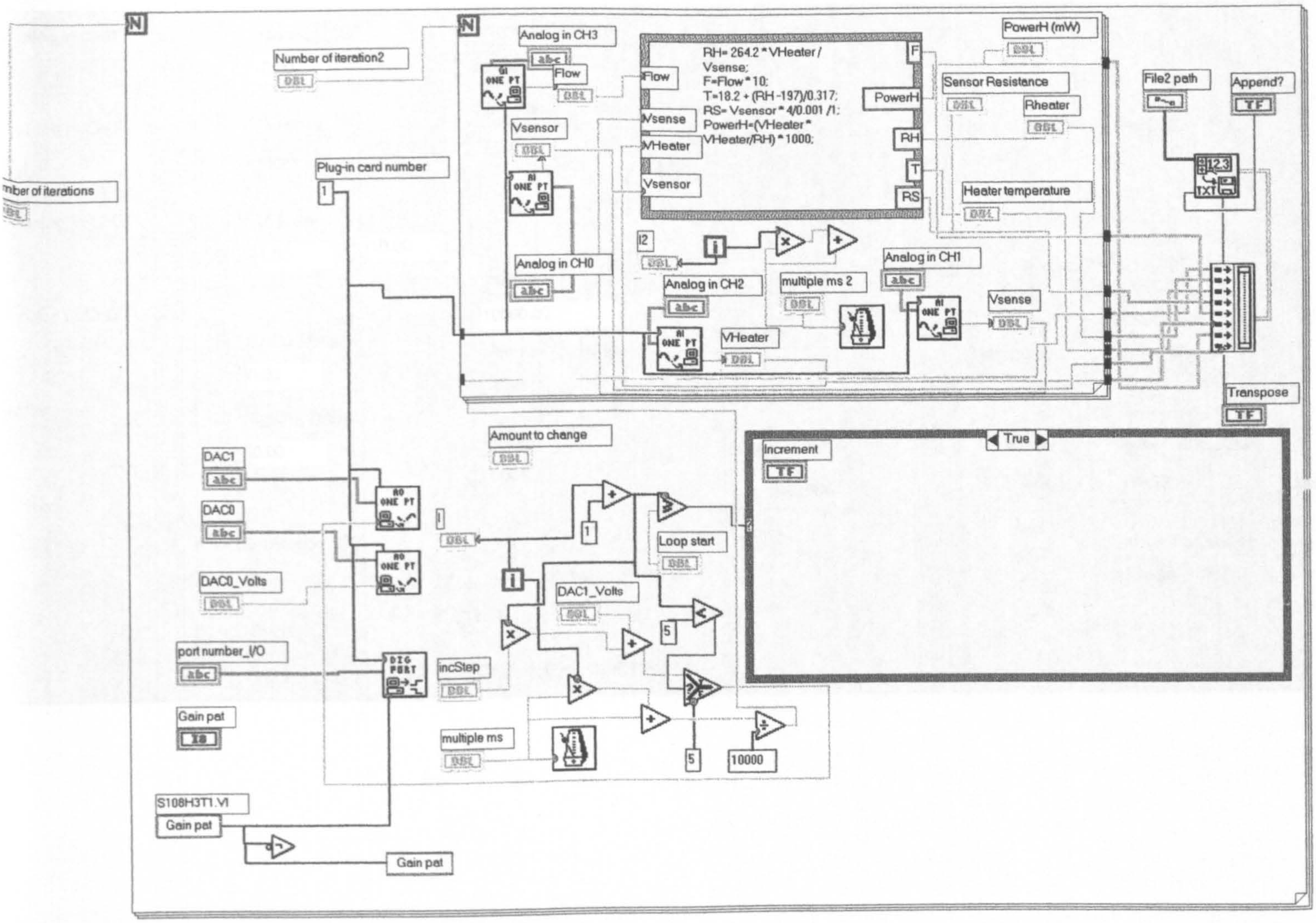

108H3T1.VI
5/07/99 11:39 AM

Analog in CH0
0

Vsensor
10.00

number of iterations
600.00

I
0.00

Analog in CH1
1

Vsense
1.21

Loop start
7.00

Number of iteration2
1.00

I2
0.00

This last steps and gives 200C

Analog in CH2
2

VHeater
1.00

Flow
10.00

multiple ms
10000.00

multiple ms 2
100.00

Append?

Analog in CH3
2

DAC0_Volts
0.00

Amount to change
1.00

Increment

Transpose

PowerH (mW)
4.58

DAC0
0

DAC1_Volts
0.00

incStep
1.00

File2 path
c:\temp.txt

Rheater
218.83

Heater temperature
118.72

DAC1
1

port number_I/O
0

Gain pat
b 11

Sensor Resistance
1249.69

G: 00=1, 01=4,10=2,11=8

5108H3_9.VI
0/28/96 12:54 PM

Analog in CH0
0

Vsensor
10.00

Analog in CH1
1

Vsense
0.01

Analog in CH2
2

I1
42.00

Multiple ms
10.00

File path
c:\temp.txt

STOP

DAC0
0

DAC_0
0.00

DAC1
1

Port number I/O
0

Gain pat.
b 0

test1
0.00

Rheater
44980.05

Heater temperature
149821.75

PowerH (mW)
0.06

Sensor Resistance
1249.69

Counter
0.00

:108H3_9.VI
0/28/96 12:54 PM

Analog in CH0
0

Vsensor
10.00

Analog in CH1
1

Vsense
0.01

Analog in CH2
2

I1
42.00

Multiple ms
10.00

File path
c:\temp.txt

STOP

DAC0
0

DAC_0
0.00

DAC1
1

Port number I/O
0

Gain pat.
0

test1
0.00

Rheater
44980.05

Heater temperature
149821.7

PowerH (mW)
0.06

Sensor Resistance
1249.69

Counter
0.00

108H3_9.VI
0/28/96 12:54 PM

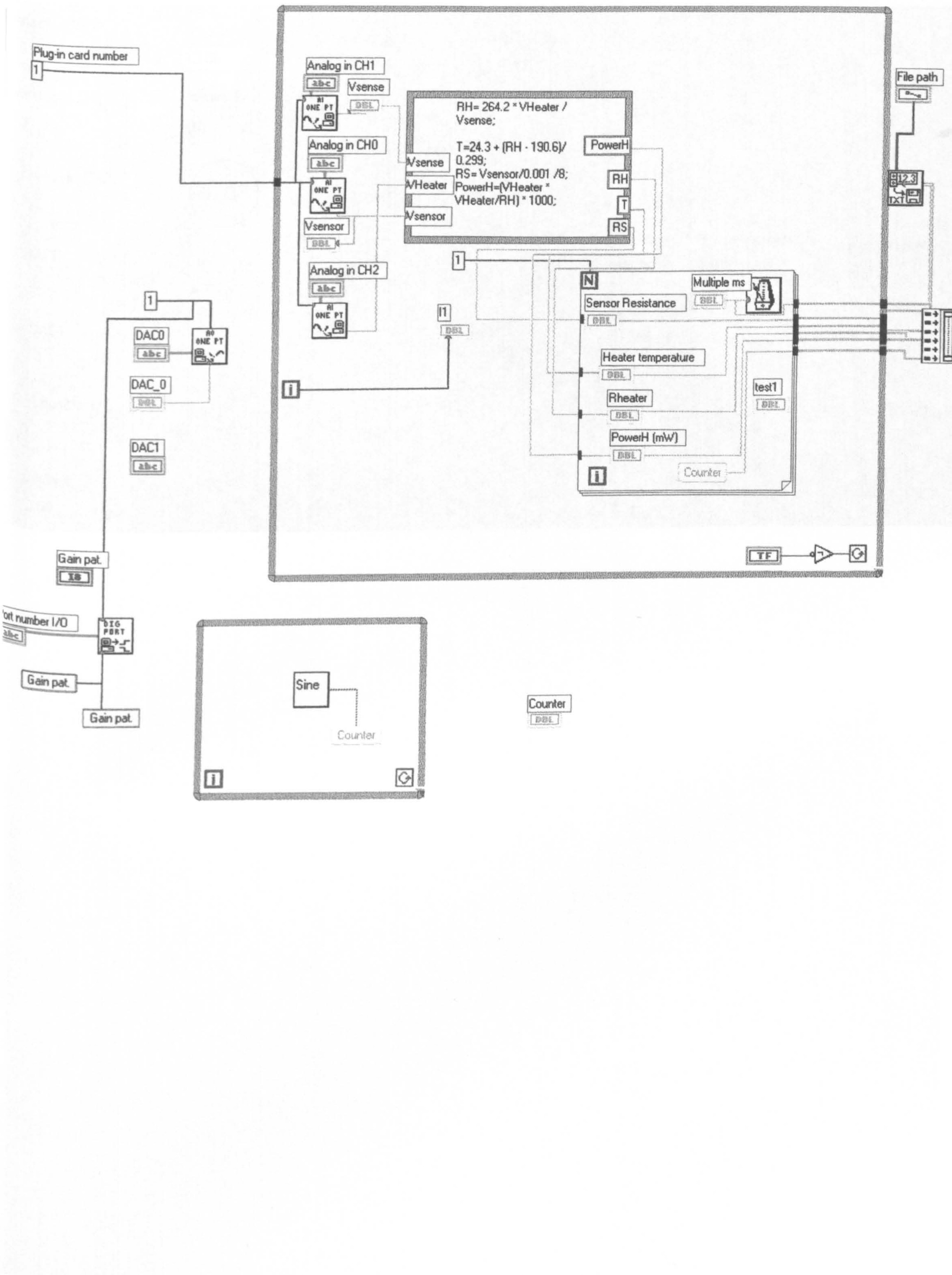

:108H310.VI
0/29/96 05:15 PM

Analog in CH0
0

Vsensor
10.00

Analog in CH1
1

Vsense
0.01

Analog in CH2
2

STOP

I1
42.00

Multiple ms
10.00

File path
c:\temp.txt

Rheater
44980.05

Heater temperature
149821.7

PowerH (mW)
0.06

Sensor Resistance
1249.69

DAC0
0

DAC_0
0.00

sin
STOP

DAC1
1

test1
0.00

Port number I/O
0

Gain pat.
0

Counter
0.00

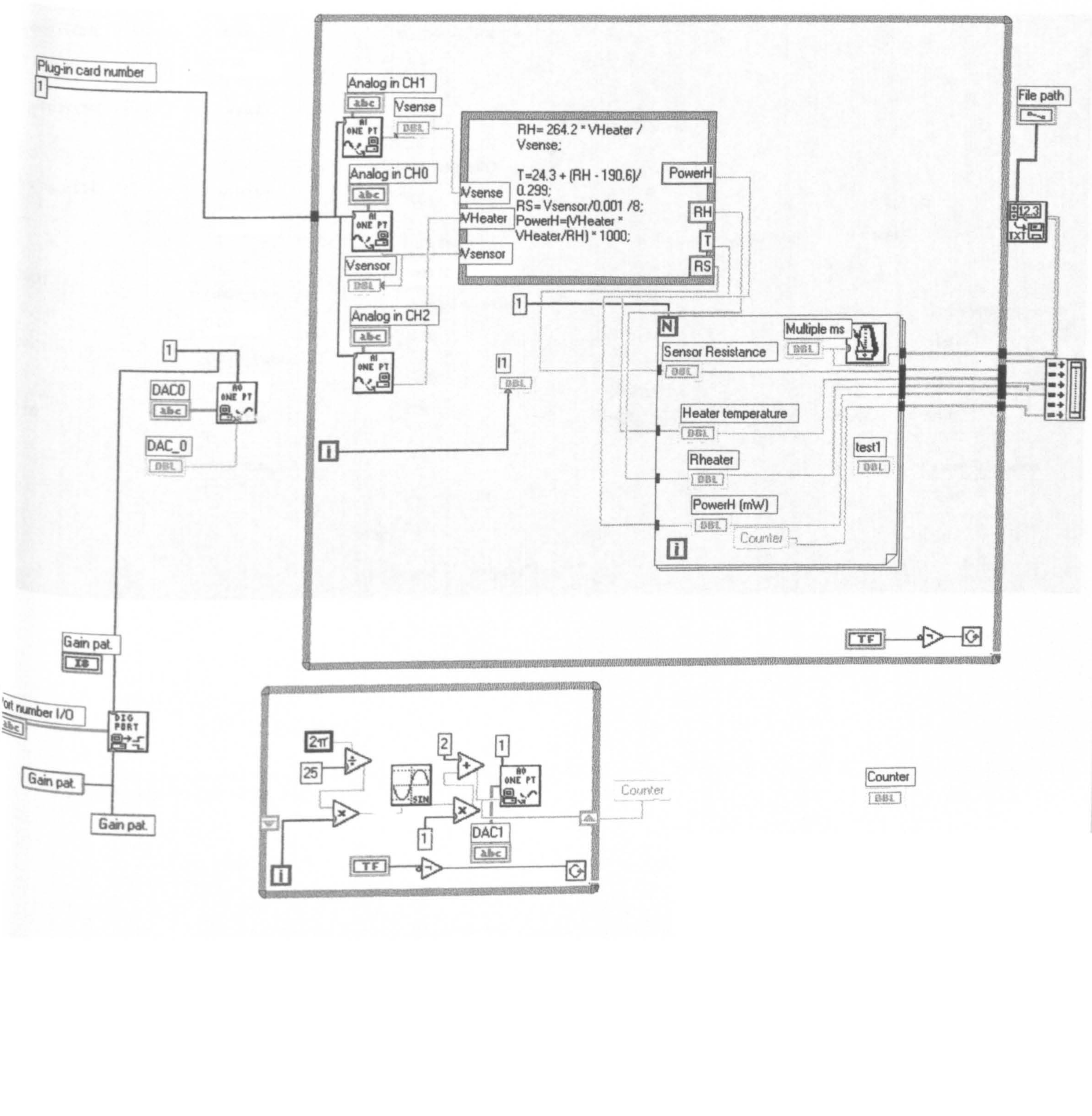
Plug-in card number
1
Analog in CH1
abc
Vsense
AI ONE PT
DBL
Analog in CH0
abc
AI ONE PT
Vsensor
DBL
Analog in CH2
abc
AI ONE PT
RH= 264.2 * VHeater / Vsense;
T=24.3 + (RH - 190.6)/ 0.299;
RS= Vsensor/0.001 /8;
PowerH=(VHeater * VHeater/RH) * 1000;
Vsense
VHeater
Vsensor
PowerH
RH
T
RS
1
N
Multiple ms
DBL
Sensor Resistance
DBL
Heater temperature
DBL
Rheater
DBL
PowerH (mW)
DBL
Counter
test1
DBL
i
I1
DBL
i
File path
12.3
TXT
1
DAC0
abc
AO ONE PT
DAC_0
DBL
Gain pat.
I8
ort number I/O
abc
DIG PORT
Gain pat.
Gain pat.
TF
2π
25
÷
SIN
2
1
+
AO ONE PT
×
1
DAC1
abc
TF
i
Counter
Counter
DBL

S108H3_2.VI
1/05/96 04:49 PM

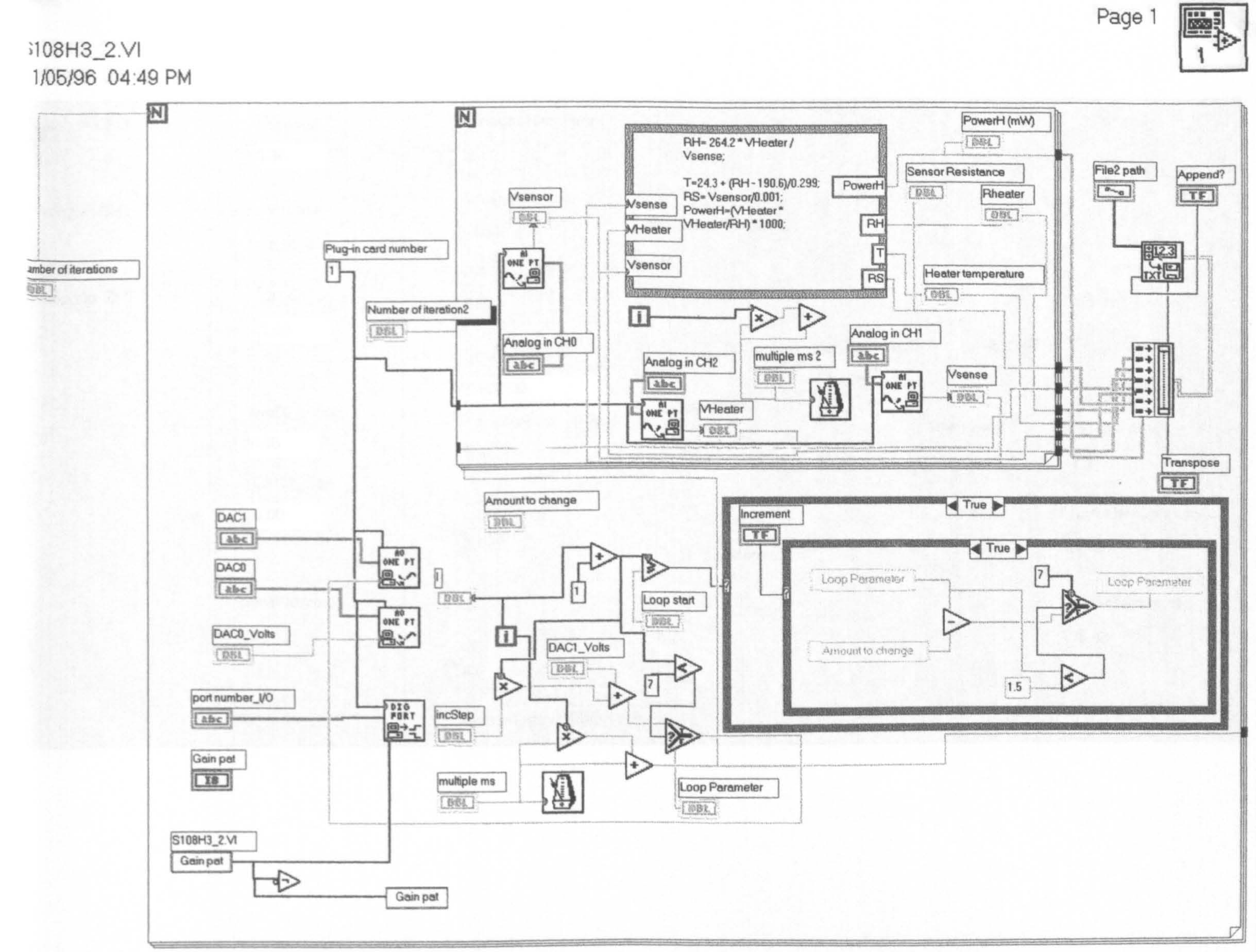

108H3_2.VI
1/05/96 04:49 PM

Analog in CH0
0

Vsensor
0.38

number of iterations
13.00

I
12.00

Analog in CH1
1

Vsense
1.31

Loop start
7.00

Number of iteration2
1.00

Analog in CH2
2

VHeater
1.00

Loop Parameter
7.00

multiple ms
1000.00

multiple ms 2
500.00

Append?

DAC0
0

DAC0_Volts
0.00

Amount to change
1.00

Increment

Transpose

PowerH (mW)
4.97

DAC1
1

DAC1_Volts
0.00

incStep
1.00

File2 path
c:\temp.txt

Rheater
201.72

Heater temperature
61.48

Sensor Resistance
378.42

port number_I/O
0

Gain pat
0

G: 00=1, 01=4,10=2,11=8

108H3_2.VI
1/05/96 04:49 PM

Analog in CH0
0

Vsensor
0.38

Analog in CH1
1

Vsense
1.31

Analog in CH2
2

VHeater
1.00

DAC0
0

DAC0_Volts
0.00

DAC1
1

DAC1_Volts
0.00

number of iterations
13.00

I
12.00

Loop start
7.00

Number of iteration2
1.00

Loop Parameter
7.00

multiple ms
1000.00

Amount to change
1.00

Increment

multiple ms 2
500.00

Append?

Transpose

PowerH (mW)
4.97

incStep
1.00

File2 path
c:\temp.txt

Rheater
201.72

Heater temperature
61.48

port number_I/O
0

Gain pat
0

G: 00=1, 01=4,10=2,11=8

Sensor Resistance
378.42

S108H3_2.VI
1/05/96 04:49 PM

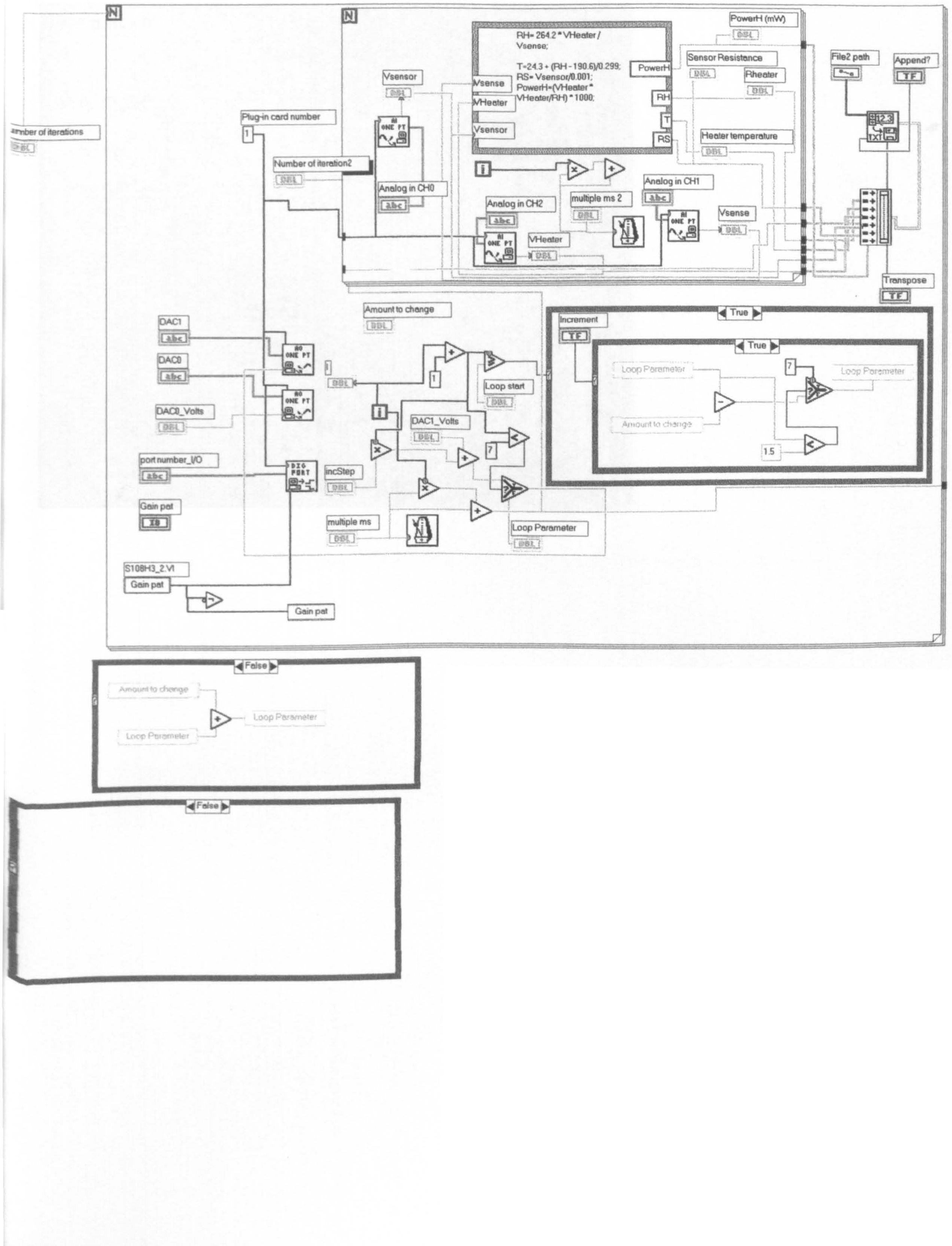

108H315.VI
1/18/96 04:42 PM

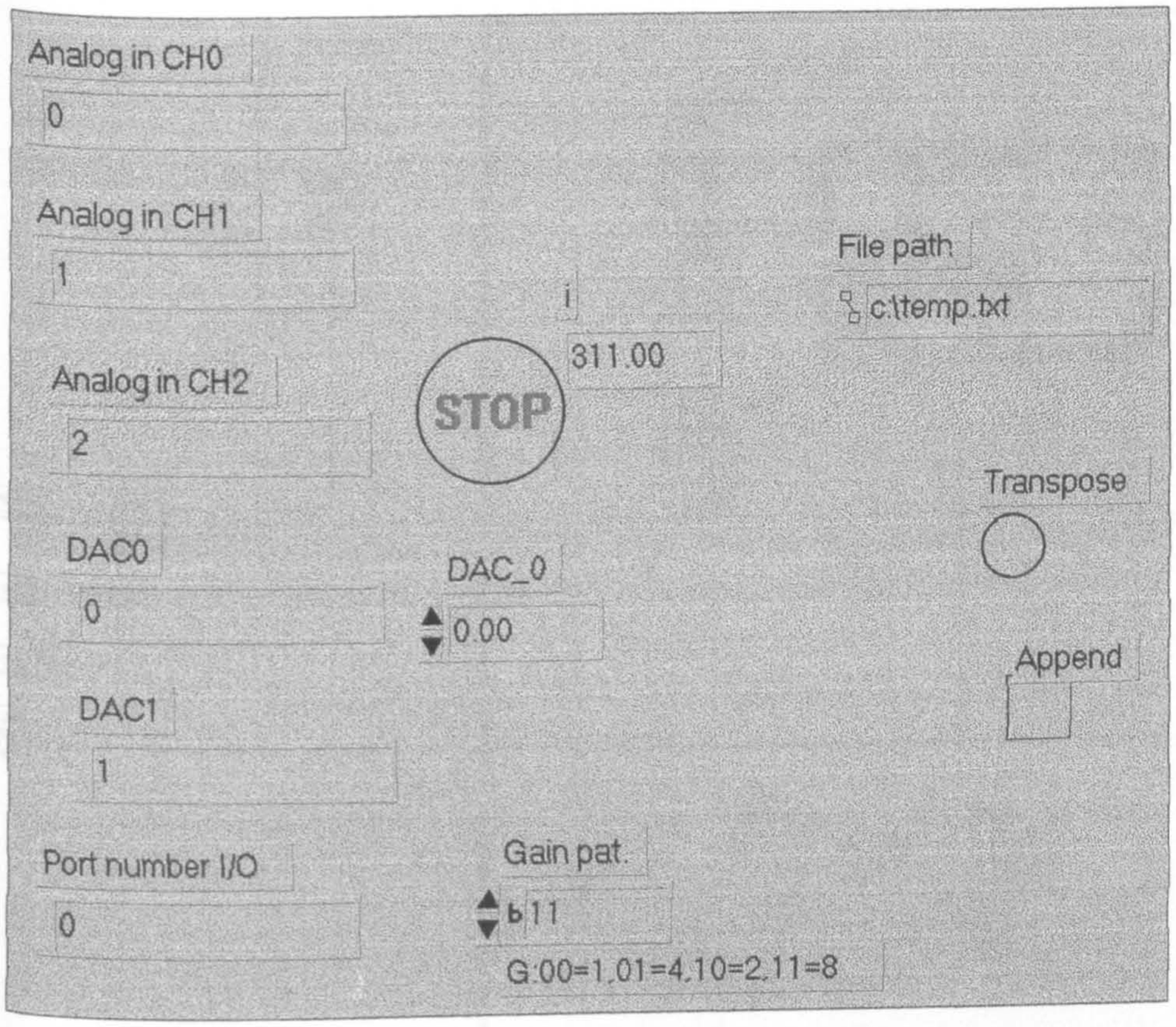

108H315.VI
1/18/96 04:42 PM

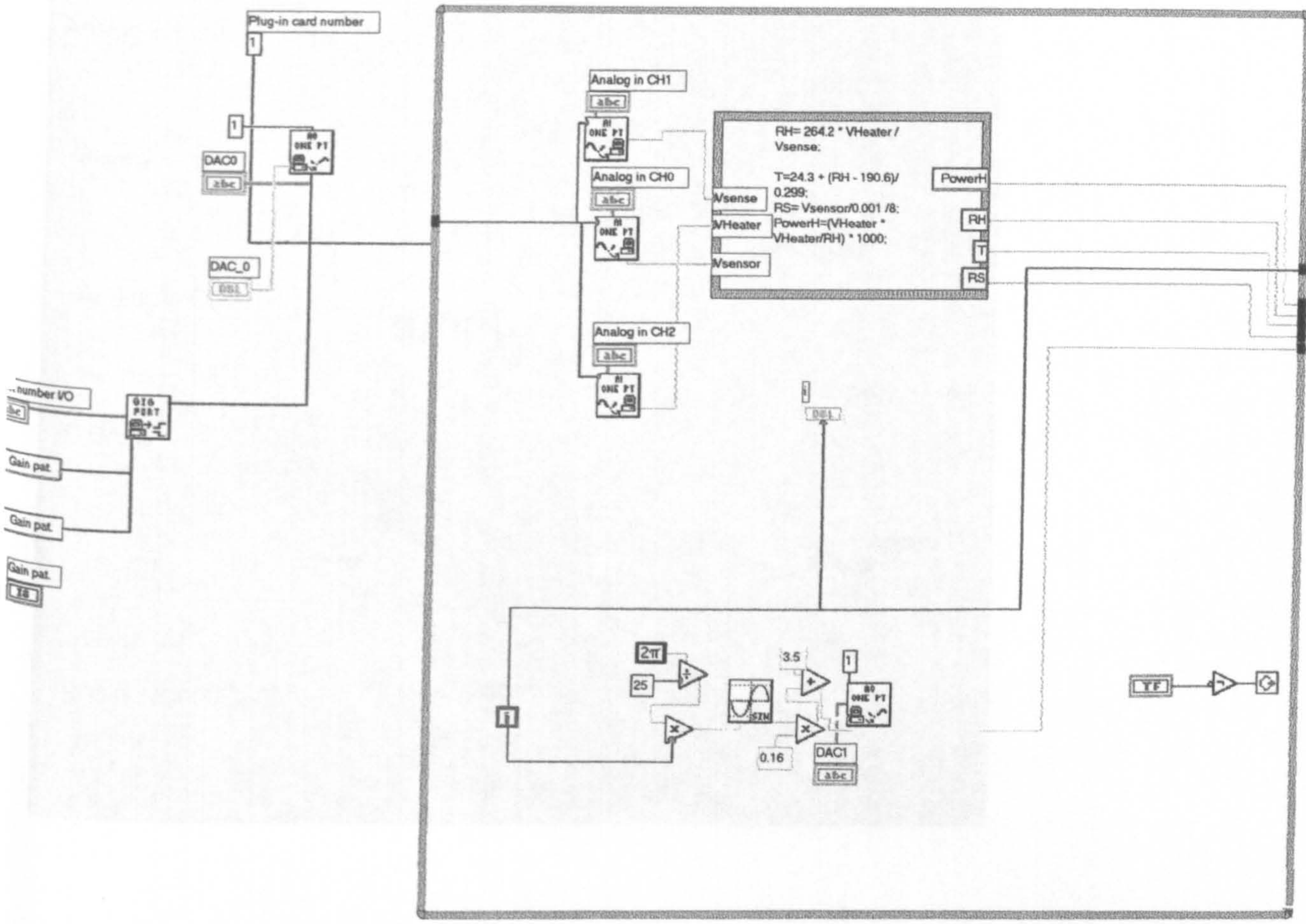

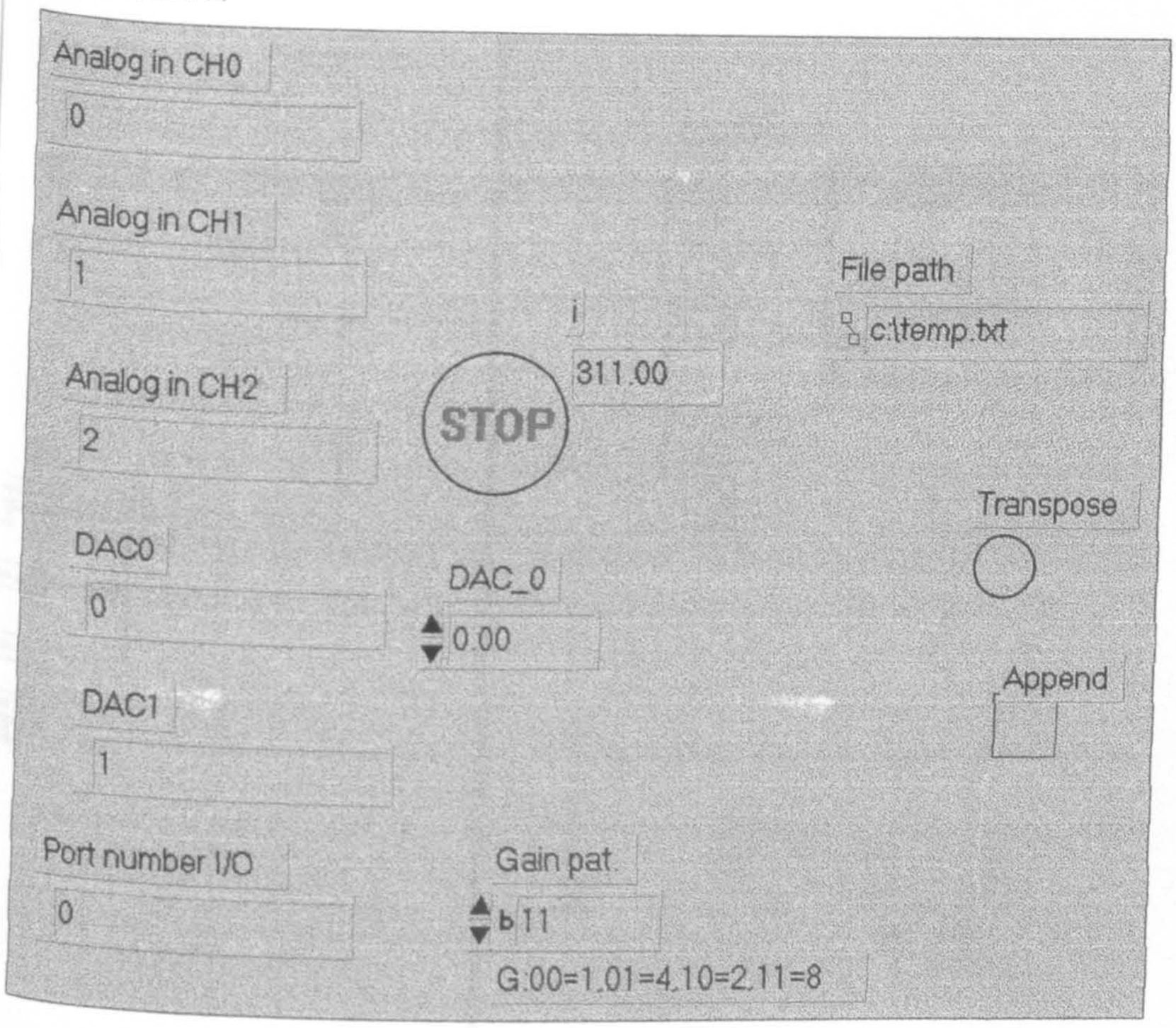
Analog in CH0
0
Analog in CH1
1
Analog in CH2
2
STOP
i
311.00
File path
c:\temp.txt
Transpose
DAC0
0
DAC_0
0.00
DAC1
1
Append
Port number I/O
0
Gain pat
b11
G:00=1,01=4,10=2,11=8

108H315.VI
1/18/96 04:42 PM

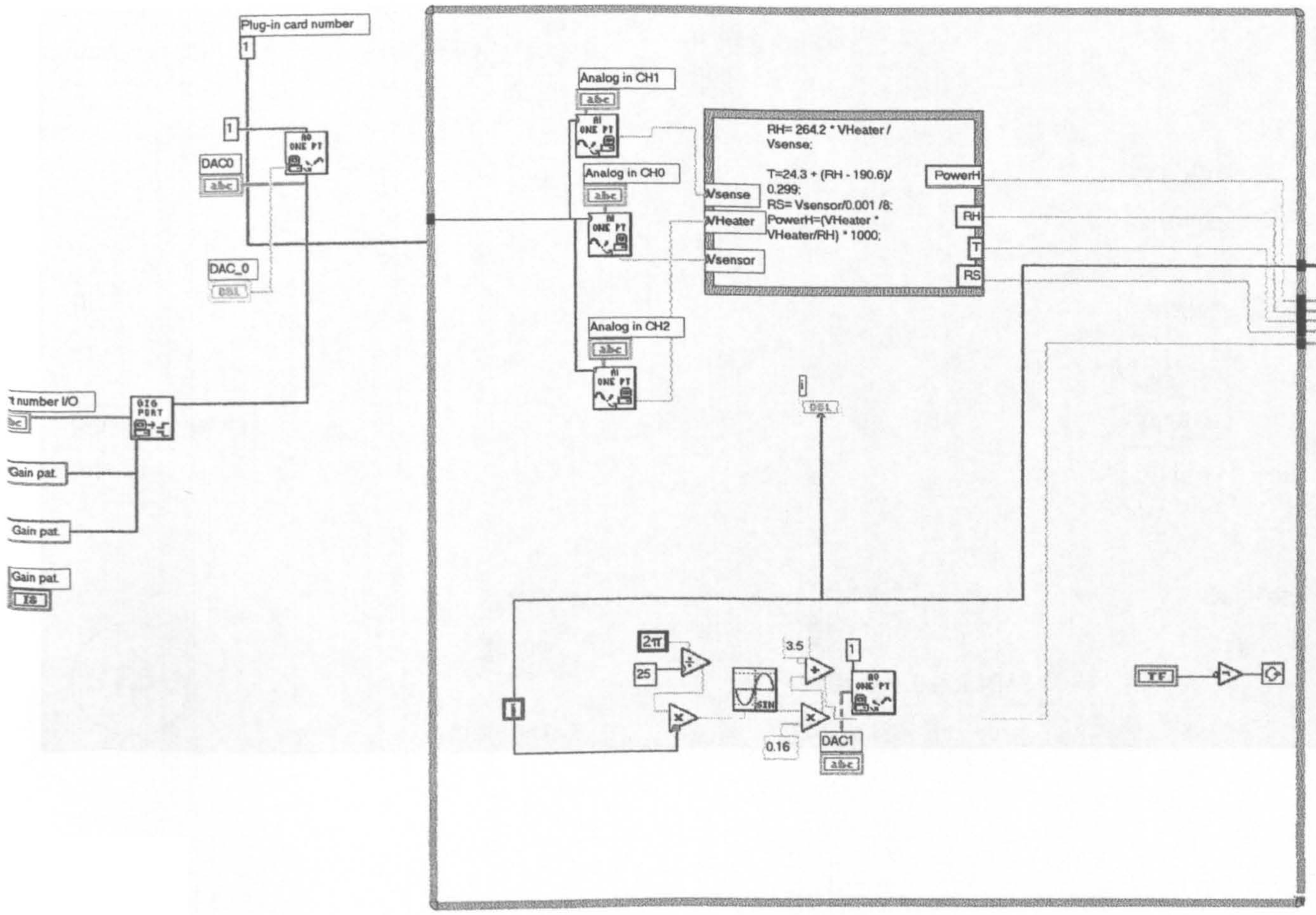

_001HZ.VI
2/19/97 03:33 PM

Analog in CH0
0

Analog in CH1
1

Analog in CH2
2

File path
c:\temp.txt

DAC0
0

DAC1
1

Transpose

0.01Hz
4000.00

Port number I/O
0

Append

i
122.00

DAC_0
0.00

Gain pat.
b 11

SenRes
0.00

G:00=1,01=4,10=2,11=8

STOP

_001HZ.VI
2/19/97 03:33 PM

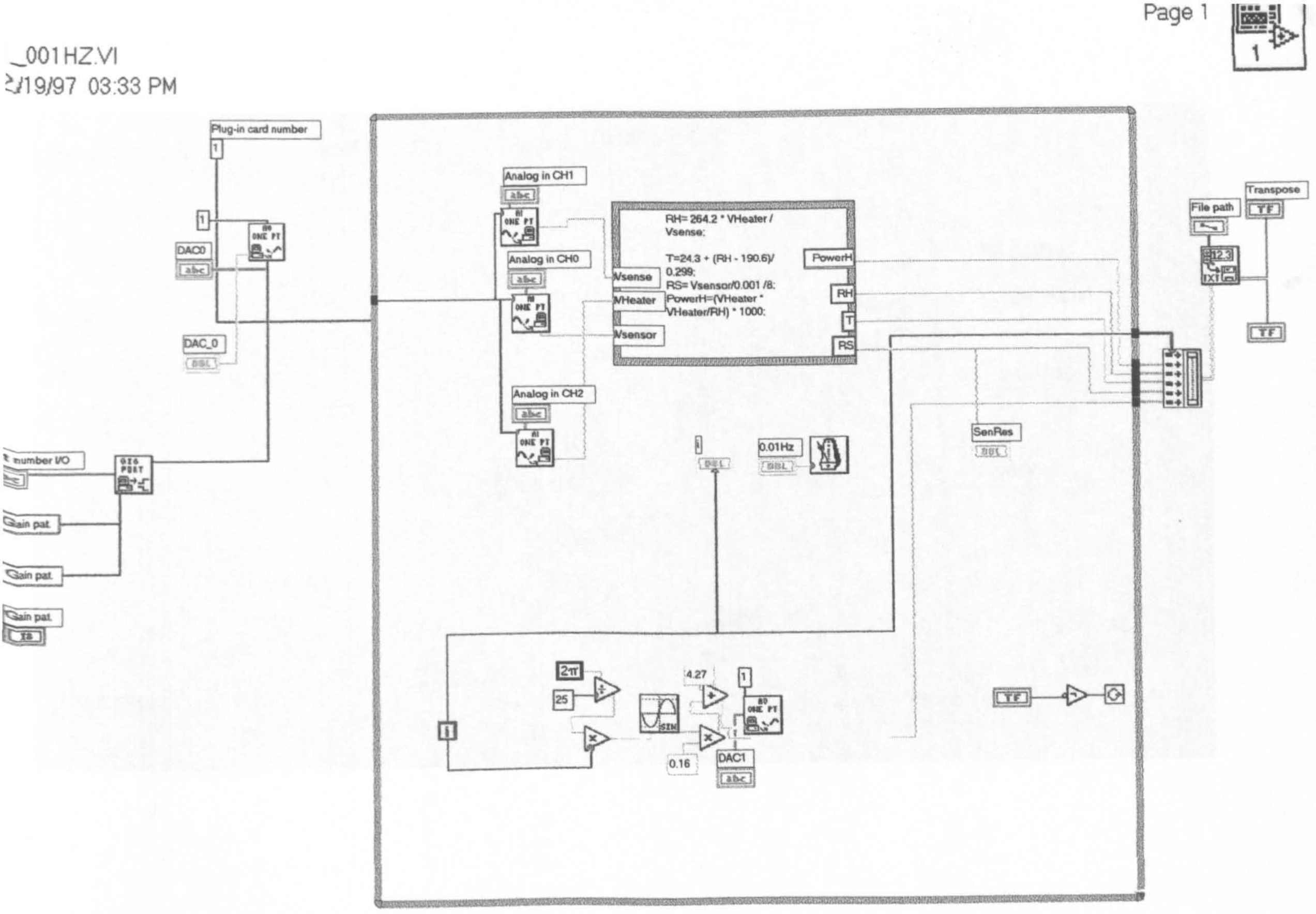

I_001HZ.VI
2/19/97 03:33 PM

Analog in CH0
0

Analog in CH1
1

Analog in CH2
2

File path
c:\temp.txt

DAC0
0

DAC1
1

Transpose

0.01Hz
4000.00

Append

Port number I/O
0

i
122.00

DAC_0
0.00

Gain pat
b11

G:00=1,01=4,10=2,11=8

SenRes
0.00

STOP

INE_1HZ.VI
7/11/97 12:11 PM

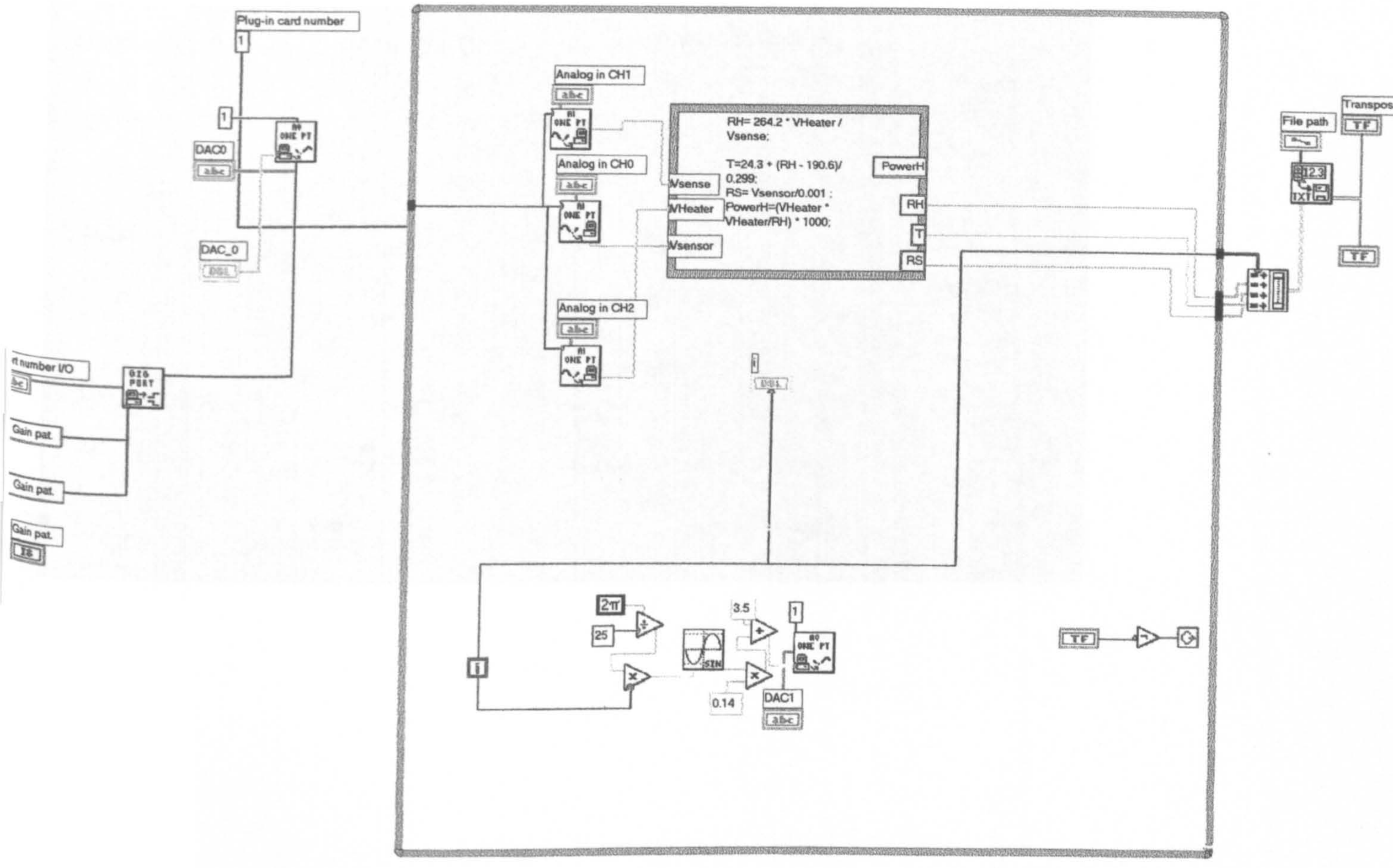

INE_1HZ.VI
7/11/97 12:11 PM


Analog in CH0
0

Analog in CH1
1

Analog in CH2
2

Transpose

DAC0
0

DAC1
1

File path
c:\temp.txt

Append

Gain pat.
b 0

Port number I/O
0

DAC_0
-3.00

G:00=1,01=4,10=2,11=8

i
70.00

STOP

INE_1HZ.VI
7/11/97 12:11 PM

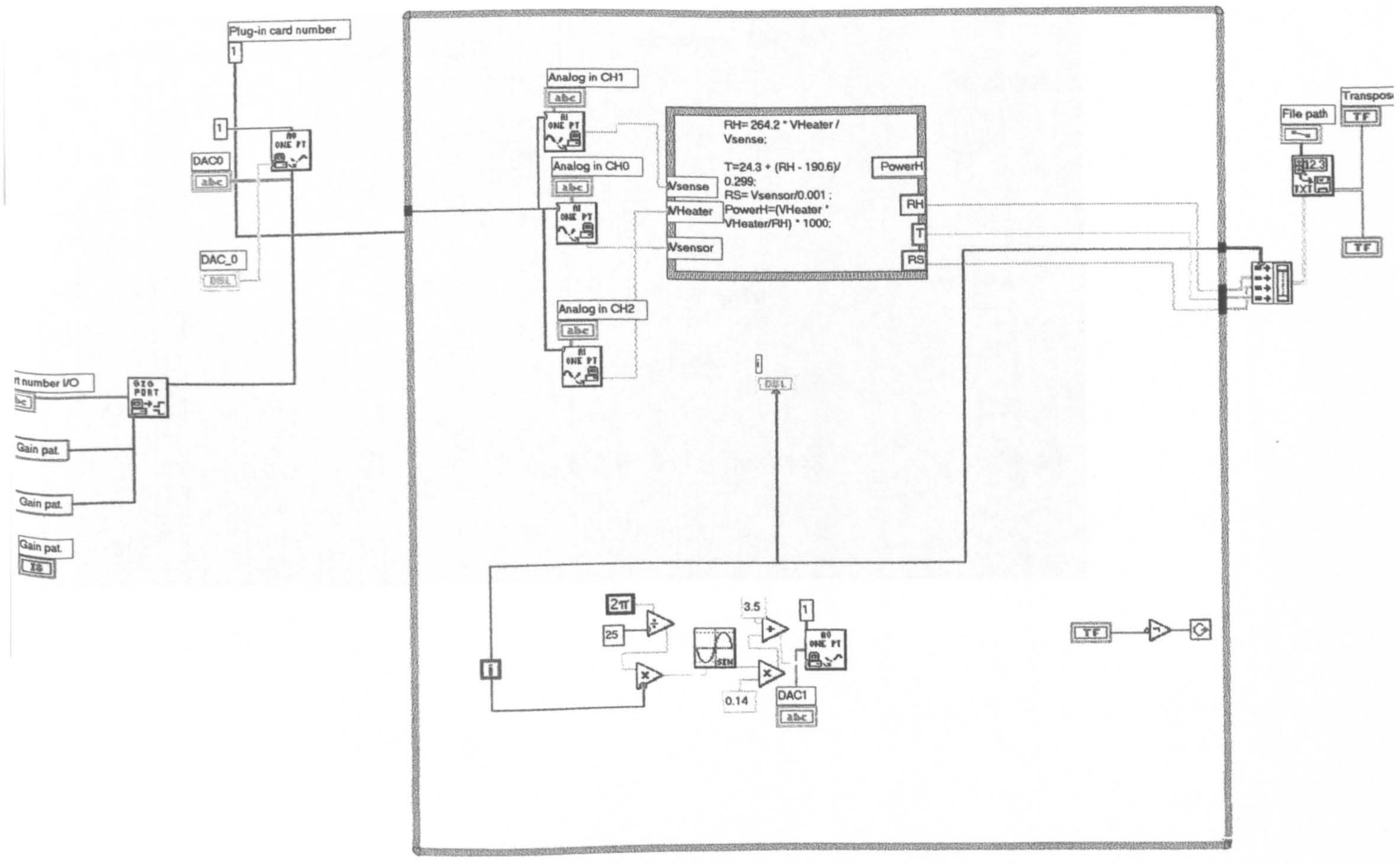

Analog in CH0
0
Analog in CH1
1
Analog in CH2
2
Transpose

DAC0
0
DAC1
1
File path
c:\temp.txt
Append

Port number I/O
0
DAC_0
-3.00
Gain pat.
b 0
G:00=1,01=4,10=2,11=8

i
70.00

STOP

NE_1HZ.VI
7/11/97 12:11 PM

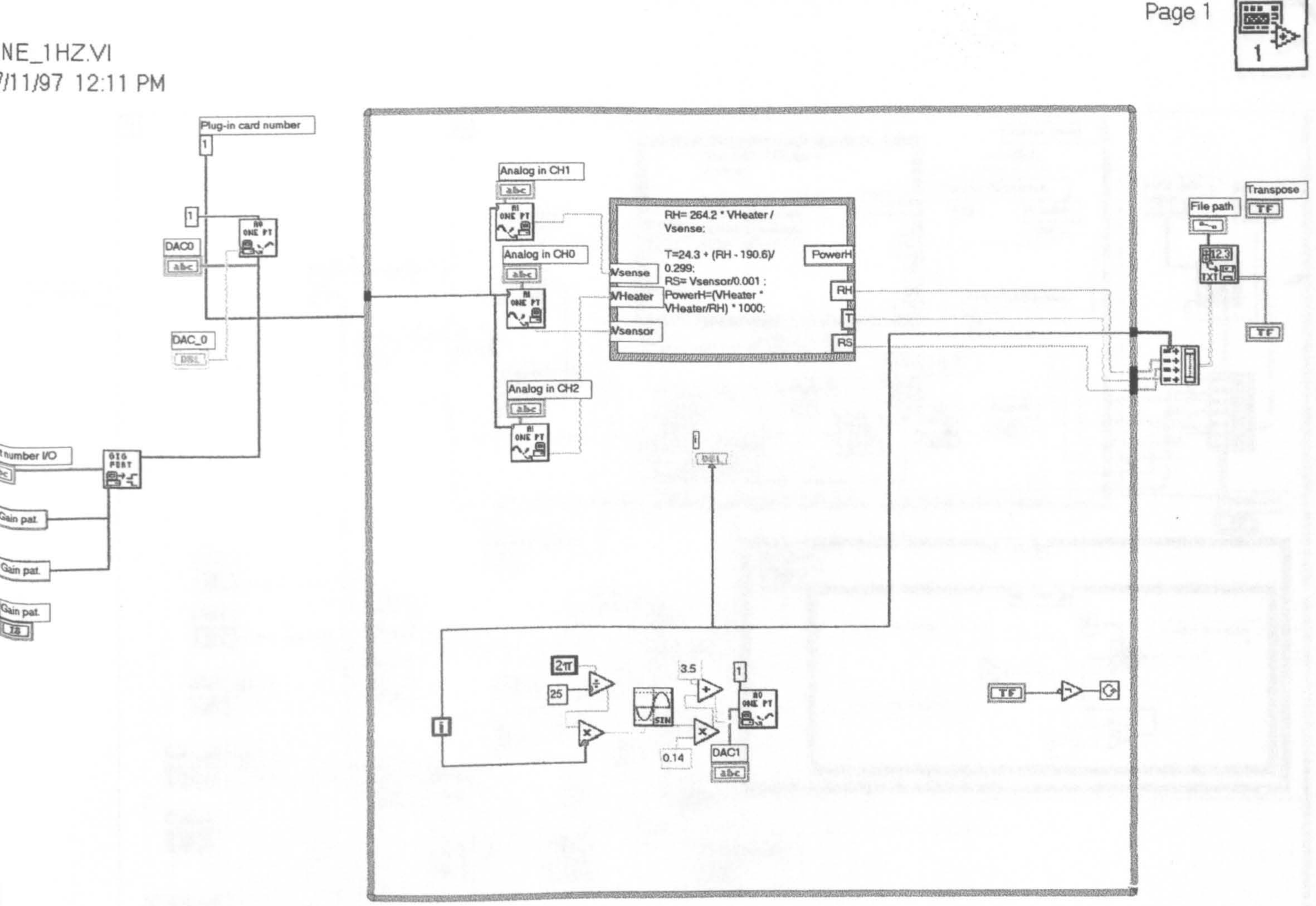

S108H3_1.VI
3/31/99 03:27 PM

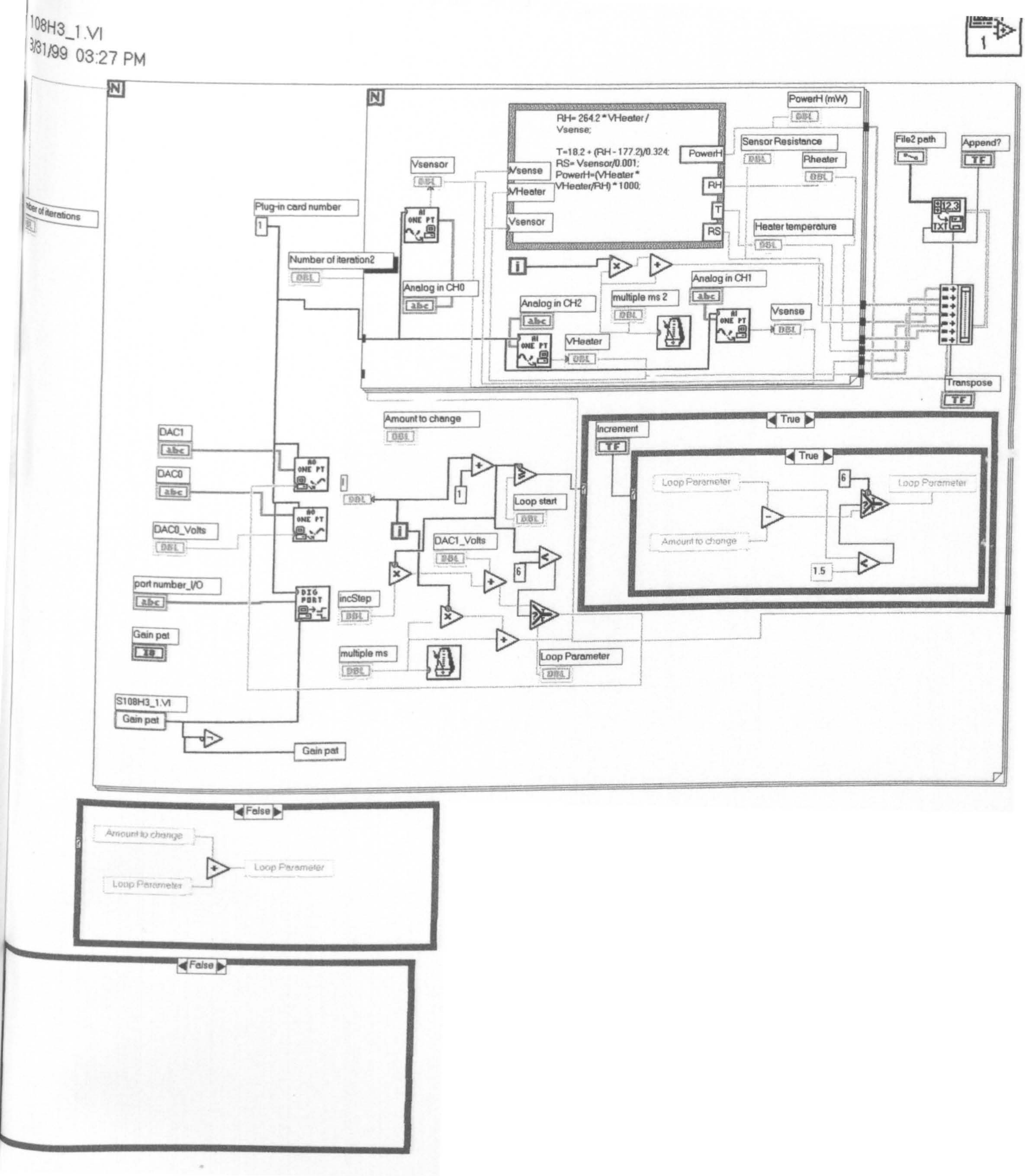

108H3_1.VI
3/31/99 03:27 PM

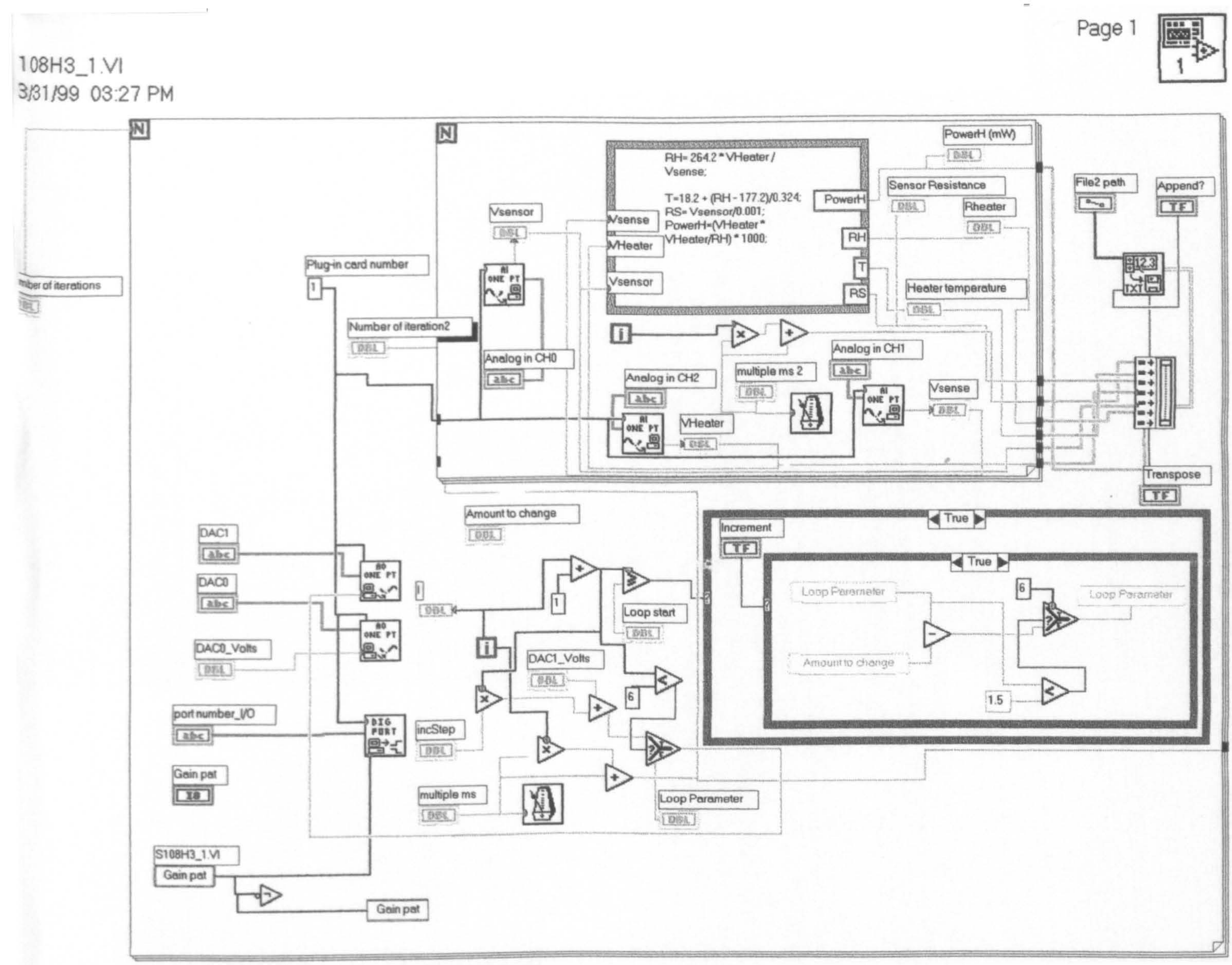

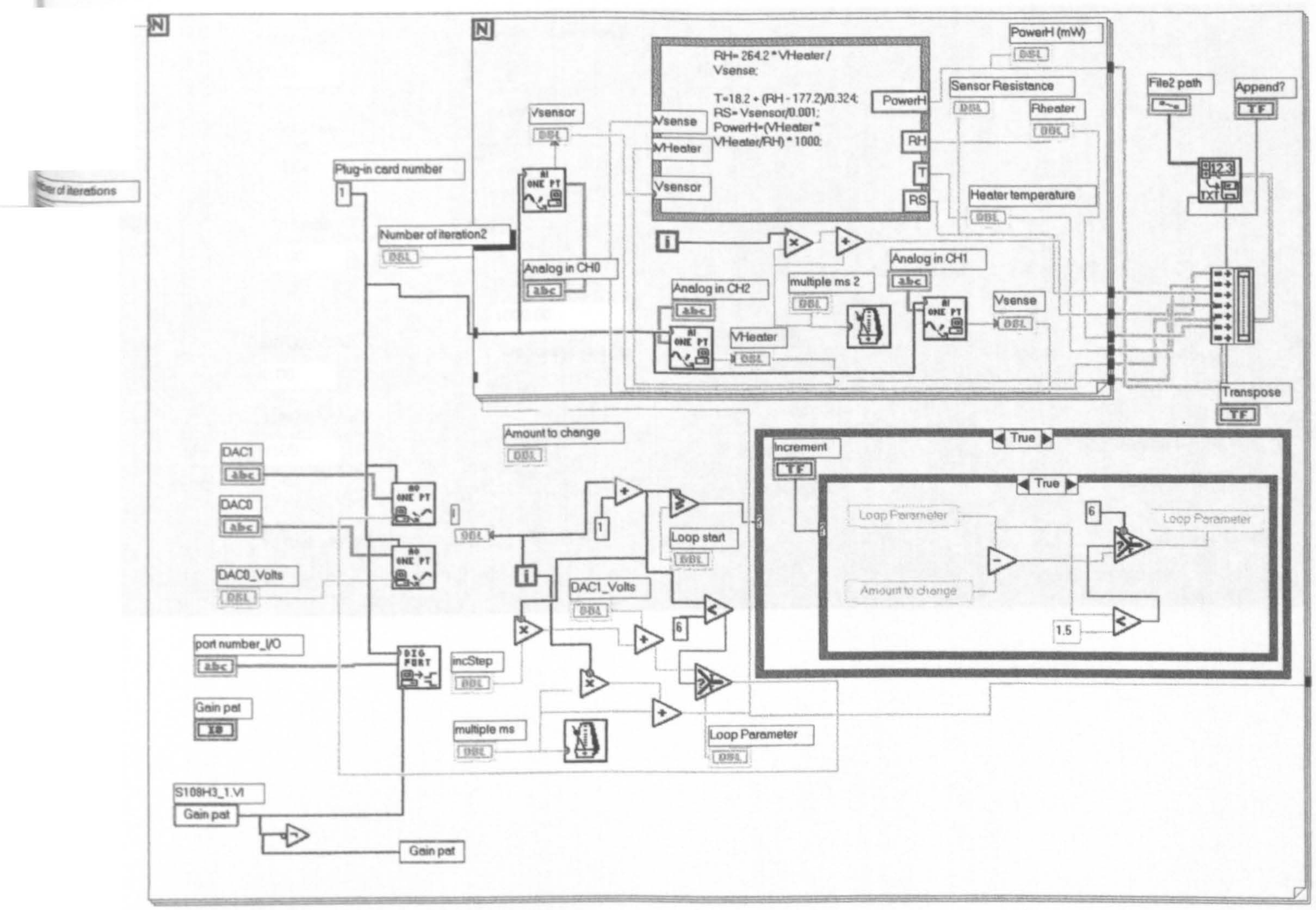
RH= 264.2 * VHeater / Vsense;
T=18.2 + (RH - 177.2)/0.324;
RS= Vsensor/0.001;
PowerH=(VHeater * VHeater/RH) * 1000;
Vsense
VHeater
Vsensor
PowerH
RH
T
RS
PowerH (mW)
Sensor Resistance
Rheater
Heater temperature
File2 path
Append?
Transpose
Vsensor
Plug-in card number
Number of iteration2
Analog in CH0
Analog in CH1
Analog in CH2
multiple ms 2
VHeater
Vsense
Amount to change
DAC1
DAC0
DAC0_Volts
port number_I/O
Gain pat
S108H3_1.VI
Gain pat
incStep
multiple ms
DAC1_Volts
Loop start
Loop Parameter
Increment
True
True
Loop Parameter
Amount to change
Loop Parameter
6
1.5
False
Amount to change
Loop Parameter
Loop Parameter
False

08H3_1.VI
31/99 03:27 PM

alog in CH0

Vsensor
0.21

number of iterations
11.00

I
10.00

alog in CH1

Vsense
1.34

Loop start
6.00

Number of iteration2
1.00

alog in CH2

VHeater
1.00

Loop Parameter
6.00

multiple ms
1000.00

multiple ms 2
100.00

Append?

C0

DAC0_Volts
0.00

Amount to change
1.00

Increment

Transpose

PowerH (mW)
5.09

AC1

DAC1_Volts
0.00

incStep
1.00

File2 path
c:\temp.txt

Rheater
196.95

Heater temperature
45.53

port number_I/O
0

Gain pat
0

Sensor Resistance
205.08

08H3_1.VI
31/99 03:27 PM

alog in CH0

alog in CH1

alog in CH2

AC0

AC1

Vsensor
0.21

Vsense
1.34

VHeater
1.00

DAC0_Volts
0.00

DAC1_Volts
0.00

number of iterations
11.00

I
10.00

Loop start
6.00

Loop Parameter
6.00

Number of iteration2
1.00

multiple ms
1000.00

Amount to change
1.00

incStep
1.00

Increment

multiple ms 2
100.00

Append?

Transpose

PowerH (mW)
5.09

File2 path
c:\temp.txt

Rheater
196.95

Heater temperature
45.53

port number_I/O
0

Gain pat
b 0

Sensor Resistance
205.08

8H3_1.VI
1/99 03:27 PM

1

log in CH0

Vsensor
0.21

number of iterations
11.00

I
10.00

alog in CH1

Vsense
1.34

Loop start
6.00

Number of iteration2
1.00

alog in CH2

VHeater
1.00

Loop Parameter
6.00

multiple ms
1000.00

multiple ms 2
100.00

Append?

C0

DAC0_Volts
0.00

Increment

Amount to change
1.00

Transpose

PowerH (mW)
5.09

AC1

DAC1_Volts
0.00

incStep
1.00

File2 path
c:\temp.txt

Rheater
196.95

Heater temperature
45.53

port number_I/O
0

Gain pat
0

Sensor Resistance
205.08